JOINT DENSITY-FUNCTIONAL METHODS FOR FIRST-PRINCIPLES CHEMISTRY IN SOLUTION

A Dissertation

Presented to the Faculty of the Graduate School

of Cornell University

in Partial Fulfillment of the Requirements for the Degree of

Doctor of Philosophy

by

Ravishankar Sundararaman

August 2013

JOINT DENSITY-FUNCTIONAL METHODS FOR FIRST-PRINCIPLES CHEMISTRY IN SOLUTION

Ravishankar Sundararaman, Ph.D.

Cornell University 2013

Solvents play an important role in many technologically relevant chemical processes and most biological systems, but thermodynamic phase-space sampling complicates their description in *ab initio* calculations. Joint density-functional theory (JDFT), which combines an electronic-density functional description of the solute with a classical density-functional description of the solvent, avoids phase-space sampling and enables an in-principle exact, intuitive description of solvated systems. In this dissertation, we develop the key ingredients for accurate joint density-functional calculations, derive simplified solvation models from JDFT and test these methods on model electrochemical systems.

First, for the solute subsystem requiring a detailed electronic-structure description, hybrid density-functionals, which mix in a fraction of the exact exchange energy, provide greater accuracy than standard semi-local approximations to electronic density-functional theory. However, for periodic systems, these functionals require denser Brillouin-zone sampling to resolve the zero wave-vector singularity in the exchange energy. We show that truncating the exchange kernel on the Wigner-Seitz cell of the $\vec{k}$-point sampled superlattice converges the energy of hybrid functionals exponentially with $\vec{k}$-points, on par with that of semi-local and screened-exchange functionals.

Next, practical JDFT calculations require computationally-efficient and accurate free energy functional approximations for real liquids. We develop the

framework for treating molecular fluids starting with the exact free energy of an ideal gas of rigid molecules. Within this framework, we construct a free energy functional for liquid water based on a microscopic picture of hydrogen bonding, present a general recipe to construct functionals for liquids of small molecules constrained to the bulk equation of state, and demonstrate that these functionals adequately capture the cavity formation energies and non-linear dielectric response of the solvent that are critical to a successful theory of *ab initio* solvation.

Simplified solvation models could further reduce the computational cost and enable a more intuitive description. However, standard polarizable continuum models (PCM's) that replace the solvent by a dielectric cavity along with empirical corrections, require a plethora of adjustable parameters. We derive a hierarchy of PCM's as limits of JDFT and demonstrate chemical accuracy for solvation energies of molecules with at most two adjustable parameters.

Finally, we study the underpotential deposition of Cu on Pt(111) as a model electrochemical system for testing theories of *ab initio* solvation, and demonstrate that an accurate solvation model is critical for a qualitatively correct description of the various adsorbate configurations on the surface, as well as for a quantitative prediction of the electrochemical potentials for the transitions between these configurations.

BIOGRAPHICAL SKETCH

Ravishankar Sundararaman was born in Mumbai, India in 1985, and grew up and attended school in Anushaktinagar (*lit.* atomic energy town), the residential campus of Bhabha atomic research center, an Indian national laboratory.

He majored in physics at the Indian Institute of Technology, Kanpur (IITK) starting in 2002, and engaged in undergraduate research in particle physics and cosmology with Prof. V. Ravishankar and Prof. Deshdeep Sahdev. He participated in summer research programs in experimental particle physics and particle accelerator design at the Tata institute of fundamental research with Dr. Vandana Nanal and Dr. R. G. Pillay in 2005 and 2006.

After graduating with an M.Sc. in Physics from IITK, he joined the graduate physics program at Cornell in 2007 with the intention of working on the international linear collider project. However, with the goal of more directly applied research, he switched to the electrical engineering research group of Prof. Sandip Tiwari in 2008 to explore the possibility of magnetophoretic lithography and to optimize the design of micro-electromechanical switches.

Shortly before scheduling his admission to candidacy exam, Ravishankar attended the density-functional theory mini-course taught by Prof. Tomás Arias and experienced a convergence of theoretical physics, practical applications to technology and his long-term hobby of computer programming. He then joined the Arias research group in the summer of 2010 to develop free energy functional approximations for real liquids, to construct simplified continuum solvation models and to apply electronic structure methods to the study of electrochemical systems. During this period, he also initiated the open-source electronic structure codebase, JDFTx, which is now the primary software for joint density-functional theory.

To all my families:
Siddharth, Amma, Appa,
my research group and
all my friends at Cornell.

ACKNOWLEDGEMENTS

If not for a beautifully mathematical as well as practical four week course on density-functional theory in the spring of 2010, this would have been a relatively uninspired treatise on why magnetophoretic lithography does not work. I am grateful to my advisor, Tomás Arias, for reintroducing me to the exciting world of theoretical physics. His excitement kept my cynicism at bay, while his caution checked my occasional bouts of boundless enthusiasm, keeping me balanced. I appreciate all his advice, research and otherwise, his help in fitting our specific research problems into a larger perspective, and perhaps most of all, his rigorous talk preparation regimen.

I am grateful to Neil Ashcroft, Sol Gruner and Carl Franck for serving on my special committee, for their valuable suggestions in research directions, including via their A exam questions, and for their help in improving this dissertation. I thank Cyrus Umrigar, Neil Ashcroft and Jim Sethna for many stimulating discussions. I also appreciate all the advice and help from Tomás Arias and Cyrus Umrigar in figuring out my plans after graduation and finding a postdoctoral appointment.

The research presented in this dissertation was supported as a part of the Energy Materials Center at Cornell (EMC^2), an Energy Frontier Research Center funded by the U.S. Department of Energy, Office of Science, Office of Basic Energy Sciences under Award Number DE-SC0001086. I thank Hector Abruña and the EMC^2 collaboration for the opportunity to participate in this exciting thrust, and suggesting interesting systems to study and test theories with.

I had no colleagues in our research group, only friends. It has been a memorable three years with Kendra Letchworth-Weaver and Katie Schwarz, working together on all our research problems, biking, climbing, hiking, pot-lucking and

conference-navigating. Deniz Gunceler joined our club for the last year, bringing his unbridled enthusiasm with him, and whole-heartedly joined the JDFTx development effort. I also thank the rest of my close friends at Cornell, Turan Birol, Hitesh Changlani, Yanjiun Chen, Colwyn Gulliford, Ben Kreis and Stephen Poprocki, for enriching my six years in Ithaca.

Finally, I am grateful to my family for getting me on the path that got me here. With a condensed matter physicist father and an organic chemist mother, I grew up with mathematics and science as a way of life. After a brief teenage rebellion involving cosmology and particle physics, I eventually found my way to our family business of material science, as did my brother Siddharth; we only managed to diversify it from experiment to computation. I thank them for all their support, encouragement and advice along the way.

TABLE OF CONTENTS

LIST OF TABLES

LIST OF FIGURES

CHAPTER 1

INTRODUCTION

The fundamental laws of physics necessary to describe most of the material world at the atomic scale, the electromagnetic interaction and non-relativistic quantum mechanics, were known by the end of the first quarter of the twentieth century. Owing to their characteristic energy and length scales, the other fundamental interactions contribute negligibly to the properties of matter. Relativistic effects become moderately important for the heavier elements, but are largely negligible for most properties of the elements in the first four rows of the periodic table, which compose over 99% of the earth's crust.

The spin-independent Schrödinger equation with the Hamiltonian,[1]

$$\hat{H} = -\frac{1}{2}\sum_i \nabla_i^2 - \sum_{\alpha,I_\alpha} \frac{1}{2M_\alpha}\nabla_{I_\alpha}^2 + \sum_{i<i'} \frac{1}{|\vec{r}_i - \vec{r}_i'|} - \sum_{i,\alpha,I_\alpha} \frac{Z_\alpha}{|\vec{r}_i - \vec{R}_{I_\alpha}|} + \sum_{(\alpha,I_\alpha)<(\alpha',I'_{\alpha'})} \frac{Z_\alpha Z_{\alpha'}}{|\vec{R}_{I_\alpha} - \vec{R}_{I'_{\alpha'}}|}, \quad (1.1)$$

comprising the kinetic energy for a set of electrons at coordinates $\{\vec{r}_i\}$ with spins $\{\sigma_i\}$ as well as sets of nuclei of atomic numbers Z_α and masses M_α at coordinates $\{\vec{R}_{I_\alpha}\}$ with spins $\{\Sigma_{I_\alpha}\}$, along with Coulomb interactions between all pairs of particles,[2] therefore adequately describes most properties at the atomic scale. We then only need to solve that equation for the many-body wavefunction $\Psi(\{\vec{r}_i\sigma_i\}, \{\{\vec{R}_{I_\alpha}\Sigma_{I_\alpha}\}\})$, antisymmetric in interchanges of any two electron coordinates $\in \{\vec{r}_i\}$ of equal σ_i and symmetric or antisymmetric in any two like nuclear

[1] Here and throughout this dissertation, we use atomic units $4\pi\epsilon_0 = e = \hbar = m_e = k_B = 1$. This leads to distances in bohrs, $a_0 = 4\pi\epsilon_0\hbar^2/(m_e e^2)$, and energies in Hartrees, $E_h = \hbar^2/(m_e a_0^2)$. Table E.1 lists the conversions from conventional units to these atomic units, for all relevant physical quantities.

[2] In finite systems such as individual molecules or ions, the number of electrons may differ from the sum of atomic numbers of all the nuclei in that system. However, for bulk matter, the extensivity of thermodynamic properties depends upon the electrical neutrality of the system [95].

coordinates $\in \{\vec{R}_{I_\alpha}\}$ of equal Σ_{I_α}, depending on the spin of nuclear species α. However, as Dirac succinctly summarized in 1929 [34],

> The underlying physical laws necessary for the mathematical theory of a large part of physics and the whole of chemistry are thus completely known, and the difficulty is only that the exact application of these laws leads to equations much too complicated to be soluble. It therefore becomes desirable that approximate practical methods of applying quantum mechanics should be developed, which can lead to an explanation of the main features of complex atomic systems without too much computation.

1.1 Electronic structure methods

The first, almost universally employed, approximation to the full many-body quantum mechanical problem (1.1) is the Born-Oppenheimer separation of electronic and nuclear motion [19]. In typical systems of interest, the energy scales of center-of-mass motion of atoms and molecules ($\sim 10^{-3} E_h$ or room temperature) are negligible on the electronic energy scale ($\sim 1 E_h$), so that the typical momenta in the nuclear and electronic degrees of freedom are comparable, implying that $\langle \nabla_i^2 \rangle \sim \langle \nabla_{I_\alpha}^2 \rangle$. Consequently the contribution of the nuclear kinetic energy is smaller than the electronic kinetic energy by a factor $\sim 1/M_\alpha < 10^{-3}$ and can be neglected as a first approximation. This leads to the many-body Hamiltonian,

$$\hat{H}_{\text{el}} = -\frac{1}{2} \sum_i \nabla_i^2 + \sum_{i<i'} \frac{1}{|\vec{r}_i - \vec{r}_i'|} + \sum_i V(\vec{r}_i) + U_{\text{nuc}}, \tag{1.2}$$

for the motion of electrons in an external potential due to fixed nuclei, $V(\vec{r}) = -\sum_{\alpha,I_\alpha} Z_\alpha/|\vec{r} - \vec{R}_{I_\alpha}|$, with a constant energy contribution from nuclear repulsion, U_{nuc} given by the final term of (1.1). Within the Born-Oppenheimer approximation, the ground state energy of this Hamiltonian as a function of nuclear coordinates, serves as the potential for nuclear motion.

The exact electronic structure problem, that is the determination of (appropriately antisymmetric) eigenfunctions $\psi(\{\vec{r}_i\})$ of the many-body electronic Hamiltonian (1.2), remains a rather formidable task. A brute force computational attempt of solving this problem for a tiny system, such as a single water molecule with just 10 electrons and a sparse discretization of three-dimensional space with 10^3 points, would require $\sim (10^3)^{10}/(5!)^2$ numbers or $\sim 10^{15}$ terabytes of memory just to store the wavefunction. It would therefore not fit on even the largest compute clusters currently available. (Compare to 200 terabytes on TACC Stampede deployed in 2013, for example.) Moreover, both the size of the wavefunction and the computational effort scale exponentially with the number of electrons.

The simpler problem of finding only the ground-state or lowest eigenfunction and energy permits a variational approach. By the Rayleigh-Ritz principle, the ground state energy minimizes the expectation value of the Hamiltonian over the space of all normalized antisymmetric wavefunctions,

$$E_0 = \min_{\psi,\langle\psi|\psi\rangle=1} \langle\psi|\hat{H}_{\text{el}}|\psi\rangle. \tag{1.3}$$

Restricting the space of full many-body wavefunctions $\psi(\{\vec{r}_i\})$ to a practicable subset then results in an approximate theory. In particular, selecting only the wavefunctions of non-interacting fermionic systems, the Slater determinant form $\psi(\{\vec{r}_i\}) = \sum_p (-1)^p \prod_i \phi_i(\vec{r}_{p_i})$ where $\{\phi_i(\vec{r})\}$ is a set of orthonormal single-

particle functions and p is a permutation, results in Hartree-Fock theory. For simplicity, we drop explicit spin indices here and assume implicit sums over spin in all energy terms (and a product in the wavefunction). The above variational principle simplifies to the minimization of the energy functional,

$$E_{\mathrm{HF}}[\{\phi_i\}] = U_{\mathrm{nuc}} + \sum_i \int d\vec{r}\,\phi_i \left(-\frac{\nabla^2}{2} + V_{\mathrm{nuc}}(\vec{r})\right)\phi_i + \sum_{i,j} \int d\vec{r} \int d\vec{r}\,' \frac{\phi_i(\vec{r})\phi_i^*(\vec{r})\phi_j^*(\vec{r}\,')\phi_j(\vec{r}\,') - \phi_i(\vec{r})\phi_j^*(\vec{r})\phi_i^*(\vec{r}\,')\phi_j(\vec{r}\,')}{2|\vec{r} - \vec{r}\,'|} \quad (1.4)$$

over all sets of orthonormal single-particle functions. The example 10-electron problem considered above would now require only 10×10^3 numbers or $\sim$ 80 kilobytes of memory to store one set of orbitals, which would fit in the L2 cache of smartphone processors released in 2013. The computational effort and storage requirements scale polynomially with the system size and number of electrons. However, the predictions of Hartree-Fock theory for the structures of molecules and solids and the energetics of processes at the atomic scale, are not accurate enough to make it a useful first-principles theory of materials.

Hartree-Fock theory instead serves as a starting point for quantum chemistry methods. The single-particle orbitals that minimize the energy functional (1.4) are the lowest eigenfunctions of the corresponding Euler-Lagrange equation with respect to one orbital. Extending that set to include higher 'unoccupied' eigenfunctions leads to a useful basis for the many-body wavefunction. First, the full many-body wavefunction can be expanded as a linear combination of Slater determinants composed of orbitals selected from this set. Minimizing over that space results in the configuration-interaction (CI) method, with the level of approximation controlled by selecting the number of orbitals in the basis. This method also scales exponentially with the number of electrons, but with a far more manageable prefactor making calculations of $O(10)$ electrons

possible. Another popular post-Hartree-Fock method, the coupled-cluster (CC) approach, restricts the many-body wavefunctions to those obtained by an exponential of a finite excitation operator applied to the Hartree-Fock wavefunction. The computational cost of this approach scales polynomially with the number of electrons, but with a high exponent: 6 when restricted to single and double excitations (CCSD), and 7 when including triple excitations perturbatively (CCSD(T)). This approach is extremely accurate when properly converged, but it is practically applicable only to small molecular systems, and it is difficult to converge with respect to the employed basis set. (See [156] for a detailed description of these methods.)

Monte-Carlo methods provide an alternate route to sample the very high-dimensional spaces characteristic of the many-body wavefunction. Variational Monte-Carlo (VMC) evaluates the expectation value of (1.3) for certain parametrized classes of beyond Slater-determinant wavefunctions by statistical sampling, and then optimizes the involved parameters. Diffusion Monte-Carlo (DMC) stochastically solves an imaginary-time Schrödinger equation which damps out the excited states in comparison to the ground state with the evolution of time. These methods scale better to larger systems, including solids with the assumption of periodic boundary conditions (see [43] for a review), and routine calculations handle $O(100)$ electrons (per simulation cell).

1.2 Electronic density-functional theory

Wave-function approximations are capable of describing electronic structure to a high degree of accuracy, but as noted, require tremendous computational re-

sources even for calculations of small systems with few electrons. The working space of these methods, a large set of Slater determinants (CI, CCSD) or an ensemble of electron configurations (QMC), contains an extraordinary amount of detailed information about the entire spectrum of excitations, beyond just the ground state energy which determines the dominant Born-Oppenheimer surface and the equilibrium properties of matter. It must therefore be possible to construct at least an approximate theory of the electronic ground state energy that avoids all the extra information and associated computational overhead of the many-body wavefunction. In fact, in the context of the Hartree-Fock approximation, Dirac [35] noted

> The whole state of the atom is completely described by the electric density; it is not necessary to specify the individual three-dimensional wave functions that make up the total electric density. Thus one can deal with any number of electrons by working with just one matrix density function.

Hohenberg and Kohn [68] showed that it is, in fact, possible to construct an exact theory of the electronic ground state energy in terms of the electron density alone. The constrained-search procedure introduced by Levy [92] most easily motivates this theorem. The minimization over all many-body wavefunctions in the variational principle (1.3) splits into a minimization over all possible wavefunctions resulting in the same ground-state density, followed by a minimization over all possible ground-state densities,

$$\begin{aligned} E_0 &= \min_{\psi} \langle \psi | \hat{H}_{\mathrm{el}} | \psi \rangle \\ &= \min_{n} \left[\min_{\psi \mapsto n} \langle \psi | \hat{H}_{\mathrm{el}} | \psi \rangle \right]. \end{aligned} \tag{1.5}$$

The key observation, then, is that the external potential on the electrons (which arises from the Coulomb interactions with the nuclei) couples to the electron density alone, so that the expectation value of the Hamiltonian (1.2) separates to

$$\langle\psi|\hat{H}_{\text{el}}|\psi\rangle = \langle\psi|\hat{H}_{\text{int}}|\psi\rangle + \int d\vec{r}V(\vec{r})n(\vec{r}) + U_{\text{nuc}}, \tag{1.6}$$

where the internal part of the Hamiltonian, $\hat{H}_{\text{int}}$, comprises only the electronic kinetic energy and electron-electron Coulomb operators. Only the first part depends on the wavefunction explicitly, and therefore

$$E_0 = \min_n \left[\underbrace{\min_{\psi\mapsto n}\langle\psi|\hat{H}_{\text{int}}|\psi\rangle}_{F_{\text{HK}}[n]} + \int d\vec{r}V(\vec{r})n(\vec{r}) \right] + U_{\text{nuc}}. \tag{1.7}$$

The inner minimization yields a universal functional, $F_{\text{HK}}[n]$, independent of the external potential on the electrons and hence the physical system. If this universal functional for the internal electronic energy given the electron density were exactly known, then minimizing the total energy functional (1.7) with respect to the electron density directly produces the exact ground state energy, without ever working with the many-body wavefunction. Figure 1.1 summarizes the reduction of the individual electron coordinate-based many-body description to the electron density level. In our tiny water example, the electron density occupies a mere 8 kilobytes and would fit even in the L1 cache of smartphone processors.

The mapping from electron density to the energy of a many-electron system extends beyond the ground state to the thermodynamic functions. Mermin [108] showed that the equilibrium electron density of a finite-temperature system completely determines its Helmholtz energy. The equilibrium Helmholtz energy at temperature T minimizes the functional, $A[\hat{\rho}] = \text{Tr}[\hat{\rho}\hat{H} + T\hat{\rho}\ln\hat{\rho}]$ over all density matrices, $\hat{\rho}$, representing the state of an ensemble of many-electron

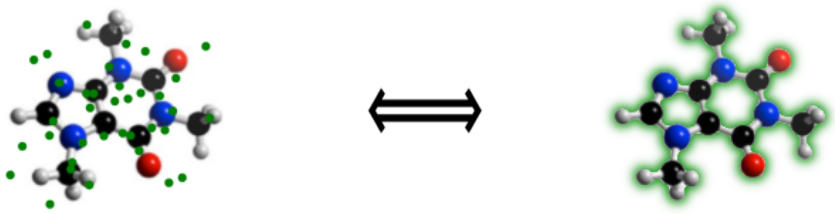

Figure 1.1: Exact equivalence between many-body theory in terms of individual electron coordinates (green dots on the left) and density-functional theory in terms of total electron density (green cloud on the right), for static nuclei.

systems. As before, the coupling to the nuclear potential occurs exclusively through the electron density $n(\vec{r}) = \mathrm{Tr}\hat{\rho}\hat{n}$, and the constrained-search procedure (minimizing over densities, followed by minimizing over density-matrices for each density) yields

$$A_0 = \min_n \left[\underbrace{\min_{\hat{\rho}\mapsto n} \mathrm{Tr}\left\{\hat{\rho}\hat{H}_{\mathrm{int}} + T\hat{\rho}\ln\hat{\rho}\right\}}_{F^T_{\mathrm{HKM}}[n]} + \int d\vec{r}V(\vec{r})n(\vec{r}) \right] + U_{\mathrm{nuc}}. \tag{1.8}$$

Once again, the inner minimization yields a universal functional, $F^T_{\mathrm{HKM}}[n]$, independent of the system or external potential. If explicitly known, this functional would enable exact calculation of the equilibrium free energy of any many-electron system by optimizing the electron density alone, again, without involving many-body wavefunctions or density matrices. (See [123] for detailed proofs of such density-functional theorems.)

This density-functional method, although exact in principle, requires knowledge of a universal functional defined as the solution to a many-body problem constrained to each electron density. The power of the method lies, however, in being able to construct approximations to the universal functional constrained to properties of special physical systems for which results are known exactly or

approximated easily.

The history of density-based methods in fact predates the Hohenberg-Kohn theorem by four decades, and begins with the Thomas-Fermi method [161, 41]. Within the density-functional perspective above, this method approximates the universal functional by

$$F_{\mathrm{TF}}[n]s = \int d\vec{r} e_{\mathrm{T}}(n(\vec{r})) + \int d\vec{r} \int d\vec{r}' \frac{n(\vec{r})n(\vec{r}')}{2|\vec{r} - \vec{r}'|}. \tag{1.9}$$

The first term approximates the kinetic energy of the electrons of an inhomogeneous system as the integral of the kinetic energy density, $e_{\mathrm{T}}(n) = \frac{3}{10}(3\pi^2)^{2/3}n^{5/3}$, of a uniform electron gas of density n equal to the local electron density $n(\vec{r})$ at each point in the system. The second term replaces the electron-electron Coulomb repulsion by its mean-field estimate, known as the Hartree term. Unfortunately, this approximation does not capture chemical bonding and predicts a set of unbound atoms as the equilibrium configuration for all systems.

Dirac [36] improved the model by accounting for the exchange energy or Fock term (the second part of the final term of (1.4)) in a local-density manner analogous to the kinetic energy. This amounts to replacing $e_{\mathrm{T}}(n)$ with $e_{\mathrm{TX}}(n) = e_{\mathrm{T}}(n) + e_{\mathrm{X}}(n)$, where $e_{\mathrm{X}}(n) = -\frac{3}{4}(3/\pi)^{1/3}n^{4/3}$ is the exchange energy-density of the uniform electron gas of density n. This correction is not sufficient to improve on Thomas-Fermi theory, however, as the deficiency lies in the description of the kinetic energy. Further, replacing $e_{\mathrm{T}}(n)$ with $e_{\mathrm{TXC}}(n)$, the exact energy density of a uniform electron gas obtained from quantum Monte-Carlo calculations, diminished by the mean-field repulsion, is also insufficient to describe chemical bonding.

To remedy the poor description of electron kinetic energy in the approximate density functional, Kohn and Sham [82] employed the exact kinetic energy of a

non-interacting electron system with the same density as the interacting system,

$$T_S[n] = \min_{\psi_{\rm NI}\mapsto n}\left[-\frac{1}{2}\sum_i \int d\vec{r}\,\phi_i\nabla^2\phi_i\right] \tag{1.10}$$

where $\psi_{\rm NI}$ is a Slater determinant composed of orthonormal orbitals $\{\phi_i(\vec{r})\}$. Consequently, the variational problem for the ground-state energy reduces to[3]

$$E_0 = \min_{\{\phi_i(\vec{r})\}}\left[-\frac{1}{2}\sum_i \int d\vec{r}\,\phi_i\nabla^2\phi_i + \int d\vec{r}\int d\vec{r}'\,\frac{n(\vec{r})n(\vec{r}')}{2|\vec{r}-\vec{r}'|} + E_{\rm XC}[n] + \int d\vec{r}\,V(\vec{r})n(\vec{r})\right] + U_{\rm nuc}, \tag{1.11}$$

which still remains exact in principle because the exchange-correlation functional is formally defined by

$$E_{\rm XC}[n] \equiv F_{\rm HK}[n] - T_S[n] - \int d\vec{r}\int d\vec{r}'\,\frac{n(\vec{r})n(\vec{r}')}{2|\vec{r}-\vec{r}'|}. \tag{1.12}$$

The local-density approximation (LDA) [127] for this remaining piece, $E_{\rm XC}[n] = \int d\vec{r}\,e_{\rm XC}^{\rm LDA}(n(\vec{r}))$, with the local function $e_{\rm XC}(n)$ constrained to produce the exact energy density of the uniform electron gas of density n [25], is now sufficient for an accurate description of the geometries of molecules and solids, and to a slightly lesser extent, energies of formation and chemical reactions.[4]

Exchange-correlation functionals beyond the local-density approximation further improve the accuracy of the Kohn-Sham approach. Generalized-gradient approximations (GGA's) [128], $E_{\rm XC}[n] = \int d\vec{r}\,e_{\rm XC}^{\rm GGA}(n(\vec{r}), \nabla n(\vec{r}))$, additionally use the gradient of the electron density ∇n to better account for the inhomogeneity in the system. Meta-generalized gradient approximations (mGGA's) [129], $E_{\rm XC}[n] = \int d\vec{r}\,e_{\rm XC}^{\rm mGGA}(n, \nabla n, \nabla^2 n, \tau)$ improve the accuracy further by including dependences on the Laplacian of the electron density and the orbital

[3] Except for subtleties of V-representability that can be resolved by working with ensembles; see [123].

[4] This approach generalizes to spin-polarized systems by working with spin densities, $n_\uparrow(\vec{r})$ and $n_\downarrow(\vec{r})$, instead of the total electron density, $n(\vec{r})$. In fact, most modern exchange and correlation functionals are formulated in terms of the spin densities. We work predominantly with non-magnetic systems here and drop the spin indices throughout for simplicity.

kinetic energy density, $\tau = \frac{1}{2}\sum_i |\nabla\phi_i|^2$ (which requires a slight generalization of the Kohn-Sham formalism to include orbital dependence in the exchange-correlation functional).

Electronic density functional theory with semi-local exchange-correlation approximations (employing density and gradients) enable routine calculations of ground state properties of systems with $O(1000)$ electrons (per unit cell) on standard workstations, and scale to over 10^6 electrons on supercomputers [20]. Additionally, they serve as a starting point for calculations employing the GW approximation [63] for quasi-particles (see [72] for details) or the Bethe-Salpeter equation [138] for optical excitations. The accuracy of semi-local density functionals is sufficient for material properties such as lattice constants, equilibrium geometries and elastic moduli, but do not meet the target accuracy $\sim 10^{-3} E_h$ necessary for reliably predicting chemical reactions at room temperature [177].[5]

Hybrid density functionals [13, 1], which mix in a fraction of the exact exchange energy (Fock term of 1.4), $E_{\text{XC}}^{\text{hyb}} = \alpha E_X[\{\phi_i\}] + (1-\alpha)E_X[n] + E_C[n]$ significantly improve upon this accuracy by more effectively canceling the self-interaction error introduced in the mean-field (Hartree) term.[6] However, in periodic systems, these functionals traditionally suffer from poorer convergence with the number of $\vec{k}$-points used for Brillouin-zone sampling than semi-local functionals, which increases their already much higher computational cost. Chapter 2 traces this issue to the regularization of the integrable singularity at zero wave-vector, and develops a method that brings the $\vec{k}$-point convergence of hybrid functionals on a par with that of traditional semi-local functionals.

[5] The energy scale for electronic excitations in many systems ($\sim$ 1 eV) is typically much larger than room temperature $\approx$ 0.026 eV; accounting for thermal nuclear motion in the Born-Oppenheimer surface corresponding to the electronic ground state suffices for these systems.

[6] Hartree-Fock is exact and self-interaction free in the one-electron limit, whereas density-functional theory with an approximate exchange-correlation functional is typically not.

1.3 First-principles calculations for solvated systems

Electronic density-functional theory enables practical first-principles calculations of the ground-state structures and energies of molecules and solids. Minima in the Born-Oppenheimer surface, that is the energy as a function of nuclear coordinates, correspond to stable or meta-stable states in the electronic ground state and infinite nuclear mass limit. The estimation of vibrational levels and zero-point energies from the second derivatives of this surface at its minima, allows perturbatively accounting for low temperatures and finite nuclear masses in systems which involve excursions of nuclei that remain overall localized to a small region of space.

A perturbative treatment of this nature is possible for solids and isolated molecules; the latter in combination with kinetic theory approximates gases in the dilute limit. Classical liquids [12] and dense gases, however, fall in neither of these two extremes, since the nuclei neither remain localized nor do they move in groups as molecules with negligible intermolecular interaction. Computer simulations of even the equilibrium properties of liquids require either molecular dynamics or Monte Carlo approaches to sample the thermodynamic phase space of nuclear motion [4]. The most straightforward first-principles approach to describe fluids [22] combines molecular dynamics with electronic density-functional theory to compute forces on the nuclei in each configuration. This requires tens to hundreds of thousands of time steps for adequate sampling, and is therefore several orders of magnitude more expensive than calculations for solid state systems of comparable size.

Solvents play a vital role in the structure of biological systems [93] and in the

pathways of chemical reactions, in particular, at catalyst surfaces [166]. Electronic structure methods have the potential to lend insight to reaction mechanisms and aid the design of functional materials, but the computational cost associated with phase-space sampling for the fluid restricts their widespread application to such systems. Further, the estimation of free energy, the key quantity in the determination of equilibria and reaction pathways, requires an additional thermodynamic integration within the molecular-dynamics based methods, further exacerbating the cost of these methods.

Electrochemical interfaces, involving a solid electrode surface in contact with a liquid electrolyte with ionic species, have important technological applications in catalysis, energy conversion and storage, and could tremendously benefit from theoretical studies at the electronic structure level. The structure of the interface including the identity and concentration of adsorbents is highly sensitive to the potential applied to the electrode (which sets the chemical potential of the electrons), which makes theoretical study of these systems challenging and interesting.

Figure 1.2 illustrates possible approaches for dealing with systems of this nature, using the example of underpotential deposition[7] of copper on platinum (which we study in detail in Chapter 9). In this system, a single crystal platinum surface in an aqueous solution with cupric and chloride ions is covered by different fractions of copper along with co-adsorbed chloride ions, depending on the electrode potential. A first-principles study of this system would ideally calculate the free energy of various candidate structures on the surface as a function of electrode potential, to determine the most stable configuration

[7] An underpotential deposition process is one that occurs at an electrode potential less favorable than the equilibrium potential for the corresponding bulk deposition.

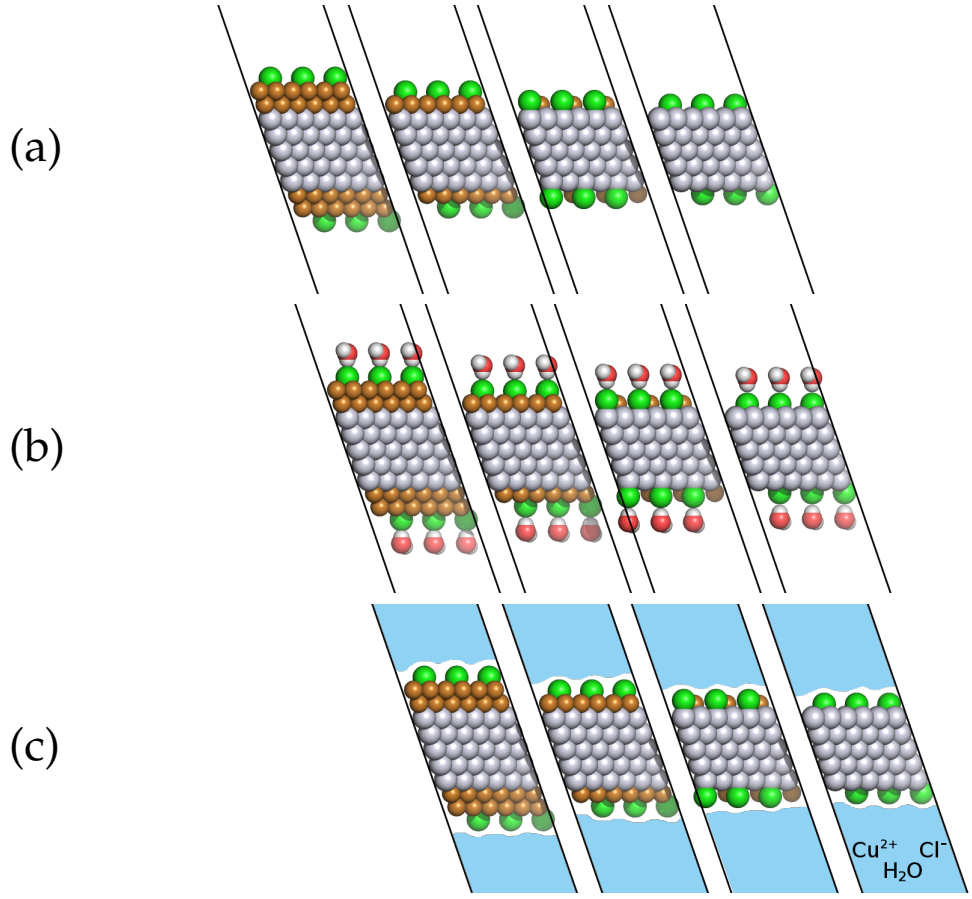

Figure 1.2: Practical approaches for first-principles calculations of solvated systems, (a) ignore solvent, (b) include explicit solvent molecules or (c) employ a direct description of the equilibrium effect of the solvent, typically using a continuum approximation of some variety.

at each potential and the potentials for transitions between them. The first question that such a study faces then, is how does one handle the electrolyte?

Many theoretical studies of such processes at solid-liquid interfaces ignore the liquid altogether [87], and approximate the system by a solid-vacuum interface (Figure 1.2(a)). The resulting simplification enables rapid exploration of many configurations to glean a qualitative understanding of the system, but the drastic approximation precludes quantitative predictions. The next level of approximation replaces the liquid with a single snapshot of one or two mono-

layers of solvent molecules on the surface [94], and requires intuitive placement of those molecules to best represent the solvent effect (Figure 1.2(b)). Often, no configuration of solvent molecules commensurate with the periodicity of the surface structure can even approximate relevant low energy snapshots of the solvent, necessitating larger, and hence more expensive, simulation cells. Such an approach may be more accurate than replacing the liquid by vacuum, but requires much more effort, human as well as computational. More importantly, there is no guarantee that a single snapshot faithfully represents the thermodynamically-averaged equilibrium effect of the solvent. The full molecular dynamics approach gets around some of these difficulties, but at a prohibitive computational cost. Additionally, the energy landscapes next to the highly polar surfaces typical of these systems introduce difficulties in ensuring ergodicity of the phase-space sampling.

Including explicit solvent molecules, either as a well-designed single snapshot or with molecular dynamics, introduces unnecessary complexity in the study, which detracts from understanding the subsystem of interest (the copper layer and co-adsorbed chloride ions in the current example). The ideal method for studying such systems would therefore focus the electronic structure description precisely on that portion of the system, while abstracting away the equilibrium effect of the liquid (Figure 1.2(c)). The following sections review theoretical frameworks that permit such a description, and the remainder of this dissertation develops accurate and computationally-efficient methods within those frameworks to enable focused quantitative studies of solvated systems.

1.4 Classical density-functional theory

The study of solvated systems would benefit from an abstract description of equilibrium properties of an inhomogeneous liquid, without invoking individual configurations of liquid molecules and phase-space sampling. We previously motivated electronic density-functional theory with a similar goal: avoid the many-body wavefunction that works with individual electron coordinates in treatments of the ground state properties of an electronic system. Not surprisingly, it is possible to generalize the Hohenberg-Kohn and Mermin theorems to enable a so-called classical density-functional description of liquids.

The equilibrium grand free energy of an arbitrary system composed of nuclei and electrons governed by the Hamiltonian (1.1) in a set of external potentials $\{V_\alpha(\vec{r})\}$ acting on each nuclear species with chemical potential μ_α,[8] is given by

$$\Phi_0 = \min_{\hat{\mathrm{P}}} \left[\mathrm{Tr}(\hat{H}\hat{\mathrm{P}} + T\hat{\mathrm{P}} \ln \hat{\mathrm{P}}) + \sum_\alpha \int d\vec{r} (V_\alpha(\vec{r}) - \mu_\alpha) N_\alpha(\vec{r}) \right], \tag{1.13}$$

where $\hat{\mathrm{P}}$ is a density matrix representing a grand-canonical ensemble of many-body (electron + nuclear) wavefunctions, and the nuclear densities N_α are the expectation values of the density operator $\hat{N}_\alpha(\vec{r})$ in the density matrix $\hat{\mathrm{P}}$. As before, since the external potential couples to the nuclear site densities alone, the constrained search procedure yields

$$\Phi_0 = \min_{\{N_\alpha\}} \left[\underbrace{\min_{\hat{\mathrm{P}} \mapsto \{N_\alpha\}} \mathrm{Tr}(\hat{H}\hat{\mathrm{P}} + T\hat{\mathrm{P}} \ln \hat{\mathrm{P}})}_{\Phi_{\mathrm{CDFT}}[\{N_\alpha\}]} + \sum_\alpha \int d\vec{r} (V_\alpha(\vec{r}) - \mu_\alpha) N_\alpha(\vec{r}) \right]. \tag{1.14}$$

[8] The definition of chemical potentials of charged species requires some care since neutrality is critical in the thermodynamic limit [95]. The simplest resolution is to work in a restricted grand canonical ensemble where the individual particle numbers may vary with the constraint of zero total charge. The energy of introducing neutral combinations of particles into the system defines the chemical potentials up to an overall additive constant. Absolute chemical potentials may be defined by coupling each species to an infinitesimal test charge $\delta\tilde{\rho}(\vec{k})$ with a single Fourier component and taking the limit $\vec{k} \to 0$ (see [164, 111] for details).

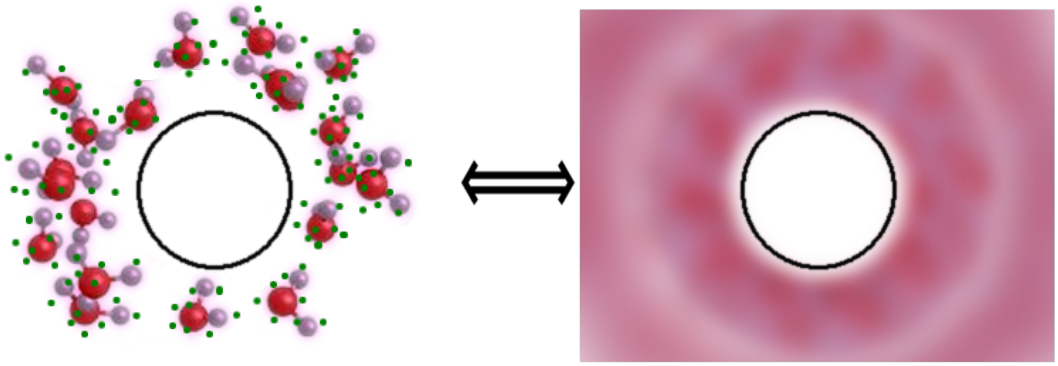

Figure 1.3: Exact equivalence between many-body theory in terms of individual nuclear (red and white circles on the left) as well as electronic coordinates (green dots on the left) and classical density-functional theory in terms of nuclear site densities alone (overlapping red and white clouds (or pink haze) on the right).

Exact predictions for physical systems require, in principle, the minimization of a universal system-independent density functional $\Phi_{\text{CDFT}}[\{N_\alpha\}]$ coupled to external potentials over nuclear densities alone, the electronic degrees of freedom having been integrated out. Figure 1.3 illustrates the reduction of the many-body description of a collection of water molecules in a repulsive external potential to a classical density-functional description in terms of oxygen and hydrogen site densities alone. Despite the prefix 'classical', the exact density functional is fully quantum-mechanical and does not even invoke the Born-Oppenheimer approximation.

As before, the exact functional is unknown and must be approximated for practical calculations. The derivation above establishes the existence of a truly universal functional that describes all matter in terms of the densities of all nuclear species. However, it would be next to impossible to construct an approximation for this 'functional of everything'. Instead, we focus on a particular substance, or even one thermodynamic phase of a substance, such as liquid water, and construct an approximation for inhomogeneous configurations of just

that material. Further, an approximate Hamiltonian suitable for the chosen material, such as one composed of pair-potentials, can replace the full many-body Hamiltonian in the above derivation (see appendix B of [57] for a proof), and the free energy functional approximation can target reproducing the properties of the simplified model instead.

The classical density functional theory of simple fluids consisting of particles interacting with pair-wise but orientation-independent interactions has been studied extensively [12]. In particular, the hard sphere fluid consisting of particles that interact with the pair potential $U(r_{ij}) = +\infty$ for $r_{ij} < 2R_{\mathrm{HS}}$ and 0 otherwise, where R_{HS} is the radius of the hard sphere, has been studied in great detail with computer simulations as well as density-functional theory. See [4] for an introduction to computer simulations of liquids and [57] for the theory of simple fluids. We briefly review the density-functional theory of simple classical liquids here and in Section 4.2.1, and refer the interested reader to chapter 6 of [57] for more details.

The free energy functionals for simple (mono-atomic) fluids are usually written as[9]

$$\Phi_{\mathrm{CDFT}}[N] = \underbrace{T \int d\vec{r} N(\vec{r})(\ln N(\vec{r}) - 1)}_{\Phi_{\mathrm{id}}[N]} + F_{\mathrm{ex}}[N], \tag{1.15}$$

separating out the exact free energy of the ideal gas $\Phi_{\mathrm{id}}[N]$, and approximating the remainder, the excess functional $F_{\mathrm{ex}}[N]$. Unfortunately, the local density approximation $F_{\mathrm{ex}}[N] \approx \int d\vec{r} f_{\mathrm{ex}}(N(\vec{r}))$, which works reasonably well in the elec-

[9]Here, we denote one-particle densities of nuclei by $N(\vec{r})$ instead of the more conventional $\rho(\vec{r})$ in the classical density-functional theory literature. We adopt this notation in order to maintain clarity and reduce the number of superscripts and subscripts in the following when we combine electronic and classical density functional theories. Throughout this dissertation, unless mentioned otherwise, $N(\vec{r})$ (with subscripts for distinguishing species) are nuclear densities, $n(\vec{r})$ are electron densities, and $\rho(\vec{r})$ are charge densities.

tronic case, is completely inadequate even for classical fluids with as simple a Hamiltonian as the hard sphere fluid. The weighted-density approximation [31] $F_{\text{ex}}[N] \approx \int d\vec{r} N(\vec{r}) A_{\text{ex}}(w * N(\vec{r}))$, with a weight function $w(r)$ constrained to reproduce the radial distribution function, $g_T(r)$, of the uniform fluid at temperature T obtained from computer simulations, compares much more favorably with computer simulations for predictions of inhomogeneous fluid properties. The hard sphere fluid in one dimension permits an exact analytical solution to the many-body problem [126]. This limit enables the construction of highly accurate analytical functionals for the three dimensional hard sphere fluid [134, 159], which do not require properties extracted from computer simulations as input. The hard sphere fluid also forms the reference system for perturbative descriptions of other simple fluids, such as the Lennard-Jones fluid with a 6-12 pair-potential [125]. (See [135] for a review of functionals for the hard sphere fluid, and Section 4.2.1 for a more detailed introduction to functionals for model fluids.)

Model Hamiltonians for molecular (poly-atomic) fluids are typically constructed in the reduced interaction site model (RISM) framework, which consist of pair-potentials between multiple sites (typically atom positions) with a rigid molecular geometry [26]. The task of constructing free energy functionals for these fluids is far more complicated; even the ideal gas free energy, $\Phi_{\text{id}}[\{N_\alpha\}]$, does not permit a closed-form analytical approximation and requires Monte-Carlo computation methods [27]. Lischner et al. [96] show that, analogously to the Kohn-Sham approach for electrons, switching from the site densities, $\{N_\alpha\}$, to effective potentials for the ideal gas that would produce a given configuration, $\{\psi_\alpha\}$, as the independent variables enables an exact analytical expression for the non-interacting fluid. However, their approach requires an angular mo-

mentum expansion that works only for model one-dimensional systems. Chapter 4 generalizes this idea and employs the probability density for finding a molecule at a given location and orientation, $p_\omega(\vec{r})$, as the independent variable, and enables practical classical density calculations for molecular fluids in real three-dimensional systems.

Approximations for the excess free energy for molecular fluids [31, 33, 97] typically require uniform fluid pair distribution functions from neutron scattering or computer simulation as input, which restricts their applicability to the fluids and state points for which such data is available. Chapters 3 and 4 construct approximate analytical free energy functionals for liquid water that adequately capture the energetics of liquid configurations typically encountered in solvated microscopic systems, without relying on fluid structure data. Chapter 5 extends these approaches to other molecular liquids, particularly chloroform and carbon tetrachloride, whose dielectric response, unlike water, is not dominated by rigid rotational response and requires the inclusion of molecular polarizability effects.

1.5 Joint density-functional theory

Electronic density functional theory provides efficient computational predictions for the ground-state structures of solids and molecules, and the energetics of chemical bonding. On the other hand, classical density functional theory efficiently describes inhomogeneous configurations of liquids at a coarser level after integrating out the electronic degrees of freedom. The first-principles study of processes in solution ideally requires an accurate electronic-structure level

description for part of the system, with a coarse-grained description of the equilibrium effect of the surrounding solvent (as illustrated in Figure 1.2(c)). Joint density-functional theory [130] introduces a variational theorem that allows an in-principle exact description of precisely this nature, in terms of electron densities for a portion of the system, and in terms of fluid nuclear densities for the remainder.

The constrained-search procedure for the free energy of a many-body system (1.1) in external potentials for the electrons, $V(\vec{r})$, as well as fluid nuclei, $\{V_\alpha(\vec{r})\}$, establishes the existence of a universal functional $\Phi[n_{\text{tot}}, \{N_\alpha\}]$ in terms of the total electron density and the fluid site densities (similarly to (1.7) and (1.14)). Petrosyan et al. [130] further show that it is possible to formally partition the total electron density into solute and solvent contributions, with the solute component $n(\vec{r})$ integrating up to a fixed number of electrons associated with the solute, and then integrate out the solvent component.[10] As a result, the equilibrium free energy of a solvated electronic system minimizes

$$\Phi_0 = \min_{n,\{N_\alpha\}} \left[\Phi_{\text{JDFT}}[n, \{N_\alpha\}] + \int d\vec{r} V(\vec{r}) n(\vec{r}) + \sum_\alpha \int d\vec{r} V_\alpha(\vec{r}) N_\alpha(\vec{r}) \right], \tag{1.16}$$

where $\Phi_{\text{JDFT}}[n, \{N_\alpha\}]$ is a universal functional of the *solute* electron density and the solvent nuclear densities alone. Figure 1.4 illustrates the reduction of a many-body description of a system in aqueous solution, for example, to a joint density-functional description in terms of oxygen and hydrogen densities for the solvent, which combines the reductions of electronic and classical density functional theories (Figures 1.1 and 1.3 respectively) for the two subsystems.

[10] The exact functional is highly degenerate with respect to this partitioning because of the indistinguishability of electrons, but practical approximations break this degeneracy and localize the solute electron density around the solute; see [130] for further details.

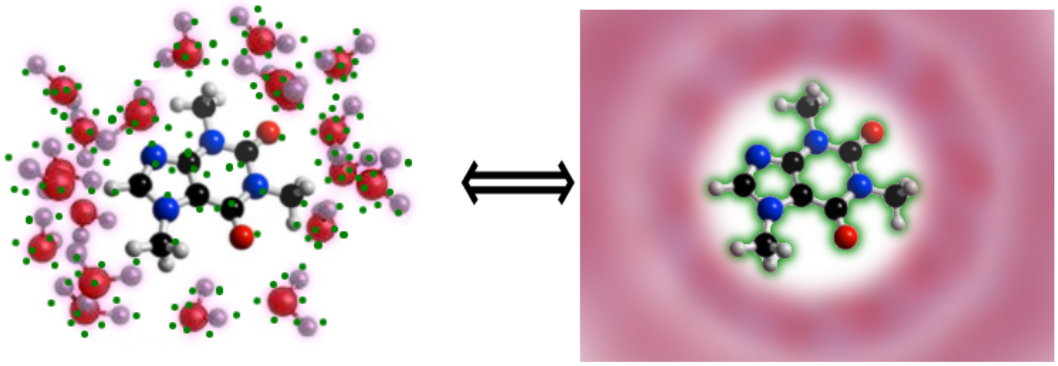

Figure 1.4: Exact equivalence between many-body theory in terms of individual nuclear (red and white circles on the left) as well as electronic coordinates (green dots on the left), and joint density-functional theory in terms of electron density (green cloud on the right) with discrete nuclei for part of the system and nuclear site densities alone (overlapping red and white clouds (or pink haze) on the right) for the remainder.

The unknown universal functional can now be decomposed exactly as

$$\Phi_{\text{JDFT}}[n, \{N_\alpha\}] = \underbrace{F_{\text{HK}}[n]}_{\text{electronic}} + \underbrace{\Phi_{\text{CDFT}}[\{N_\alpha\}]}_{\text{liquid}} + \underbrace{\Delta\Phi[n, \{N_\alpha\}]}_{\text{coupling}}, \tag{1.17}$$

where F_{HK} is the Hohenberg-Kohn (1.7) or Mermin (1.8) electronic density functional, Φ_{CDFT} is the exact free energy functional of the liquid (1.14), and the remainder, $\Delta\Phi \equiv \Phi_{\text{JDFT}} - F_{\text{HK}} - \Phi_{\text{CDFT}}$, is the free energy for the interaction of the two systems.

In practice, we need to approximate each of the in-principle exact pieces of (1.17), and the power of the framework lies in the capability of independently selecting the level of approximation for each piece depending on the type of system, desired accuracy and available computational resources.

First, for the electronic system, we can employ the Kohn-Sham formalism (1.11) with any of the standard exchange-correlation functionals, or if necessary, correlated quantum chemistry methods or quantum Monte Carlo methods as we demonstrate in [140]. Next, we may treat the liquid free energy within the

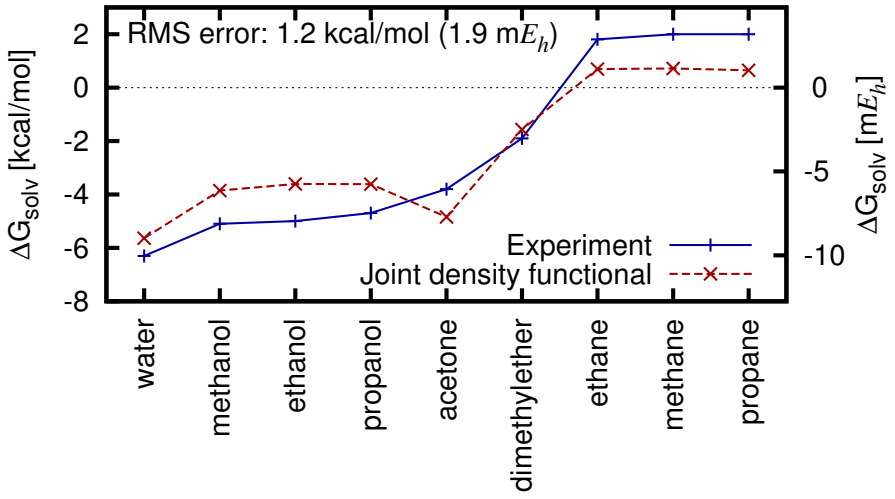

Figure 1.5: Solvation energies of organic molecules in water predicted by joint-density functional theory, combining PBE [128] for electrons with scalar-EOS for water (Chapter 5) using the density-only coupling (1.18) [91], compared to experimental data from [157, 105].

rigid molecule classical density-functional theory formalism of Chapter 4, with approximate excess free energy functionals such as those of Chapters 3, 4 and 5, or with other functionals available in the literature. (See [99] for a survey.) Finally, we can approximate the interaction between the electronic system and the fluid using a density-only electronic density functional approach [91]

$$\Delta\Phi[n,\{N_\alpha\}] = \underbrace{E_{\mathrm{TXC}}[n+n_{\mathrm{lq}}] - E_{\mathrm{TXC}}[n] - E_{\mathrm{TXC}}[n_{\mathrm{lq}}]}_{\text{Kinetic-Exchange-Correlation}} + \underbrace{\int d\vec{r} \int d\vec{r}' \frac{\rho_{\mathrm{el}}(\vec{r})\rho_{\mathrm{lq}}(\vec{r}')}{|\vec{r}-\vec{r}'|}}_{\text{Coulomb}} - \underbrace{s_6 \sum_{i,\alpha} \int d\vec{r} N_\alpha(\vec{r}) \frac{\sqrt{C_{6i}C_{6j}} f_{\mathrm{dmp}}}{|\vec{R}_i-\vec{r}|^6}}_{\text{Dispersion}}. \quad (1.18)$$

Here, the first set of terms employs an orbital-free or density-only approximation of the kinetic energy as well as the exchange-correlation energy to estimate the interaction between the electron density of the electronic system, $n(\vec{r})$, and the liquid with a model electron density $n_{\mathrm{lq}}[\{N_\alpha\}]$ determined from the nuclear site densities. As described previously, density-only functionals do not describe

chemical bonding accurately, but here they only serve to estimate the mostly repulsive interactions between non-bonded subsystems. The second term captures the mean field Coulomb interactions between the total charge density of the electronic subsystem, $\rho_{\mathrm{el}}(\vec{r}) = n(\vec{r}) - \sum_i Z_i \delta(\vec{r} - \vec{r}_i)$ (where solute nuclei of atomic numbers Z_i are fixed at coordinates $\vec{r}_i$), and the fluid, $\rho_{\mathrm{lq}}(\vec{r}) = n_{\mathrm{lq}}(\vec{r}) - \sum_\alpha Z_\alpha N_\alpha(\vec{r})$. The third term employs the semi-empirical pair-potential corrections introduced by Grimme [53] to estimate the dispersion interaction between the two subsystems, which the approximate exchange-correlation functional of the first term misses. (See Section 7.4 for details of the dispersion model.) This simple model assumes an additivity of the dispersion interactions, and contains an empirical prefactor, s_6, which absorbs some of the errors incurred in making this ansatz. Figure 1.5 shows that joint density-functional theory with the PBE generalized-gradient approximation [128] for the electrons, the scalar-EOS free energy functional for liquid water (Chapter 5), and this density-only approximation to the coupling term, predicts the solvation energies of organic molecules in water to an accuracy of 1.2 kcal/mol (1.9 mE_h), with the aforementioned single adjustable parameter, s_6, in the dispersion model.

We can improve or simplify each of these approximations, as necessary, for the system of interest and the study at hand. The full joint density-functional approach sketched above, coupling a classical density functional to an electronic density functional via an approximation such as [91], is significantly less computationally demanding than molecular-dynamics based methods, but still about an order of magnitude more expensive than vacuum electronic density functional calculations that simply ignore the solvent. Large scale exploratory calculations of electrochemical and biological systems could benefit from an even less computationally demanding description of the solvent, ideally one

Figure 1.6: Effect of the solvent (water molecules, red and white circles on the left) approximated in a polarizable continuum model primarily by placing the electronic system in a cavity in a continuum dielectric slab (cyan solid labeled ϵ on the right).

that adds negligible overhead compared to the vacuum calculation.

1.6 Polarizable continuum models

Polarizable continuum models (PCM's) [163] are a class of highly-simplified low cost solvation models that approximate most of the solvent effect by placing the solute in a dielectric cavity, which is described by the macroscopic equations of electrostatics in dielectric media even at these molecular length scales (Figure 1.6). These models then empirically account for additional energy contributions such as the free energy cost of forming a cavity in the liquid and dispersion interactions between the solute and the solvent. (See Chapter 6 for a summary and [163] for a detailed review.) These methods are extremely computationally efficient, but require a large number of adjustable parameters for each of the energy contributions, which are then typically fit to the solvation energies of small organic molecules.

PCM's are reliable and highly popular in the regime of their fit: properties and reactions of small molecules in solution, but their application to electrochemical systems with interfaces between metallic or ionic surfaces with liquids involves an uncontrolled extrapolation. Chapter 6 identifies nonlinear dielectric response as the key solvent property important for these systems, and constructs a suitable PCM-like model within the framework of joint-density functional theory that incorporates the nonlinear dielectric as well as ionic response of an electrolyte. These models all share a somewhat uncontrolled cavity assumption (see Chapter 7), but in Chapters 6-8, we extend the range of applicability of such models by successively reducing the number of unphysical assumptions.

The nonlinear PCM of Chapter 6 employs two fit parameters for each solvent, a critical electron density, n_c, that determines the cavity size, and an effective surface tension, τ, that empirically accounts for cavity formation and dispersion in the molecular regime. Both parameters need to be refit for each solvent of interest, and the effective surface tension, τ, fit to the molecular solvation regime need not extrapolate reliably to solid surfaces in solution. Chapter 7 traces the solvent dependence of the cavity size parameter to the loss of finite-size effects in reducing solvent molecules to a continuum, and develops an *ab initio* technique to compute finite-size corrections which enables the use of a single parameter n_c across solvents. Chapter 7 also develops a non-empirical model for the cavity formation energy that compares well with classical density-functional theory, and the semi-empirical dispersion model employed in (1.18) [91], which capture the true dependence of these terms on the shape and size of the cavity ranging from the molecular to the surface limits.

Finally, Chapter 8 develops a nonlocal approximation to the electric response of the solvent, which naturally captures the solvent molecule finite-size effects. Combined with the weighted-density cavity formation and dispersion models from Chapter 7, this nonlocal solvation model captures details of the solvent without empiricism and at a level closer to full joint-density functional theory, but at computational cost comparable to traditional polarizable continuum models. Chapter 9 then applies this model to theoretically investigate the underpotential deposition of copper on platinum, an experimentally well-studied, model electrochemical system that serves as an ideal testing ground for theories of the electrochemical interface.

CHAPTER 2

IDEAL REGULARIZATION OF THE COULOMB SINGULARITY IN EXACT EXCHANGE BY WIGNER-SEITZ TRUNCATED INTERACTIONS [1]

Kohn-Sham electronic density-functional theory with an approximate exchange and correlation functional forms the basis for *ab initio* theoretical studies of the ground-state electronic structure of materials, and is a key component of joint density-functional descriptions of solvated systems. Standard semi-local approximations to exchange and correlation in density-functional theory, such as the local-density and generalized-gradient approximations, are remarkably accurate for a variety of properties such as lattice constants and elastic moduli of solids, as well as equilibrium geometries of molecules, but are not sufficiently accurate for the energetics and kinetics of chemical reactions at room temperature [177].

Hybrid density functionals, which replace a fraction of the approximate semi-local exchange energy with the exact non-local Fock exchange energy, improve upon the accuracy of semi-local functionals and have been widely applied for first-principles thermo-chemistry [13]. Variants of these functionals [1] enable calculations for solids and surfaces with accuracy sufficient for predicting atomic-scale processes at room temperature. However, hybrid functionals require a greater number of $\vec{k}$-points than semi-local functionals for comparable accuracy in Brillouin-zone discretization for periodic systems. This increases their already high computational cost and limits their applicability, so that practical studies of surface reactions and phenomena such as catalysis remain tantalizingly out of reach.

[1] Published as 'R. Sundararaman and T.A. Arias, *Phys. Rev. B* **87**, 165122 (2013)'

The need for finer $\vec{k}$-point sampling in hybrid functionals stems from the Brillouin-zone integrals over the singular Coulomb kernel in the exact exchange energy of periodic systems. Similar operators also appear in GW [72] and BSE [138] calculations, and so successful methods to address this issue have implications for excited state methods as well.

The discretization error in singular reciprocal space integrals critically depends on the technique used to handle the singular contributions. The standard auxiliary-function approach [55, 169, 24] replaces the divergent terms with an average around the singularity computed using an auxiliary function with the same singularity as the Coulomb kernel. However, such methods that replace only the divergent terms lead to polynomial convergence (N_k^{-1}) with the number of $\vec{k}$-points N_k [24], compared to the standard exponential convergence ($\exp(-aN_k^{1/3})$) in the case of semi-local functionals.

Some hybrid functionals [66] achieve $\vec{k}$-point convergence comparable to fully semi-local functionals by replacing the exact exchange energy with a screened exchange energy computed using a short-ranged kernel $\mathrm{erfc}(\omega r)/r$ that is not singular at long wave-vectors. The remaining long-ranged part $\mathrm{erf}(\omega r)/r$ is treated using a semi-local (generalized-gradient) approximation. The predictions of these functionals depend on the screening parameter ω due to this additional approximation, and are less accurate than those of exact-exchange hybrids for some properties such as elastic constants of periodic systems [112]. A method with comparable computational cost but with the exact $1/r$ kernel would therefore be highly valuable.

One approach that shows promising results for the exact exchange energy avoids the singularity by imposing a real-space cutoff on the Coulomb kernel

with a length-scale dependent on the $\vec{k}$-point mesh [146, 175, 69]. The spherical truncation employed in this approach, however, works well only for high-symmetry crystals, whose Wigner-Seitz cells more or less resemble spheres. The valuable gains afforded by such an approach in these special cases indicates the need for a detailed understanding of why truncated potentials work for calculating the exchange energy of periodic systems so as to point the way to a general method applicable to all systems.

Following this program, Section 2.1.1 analyzes the singularity in the exact exchange energy of periodic systems using a formalism based on Wannier-function localization. This allows us to prove analytically that Wigner-Seitz truncation of the Coulomb potential is the ideal regularization method with accuracy limited only by Brillouin-zone discretization errors in the Kohn-Sham orbitals themselves; Appendix C develops a set of techniques necessary to truncate the Coulomb potential on Wigner-Seitz cells. Section 2.1.2 then generalizes regularization methods for the exchange energy in three-dimensional systems to slab-like (two-dimensional) and wire-like (one-dimensional) geometries using partially-truncated potentials. Finally, Section 2.2 compares truncated-potential and auxiliary-function approaches for a variety of real materials with high- and low-symmetry crystal systems, electronic structure ranging from insulating to metallic states, and dimensionality ranging from three to one.

The results indicate that employing Wigner-Seitz truncated Coulomb kernels is systematically more accurate than other methods for dealing with the singularity in Fock exchange. Moreover, at equivalent Brillouin-zone sampling, the accuracy of hybrid functionals which include exact exchange computed using the Wigner-Seitz truncated method rivals that of functionals that only include

screened exchange, and even that of *semi-local* functionals which include *no* non-local exchange contributions *whatsoever*.

2.1 Exchange in periodic systems

The exact Fock exchange energy of a finite system with Kohn-Sham orbitals $\psi_{i\sigma}(\vec{r})$ and corresponding occupation numbers $f_{i\sigma}$ is given by the non-singular expression,

$$E_X = \frac{-1}{2} \sum_{i,j,\sigma} f_{i\sigma} f_{j\sigma} \int d\vec{r} \int d\vec{r}' \frac{\psi_{i\sigma}(\vec{r}) \psi^*_{j\sigma}(\vec{r}) \psi^*_{i\sigma}(\vec{r}') \psi_{j\sigma}(\vec{r}')}{|\vec{r} - \vec{r}'|}. \tag{2.1}$$

Here, we work with atomic units $e^2/(4\pi\epsilon_0) = \hbar^2/m_e = 1$, so that the unit of distance is the Bohr (a_0) and the unit of energy is the Hartree (E_h). The exchange energy is always a sum of independent contributions for each spin channel; the rest of this section omits the spin index σ and the implicit sum over σ for clarity.

In a periodic system, the Kohn-Sham orbitals take the Bloch form $\psi_i^{\vec{k}}(\vec{r}) = e^{i\vec{k}\cdot\vec{r}} u_i^{\vec{k}}(\vec{r})$, where $u_i^{\vec{k}}(\vec{r})$ are periodic functions normalized on the unit cell of volume Ω and labeled by band index i as well as a wave-vector $\vec{k}$ in the Brillouin zone. The exchange energy (2.1) of the periodic system per unit cell (per spin) is

$$E_X = \frac{-1}{2} \sum_{i,j} \int_{\mathrm{BZ}} \frac{\Omega d\vec{k}}{(2\pi)^3} \int_{\mathrm{BZ}} \frac{\Omega d\vec{k}'}{(2\pi)^3} f_i^{\vec{k}} f_j^{\vec{k}'} \int_\Omega d\vec{r} \int d\vec{r}' \frac{\psi_i^{\vec{k}}(\vec{r}) \psi_j^{\vec{k}'*}(\vec{r}) \psi_i^{\vec{k}*}(\vec{r}') \psi_j^{\vec{k}'}(\vec{r}')}{|\vec{r} - \vec{r}'|}, \tag{2.2}$$

where $\int_{\mathrm{BZ}}$ denotes integration over the Brillouin zone. The conventional treatment of this energy begins with a plane-wave expansion of the product of orbitals,

$$\psi_i^{\vec{k}*}(\vec{r}) \psi_j^{\vec{k}'}(\vec{r}) \equiv \rho_{ij}^{\vec{k}\vec{k}'}(\vec{r}) = e^{i(\vec{k}' - \vec{k})\cdot\vec{r}} \sum_{\vec{G}} e^{i\vec{G}\cdot\vec{r}} \tilde{\rho}_{ij\vec{G}}^{\vec{k}\vec{k}'}, \tag{2.3}$$

where $\tilde{\rho}_{ij\vec{G}}^{\vec{k}\vec{k}'}$ are the Fourier components of those orbital products at reciprocal

lattice vectors $\vec{G}$. This treatment then rewrites (2.2) in Fourier space as

$$E_X = \frac{-\Omega}{2} \int_{\mathrm{BZ}} \frac{\Omega d\vec{k}}{(2\pi)^3} \int_{\mathrm{BZ}} \frac{\Omega d\vec{k}'}{(2\pi)^3} \sum_{i,j,\vec{G}} f_i^{\vec{k}} f_j^{\vec{k}'} |\tilde{\rho}_{ij\vec{G}}^{\vec{k}\vec{k}'}|^2 \tilde{K}_{\vec{G}+\vec{k}'-\vec{k}}, \tag{2.4}$$

where the periodic Coulomb kernel $\tilde{K}_{\vec{q}} \equiv 4\pi/q^2$, so that for each $\vec{k}'$ at $\vec{G} = 0$, the integral over $\vec{q} = \vec{k} - \vec{k}'$ is singular at $\vec{q} = 0$. This singularity is integrable since near $q = 0$, the integral $\sim \int 4\pi q^2 dq \frac{1}{q^2}$.

The above approach, however, is problematic for any practical calculation where Brillouin-zone integrals are approximated using a finite quadrature, that is, as a weighted sum over a set of '$\vec{k}$-points'. In this chapter, we restrict our attention to the commonly employed Gauss-Fourier quadratures, which correspond to uniform $\vec{k}$-point meshes such as the Monkhorst-Pack grid [109]. The exchange energy computed in practice is therefore

$$E_X = \frac{-\Omega}{2N_k^2} \sum_{\vec{k},\vec{k}',i,j,\vec{G}} f_i^{\vec{k}} f_j^{\vec{k}'} |\tilde{\rho}_{ij\vec{G}}^{\vec{k}\vec{k}'}|^2 \tilde{K}_{\vec{G}+\vec{k}'-\vec{k}}. \tag{2.5}$$

where N_k is the total number of $\vec{k}$-points used for Brillouin zone sampling. In principle, the exchange energy would converge with increasing density of $\vec{k}$-points even if the singular terms are dropped, or equivalently, the Coulomb kernel is regularized with $\tilde{K}_{q=0} = 0$, as usual. However, that results in an $O(\delta q)$ error, where δq is the typical distance between neighboring $\vec{k}$-points, which leads to an impractically slow $N_k^{-1/3}$ convergence.

Auxiliary-function methods [55] address this poor Brillouin zone convergence of the Fock exchange energy by choosing a value for the $G = 0$, $\vec{k} = \vec{k}'$ term in (2.5) that captures the average contribution of $4\pi/|\vec{k}' - \vec{k}|^2$ in the neighborhood of $\vec{k} = \vec{k}'$. These methods correct for the finite quadrature error by setting this term to the difference between the exact integral and the discrete $\vec{k}$-point sum over the Brillouin zone of a function $f(q)$ that matches the periodicity

and the $4\pi/q^2$ singularity of the integrand in (2.4). For a uniform $\vec{k}$-point mesh, this amounts to replacing the Coulomb kernel $\tilde{K}_{\vec{q}}$ in (2.5) with

$$\tilde{K}^{\text{aux}}_{\vec{q}} = \begin{cases} 4\pi/q^2, & \vec{q} \neq 0 \\ N_k \int_{\text{BZ}} \frac{\Omega d\vec{k}}{(2\pi)^3} f(\vec{k}) - \sum_{\delta\vec{k}} f(\delta\vec{k}), & \vec{q} = 0, \end{cases} \tag{2.6}$$

where the discrete sum runs over $\delta\vec{k}$ in the $\vec{k}$-point difference mesh excluding the Γ point.[2]

The original method of Gygi and Baldereschi presented such a function for the face-centered cubic lattice which could be integrated analytically. Wenzien and coworkers [169] constructed similar functions for a few other lattice systems and tabulated the corresponding $q = 0$ corrections numerically. Carrier and coworkers [24] constructed a general function is applicable to all Bravais lattices and prescribed a general scheme for computing the Brillouin zone integral. Below, when making comparisons to our truncated potential method, we employ this last variant of the the auxiliary-function method because of its generality, and refer the reader interested in further details of auxiliary-function methods to [24].

With the correctly chosen $G = 0$ term for $\vec{k} = \vec{k}'$, the auxiliary function methods achieve N_k^{-1} convergence [24] in the exchange energy. Duchemin and Gygi [37] have generalized the method to achieve N_k^{-2} convergence by introducing corrections for the difference in curvature between the non-singular parts of the auxiliary function and the true integrand which, in our notation above, amount to correcting the Coulomb kernel at $q = 0$ as well as $\vec{q}$ that correspond to nearest neighbor displacements in the $\vec{k}$-point mesh. For many systems, this method

[2] For a uniform $\vec{k}$-point mesh, the difference mesh is uniform and Γ-centered even if the original mesh is off-Γ.

yields reasonable accuracy with modest $\vec{k}$-point meshes; however the asymptotic polynomial convergence of the exchange energy is still slower than the exponential convergence of the total energy of semi-local density functionals. We next describe a method for calculating the exchange energy that achieves this exponential convergence.

2.1.1 Real-space analysis of asymptotic convergence

An alternate scheme to improve the Brillouin zone convergence of exact exchange imposes a real-space cutoff on the Coulomb kernel in (2.5). This scheme is reasonably accurate for high-symmetry crystals [146], but the reasons for its success remain somewhat mysterious. Two possible explanations have been offered. The first is that, with a suitably chosen cutoff, the method satisfies the normalization constraints of the exchange hole [175]. The second is that the effective distinguishability of electrons amongst different $\vec{k}$-point sampled supercells requires suppression of the exchange interaction between supercells [146]. These explanations do not elucidate the underlying reason for an infinite-range interaction to be best numerically approximated by a finite-range one nor specify what form that finite-ranged interaction should take, and they do not lend themselves to an analysis of the accuracy or convergence properties of such an approximation. To provide such an explanation and to identify the ideal form of the truncation, we now analyze the Fock exchange interaction computed on finite $\vec{k}$-point meshes in real space, and show that the need for truncating the Coulomb potential arises both naturally and in a particular form.

We start by rearranging the exchange energy of the periodic system (2.2) as

$$E_X = \frac{-1}{2} \sum_{i,j,\vec{R}} \int d\vec{r} \int d\vec{r}' \frac{\bar{\rho}_{ij}^{\vec{R}*}(\vec{r}) \bar{\rho}_{ij}^{\vec{R}}(\vec{r}')}{|\vec{r} - \vec{r}'|}, \tag{2.7}$$

a sum of Coulomb self-energies of the local products $\bar{\rho}_{ij}^{\vec{R}}(\vec{r}) = \bar{w}_i^{\vec{0}*}(\vec{r}) \bar{w}_j^{\vec{R}}(\vec{r})$ of the Wannier-like functions

$$\bar{w}_i^{\vec{R}}(\vec{r}) = \int_{\mathrm{BZ}} \frac{\Omega d\vec{k}}{(2\pi)^3} e^{-i\vec{k}\cdot\vec{R}} \psi_i^{\vec{k}}(\vec{r}) \sqrt{f_i^{\vec{k}}}. \tag{2.8}$$

Indeed, order-N calculations of the exchange energy [176] using maximally-localized Wannier functions [107] employ similar transformations. In contrast, we use (2.7), which is exactly equivalent to (2.2), only as a tool to analyze standard reciprocal-space methods.

In the case of insulators, where $f_i^{\vec{k}} = 1$ for all occupied bands, the Wannier-like functions of (2.8) are just the standard Wannier functions $w_i^{\vec{R}}$ and thus are exponentially localized around the sites $\vec{R}$ [81]. For the case of metals, where the occupations $f_i^{\vec{k}}$ are not constant, the $\bar{w}_i^{\vec{R}}$ are linear combinations of Wannier functions localized on different lattice sites

$$\bar{w}_i^{\vec{R}}(\vec{r}) = \sum_{\vec{R}'} w_i^{\vec{R}'}(\vec{r}) \underbrace{\int \frac{\Omega d\vec{k}}{(2\pi)^3} e^{i\vec{k}\cdot(\vec{R}'-\vec{R})} \sqrt{f_i^{\vec{k}}}}_{F_i(\vec{R}'-\vec{R})}, \tag{2.9}$$

with coefficients $F_i(\vec{R}' - \vec{R})$ given by a Fourier transform of the square-root of the band occupation. For metals in the ground state, the occupations are discontinuous at the Fermi surface which leads to a polynomially decaying F_i. In particular, for metals in three dimensions with a compact two-dimensional Fermi surface, $F_i(\vec{R}) \sim R^{-2}$ for large R. At finite temperature T, F_i also decays exponentially with a length scale inversely proportional to T. Consequently, the $\bar{w}_i^{\vec{R}}$ in metals are localized polynomially at $T = 0$ and exponentially with a

temperature-dependent decay length at $T \neq 0$.[3] In all these cases, the localization of $\bar{w}_i^{\vec{R}}$ closely mirrors that of the one-particle density matrix [74].

Given the above properties of the Wannier-like functions $\bar{w}_i^{\vec{R}}$, each orbital product $\bar{\rho}_{ij}^{\vec{R}}(\vec{r})$ is localized and diminishes with increasing R, since it is a product of one function localized around $\vec{0}$ and another around $\vec{R}$. The magnitude of the orbital product decreases exponentially for insulators and as R^{-2} for metals at zero temperature, so that the corresponding Coulomb self-energies decay exponentially and as R^{-4} respectively. The sum over unit cells in (2.7) converges in all these cases.

Next, to understand the convergence properties of actual calculations, we repeat the above transformations with a finite $\vec{k}$-point mesh with N_k samples instead of continuous integrals over the Brillouin zone. A uniform $\vec{k}$-point mesh centered on the Γ-point corresponds to Kohn-Sham orbitals that are periodic on a supercell of volume $N_k\Omega$. For uniform meshes not containing the Γ-point (off-Γ meshes), such as the Monkhorst-Pack grid, the orbitals share a common Bloch phase on an $N_k\Omega$ supercell. In all these cases, the orbital products $\bar{\rho}_{ij}^{\vec{R}}(\vec{r})$ are periodic on that $N_k\Omega$ supercell. Because of this periodicity, the expression for the exchange energy (2.7) then remains unmodified except that one of the integrals over space is restricted to a single $N_k\Omega$ supercell. Converting the other integral over all of space to a sum over integrals restricted to each $N_k\Omega$ supercell, and

[3] Throughout this chapter, the energies we calculate are on the Born-Oppenheimer surface, that is at fixed ionic positions. In this context, the electron temperature T controls the width of the transition in the occupations $f_i^{\vec{k}}$ at the Fermi energy, and is a commonly employed numerical device to aid integrations over the Brillouin zone. For notational convenience, we define $T = 0$ to correspond to the situation where the occupations are strictly 1 below the Fermi energy and 0 above it, which indeed is the $T \to 0$ limit of the Fermi function.

using the periodicity of the orbital product,

$$E_X = \frac{-1}{2} \sum_{i,j,\vec{R}} \int_{N_k\Omega} d\vec{r} \int_{N_k\Omega} d\vec{r}' \bar{\rho}_{ij}^{\vec{R}*}(\vec{r}) K(\vec{r} - \vec{r}') \bar{\rho}_{ij}^{\vec{R}}(\vec{r}'), \tag{2.10}$$

with

$$K(\vec{r}) = \sum_{\vec{S}} \frac{1}{|\vec{r} + \vec{S}|}, \tag{2.11}$$

where $\vec{S}$ are lattice vectors of the effective superlattice of cell volume $N_k\Omega$ which arises from finite $\vec{k}$-point sampling. The summand in (2.11) falls off only as $1/S$ causing $K(\vec{r})$ to diverge for all $\vec{r}$. In fact, $K(\vec{r}) = \frac{1}{N_k\Omega} \sum_{\vec{k},\vec{G}} e^{i(\vec{k}+\vec{G})\cdot\vec{r}} \frac{4\pi}{|\vec{k}+\vec{G}|^2}$, so that it is again the $\vec{k} = \vec{G} = 0$ component which needs special handling, as above.

Now consider a sufficiently dense $\vec{k}$-point mesh such that the corresponding supercell is much larger than the spatial extent of the localized $\bar{w}_i^{\vec{R}}$. In that case, the periodic versions of $\bar{\rho}_{ij}^{\vec{R}}$ at finite $\vec{k}$-point sampling are identical (with exponentially small errors) in one, appropriately centered, supercell to the original non-periodic localized ones. Therefore, the contribution from the $\vec{S} = 0$ term in $K(\vec{r})$ to (2.10), apart from errors decaying exponentially with the density of the $\vec{k}$-point mesh, is the true exchange energy of the infinite system (2.7). The non-exponentially decaying errors in (2.10) arise from the contributions due to all the other super-cells $\vec{S} \neq 0$, which thus can be eliminated completely by truncating the Coulomb potential so that $K(\vec{r}) = 1/r$.

Such truncation of the Coulomb potential on the Wigner-Seitz cell of the $\vec{k}$-point sampled superlattice with supercell volume $N_k\Omega$, in practice simply amounts to replacing $\tilde{K}_{\vec{q}}$ in the standard reciprocal-space expression (2.5) by the Fourier transform of the truncated potential. The minimum image convention (MIC) algorithm [106] employs

$$\tilde{K}_{\vec{q}}^{\mathrm{WS}} \approx \frac{4\pi}{q^2} \left(1 - \exp \frac{-q^2}{4\alpha^2}\right) + \frac{\Omega}{N_{\vec{r}}} \sum_{\vec{r}\in\mathrm{WS}} e^{-i\vec{q}\cdot\vec{r}} \frac{\mathrm{erf}\, \alpha r}{r}, \tag{2.12}$$

and enables efficient construction of truncated kernels in the plane-wave basis. Appendix C derives this algorithm for arbitrary lattice systems as equation (C.4); see Appendix C.1 for a detailed explanation of all the terms and approximations involved in (2.12). When such a truncated kernel replaces the periodic Coulomb kernel, the remaining error in the exchange energy arises from the deviations of the periodic $\bar{\rho}_{ij}^{\vec{R}}$ from the infinite ones, within one supercell, as discussed above. These deviations decay exponentially when the $\bar{w}_i^{\vec{R}}$ are exponentially localized, leading to exponential convergence of the exchange energy with the number of $\vec{k}$-points.

The general analysis we developed above not only allows us to establish the Wigner-Seitz super-cell truncated potential as the natural method with ideal asymptotic convergence, but also provides the framework for establishing analytically the convergence properties of other methods *a priori* by simply comparing the effective Coulomb kernels which they employ. Ultimately, each reciprocal-space method prescribes a kernel $\tilde{K}(\vec{q})$ for use in (2.5), which translates to some $K(\vec{r})$ in the real space version (2.10). The error in any method compared to the ideal case is governed by the discrepancy of $K(\vec{r})$ from $1/r$, given by

$$\delta K(\vec{r}) = \frac{1}{N_k \Omega} \sum_{\vec{k},\vec{G}} e^{i(\vec{k}+\vec{G})\cdot\vec{r}} \tilde{K}(\vec{k}+\vec{G}) - \frac{1}{r} \tag{2.13}$$

for a particular $\vec{k}$-point set.

Figure 2.1 compares the discrepancies in the effective Coulomb kernels of various methods for a cubic lattice over a radial slice of the effective supercell with different $\vec{k}$-point meshes. δK is exactly zero within the domain of truncation for any truncated Coulomb potential, and hence it is zero for the Wigner-Seitz truncated kernel in the entire supercell. Truncation on a sphere of volume

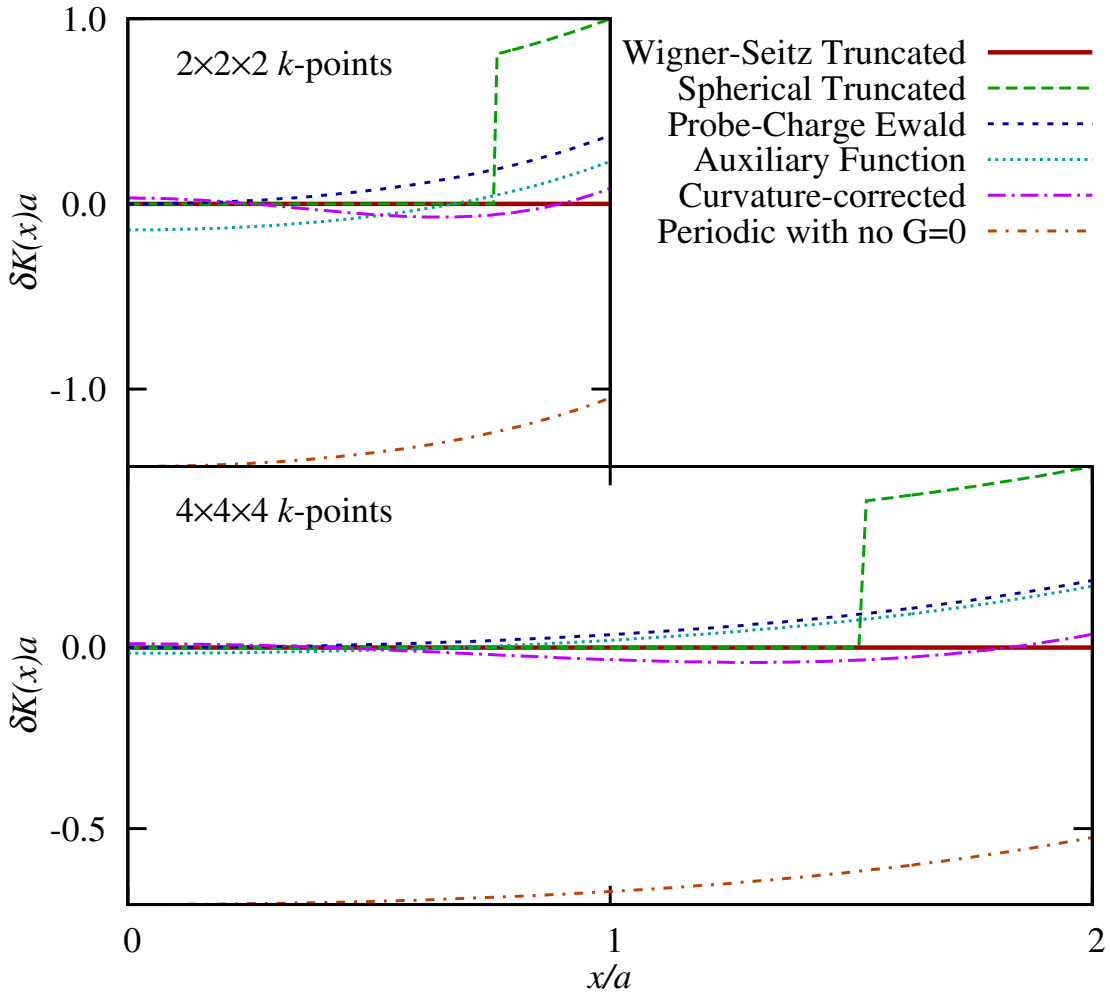

Figure 2.1: Comparison of the discrepancy in the effective Coulomb Kernel from $1/r$ of various methods for computing the Fock exchange energy. This discrepancy is plotted along the x-direction from the origin to the boundary of the cubic Wigner-Seitz cell of the $\vec{k}$-point sampled super-lattice of a simple cubic lattice of lattice constant a. Both axes have been scaled to be dimensionless. The truncated Coulomb potentials have zero discrepancy for most or all of the supercell. The auxiliary-function methods shift the periodic kernel to minimize the overall discrepancy, while the probe-charge Ewald-sum method pins the discrepancy at the origin to 0.

$N_k\Omega$, as proposed by Spencer and Alavi [146], achieves exponential convergence as well, but exhibits its asymptotic properties starting at larger N_k since spheres do not tessellate the space and this leads to some overlap between supercells.

The standard periodic kernel with $G = 0$ projected out has a large discrepancy $\sim 1/L$, where L is the linear dimension of the supercell, and hence exhibits $\sim N_k^{-1/3}$ convergence. The auxiliary-function methods add a constant offset to the periodic kernel by adjusting the $G = 0$ component, which is chosen to minimize the discrepancy over the supercell with some weight which depends on the choice of auxiliary function $f(\vec{q})$. The curvature corrections proposed by Duchemin and Gygi [37] adjust the constant offset in addition to the coefficients of $e^{i\delta\vec{k}\cdot\vec{r}}$ for the nearest-neighbors $\delta\vec{k}$ in the $\vec{k}$-point mesh. For the cubic supercell of length L plotted in Figure 2.1, this correction happens to be $(\cos(2\pi x/L) - 1)/(\pi L)$ in the x slice. This additional freedom reduces the magnitude of the discrepancy more rapidly with increasing N_k than the case when only $G = 0$ is adjusted.

An interesting alternative to the auxiliary-function method with similar accuracy is the probe-charge Ewald-sum method [120]. Here, the $G = 0$ component of the Coulomb kernel is set to the potential at the origin from an array of unit point negative charges placed at all points of the $\vec{k}$-point sampled superlattice except the origin, a Coulomb sum which can be computed readily using the Ewald method [38]. This amounts to adjusting the discrepancy at the origin, $\delta K(0)$, to zero, as can be seen in Figure 2.1. Alternately, this method attempts to cancel the contributions from $\vec{S} \neq 0$ supercells of (2.11) in (2.10) by neutralizing all those supercells with a point charge. This would be exact if each $\bar{\rho}$ was spherically symmetric, but in reality incurs an error asymptotically dominated

by dipole-dipole interactions $\sim L^{-3}$ and hence converges as N_k^{-1} with $\vec{k}$-point sampling.

The Wannier-function formalism presented here clearly establishes the advantage of the truncated-potential methods and elucidates the asymptotic convergence of the exchange energy computed using different methods. Note that none of these methods require Wannier functions in practice; each method prescribes a different replacement for the periodic plane-wave Coulomb kernel $\tilde{K}_q = 4\pi/q^2$ in the standard reciprocal-space expression (2.5). We compare the accuracy of these methods and demonstrate their analytically-predicted asymptotic behavior for real materials in Section 2.2.

2.1.2 Extension to lower-dimensional systems

The preceding section shows how the integrable singularity in reciprocal-space calculations of the exchange energy of systems with three-dimensional periodicity can be regularized using auxiliary function methods or, ideally, by truncating the Coulomb potential to the Wigner-Seitz cell simply by modifying the Fourier transform of the Coulomb kernel. Reciprocal-space methods can also be applied to systems with lower-dimensional periodicity by truncating the Coulomb potential along a subset of lattice directions. Appendix C details these types of truncations as well. Specifically, the exchange energy in these geometries can be computed using (2.5) by employing a partially truncated Coulomb potential given by (C.6) or (C.8) for $\tilde{K}_{\vec{q}}$, and restricting the $\vec{k}$-points sums to the two- or one-dimensional Brillouin zone of the periodic directions alone. The exchange energy still contains an integrable singularity, q^{-1} for slabs and $\ln q$ for wires,

that again needs to be addressed just as it did for bulk systems. Before going on to present results in the next section, here, we briefly describe how we extend each of the methods discussed above for bulk systems to the cases of these lower-dimensional geometries.

First, the auxiliary-function method for these geometries replaces the $G = 0$ component of the appropriate partially truncated Coulomb kernel to obtain

$$\tilde{K}^{\text{aux}}_{\vec{q}} = \begin{cases} \tilde{K}^{\text{slab/wire}}_{\vec{q}}, & \vec{q} \neq 0 \\ \Omega_{\perp}\left(N_k \int_{\text{BZ}_{\parallel}} \frac{\Omega_{\parallel} d\vec{k}}{(2\pi)^d} f(\vec{k}) - \sum_{\delta\vec{k}} f(\delta\vec{k})\right), & \vec{q} = 0, \end{cases} \tag{2.14}$$

where $\Omega_{\parallel}$ is the area/length of the two-/one-dimensional unit cell in the periodic directions, $\text{BZ}_{\parallel}$ is the corresponding Brillouin zone and $\Omega_{\perp}$ is the length/area of the artificial periodicity along the truncated directions. The auxiliary function needs to match the singularity of the truncated Coulomb kernel, and we adapt Carrier and coworkers' construction for arbitrary three-dimensional lattices [24] to lower dimensions. For a slab with lattice basis vectors $\vec{a}_1$ and $\vec{a}_2$ in the periodic directions, and corresponding reciprocal lattice vectors $\vec{b}_1$ and $\vec{b}_2$, the function

$$f(\vec{q}) = 2\pi^2 \left[b_1^2 \sin^2\left(\vec{a}_1 \cdot \frac{\vec{q}}{2}\right) + b_2^2 \sin^2\left(\vec{a}_2 \cdot \frac{\vec{q}}{2}\right) + \frac{1}{2}\vec{b}_1 \cdot \vec{b}_2 \sin(\vec{a}_1 \cdot \vec{q}) \sin(\vec{a}_2 \cdot \vec{q}) \right]^{-1/2} \tag{2.15}$$

is periodic on the reciprocal lattice with a single singularity in the Brillouin zone at $\vec{q} = 0$ for arbitrary lattice vectors. Similarly,

$$f(\vec{q}) = -2\gamma + \ln \frac{a^2}{\sin^2(\vec{a} \cdot \vec{q}/2)} \tag{2.16}$$

is a suitable auxiliary function for a wire with lattice vector $\vec{a}$ along the periodic direction, where γ is the Euler-Mascheroni constant. In this case, both the integral and the sum in (2.14) can be performed analytically to yield $\tilde{K}^{\text{aux}}_0 = 2\Omega_{\perp}(\ln 2N_k a - \gamma)$.

Next, the probe-charge Ewald compensation method generalizes trivially to the slab and wire geometries, and only requires the substitution of the usual three-dimensional Ewald sum with the appropriate lower-dimensional analog. (See Appendix C.3 for details.) Interestingly, this method yields the same $G = 0$ component for the wire-geometry exchange kernel as the auxiliary function method above, so that the two methods are identical for wires.

Finally, the Wigner-Seitz supercell truncated Coulomb potential requires no modification for partially periodic systems. The truncation domain remains the Wigner-Seitz cell of the $\vec{k}$-point sampled super-lattice; one or two lattice directions have only a single $\vec{k}$-point and the boundaries of the supercell coincide with the unit cell in those directions. These Wigner-Seitz cells become increasingly anisotropic with increasing N_k and spherical truncation is no longer a viable option.

2.2 Results

The analysis of Section 2.1 identifies Coulomb truncation with its asymptotic exponential convergence as the natural choice for computing the exchange energy of periodic systems, in comparison to auxiliary-function methods with polynomial convergence. Here, we compare the accuracy of all these methods and demonstrate their analytically-established asymptotic behaviors for real materials with a variety of electronic structures and dimensionalities.

Specifically, we consider four methods for computing the exact exchange energy, the Wigner-Seitz truncated potential introduced here, the spherical truncation of Spencer and Alavi [146], the probe-charge Ewald compensation method

[120], and the auxiliary-function method with the general function applicable to all lattice systems by Carrier and coworkers [24]. The first three of these methods trivially generalize to lower dimensions, while the auxiliary-function method requires minor modifications as detailed in Section 2.1.2.

We also compare the convergence of the exact exchange energy using the above methods to that of the erf-screened exchange employed in the range-separated HSE06 hybrid functional [85]. In this functional, the Coulomb kernel in the non-local exchange energy is replaced by the short-ranged $\mathrm{erfc}(\omega r)/r$ with $\omega = 0.11 a_0^{-1}$, while the long-ranged part is approximated using a semi-local functional. The screened exchange avoids the $G = 0$ singularity and the HSE06 functional has so far achieved superior $\vec{k}$-point convergence compared to regular hybrid functionals with exact exchange [121]. Here, we demonstrate that employing Wigner-Seitz truncation for the exact exchange energy puts the convergence of hybrid functionals employing the exact non-local exchange energy (e.g. PBE0 [1]) on par with that of the screened-exchange functionals (e.g. HSE06) and even that of semi-local functionals employing no non-local exchange whatsoever (e.g. PBE [128]).

2.2.1 Computational Details

We have implemented these methods in the open-source plane-wave density-functional software JDFTx [154], where they are now publicly available. The specifics of these implementations are that the auxiliary-function and probe-charge Ewald methods simply replace only the $\vec{G} = 0$ value of the $\vec{k} = \vec{k}'$ Coulomb kernel in (2.5) with a precomputed value. The truncated potential

Table 2.1: Comparison of the average computation time for the exact exchange energy using different regularization methods for hexagonal silicon carbide with $8 \times 8 \times 8$ $\vec{k}$-point sampling. The timing statistics are from ten calculations for each method on identical 12-core Xeon compute nodes.

Method	Computation Time [s]
Wigner-Seitz truncated	555 ± 11
Spherical truncated	874 ± 12
Auxiliary function	552 ± 11
Probe-charge Ewald	543 ± 10

methods, on the other hand, alter $\tilde{K}_{\vec{q}}$ in (2.5) for all $\vec{q} = \vec{G} + \vec{k}' - \vec{k}$. Spherical truncation uses $\tilde{K}_{\vec{q}}$ defined analytically via (C.2). Wigner-Seitz truncation employs a precomputed kernel calculated by applying the MIC algorithm (C.4) on the supercell, as detailed in Appendix C, and then redistributing the resulting supercell kernel to unit cell kernels for each $\vec{k}' - \vec{k}$.

Table 2.1 shows that the computational overhead for fetching the precomputed kernel from memory (look-up overhead) in the Wigner-Seitz truncated method is negligible, and results in compute times equal to the auxiliary function and probe-charge Ewald methods, within run-to-run variations. In fact, this overhead is negligible compared to that of the extra transcendental (cosine) evaluations in spherical truncation; precomputing the kernel also optimizes spherical truncation and we report the analytical evaluation time here only to illustrate the negligible look-up overhead. Next, the computational effort to calculate and predistribute the kernel is negligible compared to a single evaluation of the exchange energy: a mere 1.4 s for the example of Table 2.1. Finally, the memory overhead of the precomputed kernel is comparable to four Kohn-Sham bands, and is therefore negligible for most systems.

Table 2.2: Unit-cell parameters for the systems studied here, including citations for experimental lattice constants and references to figures with corresponding results. N_a is the number of atoms in the primitive unit cell of each calculation.

System	Unit cell	N_a	a [Å]	c [Å]	Ref.	Figure
2H-SiC	Hexagonal	4	3.076	5.048	[2]	2.3,2.9(b)
3C-SiC	FCC	2	4.3596	-	[160]	2.2(b)
Ice XIc	BCT[a]	6	4.385	6.219	[133]	2.4
Si	FCC	2	5.431	-	[62]	2.2(a),2.9(a)
Platinum	FCC	1	3.924	-	[62]	2.6,2.9(c)
Diamond	FCC	2	3.567	-	[62]	2.2(c)
Graphite	Hexagonal	4	2.461	6.709	[62]	2.5
Graphene	Hexagonal	2	2.46	10[b]	PBE[c]	2.7
(8,0) SWCNT[d]	Tetragonal	32	25[b]	4.32	PBE[c]	2.8

[a] Body-centered tetragonal.

[b] Coulomb potential is truncated along these directions.

[c] DFT lattice constants using the PBE functional [128].

[d] Single-walled carbon nanotube.

In order to study a large number of materials and $\vec{k}$-point configurations within the available computational resources, rather than performing fully self-consistent calculations, we first determine converged Kohn-Sham orbitals of a density-functional calculation using the semi-local PBE exchange and correlation functional [128], and then compute the exchange energies from these orbitals according to the above methods. The calculations employ norm-conserving pseudopotentials at a kinetic energy cutoff of 30 E_h. Table 2.2 summarizes the unit-cell parameters for the systems studied below.

Figures 2.2-2.8 show the deviations of the exact and screened exchange energies at finite $\vec{k}$-point configurations from their $\vec{k}$-point-converged values for a variety of systems. The left-hand panels show this deviation for coarse $\vec{k}$-point meshes on a linear scale, while the right-hand panels illustrate the asymptotic

convergence on a logarithmic energy scale. The base line of $\vec{k}$-points is insufficient to reliably fit power laws and the dotted lines are only a visual guide with the expected exponent for polynomial convergence. For the three-dimensional systems, we study both isotropic and anisotropic $\vec{k}$-point meshes. The plots explicitly label anisotropic $\vec{k}$-point configurations, whereas the unlabeled points at integer values of $X \equiv N_k^{1/3}$ correspond to $X{\times}X{\times}X$ $\vec{k}$-point meshes.

2.2.2 Insulators

We begin our computational studies with a sequence of semiconductors and insulators in the high-symmetry diamond structure. Figure 2.2 compares the deviation of the exchange energy of silicon, cubic silicon carbide and diamond at various finite $\vec{k}$-point configurations from the infinite limit for different singularity regularization methods.

While the order of magnitude of the error in the exact exchange energy with coarse $\vec{k}$-point meshes is comparable for all methods, Wigner-Seitz truncation typically yields significantly lower errors than do the other methods. The Wigner-Seitz truncated and the probe-charge Ewald methods (red +'s and blue $*$'s respectively in Figure 2.2) exhibit smooth convergence for all $\vec{k}$-point meshes including anisotropic ones, whereas the remaining methods incur higher errors for anisotropic $\vec{k}$-point meshes. The pattern of errors with $\vec{k}$-points for each method is similar for the three materials with the same underlying Bravais lattice and point-group symmetries.

In contrast, the asymptotic exponential convergence of the truncated methods leads to orders of magnitude reduction in error for fine $\vec{k}$-point meshes,

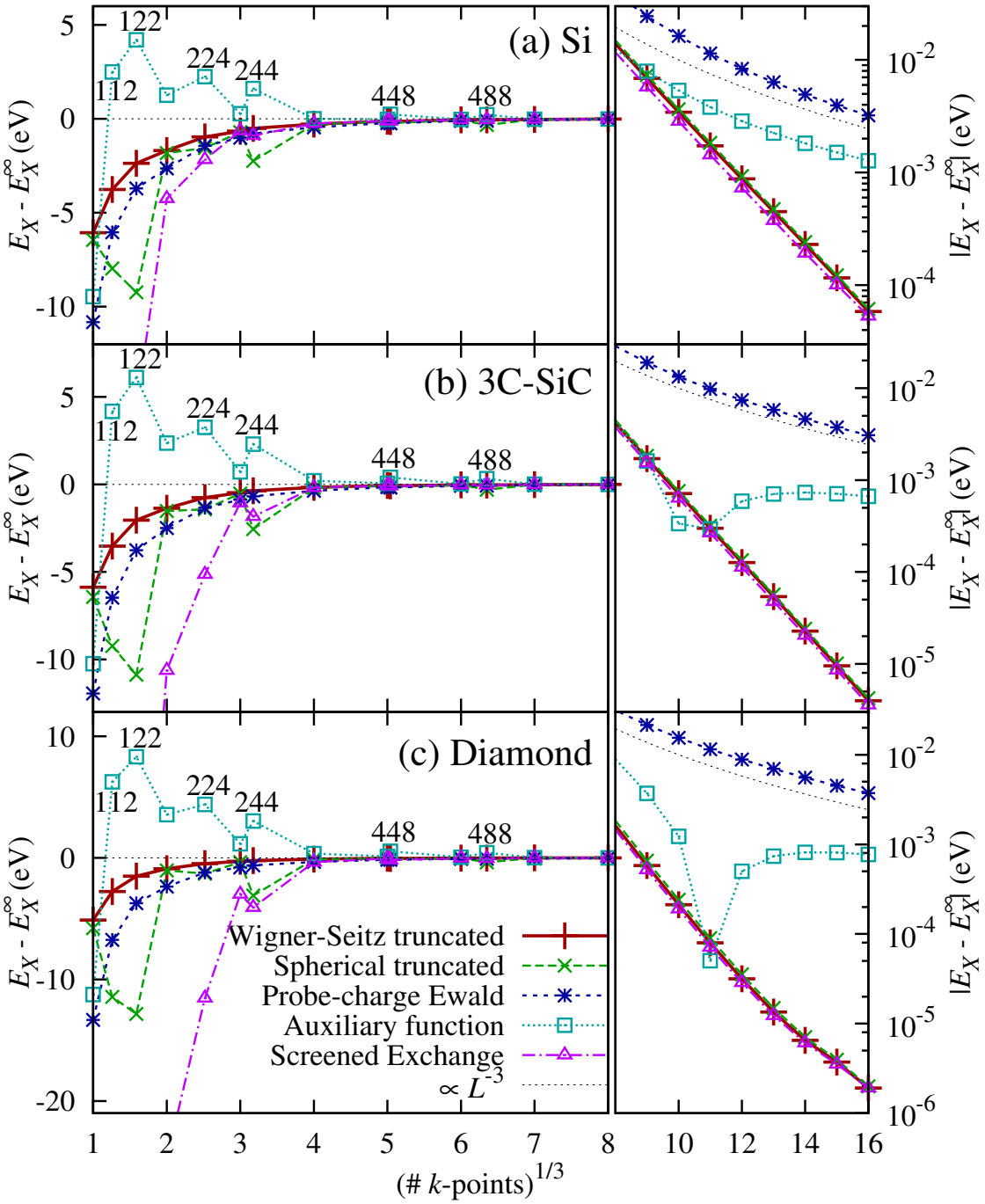

Figure 2.2: Convergence of exact and screened exchange energies per unit cell for three semiconductors and insulators in the diamond (zinc-blende) structure: (a) silicon, (b) cubic silicon carbide (phase 3C), and (c) diamond. See last paragraph of Section 2.2.1 for details. The non-monotonicity in the absolute asymptotic error of the auxiliary-function results is due to a change in sign of that error.

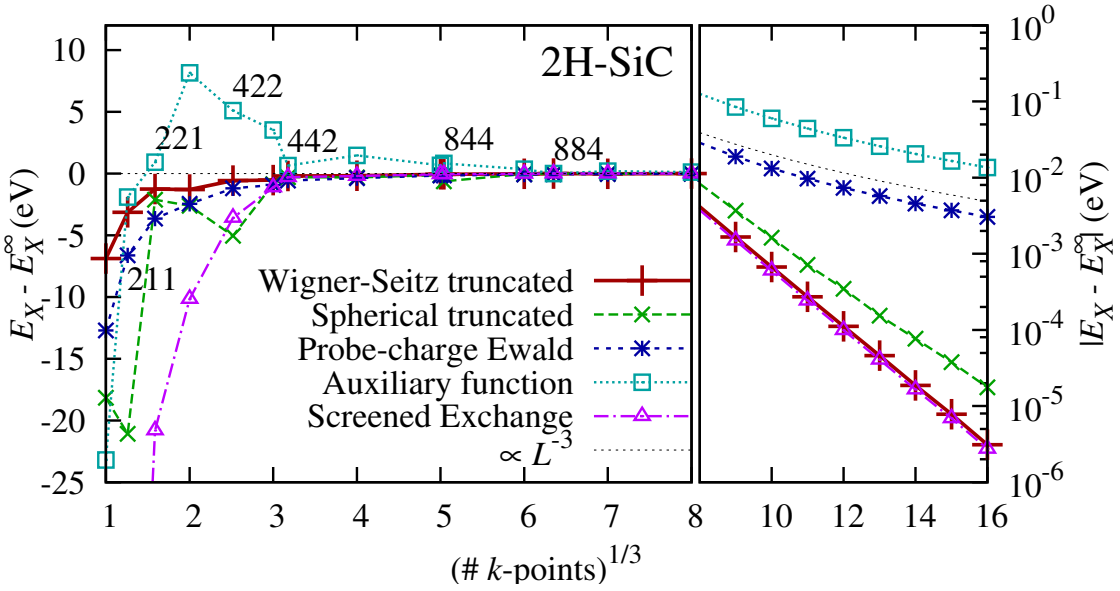

Figure 2.3: Convergence of exact and screened exchange energies per unit cell for hexagonal silicon carbide (phase 2H). See last paragraph of Section 2.2.1 for details.

compared to the probe-charge Ewald and auxiliary-function methods, which exhibit L^{-3} convergence. The exponential decay length of the error in the exchange energy with respect to L, taken here to be the nearest neighbor distance in the effective $\vec{k}$-point sampled super-lattice, decreases from 5.5 Å in silicon through 3.5 Å in cubic silicon carbide to 2.5 Å in diamond. The corresponding band gaps Δ are 1.1 eV, 2.3 eV and 5.5 eV respectively. The decay length varies roughly as $\Delta^{-1/2}$, similar to the density-matrix localization length scale of tight-binding insulators [74]. Consequently, the relative accuracy of the truncated methods for insulators increases dramatically with increasing band gap as seen in Figure 2.2. Note that the accuracy of the truncated potential methods for the exact exchange energy matches that of the screened exchange energy (red +'s and green ×'s versus pink Δ's), indicating that these methods are truly limited only by Brillouin-zone discretization errors in the underlying Kohn-Sham orbitals.

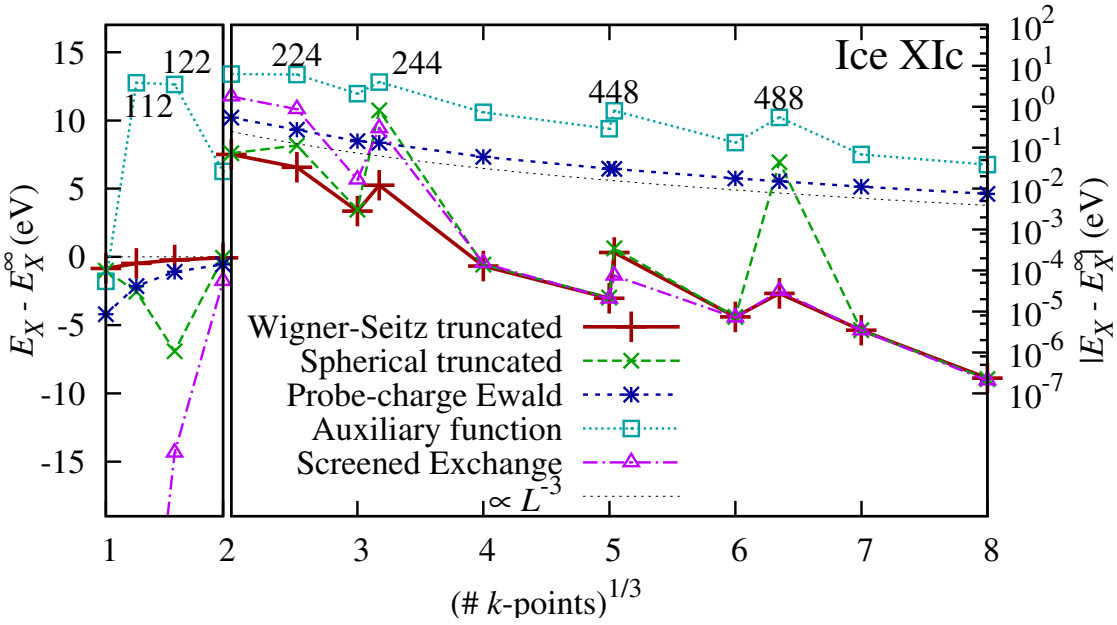

Figure 2.4: Convergence of exact and screened exchange energies per unit cell for proton-ordered cubic ice. See last paragraph of Section 2.2.1 for details.

In high-symmetry materials, the accuracy of spherical truncation is similar to Wigner-Seitz truncation for isotropic $\vec{k}$-point meshes since the Wigner-Seitz cell of the effective super-lattice is approximately spherical (rhombic dodecahedron for the FCC unit cell in the zinc-blende structure). This is no longer the case for lower symmetry crystals such as hexagonal silicon carbide (phase 2H with the wurtzite structure) shown in Figure 2.3. In this anisotropic case, the accuracy of the Wigner-Seitz truncated method (red +'s) continues to match that of screened exchange (pink Δ's). On the other hand, spherical truncation (green ×'s), although still exponentially convergent, is an order of magnitude less accurate. Similarly, amongst the asymptotically L^{-3} convergent methods, the superior accuracy of the probe-charge Ewald method for anisotropic $\vec{k}$-point meshes in the high-symmetry crystal carries forward to superior accuracy overall for lower-symmetry crystals, in comparison to the auxiliary-function method.

The differences between the methods are most dramatic for proton-ordered

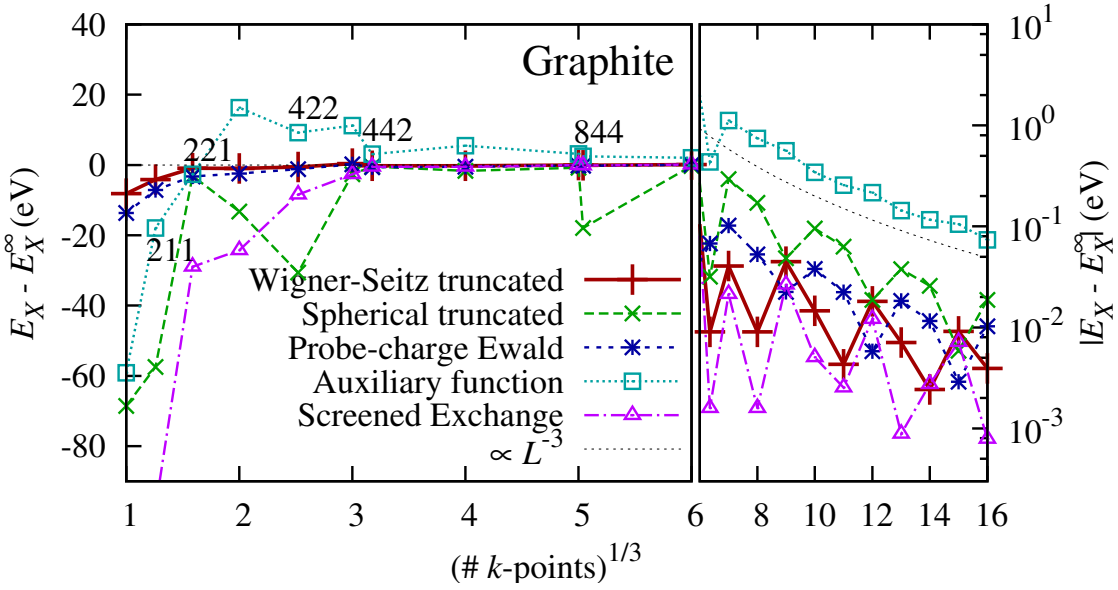

Figure 2.5: Convergence of exact and screened exchange energies per unit cell for graphite. See last paragraph of Section 2.2.1 for details.

cubic ice XIc (the proposed ground state structure [133]) shown in Figure 2.4. The highly-localized states in this material cause dramatic improvements in accuracy for the truncated methods even for coarse $\vec{k}$-point meshes. Once again, lowered symmetry significantly favors the probe-charge Ewald method in comparison to the auxiliary-function method (blue ∗'s versus cyan □'s).

2.2.3 Metals

As demonstrated above, the exponential localization of Wannier functions leads directly to exponential convergence in the case of truncated Coulomb interaction methods. In contrast, we expect the discontinuity at the Fermi energy in the ground state to lead to algebraic convergence in metallic systems, which we explore now.

Figure 2.5 shows the convergence behavior of the various methods for the

case of graphite, which is semi-metallic. Once again, the probe-charge Ewald and auxiliary-function methods exhibit L^{-3} convergence. Wigner-Seitz truncation no longer exhibits exponential convergence, but remains the most accurate method for computing the exchange energy, with accuracy comparable to that of screened exchange as before. Spherical truncation and the auxiliary-function method are less accurate due to the lower symmetry of the crystal structure in this case.

The exponents governing the localization in graphite are complicated by the layered quasi-two-dimensional structure with weak inter-planar coupling due to dispersion interactions. We analyze those details in the related two-dimensional material graphene in Section 2.2.4, and here now focus on a simpler, three-dimensional metal, platinum.

In simple metals, the Wannier-like functions $\bar{w}_i^{\vec{R}}(\vec{r})$ given by (2.9) decay $\sim r^{-2}$, as discussed in Section 2.1.1. This leads to r^{-4} decay of the orbital products and consequently $\sim \int_L^\infty 4\pi r^2 dr (1/r) r^{-4} \sim L^{-2}$ errors due to truncation in the Coulomb self energies in (2.10). The L^{-2} errors dominate the asymptotic convergence of all the methods for metals at low temperatures, as shown in Figure 2.6(a) for platinum. However, Wigner-Seitz truncation (red +'s) continues to yield the highest accuracy for exact exchange in practice, particularly for coarse $\vec{k}$-point meshes.

At finite Fermi temperature T for the electrons, the exponential decay length scales as at/T, where a is the lattice constant and t is the typical band width. When the number of $\vec{k}$-points along each dimension exceeds approximately t/T, this decay length plays an analogous role to the Wannier-function length scale of insulators. For example, for a metal with bandwidth $t = 5$ eV, an electron

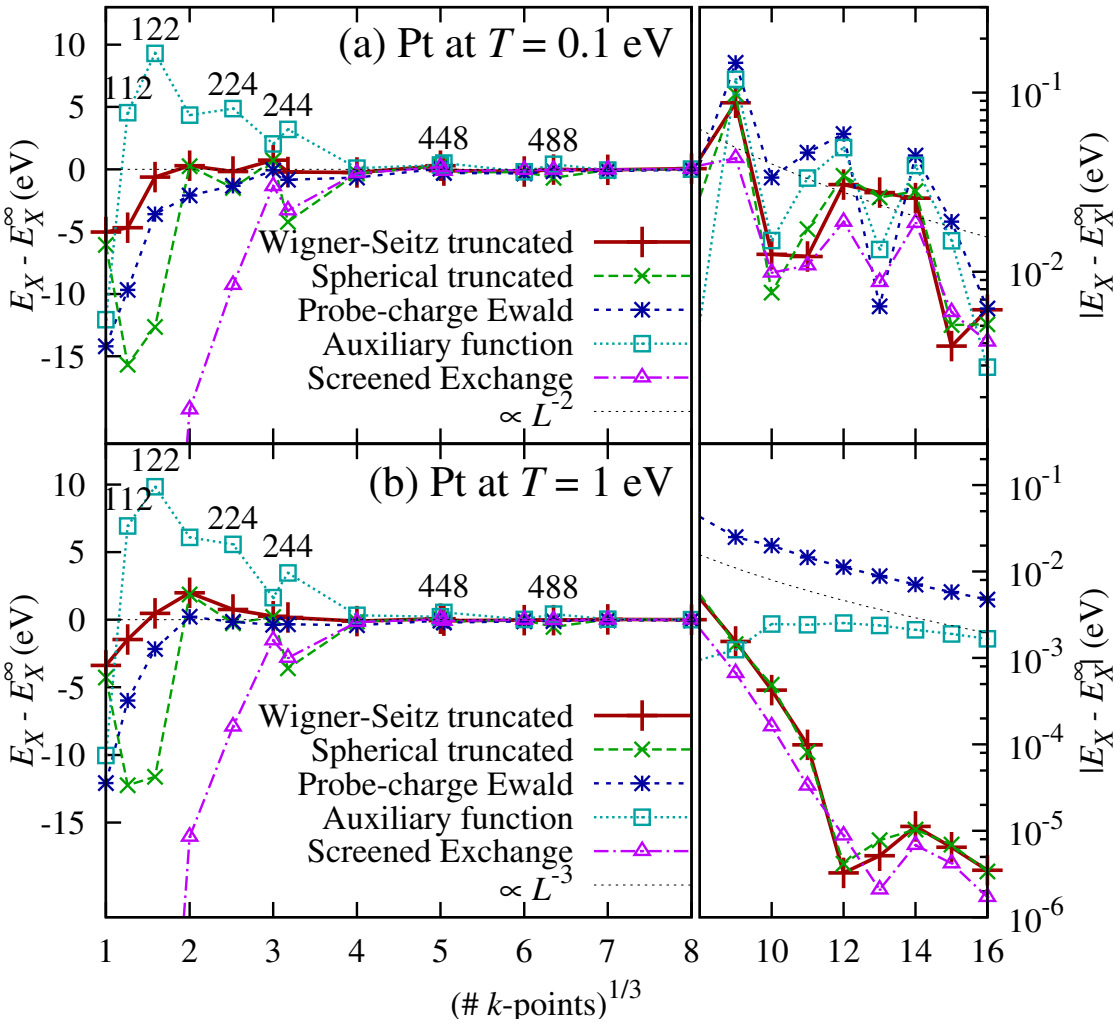

Figure 2.6: Convergence of exact and screened exchange energies per unit cell for face-centered cubic metallic platinum at electron temperatures, (a) $T = 0.1$ eV and (b) $T = 1$ eV. See last paragraph of Section 2.2.1 for details. The non-monotonicity in the exponentially-convergent results in (b) for exact exchange with truncated-potentials and screened exchange is due to a change in sign of the error near $N_k^{1/3} \sim 12$.

temperature, $T \sim 1$ eV is necessary to obtain exponential convergence beyond 5 $\vec{k}$-points per dimension. Figure 2.6(b) shows the restored exponential convergence of the truncated methods and screened exchange, and the L^{-3} convergence of the other methods, in this regime.

2.2.4 Lower dimensional materials

In lower dimensional semiconducting or insulating systems, we should expect the localization of the underlying Wannier functions to allow for exponential $\vec{k}$-point convergence with an appropriately chosen method from Section 2.1.2. For the metallic cases, the reduced dimensionality can lead to different exponents for the polynomial convergence, which we also explore here.

The semi-metallic behavior of the two-dimensional material graphene is particularly interesting. In this case, the localization properties are determined by the phase twist of Bloch functions in k-space about the Dirac points.[4]. The two-dimensional Fourier transform of that phase twist yields an r^{-2} decay of the Wannier-like functions. The orbital products fall off as r^{-4} leading to truncation errors in the Coulomb self energies in (2.10) that scale as $\int_L^\infty 2\pi r dr (1/r) r^{-4} \sim L^{-3}$. Figure 2.7(a) shows that all methods, therefore, exhibit L^{-3} asymptotic convergence for graphene at zero temperature. The errors oscillate with a period of 3 $\vec{k}$-points per dimension because the discrete $\vec{k}$-point mesh includes the Dirac points when the sampling is a multiple of 3.

At sufficiently high temperatures, the exponential length scale at/T of the Wannier-like functions becomes relevant at practical $\vec{k}$-point meshes, just as in

[4]Near these points, the energy varies linearly with momentum, so that the electrons behave like massless relativistic fermions described by the Dirac equation

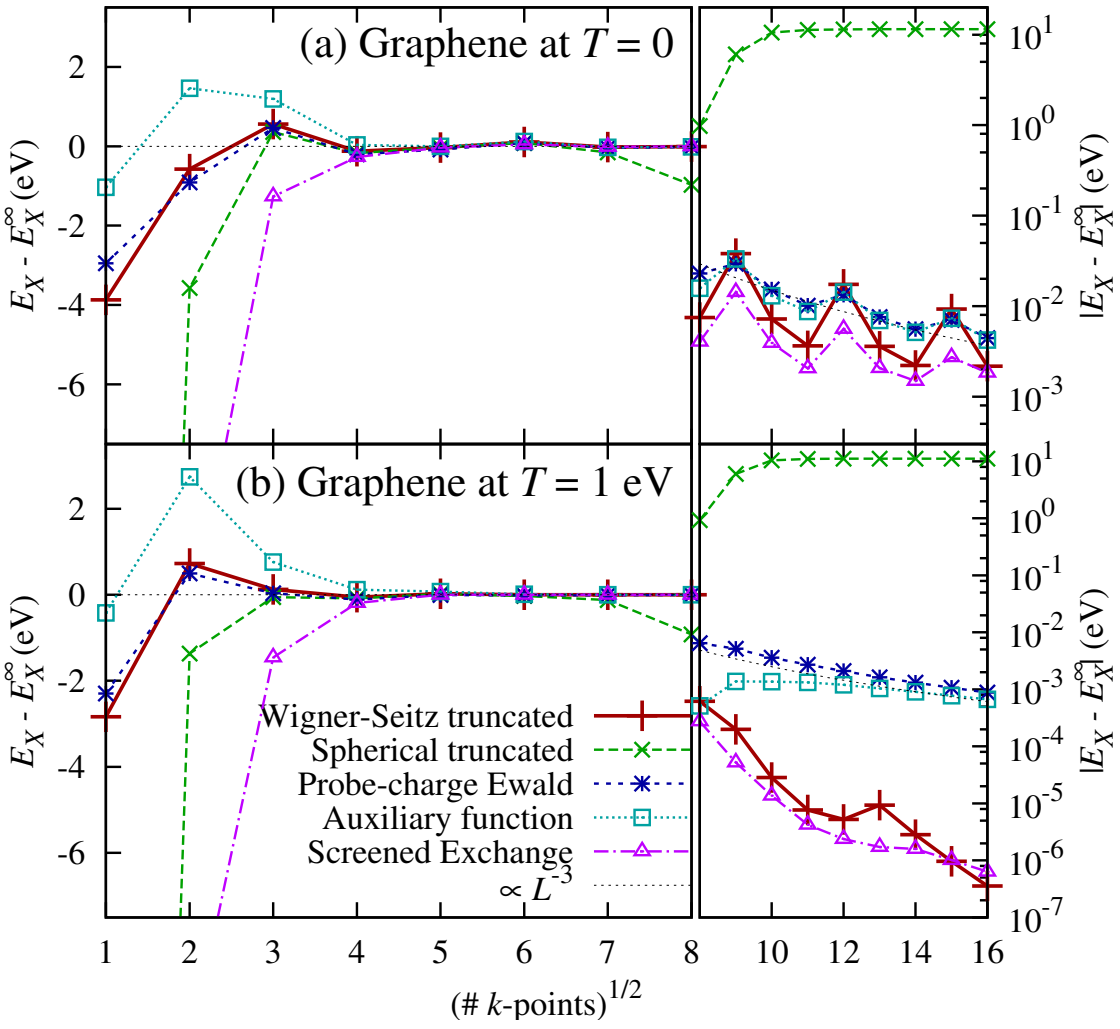

Figure 2.7: Convergence of exact and screened exchange energies per unit cell for graphene at electron temperatures, (a) $T = 0$ and (b) $T = 1$ eV. See last paragraph of Section 2.2.1 for details. The non-monotonicity in the exponentially-convergent results in (b) for Wigner-Seitz truncated exact exchange is due to a change in sign of the error near $N_k^{1/2} \sim 11$.

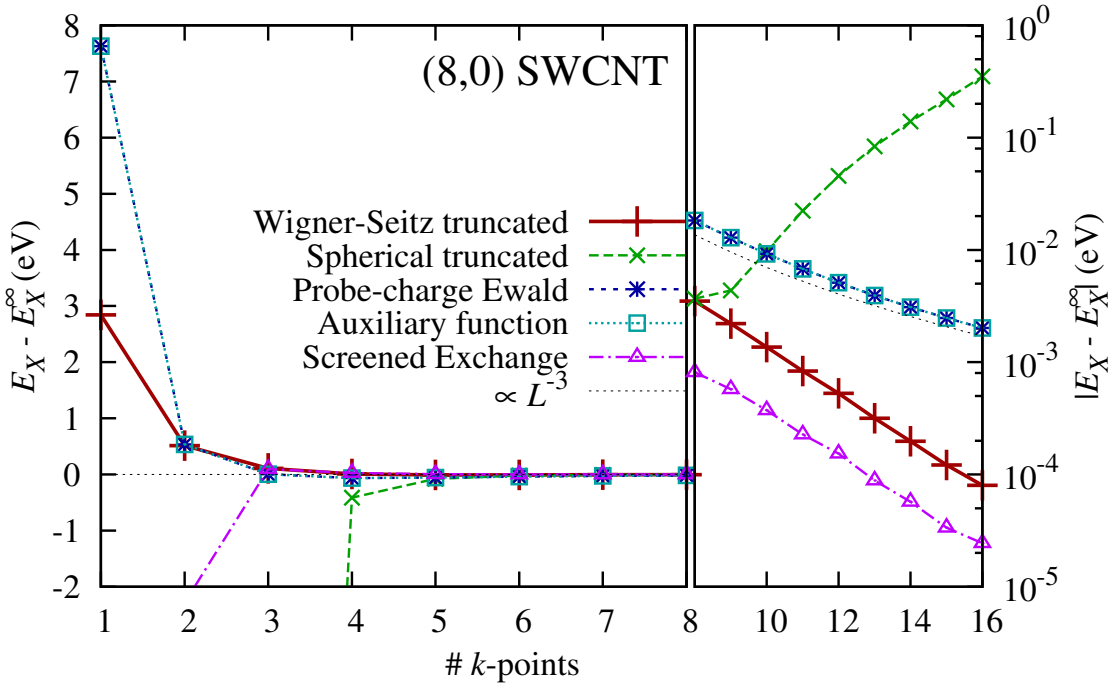

Figure 2.8: Convergence of exact and screened exchange energies per unit cell for the semiconducting (8,0) single-walled carbon nanotube. See last paragraph of Section 2.2.1 for details.

three-dimensional metals. Figure 2.7(b) shows that this length scale restores the exponential convergence of the Wigner-Seitz truncated method and screened exchange (red +'s and pink Δ's respectively).

Truncation on a three-dimensional sphere is no longer meaningful in these lower dimensional materials, and it gives reasonable results only for intermediate $\vec{k}$-point meshes which minimize the aspect ratio of the supercell. Analytically Fourier transforming the Coulomb potential truncated on the appropriate 'lower-dimensional spheres', finite cylinders in two-dimensional materials and finite right prisms in one-dimensional materials, is no longer possible. Wigner-Seitz truncation using the MIC algorithm (C.4) is clearly the method of choice in these geometries.

Finally, in one dimensional systems, the probe-charge Ewald and auxiliary-function methods are identical as proved in Section 2.1.2. As Figure 2.8 shows, for a semiconducting (8,0) single-walled carbon nanotube (SWCNT), both of these methods yield rather poor L^{-3} convergence, in contrast to the exponential convergence of the Wigner-Seitz truncation and the screened exchange interaction for this system.

2.2.5 Total Energy Convergence

The results in the preceding sections demonstrate that calculation of exact exchange with Wigner-Seitz truncation, with relatively few exceptions, generally requires fewer $\vec{k}$-points to reach a given level of convergence than all other methods. Moreover, we have seen that calculation of the long-ranged exact exchange, when performed with the Wigner-Seitz truncated method, competes with the short-ranged screened exchange of the HSE06 functional, which models the long-ranged components of the exchange energy within a semi-local approximation. We now ask whether the Wigner-Seitz method makes it possible to evaluate exact-exchange functionals on the same, relatively modest $\vec{k}$-point meshes needed for semi-local density-functional theory calculations?

To address the above issues, Figure 2.9 compares the total energy convergence of a purely semi-local density functional (PBE [128]), a standard hybrid functional (PBE0 [1]) employing exact exchange computed using various standard approaches as well as our Wigner-Seitz approach, and a hybrid functional (HSE06 [85]) employing short-ranged screened exchange. The results in Figure 2.9 show that the total energy convergence of the exact-exchange hybrid

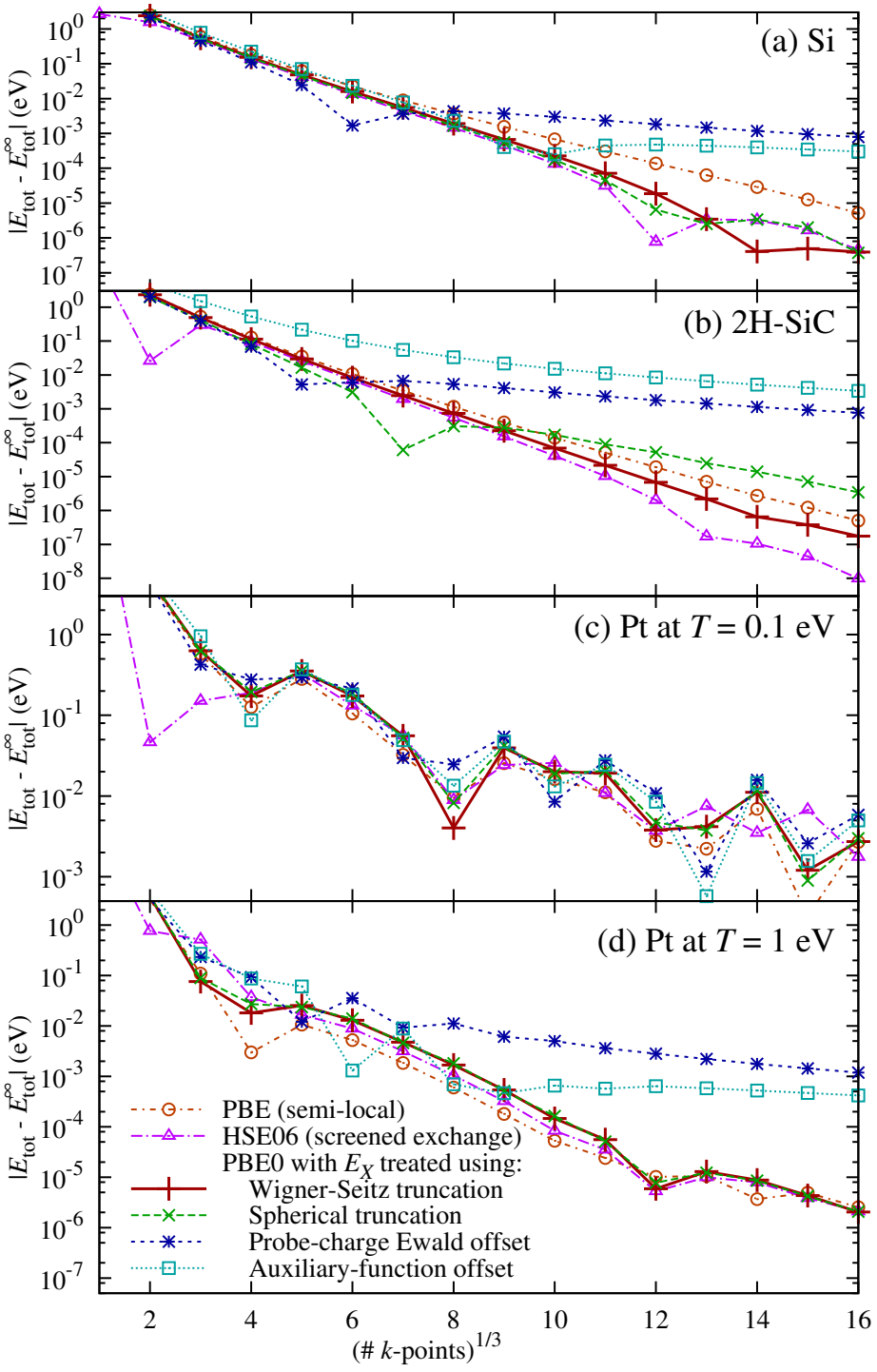

Figure 2.9: Total energy convergence (per unit cell) of the semi-local functional PBE and the screened-exchange hybrid functional HSE06 compared to the hybrid functional PBE0 with exact exchange computed using various methods for (a) silicon (b) hexagonal silicon carbide (phase 2H) and metallic platinum at (c) $T = 0.1$ eV and (d) $T = 1$ eV.

functional PBE0, when computed using truncated potentials, is indeed comparable to that of the screened-exchange hybrid functional HSE06. Moreover, computing exact exchange with truncated methods not only matches the convergence of traditional semi-local density functionals, but sometimes even outperforms their convergence for insulators (as in Figure 2.9a,b).

Spherical truncation yields similar convergence to Wigner-Seitz truncation for high-symmetry insulators (green $\times$'s versus red +'s in Figure 2.9a), and is less accurate for lower symmetry ones (Figure 2.9b), as expected. The auxiliary function and probe-charge Ewald methods limit the total energy convergence of PBE0 to L^{-3} (cyan $\square$'s and blue $*$'s in Figure 2.9(a,b,d)), in contrast to the exponential convergence of PBE and HSE06.

The r^{-2} localization of the Wannier-like functions in metals at low temperature limit the convergence of all methods, including the semi-local functionals (Figure 2.9c). The L^{-2} errors in the tails of the Kohn-Sham orbitals lead to L^{-2} errors in the Kohn-Sham kinetic energy, which dominate in this situation. Consequently, all methods for treating exchange yield total-energy convergence of PBE0 similar to that of PBE and HSE06 for low-temperature metals, with Wigner-Seitz truncation only marginally better than the others.

At sufficiently high electron temperatures (Figure 2.9d), the exponential length scale at/T becomes relevant at practical $\vec{k}$-point configurations as before, leading to exponential total-energy convergence of the semi-local functionals. As in the case of insulators, the auxiliary-function methods limit the accuracy of the hybrid functional while the truncated-potential methods yield total-energy convergence for the exact-exchange hybrid functional on par with the screened-exchange and traditional semi-local functionals.

2.3 Summary

Hybrid density-functionals enable high-accuracy predictions within Kohn-Sham theory, but state-of-the-art methods for computing such functionals necessitate dense $\vec{k}$-point meshes in calculations of periodic systems due to the regularization methods commonly employed for the singular Coulomb integrals in the exact-exchange energy. Analyzing the exchange energy in a real-space formalism based on Wannier functions reveals that the dominant errors at finite $\vec{k}$-point meshes arise from the resultant artificial periodicity of the Wannier functions. Truncating the Coulomb potential on the Wigner-Seitz cell of the effectively-sampled super-lattice is therefore the ideal method to minimize these errors.

Wigner-Seitz truncation systematically yields the most accurate exchange energy for systems with different electronic structures and dimensionalities, and delivers $\vec{k}$-point convergence for hybrid functionals on par with that of screened-exchange and even traditional semi-local functionals. Along with the accurate free energy functional and polarizable continuum approximations to solvent effects presented in the following chapters, this brings us one step closer to widespread *ab initio* studies of processes such as catalysis at solid surfaces that require chemical accuracy.[5]

[5] In the quantum chemistry literature, chemical accuracy refers to the energy accuracy necessary to make reasonable predictions for chemical reactions at room temperature, and is usually taken to be around 1 kcal/mol $\approx$ 1.6 mE_h $\approx$ 1.7k_BT at 298 K. [156].

CHAPTER 3

BONDED-TRIMER FREE ENERGY FUNCTIONAL FOR LIQUID WATER [1]

Joint density-functional theory provides a rigorous framework to treat the electronic structure of solvated systems without thermodynamic phase-space sampling by employing a classical density-functional description of the solvent environment. In practice, this requires an accurate and computationally efficient free energy functional approximation for the liquid of interest. The most accurate, currently available functionals for polar molecular fluids such as water [31, 33, 96, 97, 180] rely, however, on direct correlations (from neutron scattering or computer simulation) at each temperature and pressure of interest, restricting their efficiency and applicability.

This chapter addresses the need for a computationally efficacious microscopic theory of water that is capable of providing accurate free energies under inhomogeneous conditions without the dependence on fluid structure data. The strategy is to identify a simple effective microscopic Hamiltonian which (a) reproduces the equation of state for homogeneous water and (b) is readily represented by a free-energy functional even in the inhomogeneous case.

Statistical associating fluid theory (SAFT) [50], based on Wertheim's thermodynamic perturbation theory [171], is one such approach which has been successfully applied to the study of vapor-liquid interfaces [49], with model parameters for water determined from the equation of state [29]. However, the predictions of this theory have not yet included quantities of interest in solvation methods such as cavity formation energies and dielectric response, partly

[1] Published as 'R. Sundararaman, K. Letchworth-Weaver and T.A. Arias, *J. Chem. Phys.* **137**, 044107 (2012)'. KLW contributed to the Bayesian ensemble-of-models error estimation.

due to the relative complexity of the model Hamiltonian. Below, we develop an alternate simpler Hamiltonian based upon microscopic intuition about hydrogen bonding, and we demonstrate that the resulting functional (also based on Wertheim theory) leads to a relatively accurate free-energy description of inhomogeneous water, especially given the simplicity of the underlying model.

3.1 Model molecular Hamiltonian and equation of state

Within the constraints of condition (b) above, a natural starting point would be the standard approach of perturbations about the hard-sphere fluid,[2] for which Fundamental Measure Theory [134, 159, 58, 135] provides a highly accurate functional. The hard-sphere diameter required to reproduce bulk properties can be inferred from the excluded volume in the equation of state, and fits [77] to experimental data suggest a value that strongly decreases with temperature and is ~ 3.3 Å at 298 K. This is clearly incompatible with the almost temperature-independent ~ 2.8 Å location of the first peak in the experimentally observed oxygen-oxygen partial radial distribution [145].

This incompatibility stems from the discrepancy between the close-packed coordination of the hard-sphere fluid and the tetrahedral coordination favored by water. Water prefers the formation of open tetrahedral networks at lower temperatures, which leads to empty space, 'voids', within cages of water molecules, as manifested by the temperature-dependent excess excluded volume in the equation of state. Consequently, we propose a reference fluid consisting of a compound object (Figure 3.1(a)): a hard sphere of radius R_O at the

[2]The hard sphere fluid does not include orientational degrees of freedom; we treat the orientational degrees of freedom of a molecular liquid exactly at the level of an ideal gas of orientable rigid molecules, and only employ the excess free energy of the hard sphere fluid. See the discussion following (3.6) for details.

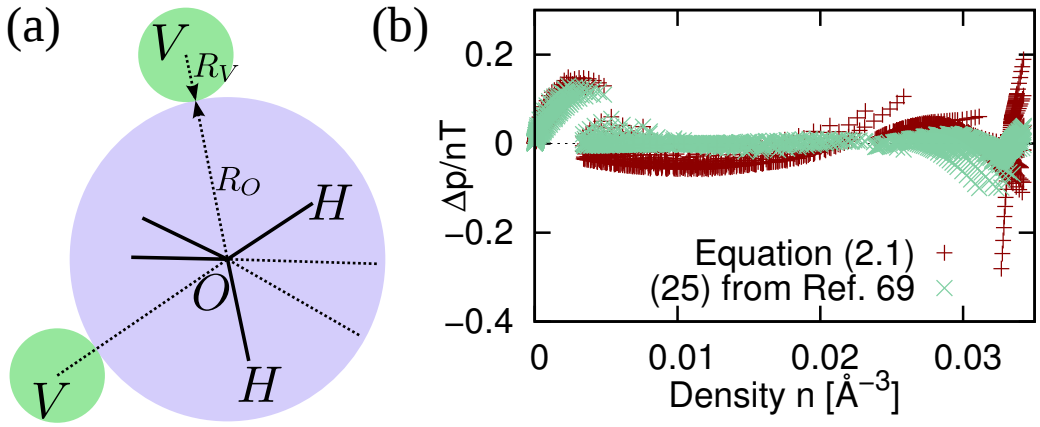

Figure 3.1: (a) Tangentially bonded hard-sphere model for liquid water: O (oxygen) sphere with two V spheres in contact diametrically opposite to the H (hydrogen) sites (b) Residual for the equation of state (3.1) fit to experimental data [56, 61], compared to the semi-empirical Jeffery-Austin equation of state [77].

O (oxygen) site with smaller spheres of radii R_V at two void sites V placed in contact (at a distance $\sigma_{OV} = R_O + R_V$) along two of the conjugate tetrahedral directions to the hydrogen bond directions. For our model, we take the O-H distance to be 1 Å with a tetrahedral H-O-H angle, as in the frequently employed SPC/E interatomic potential model [15]. The geometry of this compound object is chosen to favor closest approach along the hydrogen bond directions.

Our ansatz for the intermolecular Hamiltonian is the repulsive pair potential corresponding to the tangentially bonded hard-sphere trimer of Figure 3.1(a), perturbed by an isotropic attractive pair potential $U_a(r)$ between the O sites. The equation of state of this fluid is well approximated by

$$p(n,T) = p_{\mathrm{id}} + p_{\mathrm{HS}}^{\mathrm{ex}} - 2n^2T \left.\frac{\partial \ln g_{OV}^{\mathrm{HS}}\big|_{\sigma_{OV}}}{\partial n}\right|_T - \frac{\kappa n^2}{2}, \tag{3.1}$$

where the first three terms correspond to the BHS equation of state [6] for a fluid composed of molecules with tangentially-bonded hard spheres, and the final term is the mean-field contribution from the as yet undetermined attractive perturbation $U_a(r)$, with $\kappa \equiv -\int \mathrm{d}r 4\pi r^2 U_a(r)$.

The BHS equation of state is based on Wertheim perturbation theory [171] about the hard sphere mixture, consisting of density n of O-spheres and $2n$ of V-spheres. The pressure of this reference system is $p_{\rm HS} = 3nT + p^{\rm ex}_{\rm HS}$, where we separate and collect the $O(n)$ ideal gas parts to elucidate the connection with the density functional (3.6). For $p^{\rm ex}_{\rm HS}$, we employ the accurate generalization [59] of the Carnahan-Starling excess pressure to hard sphere mixtures

$$p^{\rm ex}_{\rm HS} = T\left[\frac{n_0 n_3}{1-n_3} + \frac{n_1 n_2}{(1-n_3)^2}\left(1+\frac{n_3^2}{3}\right) + \frac{n_2^3}{12\pi(1-n_3)^3}\left(1-\frac{2n_3}{3}+\frac{n_3^2}{3}\right)\right], \tag{3.2}$$

where $n_0 = 3n$, $n_1 = (R_O + 2R_V)n$, $n_2 = 4\pi(R_O^2 + 2R_V^2)n$ and $n_3 = \frac{4\pi}{3}(R_O^3 + 2R_V^3)n$ are the uniform fluid fundamental measures.[3]

First order Wertheim perturbation for the bonding constraints accounts for the fixed O-V separation and not the V-O-V angle; nonetheless it has been shown to well approximate the equation of state of objects with this geometry [6]. We accumulate its contribution at $O(n)$ into the first term of (3.1): this exactly corrects the ideal gas mixture value of $3nT$ to the rigid-molecule ideal gas value of $p_{\rm id} = nT$. (We use this fact later to restore the intramolecular bond angle constraints in the model for inhomogeneous water.) The remaining contribution of this perturbation, the third term of (3.1), corrects the excluded volume effects of the hard sphere mixture to account for the O-V distance constraints. There,

$$g^{\rm HS}_{OV}\big|_{\sigma_{OV}} = \frac{1}{1-n_3} + \frac{n_2 R_{\rm hm}}{(1-n_3)^2} + \frac{2(n_2 R_{\rm hm})^2}{9(1-n_3)^3}, \tag{3.3}$$

is the contact value of the O-V partial radial distribution in the hard sphere mixture with $R_{\rm hm} = R_O R_V/\sigma_{OV}$.

As motivated earlier, the temperature dependence of the exclusion volume is a critical feature of the equation of state for water [77]. Because the location of

[3]The fundamental measure n_0 has the dimensions of density (a_0^{-3}), n_1 of number per unit area, and n_2 of number per unit length, while n_3 is dimensionless.

the first peak in the *O-O* partial radial distribution does not change appreciably with temperature, we attribute this dependence to changes in the radii of the V spheres, modeled as a decreasing function $R_V(T) = R_V^{(0)} e^{-T/T_V}$ to qualitatively capture the effect of the empty spaces in the open tetrahedral network. This leads to a model equation of state (3.1) with only four adjustable parameters ($R_V^{(0)}$, T_V, κ, and R_O), which we fit to experimental data for the bulk liquid and vapor [56] including data for the supercooled liquid [61].

The root mean-square error in the ratio of the pressure to the ideal-gas pressure, p/nT, is 4.8×10^{-2} for the current 4-parameter fit, which compares very favorably with 2.9×10^{-2} for the standard semi-empirical Jeffery-Austin equation of state [77] (comparison in Figure 3.1(b)), especially considering the fact that the latter fit employs more than twice as many (~ 9) adjustable parameters. Beyond providing a reasonable fit to the equation of state, the key advantage of the present work is that these results stem directly from a model microscopic Hamiltonian, which we exploit below to construct a theory for inhomogeneous water.

To ensure that our model parameters are indeed independent and physically meaningful, we employ Bayesian error estimation following [21, 110]. Specifically, we generate a canonical ensemble of parameter sets (Figure 3.2) with a Metropolis walk in parameter space, where the residual is the 'energy' and the 'temperature' is $2C_0/N_p$ where C_0 is the minimum residual and $N_p = 4$ is the number of fit parameters. The optimum parameters with standard deviations

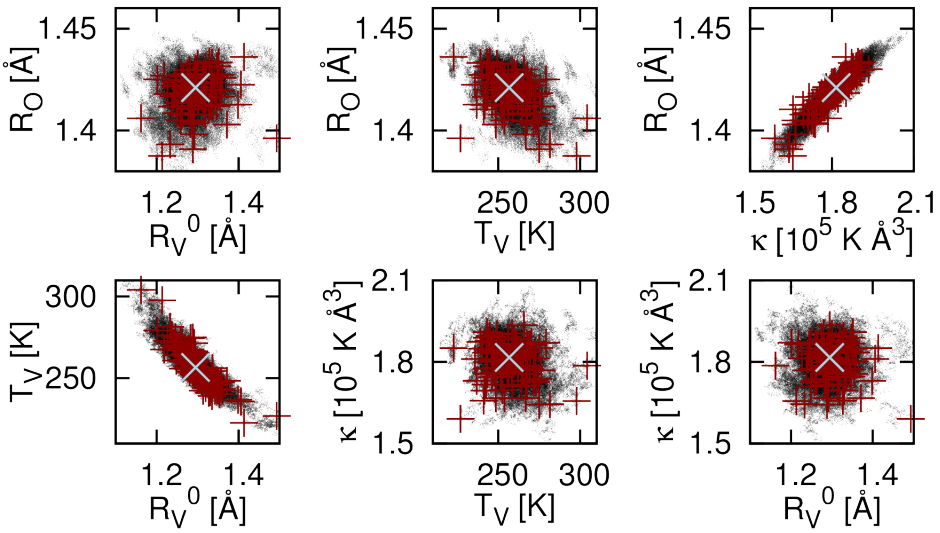

Figure 3.2: Metropolis sampling of a canonical ensemble of parameters, shown in all six projections of the four-dimensional parameter space. One hundred random samples (+) are drawn from the full set (·) for error estimation of all subsequent results; ×'s mark the optimum parameter set.

thus estimated are

$$\begin{aligned} R_V^{(0)} &= (1.290 \pm 0.049)\text{Å} \\ T_V &= (258.7 \pm 12.3)K \\ \kappa &= (1.805 \pm 0.074) \times 10^5 K\text{Å}^3 \\ R_O &= (1.419 \pm 0.010)\text{Å}. \end{aligned} \tag{3.4}$$

The modest eccentricities of the ensemble slices in Figure 3.2 indicate that the covariances of these parameters are nominal, suggesting that the parameters have physical meaning rather than merely controlling a flexible fit function for the equation of state.

An advantage of this ensemble-of-models approach, which we exploit below, is that one can estimate how well the fit to bulk data constrains all subsequent predictions, including those for inhomogeneous water, by evaluating

those predictions for a sampling of the ensemble of parameters (indicated in Figure 3.2 as +'s), instead of just the one optimum parameter set.

3.2 Model for inhomogeneous water

So far, we have discussed the implications of our model molecular Hamiltonian for properties of bulk liquid water. The application of this model in *ab initio* solvation theories requires description of the free energy for microscopically inhomogeneous configurations of liquid water, such as those surrounding molecules in solution.

Capturing the behavior of inhomogeneous water requires information beyond merely the integrated strength κ of the pair-potential interaction $U_a(r)$. This work demonstrates that the simplest next step, including information about the range of the interaction, suffices to capture surprisingly well the main features of the short-range correlations in the liquid. To this end, we employ the attractive-part of the Lennard-Jones potential

$$U_a(r) = \frac{-9\kappa}{8\pi\sqrt{2}\sigma_U^3} \begin{cases} (\sigma_U/r)^6 - (\sigma_U/r)^{12}, & r \geq 2^{1/6}\sigma_U \\ 1/4, & r < 2^{1/6}\sigma_U \end{cases} \tag{3.5}$$

which has the correct long range r^{-6} tail for the orientation-averaged interaction of a dipolar fluid.[4] We fit the range σ_U to reproduce the bulk surface tension at 298 K (based on calculations with the free-energy functional below), finding $\sigma_U = 2.62$ Å. When applied to inhomogeneous water, the model is therefore

[4]Despite the r^{-12} short-ranged repulsion lacking a physical origin, the Lennard-Jones interaction potential is highly popular in molecular dynamics and fluid theory. The predictions of the free energy functional we present here are not very sensitive to the details of the repulsive part of the perturbation potential, most of which is replaced by the hard sphere functional after separating out the attractive part.

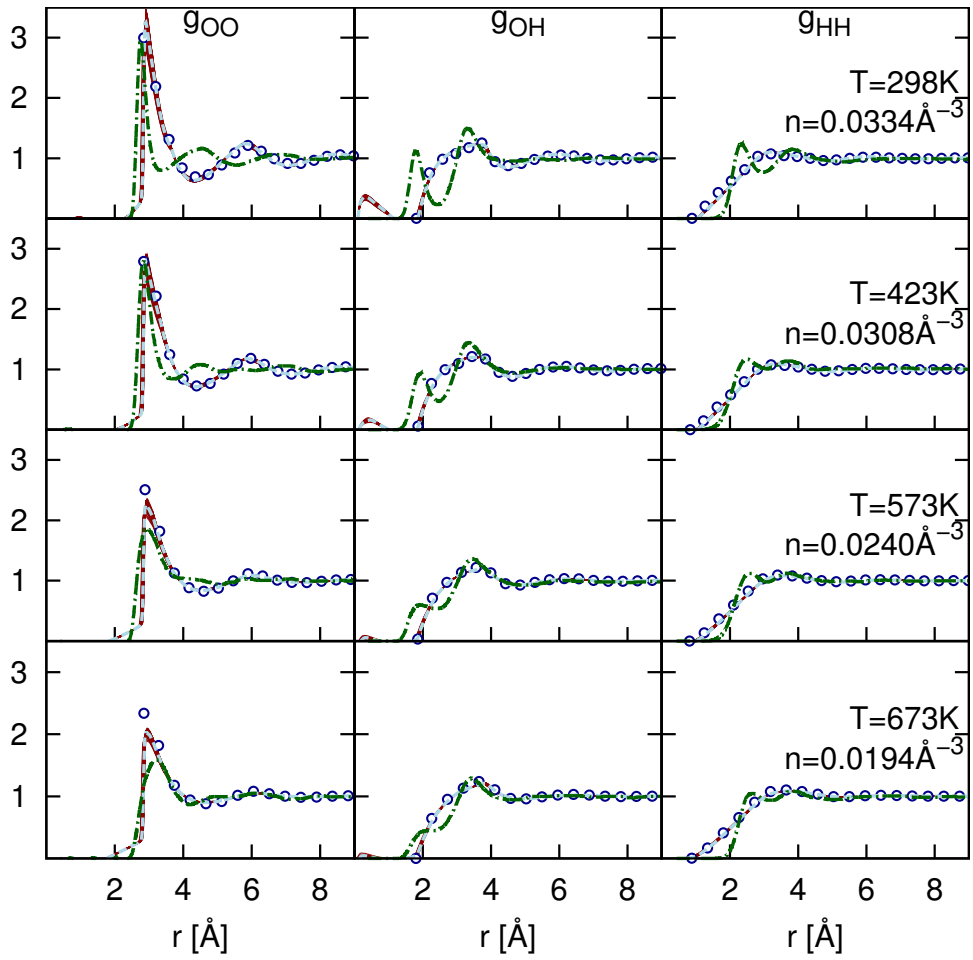

Figure 3.3: Partial radial distribution functions from the density functional (3.6) (bundle of thin red lines for the ensemble, with results for optimum parameters highlighted by dashed line) and Monte Carlo simulations for the model Hamiltonian (blue circles), compared to experimental pair correlations of water from Soper et al. [145] (green dot-dashed line)

sensitive to one additional fit parameter, in comparison to its application to bulk water.

To evaluate the viability of this simple model Hamiltonian for describing inhomogeneous water, we first compute its pair correlation functions[5] (for each

[5]The pair correlation functions or partial radial distributions, $g_{\alpha\beta}(r)$, are defined as the probability of simultaneously finding atoms α and β at two points separated by r in a uniform interacting fluid, divided by the square of the corresponding probabilities for a non-interacting system at the same density.

of the state points for which experimental correlations were measured in Soper et al. [145]) directly with canonical-ensemble Monte Carlo simulations of 2048 molecules. The comparison (Figure 3.3) between the behavior of this model microscopic Hamiltonian (circles) and the actual experimental correlations in *physical* water (green dash-dot line) is remarkable given the highly simplified form for the model. Although the secondary peaks in the *O-O* correlations of this model Hamiltonian do appear more at the characteristic distances for a hard-sphere rather than at those for a tetrahedrally bonded fluid, the temperature and pressure dependence of the locations and heights of the first *O-O* peak compare reasonably to water. Similarly, although the first two peaks of the *O-H* and *H-H* correlations are fused into a single broader peak, the general location and particle content of these peaks are in reasonable agreement for such a simple model. These details could be corrected in future work by fitting perturbation pair potentials of zero integral $\Delta U_{\alpha\beta}(r)$ with $\alpha, \beta \in \{O, H\}$ to the experimental correlation data, but the focus of the present work is the quality of predictions which can be made from a simple microscopic model with very few adjustable parameters (five) constrained purely by the macroscopic data.

Having established a *short-ranged* microscopic model Hamiltonian which reproduces relatively well the experimental correlations in water, we turn next to development of a corresponding free-energy functional. The form of this functional,

$$\Phi[\psi] = \Phi_{\text{id}} + \Phi_{\text{HS}}^{\text{ex}} + \Phi_b + \frac{1}{2}\int n_O \left(U_a * n_O\right), \tag{3.6}$$

with $n_O(\vec{r})$ being the oxygen density and U_a given by (3.5), mirrors the equation of state (3.1), and is composed of the ideal gas free energy, hard sphere excess functional, bonding correction and mean field perturbation.

We start with the exact grand free energy functional for the ideal gas of orientable rigid molecules and thereby restore exact treatment of the intramolecular bond-angle constraints; this approach is consistent with Wertheim theory since the latter yields the exact rigid-molecular ideal gas pressure $p_{id} = nT$ at $O(n)$ in the uniform limit. The free energy of the inhomogeneous ideal gas with chemical potential μ in external site potentials $V_\alpha(\vec{r})$ is written as

$$\Phi_{\mathrm{id}}[\psi, n[\psi]] = \sum_\alpha \int d\vec{r} n_\alpha(\vec{r})(V_\alpha(\vec{r}) - \psi_\alpha(\vec{r})) - (\mu + T) \int d\vec{r} n_O(\vec{r}), \tag{3.7}$$

employing ideal gas effective potentials [26, 27] $\psi_\alpha(\vec{r})$ for $\alpha \in \{O, H, V\}$ as the sole independent variables [96]. Here, the site densities are dependent variables computed using

$$n_\alpha(\vec{r}) = \frac{\delta}{\delta\psi_\alpha(\vec{r})} \int \frac{d\omega d\vec{r}'}{4\pi^2} \exp \frac{-1}{T} \sum_{\alpha',i} \psi_{\alpha'}(\vec{r}' + \omega \circ \vec{R}_{\alpha' i}), \tag{3.8}$$

where $\omega \in \mathrm{SO}(3)/\mathbb{Z}_2$, where $\omega\circ$ denotes the corresponding rotation for a vector, and where $\vec{R}_{\alpha i}$ are the site coordinates for a molecule in the reference orientation centered at the origin with $i = 1$ for $\alpha = O$ and $i \in \{1, 2\}$ for $\alpha \in \{H, V\}$. Note that we have simplified the above expression using the $\mathbb{Z}_2$ rotation symmetry of the molecule about its dipole axis.

To treat the hard sphere mixture excess free energy $\Phi^{\mathrm{ex}}_{\mathrm{HS}}$, we use the 'White-Bear mark II' version of fundamental measure theory [58] (incorporating Tarazona's tensor modifications [159])

$$\Phi^{\mathrm{ex}}_{\mathrm{HS}} = T \int \left[n_0 \ln \frac{1}{1-n_3} + \frac{n_1 n_2 - \vec{n}_{v1} \cdot \vec{n}_{v2}}{1-n_3} f_2(n_3) + \frac{n_2^3 - 3n_2 \vec{n}_{v2}^2 + 9\vec{n}_{v2} \bar{n}_{m2} \vec{n}_{v2} - \frac{9}{2}\mathrm{Tr}\bar{n}_{m2}^3}{24\pi(1-n_3)^2} f_3(n_3) \right], \tag{3.9}$$

in terms of the scalar, vector and tensor weighted densities $n_i = w_i^O * n_O + w_i^V * n_V$ for $i \in \{0, 1, 2, 3, v1, v2, m2\}$, where

$$f_2(n_3) = 1 + \frac{n_3(2 - n_3) + 2(1 - n_3)\ln(1 - n_3)}{3n_3}$$
$$\text{and } f_3(n_3) = 1 - \frac{2n_3 - 3n_3^2 + 2n_3^3 + 2(1 - n_3)^2 \ln(1 - n_3)}{3n_3^2}. \tag{3.10}$$

(See the comprehensive review by R. Roth [135] for details.) Note that this functional corresponds exactly to the hard sphere excess pressure (3.2) in the uniform fluid limit.

Next, Φ_b accounts for the tangential bonding constraints on the hard-sphere exclusion effects; note that the contribution from Wertheim perturbation to the ideal gas part has been absorbed into the exact rigid-molecule ideal gas free energy Φ_{id}. The Helmholtz-energy density for this term in the uniform fluid limit is determined from the third term of (3.1) to be $-2nT \ln g_{OV}^{\text{HS}}(\sigma_{OV})$, which we generalize to the inhomogeneous version

$$\Phi_b = \int \frac{-2n_0 T}{3} \ln\left[\frac{1}{1 - n_3} + \frac{\zeta n_2 R_{\text{hm}}}{(1 - n_3)^2} + \frac{2\zeta n_2^2 R_{\text{hm}}^2}{9(1 - n_3)^3}\right], \tag{3.11}$$

with the vector correction factor $\zeta = 1 - |\vec{n}_{v2}|^2/n_2^2$. We include this factor here following the proposal of Yu et al. [179], where ζ was introduced in analogy with the occurrence of the vector weighted densities in the hard sphere mixture functional in order to improve agreement with Monte Carlo calculations. Finally, the last term in (3.6) describes the attractive perturbation potential within a mean-field picture.

The partial radial distribution functions implied by the free energy functional (3.6), as evaluated from its analytic second variational derivatives using the Ornstein-Zernike relation, are in excellent agreement with the Monte Carlo simulations (circles and corresponding curve in Figure 3.3). (The minor artifacts

in the interior of the hard cores are caused by the bonding correction, whose inhomogeneous generalization is not perfect.) The small spread in these results with variation of parameters in the ensemble exemplifies how tightly the bulk data indeed constrain these predictions within the assumed model.

3.3 Predictions for the inhomogeneous liquid

To evaluate the predictions of the above density functional for the inhomogeneous fluid, we perform direct minimization of (3.6) using the nonlinear conjugate gradients algorithm [42] with the values of $\psi_\alpha(\vec{r})$ on a discretized grid as the independent variables. The orientation integrals involved in evaluating the site densities from the site potentials (3.8) are discretized using quadratures on $\mathrm{SO}(3)/\mathbb{Z}_2$. The calculations presented below are performed on radial or planar $d = 1$ dimensional grids [6] where the azimuthal symmetry simplifies the orientation quadrature from $\mathrm{SO}(3) \equiv \mathbb{S}_2 \times \mathbb{S}_1$ to $\mathbb{S}_2$, which we tessellate using a recursively subdivided icosahedron. [7]

We find remarkable agreement with available data for the behavior and free energies of microscopically inhomogeneous aqueous systems that resemble water surrounding solvated molecules, especially given that *only* bulk data, including the bulk surface tension at a *single* temperature, were employed in determining the limited number of parameters in the functional. For example, Figure 3.4 compares our prediction of the temperature dependence of the interfacial ener-

[6] An implementation of this free energy functional in $d = 3$ dimensions is available in the open source plane-wave electronic density functional theory software, JDFTx [154], and supports efficient orientation quadratures based on platonic solid rotation groups and spherical t-designs [52], in addition to outer product quadratures on Euler angles.

[7] The results obtained at a subdivision depth of 3 (642 quadrature nodes) are within 0.1% of those at depth 4 (2562 nodes), and we used the latter for generating all the plots in the chapter.

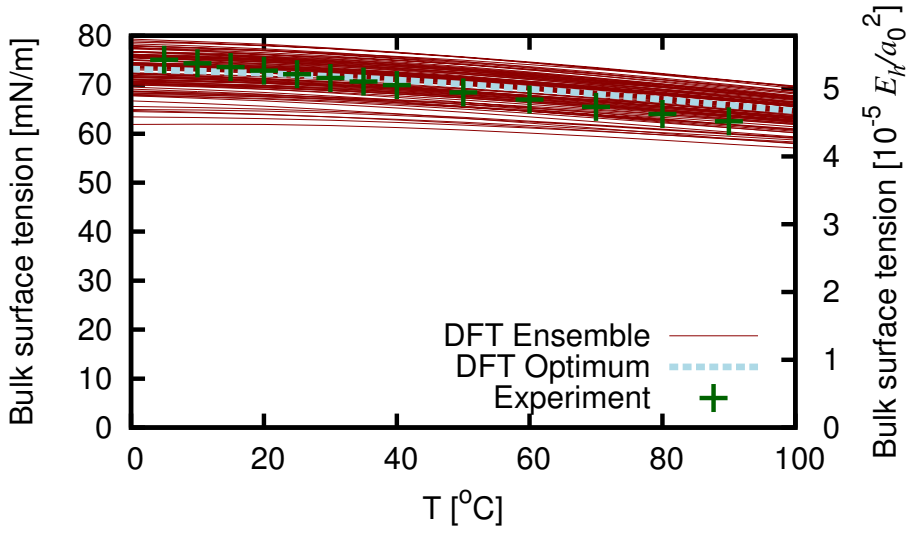

s

Figure 3.4: Energy of the vapor-liquid interface as a function of temperature, compared to the experimental values for surface tension [32].

gies with experimental data. Over the entire range of accessible temperatures at standard atmospheric pressure, we find the experiment to lie within the relatively narrow variations within our ensemble of models. Moving beyond planar interfaces, Figure 3.5 explores the radial distribution around hard spheres and the variation of free energy of hard-sphere insertion with radius, and demonstrates that the predictions of our model are in qualitative agreement with the SPC/E molecular dynamics results [70]. The contact densities and the free energies from our model are somewhat higher than those from the SPC/E model results, a situation which could potentially be improved in future work by including additional perturbation pair-potentials.

In addition to the bulk and short-ranged correlations described above, a successful theory of solvation requires accurate dielectric response. Apart from expelling water from a region of space, a solvated molecule also imposes extremely strong electric fields on the water molecules immediately surrounding it. The water molecules, which possess a permanent dipole moment, reorient in

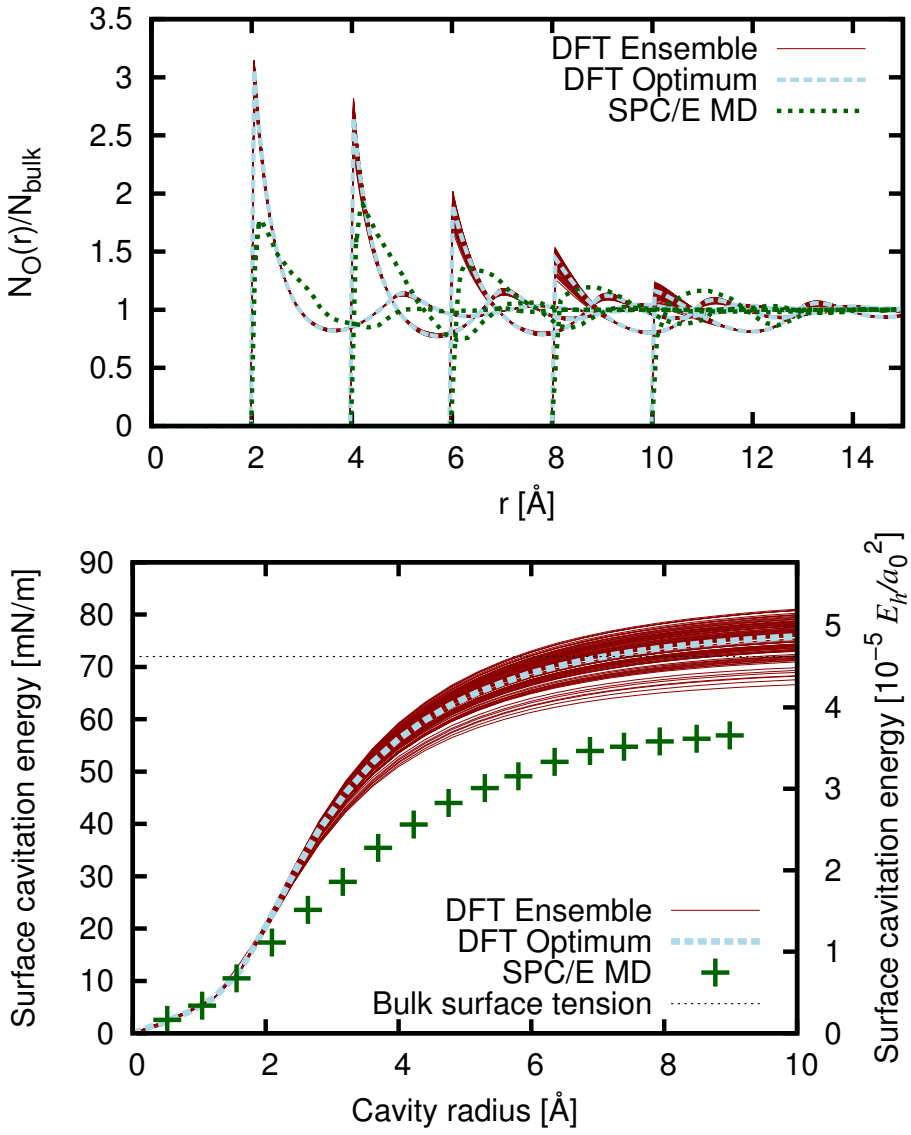

Figure 3.5: Comparison of density functional predictions with SPC/E molecular dynamics results [70] for (a) Radial distribution around spheres of radii 2, 4, 6, 8, and 10Å that exclude the oxygen sites and (b) the variation of solvation energy of such spheres per surface area with radius.

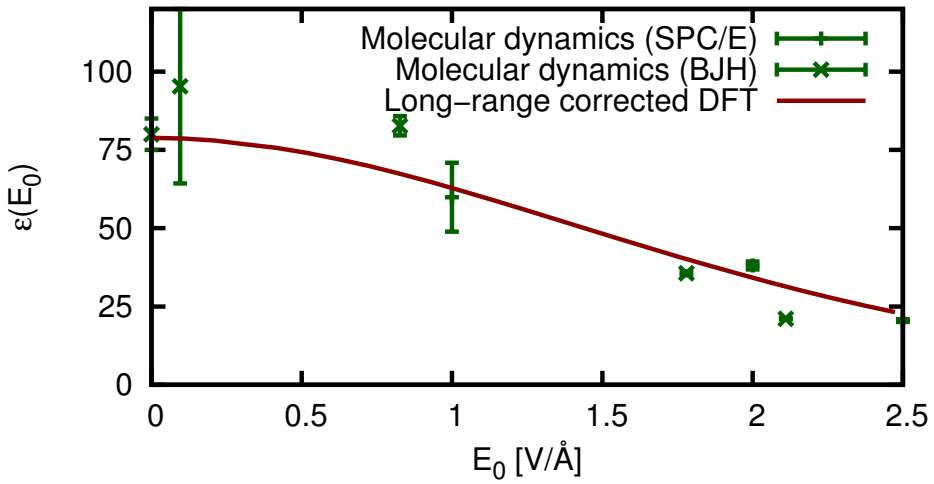

Figure 3.6: Nonlinear dielectric response: variation of relative dielectric constant ϵ with externally applied field E_0 at room temperature in comparison to SPC/E [178] and BJH [155] molecular dynamics simulations. By construction, the linear dielectric constant matches experiment due to the long-range corrections.

response to this field. To include this effect, following Lischner et al. [97], we add a scaled mean-field long range electrostatic correction

$$\Phi_\epsilon = \frac{A_\epsilon(T)}{2} \sum_{\alpha,\beta\in\{O,H\}} Z_\alpha Z_\beta \int n_\alpha K * n_\beta, \tag{3.12}$$

where the site charges Z_α are taken to be the SPC/E values [15] and $K \equiv \frac{4\pi}{G^2(1+(G/G_c)^4)}$ with $G_c = 0.33$ is the Coulomb kernel with a high frequency (short range in space) cutoff [97]. The prefactor $A_\epsilon(T) = 1 - T/(7.35 \times 10^3\ \mathrm{K})$ serves to correct for dipole correlations beyond mean field, and is fit to reproduce the bulk dielectric constant at small field. Fig. 3.6 shows that the nonlinear response at high fields (which is not fit) is well captured by the interplay between Φ_ϵ and Φ_{id}.

3.4 Summary

This chapter presents a computationally tractable free-energy functional for studies of inhomogeneous water based upon a microscopic Hamiltonian constrained by experimental data for the bulk equation of state. Following this approach gives a remarkably high-quality fit to the equation of state with only four tightly constrained parameters. With one additional parameter, the range of the model interaction, the resulting functional captures the free energies associated with inhomogeneous systems such as the liquid-vapor interface and the embedding free energy of microscopic objects, as well as essential features of the partial radial distributions and density profiles around microscopic objects. With long-range corrections, the model gives an accurate description of the non-linear dielectric response.

The bonded-trimer functional for water shows good promise for capturing the key quantities which require description in solvation studies, based on calculations in one-dimensional planar and spherical geometries. The next chapter sets up the general machinery necessary to perform calculations with such functionals for real three-dimensional systems, including those with strong electric fields.

CHAPTER 4

CLASSICAL DENSITY-FUNCTIONAL THEORIES OF RIGID-MOLECULAR FLUIDS [1]

The bonded-trimer water functional of Chapter 3 is based on a model Hamiltonian written in terms of oxygen, hydrogen and exclusion sites constrained by a rigid molecular geometry. A critical component of this functional is the exact free energy of the ideal gas of rigid molecules expressed in terms of effective ideal-gas site potentials as independent variables [96], but that approach suffers from numerical problems in practical solvation calculations. This chapter presents a more general framework for the classical density-functional theory of molecular fluids, addresses these numerical issues, and introduces a simplified free energy functional for liquid water that is more accurate than the bonded-trimer model, and is easier to generalize to other liquids.

Free-energy functional approximations for fluids of spherical particles often employ thermodynamic perturbations about the hard sphere fluid described accurately by fundamental measure theory [134, 135]. These may be extended to model polar fluids such as the Stockmeyer fluid [46], but the accuracy of such theories for real molecular fluids is not satisfactory.

Molecular fluids are best described within the reduced interaction-site models (RISM) [26], which express the interactions in terms of a few sites on each molecule, usually on atomic centers constrained by a rigid model molecular geometry. The free energy functional descriptions in terms of these site densities, however, is complicated by the molecular geometry constraints; even the ideal-

[1] Preprint online as 'R. Sundararaman and T.A. Arias, *arXiv*:**1302.0026**' (under review in *Comp. Phys. Comm.*)

gas free-energy is no longer expressible as an analytical closed-form functional of the site-densities alone. An explicit functional can be written by introducing effective ideal-gas site potentials as auxiliary variables [27], but this still requires inversion of an integral equation to obtain these potentials from the site densities, a problem which can be solved explicitly only in some limits such as reducing the molecule to a point [33], and requires an expensive Monte Carlo integration for the general case.

The above inversion problem can effectively be avoided [96] by switching to the site potentials as the independent variables *instead* of the site densities. This method was applied successfully to fluids of hydrogen chloride [96] and water [97] in one dimensional (planar) geometries. The convergence of free energy minimization with respect to these independent variables turns out to be quite slow, however, particularly in the presence of strong electric fields.

This chapter presents a simple general scheme of choosing independent variables that can generate the site densities for the free-energy functional treatment of molecular fluids. In Section 4.1, we demonstrate the site-potential solution as a special case of this general scheme and present other representations with better iterative convergence during free energy minimization. In Section 4.2, we construct a simplified semi-empirical excess functional for liquid water which adequately captures the properties most critical to successful *ab initio* treatment of solvation within the framework of joint density-functional theory. Finally in Section 4.3, we detail the computational implementation of the above theories in the open-source plane-wave density-functional theory software JDFTx [154], using the basis-independent DFT++ algebraic formulation [75], and present numerical studies of the molecular classical density-functional framework and the

free energy functional for liquid water.

4.1 Free energy of an ideal gas of rigid molecules

The site-density-functional theory of molecular fluids is based on functional approximations to the in-principle exact free-energy functional

$$\Phi[\{N_\alpha(\vec{r})\}] = \Phi_{\text{id}}[\{N_\alpha\}] + F_{\text{ex}}[\{N_\alpha\}], \tag{4.1}$$

where Φ is the grand free energy of the interacting fluid, Φ_{id} is the exact grand free energy for the molecular ideal gas, that is a system of non-interacting molecules with the same density, $N_\alpha(\vec{r})$ are the densities of distinct sites (indexed by α) in the molecule, and F_{ex} captures the effect of all the interactions and correlations. Minimizing the free energy over all allowed densities yields the equilibrium densities and free energy.

The heart of the inversion problem lies in the fact that the site densities $N_\alpha(\vec{r})$ are not independent variables, but are constrained by the assumption of a rigid-molecular geometry. For definiteness, let the molecule geometry be specified by $\vec{R}_{\alpha k}$, the positions of the sites for a molecule centered at the origin in some reference orientation. Here, α indexes the distinct sites while k indexes multiple sites of the same type equivalent under the symmetry of the molecule (e.g. for a 3-site water model, $\alpha \in \{O, H\}$, $k = 1$ for $\alpha = O$ and $k \in \{1, 2\}$ for $\alpha = H$.)

4.1.1 Treatment of site-density constraints

The inversion problem in the original approach of [27, 33], which includes ideal-gas effective potentials $\psi_\alpha(\vec{r})$ as auxiliary independent variables in addition to

the site densities, is avoided in [96] by switching to $\psi_\alpha(\vec{r})$ as the sole independent variables. The site densities and ideal-gas free energy in the presence of external site potentials V_α and for chemical potentials μ_α are then expressed in terms of the $\psi_\alpha(\vec{r})$ using

$$\Phi_{\mathrm{id}}[\{\psi_\alpha(\vec{r})\}] = \Omega^{(ni)}[\{\psi_\alpha\}] + \sum_\alpha \int \mathrm{d}\vec{r} N_\alpha(\vec{r})(V_\alpha(\vec{r}) - \mu_\alpha - \psi_\alpha(\vec{r})) \tag{4.2}$$

$$\Omega^{(ni)} \equiv -N_{\mathrm{ref}} T \int \prod_{\alpha,k} e^{-\psi_\alpha(\vec{r}_{\alpha k})/T} \mathrm{d}\vec{r}_{\alpha k} s(\{\vec{r}_{\alpha k}\}) \tag{4.3}$$

$$N_\alpha(\vec{r}) \equiv \frac{\delta \Omega^{(ni)}}{\delta \psi_\alpha(\vec{r})}, \tag{4.4}$$

Here, the reference density N_{ref} sets the zero of chemical potential and the constraint function $s(\{\vec{r}_{\alpha k}\})$ picks out configurations $\{\vec{r}_{\alpha k}\}$ which satisfy the rigid molecule geometry (i.e. equivalent to $\{\vec{R}_{\alpha k}\}$ under rotations and translations).

Employing a spherical harmonic expansion of the constraint function, [96] and [97] specialize (4.3) for diatomic and triatomic molecules respectively. However, that expansion also becomes computationally challenging as one moves to calculations without planar symmetry. Instead, we transform (4.3) to

$$\Omega^{(ni)} = -N_{\mathrm{ref}} T \int \frac{\mathrm{d}\vec{r}\mathrm{d}\omega}{8\pi^2} \prod_{\alpha,k} e^{-\psi_\alpha(\vec{r}+\omega\circ\vec{R}_{\alpha k})/T} \tag{4.5}$$

where $\omega \in \mathrm{SO}(3)$ is a rotation and $\omega \circ \vec{R}$ is the result of rotating vector $\vec{R}$ by ω, and we directly discretize the integral over orientations as described in Appendix A for practical calculations in three dimensions.

It is instructive to further transform the above equations to

$$\Phi_{\mathrm{id}} = T \int \frac{\mathrm{d}\vec{r}\mathrm{d}\omega}{8\pi^2} p_\omega(\vec{r}) \left(\ln \frac{p_\omega(\vec{r})}{N_{\mathrm{ref}}} - 1 \right) + \sum_\alpha \int \mathrm{d}\vec{r} N_\alpha(\vec{r})(V_\alpha(\vec{r}) - \mu_\alpha) \tag{4.6}$$

$$N_\alpha(\vec{r}) = \sum_k \int \frac{\mathrm{d}\omega}{8\pi^2} p_\omega \left(\vec{r} - \omega \circ \vec{R}_{\alpha k} \right) \tag{4.7}$$

with

$$p_\omega(\vec{r}) = N_{\text{ref}} \prod_{\alpha,k} e^{-\psi_\alpha(\vec{r}+\omega\circ\vec{R}_{\alpha k})/T}. \tag{4.8}$$

Here, $p_\omega(\vec{r})$ represents the probability density of finding a molecule centered at location $\vec{r}$ with orientation ω. For an ideal molecular gas, $p_\omega(\vec{r})$ is simply a product of Boltzmann factors for each site given that $\psi_\alpha(\vec{r})$ are ideal-gas effective potentials since they equal $V_\alpha(\vec{r}) - \mu_\alpha$ when Φ_{id} is minimized.

Note that, given the explicit expressions for the ideal-gas free energy (4.6) and site densities (4.7), $p_\omega(\vec{r})$ is a natural choice for the independent variables for *unconstrained* free-energy minimization. Section 4.3.2 demonstrates that conjugate-gradients minimization over $p_\omega(\vec{r})$ as the independent variables converges much faster than minimization over the $\{\psi_\alpha(\vec{r})\}$. A possible disadvantage of using $p_\omega(\vec{r})$ is the increased memory requirement, but practical calculations of reasonable size are possible using the efficient orientation quadratures of Appendix A. Moreover the superior convergence properties can be retained, while mitigating the memory requirements, by switching to *compressed* multipole representations of $p_\omega(\vec{r})$, as we now discuss.

4.1.2 Representations of the Orientation Density

Our first task in this development is to demonstrate that minimizing free energy functionals over $p_\omega(\vec{r})$ yields the same results as minimizing over $\{\psi_\alpha(\vec{r})\}$. To

demonstrate this we employ a constrained search procedure, to find

$$\begin{aligned}\Phi &= \min_{p_\omega(\vec{r})} \left(\Phi_{\text{id}}[p_\omega(\vec{r})] + F_{\text{ex}}[\{N_\alpha\}]\right) \\ &= \min_{p_\omega(\vec{r})} \Bigg(T \underbrace{\int \frac{\mathrm{d}\vec{r}\mathrm{d}\omega}{8\pi^2} p_\omega(\vec{r}) \ln \frac{p_\omega(\vec{r})}{N_{\text{ref}}}}_{-S_{\text{id}}[p_\omega(\vec{r})]} + F_{\text{id-ex}}[\{N_\alpha\}]\Bigg),\end{aligned}$$

which follows because all the terms in Φ_{id} are explicit site-density functionals except for the molecular ideal gas entropy (S_{id}) contribution separated out above. Next, the minimization over all $p_\omega(\vec{r})$ can be performed by minimizing over those $p_\omega(\vec{r})$ that yield a specific set of site densities $\{N_\alpha(\vec{r})\}$, and then minimizing over all $\{N_\alpha(\vec{r})\}$,

$$\Phi = \min_{\{N_\alpha(\vec{r})\}} \left(\min_{p_\omega(\vec{r}) \mapsto \{N_\alpha(\vec{r})\}} T \int \frac{\mathrm{d}\vec{r}\mathrm{d}\omega}{8\pi^2} p_\omega(\vec{r}) \ln \frac{p_\omega(\vec{r})}{N_{\text{ref}}} + F_{\text{id-ex}}[\{N_\alpha\}] \right).$$

Finally, the inner, constrained minimization over $p_\omega(\vec{r})$ that leads to given site densities can be performed explicitly by introducing Lagrange multipliers $\psi_\alpha(\vec{r})$ for each $N_\alpha(\vec{r})$ constraint. It is straightforward to verify that the Euler-Lagrange equation for that extremization is precisely (4.8), so that the result of free energy minimization over $p_\omega(\vec{r})$ is exactly the same as the ideal-gas effective potential methods of [27, 96].

To generalize this approach, we note that the exact equivalence between minimization over $p_\omega(\vec{r})$ and minimization over $\{\psi_\alpha(\vec{r})\}$, shown above using constrained minimization at fixed site densities, holds only when the external potential takes the form of external site potentials $V_\alpha(\vec{r})$ and couples only to the site densities. In principle, we could go beyond the reduced-interaction site model and consider arbitrary orientation dependent external potentials $V_\omega(\vec{r})$ (of which site potentials $V_\alpha(\vec{r})$ are a special case). From this perspective, the minimization over $\{\psi_\alpha(\vec{r})\}$ can be reinterpreted as a minimization over only those $p_\omega(\vec{r})$ that maximize the molecular ideal gas entropy $S_{\text{id}}[p_\omega(\vec{r})]$ subject to site-density

constraints $\{N_\alpha(\vec{r})\}$ (whose Lagrange-multiplier constraints become the site potentials.) The variational principle implies that this procedure will always result in a free-energy greater than or equal to direct, unconstrained minimization over $p_\omega(\vec{r})$, with equality guaranteed only when the external orientation potential $V_\omega(\vec{r})$ can be reduced to site potentials $V_\alpha(\vec{r})$.

These considerations lead to the perspective of the $\{\psi_\alpha(\vec{r})\}$ as a *compressed representation* of $p_\omega(\vec{r})$, with decompression carried out by maximizing the entropy subject to constraints for which the $\{\psi_\alpha(\vec{r})\}$ are Lagrange multipliers. From the most general perspective, then, any set of functional constraints $\{X_i = \hat{X}_i[p_\omega(\vec{r})]\}$ corresponds to a maximum-entropy compressed representation of $p_\omega(\vec{r})$, where the independent variables χ_i for the free-energy functional minimization are the Lagrange multipliers for the corresponding X_i constraint in the maximization of $S_{\text{id}}[p_\omega(\vec{r})]$. Specifically,

$$\Phi = \min_{\{\chi_i\}} \left(\Phi_{\text{id}} \left[p_\omega(\vec{r})[\chi_i] \right] + F_{\text{ex}} \left[\{ N_\alpha[p_\omega(\vec{r})[\chi_i]] \} \right], \right) \tag{4.9}$$

where $p_\omega(\vec{r})[\chi_i]$ is the solution of

$$\frac{\delta}{\delta p_\omega(\vec{r})} \left(TS_{\text{id}}[p_\omega(\vec{r})] + \sum_i (\hat{X}_i[p_\omega(\vec{r})] - X_i)\chi_i \right) = 0. \tag{4.10}$$

Here, $\Phi_{\text{id}}[p_\omega(\vec{r})]$ and $N_\alpha[p_\omega(\vec{r})]$ are given by (4.6) and (4.7) respectively. Note that i typically includes a continuous index such as $\vec{r}$, and $\sum_i$ then denotes the corresponding integrals.

From this new perspective, picking $\hat{X}_i[p_\omega(\vec{r})] = N_\alpha[p_\omega(\vec{r})]$ yields the ideal-gas site-potential representation with $\chi_i = \psi_\alpha(\vec{r})$ as the independent variables and $p_\omega(\vec{r})$ given by (4.8). Similarly, picking $\hat{X}_i[p_\omega(\vec{r})] = p_\omega(\vec{r})$ yields the trivial self-representation, with $p_\omega(\vec{r})$ as the independent variables. As shown earlier, both these representations are exact when the external potentials are site potentials,

while the former is a variational approximation to the latter in the most general case of orientation potentials.

The advantage of this general framework is that we can develop new, physically motivated representations which then are guaranteed to be variational approximations. Of particular interest are representations based on multipole probability densities

$$\hat{M}^j_{m_1 m_2}(\vec{r})[p_\omega(\vec{r})] = \frac{2j+1}{8\pi^2}\int \mathrm{d}\omega p_\omega(\vec{r}) D^j_{m_1 m_2}(\omega), \tag{4.11}$$

where $D^j_{m_1 m_2}(\omega)$ are the Wigner D-matrices [174] (irreducible matrix representations of SO(3)). The Lagrange-multiplier independent variables $\mu^j_{m_1 m_2}(\vec{r})$ resulting from this choice then generate the orientation probability

$$p_\omega(\vec{r})[\mu^j_{m_1 m_2}(\vec{r})] = N_{\mathrm{ref}} \prod_j \prod_{m_1, m_2 = -j}^{+j} \exp\left(-\frac{\mu^j_{m_1 m_2}(\vec{r}) D^j_{m_1 m_2}(\omega)}{T}\right). \tag{4.12}$$

By the completeness of the $D^j_{m_1 m_2}$ on SO(3), this representation is exact if all components $j \to \infty$ are included. In practice, we truncate the expansion at finite j.[2]

We find below that including terms up to $j = 1$ is sufficient for many practical problems, particularly when the external potential is dominated by strong electric fields. We choose to label the corresponding independent variables for this truncation as $\mu(\vec{r})$ for $j = 0$ and $\vec{\epsilon}(\vec{r})$ for $j = 1$, because they correspond to the ideal-gas effective local chemical potential and local electric field (up to factors of T and the molecule's dipole moment). Section 4.3.2 below compares the accuracy and convergence properties of this $\{\mu, \vec{\epsilon}\}$ representation to those of the site-potential ($\{\psi_\alpha\}$) representation and the self-representation (p_ω).

[2] This expansion in j is different from the spherical harmonic expansion of $\Omega^{(ni)}$ for triatomic molecules introduced in [97]. In particular, truncating expansion (4.12) at $j = 1$ retains the exact nonlinear dielectric response for axisymmetric molecules, whereas the corresponding truncation in [97] would incur a 20% error in the $O(E^2)$ term of $\epsilon(E)$ at room temperature.

Finally, we would like to point out that this general perspective opens up a promising avenue for excess functional development. Our framework enables the computation of site densities *and* multipole densities irrespective of the independent variables used for minimization, which facilitates the generalization of site-density excess functionals $F_{\mathrm{ex}}[\{N_\alpha\}]$ to combined site-multipole functionals $F_{\mathrm{ex}}[\{N_\alpha\},\{M^j_{m_1m_2}\}]$ or even to full orientation density functionals $F_{\mathrm{ex}}[p_\omega]$. In particular, it should now be possible to combine the best features of site-density functionals, which better capture short-ranged correlations, with those of multipole functionals, which allow for analytically derivable longer-ranged correlations.

4.2 Excess functionals

So far we have focused on accurate and efficient representations of the ideal gas of rigid molecules. These need to be combined with good approximations for the excess functional $F_{\mathrm{ex}}[\{N_\alpha\}]$ to obtain a practicable theory for inhomogeneous liquids.

4.2.1 Excess functionals for model fluids

The fluid of hard spheres has been extensively studied theoretically as well as with computer simulations. Within classical density-functional theory, it is accurately described by Rosenfeld's fundamental measure theory [134], which satisfies several rigorous conditions such as reducing to the exact Percus functional in the inhomogeneous one dimensional limit [126] and reproducing the Percus-

Yevick pair correlations [170] in the bulk three dimensional limit.

There are several variants of the fundamental measure theory functional corresponding to different bulk equations of state and regularizations for the zero-dimensional limit. (See [135] for a detailed review.) The excess functional F_{ex} for the highly accurate 'White Bear mark II' variant [58] based on the Carnahan-Starling equation of state for the bulk hard sphere fluid [23], including tensor regularizations due to Tarazona [159], is

$$\Phi_{\text{HS}}[N] = T \int \mathrm{d}\vec{r} \begin{pmatrix} n_0 \ln \dfrac{1}{1-n_3} + f_2(n_3)\dfrac{n_1 n_2 - \vec{n}_{v1}\cdot\vec{n}_{v2}}{1-n_3} + \\ f_3(n_3)\dfrac{n_2^3 - 3n_2|\vec{n}_{v2}|^2 + 9\left(\vec{n}_{v2}\cdot\vec{\vec{n}}_{m2}\cdot\vec{n}_{v2} - \mathrm{Tr}\frac{\vec{\vec{n}}_{m2}^3}{2}\right)}{24\pi(1-n_3)^2} \end{pmatrix}, \tag{4.13}$$

with

$$f_2(n_3) \equiv 1 + \frac{n_3(2-n_3) + 2(1-n_3)\ln(1-n_3)}{3n_3} \text{ and}$$
$$f_3(n_3) \equiv 1 - \frac{2n_3 - 3n_3^2 + 2n_3^3 + 2(1-n_3)^2\ln(1-n_3)}{3n_3^2},$$

where the n_i's are scalar ($i = 0, 1, 2, 3$), vector ($i = v1, v2$) and rank-2 tensor ($i = m2$) weighted densities defined as $n_i(\vec{r}) \equiv w_i * N \equiv \int \mathrm{d}\vec{r'} w_i(\vec{r} - \vec{r'}) N(\vec{r'})$ for hard sphere density $N(\vec{r})$. The weight functions w_i are spherical measures of various dimensions (volume, surface etc.) given by

$$\begin{aligned} w_0(\vec{r}) &= \delta(R_{\text{HS}} - r)/(4\pi r^2), \quad \vec{w}_{v1}(\vec{r}) = \frac{\vec{r}}{r}\delta(R_{\text{HS}} - r), \\ w_1(\vec{r}) &= \delta(R_{\text{HS}} - r)/(4\pi r), \quad \vec{w}_{v2}(\vec{r}) = \frac{\vec{r}}{4\pi r^2}\delta(R_{\text{HS}} - r), \\ w_2(\vec{r}) &= \delta(R_{\text{HS}} - r), \quad \vec{\vec{w}}_{m2}(\vec{r}) = \left(\frac{\vec{r}\vec{r}}{r^2} - \frac{1}{3}\vec{\vec{1}}\right)\delta(R_{\text{HS}} - r), \\ \text{and} \quad w_3(\vec{r}) &= \theta(R_{\text{HS}} - r). \end{aligned} \tag{4.14}$$

The hard sphere fluid also serves as an excellent reference for perturbation theory for other model systems. We briefly mention a few examples here; see

chapter 6 of [57] for a detailed review. For example, the pair-potential for the Lennard-Jones fluid

$$U_{\mathrm{LJ}} = 4\epsilon\left[\left(\frac{\sigma}{r}\right)^{12} - \left(\frac{\sigma}{r}\right)^{6}\right] \tag{4.15}$$

with energy scale parameter ϵ and range parameter σ is often split into repulsive and attractive parts [168] as

$$U_R(r) = \begin{cases} \epsilon + 4\epsilon\left[\left(\frac{\sigma}{r}\right)^{12} - \left(\frac{\sigma}{r}\right)^{6}\right], & r < 2^{1/6}\sigma \\ 0, & r \geq 2^{1/6}\sigma \end{cases} \tag{4.16}$$

$$U_A(r) = \begin{cases} -\epsilon, & r < 2^{1/6}\sigma \\ 4\epsilon\left[\left(\frac{\sigma}{r}\right)^{12} - \left(\frac{\sigma}{r}\right)^{6}\right], & r \geq 2^{1/6}\sigma. \end{cases} \tag{4.17}$$

The free energy functional for this fluid can be approximated by treating the fluid interacting with $U_R(r)$ alone using fundamental measure theory, typically with a hard sphere radius $R_{\mathrm{HS}} = \sigma/2$, and then accounting for the effects of $U_A(r)$ perturbatively. Mean field perturbation then leads to the excess functional

$$F_{\mathrm{ex}}^{(\mathrm{MF})}[N(\vec{r})] \approx \Phi_{\mathrm{HS}}[N] + \frac{1}{2}\int \mathrm{d}\vec{r} \int \mathrm{d}\vec{r}' N(\vec{r}) U_A(|\vec{r} - \vec{r}'|) N(\vec{r}'), \tag{4.18}$$

and several beyond-mean-field approaches have been developed to improve upon this starting point.

Of particular interest is the recent approach of Peng and Yu [125] to recast the mean-field term into a nonlinear weighted-density form

$$F_{\mathrm{ex}}^{(\mathrm{MWF})}[N(\vec{r})] \approx \Phi_{\mathrm{HS}}[N] + \int \mathrm{d}\vec{r} N(\vec{r}) A_{\mathrm{att}}^{\mathrm{LJ}}(w_A * N), \tag{4.19}$$

with the mean-field weight function set to the normalized perturbation potential

$$w_A(r) = \frac{U_A(r)}{\int 4\pi r'^2 \mathrm{d}r' U_A(r')} = \frac{9}{8\sqrt{2}\pi\sigma^3} \begin{cases} 1/4, & r < 2^{1/6}\sigma \\ \left(\frac{\sigma}{r}\right)^{6} - \left(\frac{\sigma}{r}\right)^{12}, & r \geq 2^{1/6}\sigma. \end{cases} \tag{4.20}$$

Here, $A^{\mathrm{LJ}}_{\mathrm{att}}(N) \equiv A_{\mathrm{LJ}}(N) - A_{\mathrm{HS}}(N)$ is the difference between the Helmholtz energy per particle for the uniform Lennard-Jones fluid and the uniform hard sphere fluid at the same bulk density N. Peng and Yu demonstrate that this functional does an excellent job of reproducing the inhomogeneous density profiles and vapor-liquid interface energies in comparison to Monte Carlo simulations of the Lennard-Jones fluid.

4.2.2 Excess functional for liquid water

The situation for a polar molecular fluid such as water is much more complicated than the model fluids mentioned above. Most approaches to the excess free energy of inhomogeneous water [31, 33, 97] are constructed to reproduce the pair-correlations in the uniform fluid limit obtained by computer simulations or from neutron-scattering data. They can be reasonably accurate for modest inhomogeneities, but their practicality is limited as they are tied to the temperature and pressure of the simulation/experiment data that they are based on, and usually lack a simple analytic formulation.

An alternate strategy is based on identifying a simple model Hamiltonian for which an approximate analytic free energy functional is readily formulated, and then constraining the parameters of the model Hamiltonian to the bulk properties of the fluid, such as the equation of state. Wertheim's thermodynamic perturbation theory [171] is a useful framework for generating free energy functionals; one class of Hamiltonians considered for water within this framework is based on tetrahedral association sites for hydrogen bonds [29], but these models have yet to successfully predict the quantities relevant to solvation such as pair

correlations, cavity formation energies and dielectric response, partly due to the relative complexity of the model Hamiltonian.

Recently, we proposed an alternative model Hamiltonian [153] based on capturing the effects of the empty space in the tetrahedral hydrogen bond network by attaching 'void' spheres to the molecule in the directions conjugate to the tetrahedral hydrogen-bond directions. The bonding constraints in the resulting rigid trimers of hard spheres was also treated using Wertheim perturbation theory, but the relative simplicity of that model enabled an accurate free energy functional description of the inhomogeneous fluid capable of predicting the aforementioned quantities relevant for solvation.

This 'bonded-trimer' free energy functional for water is adequately accurate for cavity formation energies, dielectric response and the height and particle content of the first peak in the pair correlation. However, the secondary peaks in its pair correlation occur at the characteristic distances for a close-packed hard sphere fluid rather than for a tetrahedrally-bonded one. Evidently the cavity formation energies are not sensitive to this deficiency in the secondary structure of the pair correlation; the height of the first peak and the exclusion volume (location of pole) in the equation of state are the important factors, which are captured correctly by the bonded void spheres ansatz.

Here, we present a simplified free energy functional for water which retains only the critical features of the bonded-trimer model [153], while eliminating the complexity of Wertheim perturbation. This functional employs a hard sphere reference with a weighted density term constrained to reproduce the equation of state in the spirit of the approach of [125] for the Lennard-Jones fluid. Because of the polar nature, we need to distinguish between short-ranged orientation-

averaged interactions with a r^{-6} tail similar to the Lennard-Jones pair potential and long-range orientation-dependent interactions with a r^{-1} tail between individual charged sites resulting in r^{-3} for neutral molecules with a net dipole moment.

We deal with the long range orientation-dependent part by taking advantage of the rigid molecule site-model capability developed in Section 4.1. In particular, we adopt the molecule geometry and site charges of the popular SPC/E pair potential model [15] for molecular dynamics simulations of water, which consists of an O site with charge $Z_O = +0.8476\ e^-$ and two H sites with charge $Z_H = -0.4238\ e^-$ in a bent geometry with an O-H distance of 1 Å and a tetrahedral H-O-H angle ($\cos^{-1}(-1/3) \approx 109.5°$).

For the shorter-ranged orientation-dependent part, we assume a Lennard-Jones interaction between the O-sites since it has the correct r^{-6} tail.[3] We arrive at the excess functional ansatz

$$F_{\text{ex}}^{H_2O}[N_O(\vec{r}), N_H(\vec{r})] \approx \Phi_{\text{HS}}[N_O] + \int \mathrm{d}\vec{r} N_O(\vec{r}) A_{\text{att}}^{H_2O}(w_A * N_O) + \frac{A_\epsilon(T)}{2} \sum_{\alpha,\beta\in\{O,H\}} Z_\alpha Z_\beta \int \mathrm{d}\vec{r} \int \mathrm{d}\vec{r}' N_\alpha(\vec{r}) K(|\vec{r} - \vec{r}'|) N_\beta(\vec{r}'), \quad (4.21)$$

by adding a long-range polar correction (third term) to the Lennard-Jones functional of [125] (first two terms). The following paragraphs specify the Helmholtz energy function $A_{\text{att}}^{H_2O}(N)$, the dipole correlation factor $A_\epsilon(T)$ and the modified Coulomb kernel $K(r)$. We shall refer to this excess functional (4.21) as 'scalar-EOS' because the excess free energy density is attributed to the scalar moment of the orientation density and is constrained to the equation of state.

[3] As in Chapter 3, the predictions of this functional are relatively insensitive to the precise functional form of the interaction potential, and we employ the Lennard-Jones form because it is commonly used in the molecular dynamics and fluid theory literature.

In (4.21), Φ_{HS} is the White Bear mark II fundamental theory functional, given by (4.13), for a fluid of hard spheres of radius R_{HS}. The second weighted density term employs the mean-field weight function $w_A(r)$ given by (4.20) with $\sigma = 2R_{\text{HS}}$.

The third term of (4.21) is the mean-field electrostatic interaction between the charge-site densities scaled by a dipole-correlation factor $A_\epsilon(T)$. Following [97], the Coulomb kernel $K(r)$ is attenuated at high frequencies as

$$\tilde{K}(G) = \frac{4\pi}{G^2}\left[1 + \left(\frac{G}{G_c}\right)^4\right]^{-1} \tag{4.22}$$

with $G_c = 0.33$ bohr^{-1}. The dipole correlation factor, $A_\epsilon = \epsilon_b/(\epsilon_b - 1) - 3T/(4\pi N_{\text{bulk}} p_{\text{mol}}^2)$, is constrained to reproduce the bulk linear dielectric constant, ϵ_b, where N_{bulk} is the bulk density of the liquid and p_{mol} is the permanent dipole moment of each molecule (see [97] for details). Without the correlation factor, i.e. with $A_\epsilon = 1$, the SPC/E molecular geometry would yield a static dielectric constant of 19.7 at room temperature instead of the experimental value of 78.4. The single parameter fit

$$A_\epsilon(T) = 1 - \frac{T}{7.35 \times 10^3 \text{ K}} \tag{4.23}$$

reproduces the bulk linear dielectric constant over the entire liquid phase with a relative RMS error $\sim 1\%$.

Next, we constrain $F_{\text{ex}}^{H_2O}$ to reproduce the correct Helmholtz energy density for the uniform fluid of molecular density N, which may be obtained by integrating the equation of state ($p(N,T)$). Note that the third term of (4.21) does not contribute to the uniform fluid free energy, and hence $A_{\text{att}}^{H_2O}$ must be the difference between the per-molecule Helmholtz free energy in water and the hard sphere fluid. Using the Jefferey-Austin equation of state [77] for water, this con-

strains

$$A_{\text{att}}^{H_2O}(N) = \frac{\alpha T}{\lambda b(T)} \ln \frac{1}{1-\lambda b(T) N} - (a_{\text{VW}} + b^* T) N \\ - 2T f^{**}(T) \frac{1 + C_1}{1 + C_1 \exp \frac{(N-\rho_{\text{HB}})^2}{\sigma^2}} \ln \frac{\Omega_0 + \Omega_{\text{HB}} e^{-\epsilon_{\text{HB}}/T}}{\Omega_0 + \Omega_{\text{HB}}} \\ - T \frac{V_{\text{HS}} N (4 - 3 V_{\text{HS}} N)}{(1 - V_{\text{HS}} N)^2} \quad (4.24)$$

up to a temperature-dependent constant which is absorbed into the arbitrary reference for the chemical potential μ. The first two lines of (4.24) represent the free energy density corresponding to the excess pressure for liquid water as parametrized in [77] by fits to experimental data for bulk liquid water, and the definitions of the numerous constants and functions of temperature may be found therein.[4] The last line of (4.24) subtracts the uniform fluid per-particle free energy corresponding to Φ_{HS} given by (4.13), with $V_{\text{HS}} = 4\pi R_{\text{HS}}^3/3$.

Now, (4.21) is completely specified except for the value of the hard sphere radius R_{HS}. Unlike the Lennard-Jones fluid, there is no prescribed pair potential from which it may be derived. We require that calculations with the excess functional (4.21) result in the surface-energy of the planar water liquid-vapor interface in agreement with the experimental surface tension of 72.0×10^{-3} N/m at room temperature 298 K, and obtain

$$R_{\text{HS}} = 1.36 \text{ Å}, \quad (4.25)$$

which corresponds to a peak in the oxygen-oxygen partial radial distribution at $2R_{\text{HS}} = 2.72$ Å, in agreement with experimental data [145]. The details of the planar interface calculation are presented in Section 4.3.1, and tests of the accuracy of the scalar-EOS functional for inhomogeneous liquid water are in Section 4.3.3.

[4] Note that the constants listed in [77] are in SI/CGS units, and should be converted to atomic units (with $k_B = 1$) before substitution in (4.24). See Table E.1 for the relevant conversion factors.

4.3 Results

The efficient rigid-molecular ideal gas representations of Section 4.1 combined with the excess functional for water from Section 4.2.2 forms a practical theory of inhomogeneous liquid water as we show below. We use this system to study the convergence properties of the various molecular ideal gas representations in Section 4.3.2, and then test the accuracy of the scalar-EOS water functional against experiment and molecular dynamics simulations in Section 4.3.3.

4.3.1 Discretization

The free energy functional approximations presented here involve integrals over space and orientations, which must all be discretized in a practical calculation. The discretization of three dimensional space may be performed in a variety of bases including plane-waves, wavelets and specialized bases such as planar and radial one dimensional grids for high symmetry cases.

We present the details of the numerical formulation of the free energy functionals for rigid-molecular liquids using the basis-independent algebraic formulation developed for electronic density-functional theory [75]. Within this formulation, the physics is expressed in terms of a handful of abstract operators independent of the basis, while the implementation of these operators in code is basis dependent. This allows for the same top-level physics code to be used with multiple basis sets with no modification. A three-dimensional plane-wave basis implementation of the fluid framework and excess functionals (using the notation and operators described below) is distributed with the

open-source electronic density-functional theory software JDFTx [154], which specializes in solvated *ab initio* calculations. An analogous code base for high-symmetry one-dimensional basis sets, suitable for development and testing of new fluid functionals, is distributed as a sub-project of JDFTx [152].

Here, we briefly introduce the notation and operators required for classical density-functional theory; see [75] for a detailed description. A function of space $f(\vec{r})$ is expanded in terms of basis functions $\{b_i(\vec{r})\}$ with coefficients $\tilde{f}_i$ (often written as a vector $\tilde{f}$) i.e. $f(\vec{r}) = \sum_i \tilde{f}_i b_i(\vec{r})$.

The overlap of two functions $f(\vec{r})$ and $g(\vec{r})$ is

$$\int \mathrm{d}\vec{r} f^*(\vec{r}) g(\vec{r}) = \sum_{i,j} \tilde{f}_i^* \tilde{g}_j \underbrace{\int \mathrm{d}\vec{r} b_i^*(\vec{r}) b_j(\vec{r})}_{O_{ij}} = \tilde{f}^\dagger O \tilde{g} \tag{4.26}$$

which defines the basis overlap matrix O (which would be diagonal for orthogonal basis sets). Similarly, any linear operator reduces to a matrix. For example, $\int \mathrm{d}\vec{r} f^*(\vec{r}) \nabla^2 g(\vec{r}) = \tilde{f}^\dagger \mathcal{L} \tilde{g}$ defines the Laplacian matrix $\mathcal{L}_{ij} = \int \mathrm{d}\vec{r} b_i^*(\vec{r}) \nabla^2 b_j(\vec{r})$.

The density functionals also involve integrals over nonlinear functions which of course cannot be reduced to basis-space matrices like the linear operators considered above. Consequently, the basis sets are accompanied by a quadrature grid consisting of a set of nodes $\{\vec{r}_j\}$ over which integration of nonlinear functions is performed. A function $f(\vec{r})$ sampled on this quadrature grid $f_j = f(\vec{r}_j)$ is denoted simply by the vector f. This introduces the linear basis-to-real space operator $\mathcal{I}$ defined by $f = \mathcal{I}\tilde{f}$ with matrix elements $\mathcal{I}_{ji} = b_i(\vec{r}_j)$, and the real-to-basis space operator, $\mathcal{J} = \mathcal{I}_{\text{left}}^{-1}$.[5] Armed with these operators, we can

[5] $\mathcal{J} = \mathcal{I}^{-1}$ is the natural choice when the number of basis functions equals the number of quadrature grid points, which is the case for the plane-wave basis for example. When the number of grid points exceeds the number of basis functions, one possibility is to use the left-inverse as indicated so that $\mathcal{J}\mathcal{I} = 1$, although this is not necessary.

discretize the commonly encountered integral $\int \mathrm{d}\vec{r} f(\vec{r}) A(g(\vec{r})) = \tilde{f}^\dagger \mathcal{O}\mathcal{J} A(\mathcal{I}\tilde{g}) = f^\dagger \mathcal{J}^\dagger \mathcal{O}\mathcal{J} A(g)$ where A is some nonlinear function (which operates element-wise on vectors).

In the particular case of plane-wave basis on a periodic unit cell, the quadrature grid $\vec{r}_j$ is a uniform parallelepiped mesh, the basis functions are $e^{-i\vec{G}\cdot\vec{r}}$ for reciprocal lattice vectors $\vec{G}$, and the operators $\mathcal{I}$ and $\mathcal{J}$ are implemented as Fast Fourier Transforms. $\mathcal{O}$ is the scalar matrix Ω, and $\mathcal{L}$ is the diagonal matrix $-\Omega|\vec{G}|^2$, where Ω is the unit cell volume. For a detailed specification of these operators, see [75] for the three-dimensional plane-wave basis, [10] for a multiresolution (wavelet) basis, and Appendix B for the planar, cylindrical and spherical one-dimensional grids.

In fact, the six operators introduced above (counting hermitian adjoints separately) are the *only* ones required for electronic density functional theory in the local density approximation (LDA).[6] The advantage of writing code in this framework is that implementing a new basis only requires reimplementing this small number of operators.

To express the classical density functionals, we need to introduce two additional operators. Firstly, the computation of weighted densities involves convolutions $h(\vec{r}) = \int d\vec{r}' f(\vec{r} - \vec{r}') g(\vec{r}')$, which may be discretized using a basis dependent tensor C^k_{ij} to $\tilde{h}_k = \sum_{i,j} C^k_{ij} \tilde{f}_i \tilde{g}_j$, which we also denote by $\tilde{h} = \tilde{f} * \tilde{g}$ for brevity. Integrating the defining relation multiplied by basis functions, we see that the convolution tensor elements must be

$$C^k_{ij} = \sum_l (\mathcal{O}^{-1})_{kl} \int \mathrm{d}\vec{r} \int \mathrm{d}\vec{r}' b^*_l(\vec{r}) b_i(\vec{r} - \vec{r}') b_j(\vec{r}'). \tag{4.27}$$

[6] The generalized gradient approximation (GGA) would additionally require gradient and divergence operators. See [75] for details.

C^k_{ij} is symmetric under $i \leftrightarrow j$ when the space is translationally invariant, and reduces to the element-wise multiply $C^k_{ij} = \Omega\delta_{ki}\delta_{kj}$ for the plane-wave basis, as is well known.

Secondly, the rigid molecule formalism of Section 4.1 requires sampling functions with arbitrary displacements in order to generate orientation densities from the effective site potentials, and to generate the site densities from the orientation densities. This requires the inclusion of a translation operator defined by $\mathcal{T}_{\vec{a}} f(\vec{r}) = f(\vec{r}+\vec{a})$ in our toolkit. This may be discretized to $\tilde{g}_i = \sum_j (\mathcal{T}_{\vec{a}})_{ij} \tilde{f}_j$ where $\tilde{f}$ and $\tilde{g}$ are the discretizations of $f(\vec{r})$ and $f(\vec{r}+\vec{a})$ respectively. The natural translation operator for a given basis set obtained by integrating the definition multiplied by basis functions is

$$(\mathcal{T}_{\vec{a}})_{ij} = \sum_k (O^{-1})_{ik} \int \mathrm{d}\vec{r} b^*_k(\vec{r}) b_j(\vec{r}+\vec{a}), \tag{4.28}$$

and satisfies $\mathcal{T}^\dagger_{\vec{a}} = \mathcal{T}_{-\vec{a}}$ by definition. In the plane-wave basis, this operator takes the diagonal form $(\mathcal{T}_{\vec{a}})_{ij} = \delta_{ij} e^{-i\vec{G}_i \cdot \vec{a}}$.

However, this 'Fourier' translation operator introduces severe ringing in functions that have components that extend up to the Nyquist frequency. This can be quite problematic for the classical density-functional theory of rigid molecules, particularly since positive functions can ring negative on translation, leading to artificial and unphysical regions of negative site densities even when $p_\omega \geq 0$, due to numerical truncation errors. The free energy functionals evaluated for these negative site density artifacts can be unphysically favorable which encourages further ringing, resulting in a numerical divergence.[7]

We remedy this by using inexact translation operators which have the prop-

[7] In principle, we could zero out the contributions to the free energy from regions of negative site densities (arising from numerical errors). However, this results in a highly non-analytic energy landscape with extremely poor convergence for minimization algorithms

erty that they map the set of functions with all-non-negative samples on the quadrature grid onto itself. The action of the translation operator on the quadrature grid $\mathcal{S}_{\vec{d}} \equiv \mathcal{I}\mathcal{T}_{\vec{d}}\mathcal{J}$ can be viewed as sampling the function on the grid with displacement $\vec{d}$. The natural translation operator for the plane-wave basis corresponds to a sampling operator $\mathcal{S}$ based on Fourier interpolation. Amongst the piece-wise polynomial spline interpolations, only the constant spline (pick nearest neighbor) and linear spline (linear interpolation in each cell) guarantee non-negative results for a non-negative sample set; we denote the corresponding approximate sampling operators by $\mathcal{S}^C$ and $\mathcal{S}^L$ respectively.

The discretization of spatial integrals in the rigid-molecule classical density functional framework can be achieved using the above operators; the final ingredient is the discretization of the orientation integrals. We achieve this by using a quadrature rule directly on SO(3)/G, where G is the symmetry group of the fluid molecule, so that

$$\int_{\omega\in\mathrm{SO}(3)} \frac{\mathrm{d}\omega}{8\pi^2} f(\omega) \to \sum_i W_i f(\omega_i) \tag{4.29}$$

with a finite set of orientations ω_i and weights W_i. Appendix A describes various methods for the generation of quadrature rules on SO(3)/$\mathbb{Z}_n$ ranging from outer product quadratures on Euler angles to uniform sampling sets based on platonic solid rotation groups. Section 4.3.2 explores the convergence of the orientation integrals with quadrature for the scalar-EOS water functional (symmetry group $\mathbb{Z}_2$), and the list of explored quadratures is summarized in Table A.1.

We can now discretize the molecular ideal gas free energy (4.6) given the orientation density p_{ω_i} on the quadrature grid for each discrete orientation and the site densities $\tilde{N}_\alpha$ in the chosen basis set, as

$$\Phi_{\mathrm{id}} = T\tilde{\mathbb{1}}^\dagger \mathcal{O}\mathcal{J} \sum_i W_i p_{\omega_i} \left(\ln \frac{p_{\omega_i}}{N_{\mathrm{ref}}} - 1 \right) + \sum_\alpha \tilde{N}_\alpha^\dagger \mathcal{O}(\tilde{V}_\alpha - \mu_\alpha \tilde{\mathbb{1}}) \tag{4.30}$$

Note that all unary real functions are understood to operate element-wise on vectors on the quadrature grid, unless otherwise specified.

The expression of the orientation density on the quadrature grid in terms of the independent variables for minimization depends on the chosen representation. In the self representation, the independent variables are $\tilde{p}_{\omega_i}$ in basis space and therefore $p_{\omega_i} = \mathcal{I}\tilde{p}_{\omega_i}$. The independent variables in the site-potential representation are $\tilde{\psi}_\alpha$ and the orientation density is generated using (4.8) as

$$\begin{aligned} p_{\omega_i} &= N_{\text{ref}} \exp\left(\frac{-1}{T}\mathcal{I}\sum_{\alpha,k}\mathcal{T}_{\omega_i\circ\vec{R}_{\alpha k}}\tilde{\psi}_\alpha\right) \\ &= N_{\text{ref}} \exp\left(\frac{-1}{T}\sum_{\alpha,k}\mathcal{S}_{\omega_i\circ\vec{R}_{\alpha k}}\mathcal{I}\tilde{\psi}_\alpha\right), \end{aligned} \tag{4.31}$$

where the latter expression with an approximate sampling operator $\mathcal{S}$ is used in practice. In the multipole representation, the independent variables are $\tilde{\mu}^j_{m_1m_2}(\vec{r})$ for $|m_1|, |m_2| \le j \le j_{\max}$ and the orientation density is generated using (4.12) as

$$p_{\omega_i} = N_{\text{ref}} \exp\left(\frac{-1}{T}\mathcal{I}\sum_{j=0}^{j_{\max}}\sum_{m_1,m_2=-j}^{+j} D^j_{m_1m_2}(\omega_i)\tilde{\mu}^j_{m_1m_2}\right), \tag{4.32}$$

which simplifies for $j_{\max} = 1$ in terms of independent variables $\tilde{\mu}$ and $\vec{\tilde{\epsilon}}$ to

$$p_{\omega_i} = N_{\text{ref}} \exp\frac{-\mathcal{I}\left(\tilde{\mu} + (\omega_i \circ \hat{z})\cdot\vec{\tilde{\epsilon}}\right)}{T}. \tag{4.33}$$

Finally, the site densities are generated from the orientation density by a discretization of (4.4), given by $N_\alpha \equiv \frac{\delta}{\delta\psi_\alpha}\Omega^{(ni)}$, with $\Omega^{(ni)} = -T\tilde{1}^\dagger O\mathcal{J}\sum_i W_i p_{\omega_i}$ and p_{ω_i} given by (4.31), so that[8]

$$N_\alpha = \text{Diag}(\mathcal{J}^\dagger O\tilde{1})^{-1}\sum_i W_i \sum_k \mathcal{S}^\dagger_{\omega_i\circ\vec{R}_{\alpha k}}\text{Diag}(\mathcal{J}^\dagger O\tilde{1})p_{\omega_i}. \tag{4.34}$$

[8]This is derived from $d\Omega = \int \frac{\delta\Omega}{\delta\psi}d\psi = \tilde{1}^\dagger O\mathcal{J}\text{Diag}(\frac{\delta\Omega}{\delta\psi})d\psi$, which leads to $\text{Diag}(\mathcal{J}^\dagger O\tilde{1})\frac{\delta\Omega}{\delta\psi} = \frac{\partial\Omega}{\partial\psi^\dagger}$. Here, $\text{Diag}(x)$ is the diagonal operator with the elements of x on its diagonal, i.e. $\text{Diag}(x)y = \text{Diag}(y)x$ is the element-wise multiplication of x and y.

For the translationally invariant plane-wave basis set, the above expression is equivalent to $N_\alpha = \sum_i W_i \sum_k \mathcal{S}_{-\omega_i \circ \vec{R}_{\alpha k}} p_{\omega_i}$, the intuitive discretization of (4.7), and this holds approximately for other three-dimensional basis sets. However, (4.34) holds even when $\mathcal{S}_{\vec{a}}$ is generalized to a non-uniform translation $\mathcal{S}_{\vec{a}(\vec{r})}$, which is required for the reduced-dimensionality basis sets of Appendix B.

Moving on to excess functionals, the hard sphere excess free energy $\Phi_{\text{HS}}[N]$ given by (4.13) is discretized by replacing $\int \mathrm{d}\vec{r} \to \tilde{1}^\dagger \mathcal{O}\mathcal{J}$ and computing the integrand element-wise on the quadrature grid, where the weighted densities are computed from convolutions in basis space $n_i = \mathcal{I}(\tilde{w}_i * \tilde{N})$. These convolutions may be computed efficiently in the plane-wave basis by multiplying with the analytic Fourier transforms of the weight functions (4.14), but in other bases, they should be computed with specialized routines that take advantage of the finite range of the weight functions. (See [135] for examples.) The excess free energy of the Lennard-Jones fluid [125], given by (4.19), discretizes to $F_{\text{ex}}^{(\text{MWF})} = \Phi_{\text{HS}}[N] + \tilde{N}^\dagger \mathcal{O}\mathcal{J} A_{\text{att}}^{\text{LJ}}(\mathcal{I}(\tilde{w}_A * \tilde{N}))$. The convolution $\tilde{w}_A *$ is trivial in the plane-wave basis, but may require specialized routines in other basis sets due to the polynomial tail of the Lennard-Jones weight function.[9]

Finally, the scalar-EOS excess functional for water (4.21) is discretized to

$$F_{\text{ex}}^{H_2O} = \Phi_{\text{HS}}[N_O] + \tilde{N}_O^\dagger \mathcal{O}\mathcal{J} A_{\text{att}}^{H_2O}(\mathcal{I}(\tilde{w}_A * \tilde{N}_O)) + \frac{A_\epsilon(T)}{2} \sum_{\alpha,\beta \in \{O,H\}} Z_\alpha Z_\beta (\tilde{w}_K * \tilde{N}_\alpha)^\dagger \bar{\mathcal{O}}(-4\pi\mathcal{L}^{-1})\bar{\mathcal{O}}(\tilde{w}_K * \tilde{N}_\beta). \quad (4.35)$$

Here, the high-frequency cutoff Coulomb Kernel (4.22) has been rewritten in terms of the bare Coulomb operator, $(-4\pi\mathcal{L}^{-1})\bar{\mathcal{O}}$, computed by solving the Pois-

[9] For example, in wavelet bases, this may be performed by decomposition into a finite-ranged part treated at all grid levels, and a bandwidth-limited long-range part performed using the Fourier method on the coarsest grid.

son equation,[10] and by applying the high-frequency cutoff to the site densities instead (integration by parts). This is equivalent to an effective charge distribution for each site, described by the convolution kernel

$$\tilde{w}_K(G) = 1/\sqrt{1 + \left(\frac{G}{G_c}\right)^4}. \tag{4.36}$$

This modification has no effect for the plane-wave basis, but is important for other basis sets because it decomposes the long-range convolution with $\tilde{K}(G)$ into a short-ranged convolution ((4.36) is confined exponentially in real space), and the solution of Poisson equation which is a standard operation in any basis set [75, 10].

4.3.2 Convergence

Section 4.3.1 presented the discretization of the general rigid-molecular ideal gas framework of Section 4.1 with various choices for the independent variables, and excess functionals including the scalar-EOS functional for liquid water constructed in Section 4.2.2. Next, we briefly discuss the minimization of the liquid free energy given a set of external potentials, compare the performance of the different choices of independent variables, and explore the accuracy of the discretization of the orientation integrals.

The free energy of the fluid for a particular excess functional and choice of independent variables is expressed in the basis-independent algebraic formulation of [75], including the operators introduced in Section 4.3.1. The gradient of the free energy with respect to the independent variables may be derived

[10] $\bar{O}$ is the overlap operator with the null-space of $\mathcal{L}$ projected out, and $\mathcal{L}^{-1}$ is understood to be the inverse of $\mathcal{L}$ in orthogonal complement of the null-space with zero projection in the null-space. See [75] for details.

in the same notation in a straightforward manner as shown in [75], and the computational cost for evaluating the gradient is comparable to that for the free energy. We can therefore minimize the free energy functional to find the equilibrium configuration of the fluid directly using the non-linear conjugate gradients method [42].

First, we compare the convergence of the conjugate gradients method for different choices of independent variables. For the remainder of this section, we work with the scalar-EOS functional for water at a temperature of 298 K in the three-dimensional plane-wave basis set, and perform all calculations using JDFTx [154]. We focus on two physical systems which capture different extremes of the typical external potentials encountered in ab-initio solvation: water surrounding a microscopic hard sphere, and water in a parallel plate capacitor with a strong enough electric field that the rotational dielectric response of the fluid almost saturates because of almost complete alignment of all fluid molecules with the field.

The hard sphere system consists of an external potential $V_O(\vec{r}) = V_0\theta(R - |\vec{r}|)$ which excludes the O sites of water from a sphere of radius R, with no potential on the H sites ($V_H(\vec{r}) = 0$). We pick $R = 4$ Å, a reasonable size for the region excluded by a molecule solvated in water, and $V_0 = 1\ E_h$ (≈ 27.2 eV) which is sufficient to completely exclude the liquid from that region. The calculations are performed in a cubic unit cell of side 32 bohrs (≈ 17 Å) with a $128 \times 128 \times 128$ fast Fourier transform (FFT) grid; the grid spacing of 0.25 bohrs corresponds roughly to the charge density grid of a typical electronic density-functional theory calculation at a wave-function kinetic energy cutoff of 20 E_h.

The parallel plate capacitor system consists of two plates 112 bohrs apart,

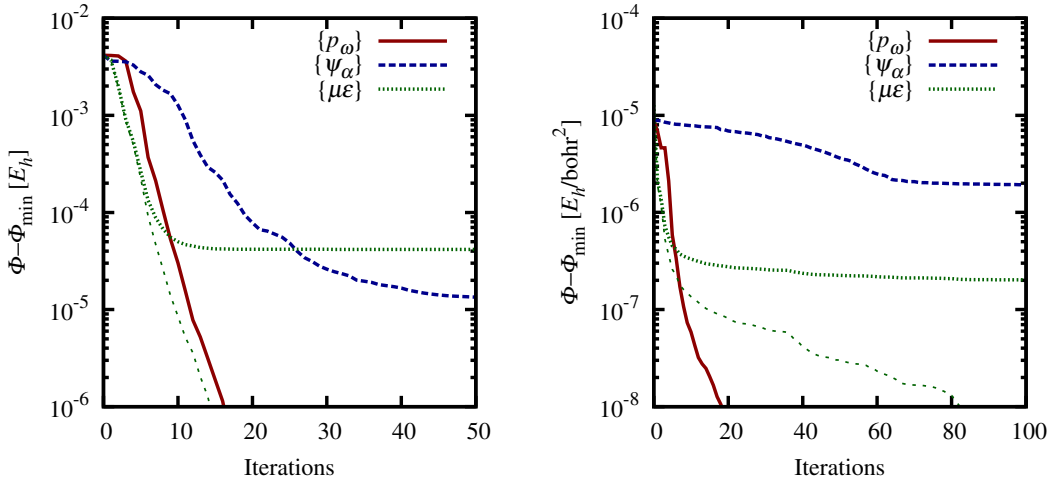

(a) 4 Å hard sphere (b) Capacitor with E_0 = 1 V/Å

Figure 4.1: Convergence of conjugate gradients minimization of the free energy of scalar-EOS water (a) surrounding a hard sphere of radius 4 Å, and (b) in a parallel plate capacitor with externally applied field strength E_0 = 1 V/Å (typical in the first solvation shell of a polar molecule), for different independent variables. The difference of free energy from the final equilibrium value as a function of iteration count is shown on a logarithmic scale for the self representation $\{p_\omega\}$ (solid red line), the site-potential representation $\{\psi_\alpha\}$ (blue dashed line), and the multipole representation $\{\mu, \vec{\epsilon}\}$ (thicker green dotted line). The fainter green dotted line is the difference of the free energy in the $\{\mu, \vec{\epsilon}\}$ representation from the converged value within that representation (which is variationally higher than the equilibrium value). Note the rapid exponential convergence in the self and multipole representations, compared to the site potential representation.

with an external potential corresponding to an applied electric field of E_0 = 1 V/Å (10^{10} V/m), which is typical in the first solvation shell of a polar molecule, and corresponds to a regime of strongly non-linear dielectric response. (See Figure 4.8.) Repulsive potentials of strength 1 E_h on both the O and H sites confine the fluid to the region between the capacitor plates. The calculation is performed in a periodic cell of length 256 bohrs containing two capacitors back-to-back so that the cell has no net dipole, and is sampled using a one-dimensional FFT grid with 4096 points. The transverse dimensions are translationally invariant, and the free energies reported are per bohr^2 of transverse area.

Figure 4.1 shows the convergence of the Polak-Ribiere variant of the nonlinear conjugate gradients algorithm [132] for the hard-sphere and capacitor systems with the site-potential ($\{\psi_\alpha\}$), $j = 1$ truncated multipole ($\{\mu, \vec{\epsilon}\}$) and self ($\{p_\omega\}$) representations of the orientation density as independent variables. The initial guess in each case corresponds to a uniform bulk density of water in the allowed regions and no density in the disallowed regions, with a uniform orientation distribution for the sphere geometry, and a dipolar orientation distribution corresponding to bulk linear dielectric response for the capacitor geometry. The 7-design quadrature with 96 nodes on $\mathrm{SO}(3)/\mathbb{Z}_2$ (see Table A.1) was used for orientation sampling.

The self representation ($\{p_\omega\}$) exhibits the best exponential convergence, and is the method of choice when it is practical to store the orientation density. The multipole representation ($\{\mu, \vec{\epsilon}\}$) also converges quite rapidly, but it is a variational approximation and will result in a higher free energy than that in $\{p_\omega\}$. Note that for a typical molecule cavity formation (the hard sphere case), the error in the $\{\mu, \vec{\epsilon}\}$-representation is $\sim 4 \times 10^{-5}\ E_h$ or ~ 0.03 kcal/mol, which is negligible in the computation of solvation energies. Likewise, the relative error in the free energy of the strong-field capacitor corresponds to an error of less than $\sim 1\%$ in the effective dielectric constant, which again is acceptable in the calculation of solvation energies. Finally, the site-potential representation ($\{\psi_\alpha\}$) of [27, 96] exhibits the poorest convergence, particularly in the strong electric field case. Although the $\{\psi_\alpha\}$ entropy will eventually converge to the same value as that of the $\{p_\omega\}$ representation, the approximate $\{\mu, \vec{\epsilon}\}$ representation yields a more accurate free energy at practical iteration counts.

Next, we turn to the convergence of the free energies with respect to the

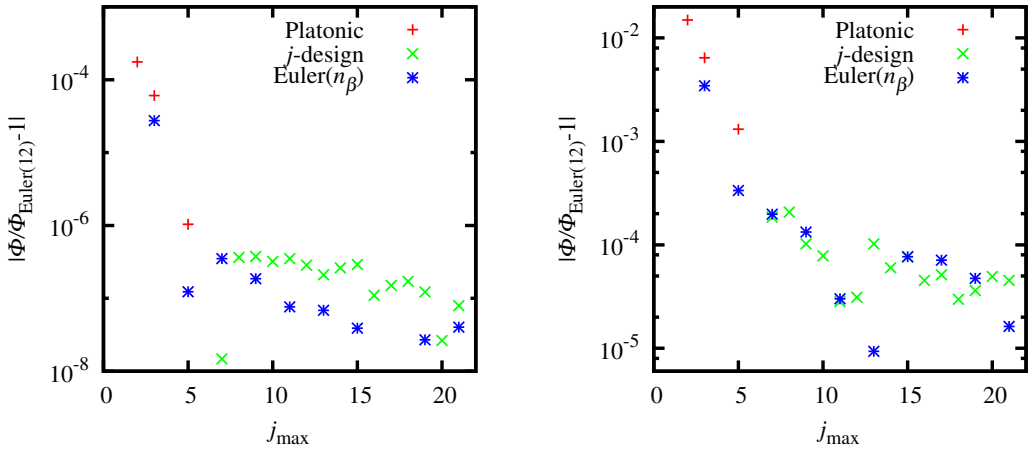

(a) 4 Å hard sphere (b) Capacitor with $E_0 = 1$ V/Å

Figure 4.2: Convergence of free energy with orientation quadrature for the two systems considered in Figure 4.1. The orientation quadratures studied are listed in Table A.1, and the free energy at the Euler(12) quadrature (which has 3456 nodes on $SO(3)/\mathbb{Z}_2$) is used as the reference in computing relative errors for all the smaller quadratures. Note that the error due to the orientation quadrature plateaus at $j_{max} \sim 7$ for the sphere geometry, and at $j_{max} \sim 10$ for the strong-field capacitor; these would therefore be reasonable choices in *ab initio* solvation calculations for non-polar and strongly-polar molecules respectively.

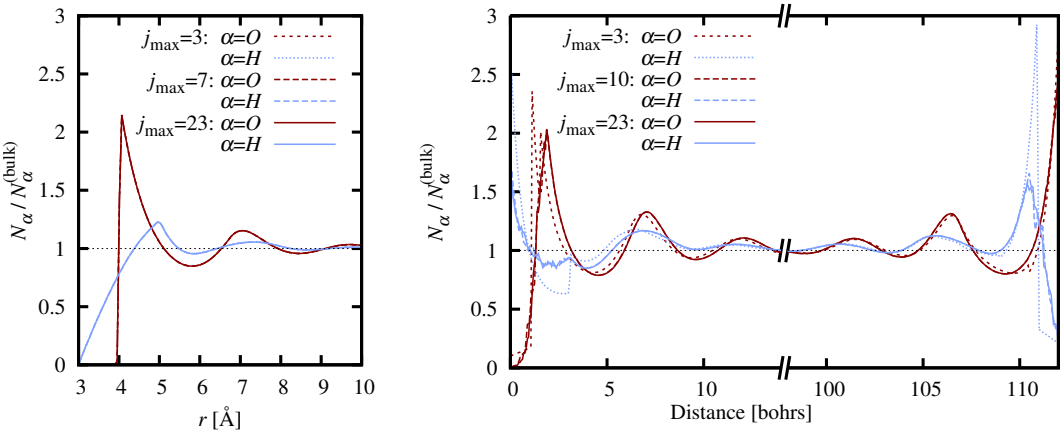

(a) 4 Å hard sphere (b) Capacitor with $E_0 = 1$ V/Å

Figure 4.3: Convergence of density profiles with orientation quadrature for the two systems considered in Figure 4.1. The plotted site-densities are scaled by their corresponding bulk values, so that the profiles equilibrate at 1 far from the sphere / plates. Note that the densities at the lowest and highest quadratures are indistinguishable for the hard sphere, whereas the densities become similar to the fully-converged ones only around $j_{max} \sim 10$ for the strong-field capacitor.

discretization of the orientation integrals. Figure 4.2 shows the relative error in the free energy for each orientation quadrature in Table A.1 compared to the Euler(12) quadrature (taken to be the converged value) for the two systems considered above. The quadratures are sorted by j_{max}, the maximum degree of Wigner functions $D^j_{m_1 m_2}$ for which they are exact. (See Appendix A for details.) The error in the free energy decreases rapidly with quadrature size and plateaus at a fractional error $\sim 10^{-7}$ at $j_{max} \sim 7$ for the hard sphere, limited by other discretization errors. For the highly polarized case (induced by the capacitor), higher quadratures are needed for the same level of accuracy, and the plateau occurs $\sim 10^{-4}$ at $j_{max} \sim 10$. A reasonable choice for j_{max} for a typical system should therefore range from 7 to 10 depending on the strength of electric fields involved.

Figure 4.3 shows the density profiles next to the hard sphere and the walls of the capacitor for various orientation quadratures. In the case of the hard sphere, the density profiles are virtually identical for all considered quadratures, as is expected given that the relative error in the free energy is $\sim 10^{-4}$ even for the Octahedron group, one of the lowest quadratures considered with $j_{max} = 3$. However, there are qualitative differences in the density profiles near the capacitor walls for $j_{max} = 3$ from the converged ones at $j_{max} = 23$ (Euler(12) quadrature), and the differences begin to disappear only around $j_{max} = 10$. At these field strengths, the orientation distribution is highly polarized (close to saturation) and hence requires a dense orientation quadrature to resolve. (In the limit of an infinite electric field, the orientation distribution approaches a δ-function centered on the orientations for which the permanent dipole moment of the molecule is parallel with the field.)

4.3.3 Accuracy of water functionals

Finally, we turn to a comparison of the excess functionals for water suitable for *ab initio* solvation methods. In particular, we focus on the scalar-EOS functional of Section 4.2.2, the bonded-trimer functional [153] and the functional of Lischner et al. [97]. The last functional is based on experimental correlations functions, which we will refer to as the 'fitted-correlations' functional. We perform all calculations on one-dimensional planar or radial grids, using the Fluid1D sub-project of JDFTx [152]. We use the Euler(20) orientation quadrature, with $n_\alpha = 1$ to exploit rotational symmetry in the transverse directions. (See Appendix B.)

First we examine the partial pair correlation functions $g_{\alpha\beta}$ of the bulk fluid computed using the Ornstein-Zernike relation for the rigid-molecular fluid which may be written as

$$\tilde{h} = (1 - \tilde{I}\tilde{c}\bar{N})^{-1}\tilde{I}\tilde{c}\tilde{I}, \tag{4.37}$$

which is a matrix equation in Fourier space for each wave vector k. Here, $\tilde{h}_{\alpha\beta}(k)$ is the Fourier transform of $g_{\alpha\beta}(r) - 1$,[11] $\tilde{I}_{\alpha\beta}(k) = j_0(kR_{\alpha\beta})$ is the intramolecular structure factor with $R_{\alpha\beta}$ being the distance between sites α and β within the molecule, $\bar{N}$ is the bulk number density of fluid molecules, and $\tilde{c}_{\alpha\beta}(k)$ is the Fourier transform of the direct correlation function $c_{\alpha\beta}(\vec{r} - \vec{r}') = (-1/T)\delta^2 F_{\text{ex}}/\delta N_\alpha(\vec{r})\delta N_\beta(\vec{r}')$ evaluated in the limit of the uniform fluid.[12]

[11] In fact, $\tilde{h}_{\alpha\beta}(k)$ are related to the partial static structure factors $S_{\alpha\beta}(k)$ by $S_{\alpha\beta}(k) = 1 + N_{\text{bulk}}\tilde{h}_{\alpha\beta}(k)$, where N_{bulk} is the bulk density of the liquid. The partial static structure factors, in turn, are obtained from static structure factors for neutron diffraction in water, heavy water and mixtures of the two, taking advantage of the marked differences in neutron scattering lengths of hydrogen and deuterium nuclei. See [145] for details.

[12] The relation (4.37) may be generalized to mixtures of rigid-molecular fluids by replacing $\bar{N}$ with a diagonal matrix with the bulk number density of each component in the mixture, and setting $\tilde{I}_{\alpha\beta} = 0$ when α and β belong to different components of the mixture.

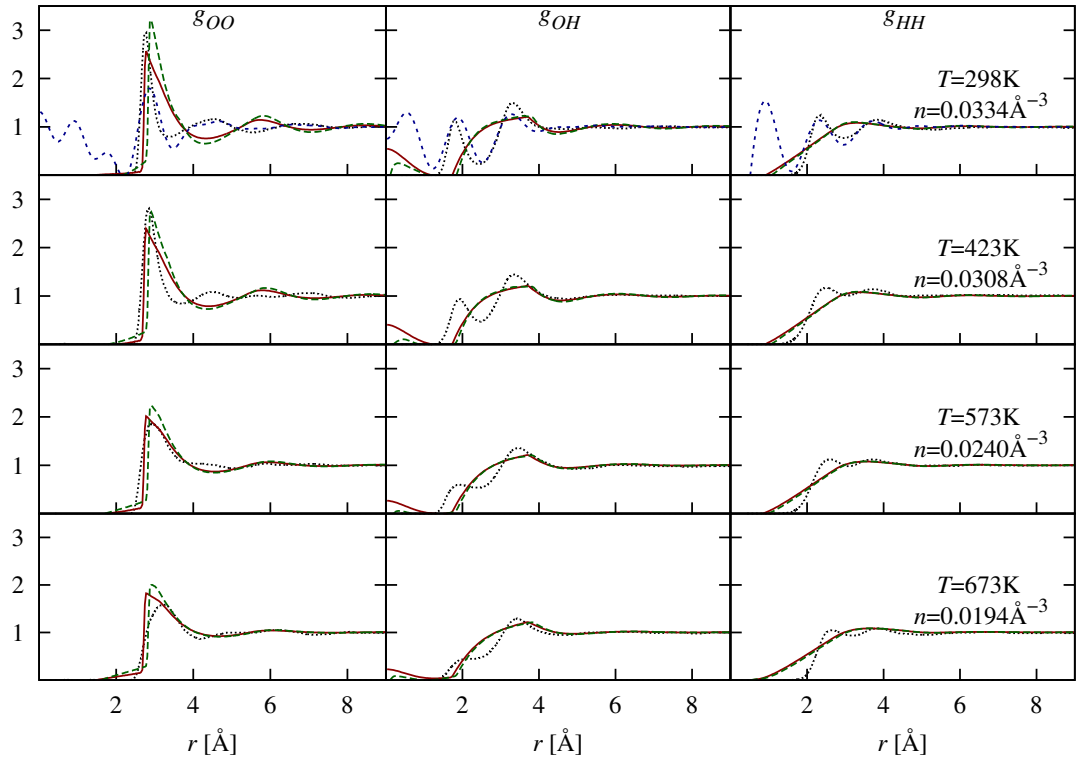

Figure 4.4: Partial radial distributions (site-site correlation functions) for the scalar-EOS water functional (solid red lines), bonded-trimer functional [153] (long-dashed green lines) and fitted-correlations functional [97] (short-dashed blue lines), compared to experimental pair correlations of water from Soper et al. [145] (black dotted lines). The position and location of the first g_{OO} peak for scalar-EOS and bonded-trimer are in reasonable agreement with experiment, but the remaining structure resembles that of a close-packed hard sphere fluid rather than a tetrahedrally bonded one. The fitted-correlations functional is defined only at 298 K and captures the features of the correlation functions by construction, but suffers from short-ranged artifacts due to the bandwidth-limited fitting procedure of [97].

The direct correlation functions are computed analytically in Fourier space for a set of wave vectors corresponding to the spherical Bessel function basis with 1024 basis functions and a radial extent $r_{\max} = 64$ bohrs (see Appendix B), and the pair correlation functions are computed via (4.37) using numerical spherical Bessel transforms. Figure 4.4 compares the pair correlations for all three functionals under consideration compared against those obtained

by Soper et al [145] from neutron diffraction data by empirical-potential structure refinement (EPSR).

The scalar-EOS functional correctly captures the location and height of the first peak in $g_{OO}(r)$, but produces a secondary structure reminiscent of the close-packed coordination of the hard sphere fluid rather than the tetrahedral coordination exhibited by experimental water. The split hydrogen peaks in the experimental data are fused into a single broader one with the same particle content. These are qualitatively the same features as the bonded-trimer functional, but with slightly better agreement for the scalar-EOS functional. After all, the motivation for the scalar-EOS functional was to simplify the bonded-trimer functional because it captured free energies of cavity formation reasonably *despite* not exhibiting features of tetrahedral correlation. The fitted-correlations functional reproduces some of the features of the experimental partial radial distribution functions by construction, but exhibits ringing artifacts at short distances, because it fits the experimental partial structure data in a limited range of wave-vectors. The missing data at low wave-vectors (see [97]) leads to the artifacts in the $g_{\alpha\beta}$ predicted by this functional; the reference experimental correlations in Figure 4.4, on the other hand, use molecular dynamics with an empirical potential to refine the data at low wave-vectors (see [145]).

Next, we examine the free energies of planar liquid-vapor interface for each functional. The calculations are performed on a one-dimensional planar grid of length 96 bohrs with 768 sample points and basis functions. For each temperature, the pressure is adjusted to the boiling point, which corresponds to equal chemical potentials and bulk grand free energy densities for the two phases. The hard sphere radius $R_{\mathrm{HS}} = 1.36$ Å for the scalar-EOS functional was determined

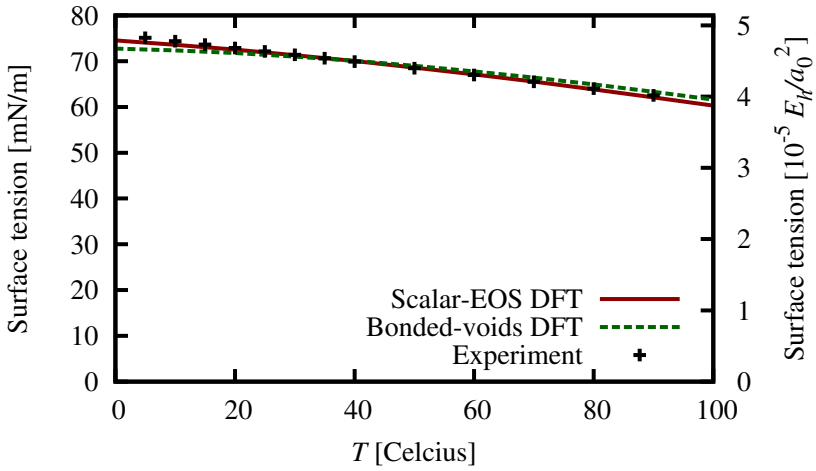

Figure 4.5: Energy of the planar vapor-liquid interface for the scalar-EOS and bonded-trimer water functionals as a function of temperature, compared to the experimental values for surface tension [32]. Both functionals fit the range parameter of the Lennard-Jones pair potential to the experimental surface tension at 298 K, and the scalar-EOS functional reproduces the temperature dependence more accurately than the bonded-trimer one. (The fitted-correlations functional is omitted from this plot, since it is defined only at 298 K.)

by matching the interface energy obtained from such a calculation at 298 K to the experimental value for the surface tension 72.0 mN/m.[13] Figure 4.5 compares the temperature dependence of this interface energy against experimental values for the surface tension. The scalar-EOS functional captures the trend in the experimental data slightly better than the bonded-trimer functional.

The planar interface energies provide a means to calibrate the liquid functionals against experimental measurements, and the excellent agreement for the temperature dependence after adjusting the surface tension at one temperature is promising. However, the applicability of a functional for molecular solvation calculations depends on its ability to accurately describe the free energies

[13] The attraction range parameter σ_U in the bonded-trimer model [153] and the smoothing parameter r_0 of the fitted-correlations model [97] were also fit to reproduce the surface tension at 298 K using similar calculations.

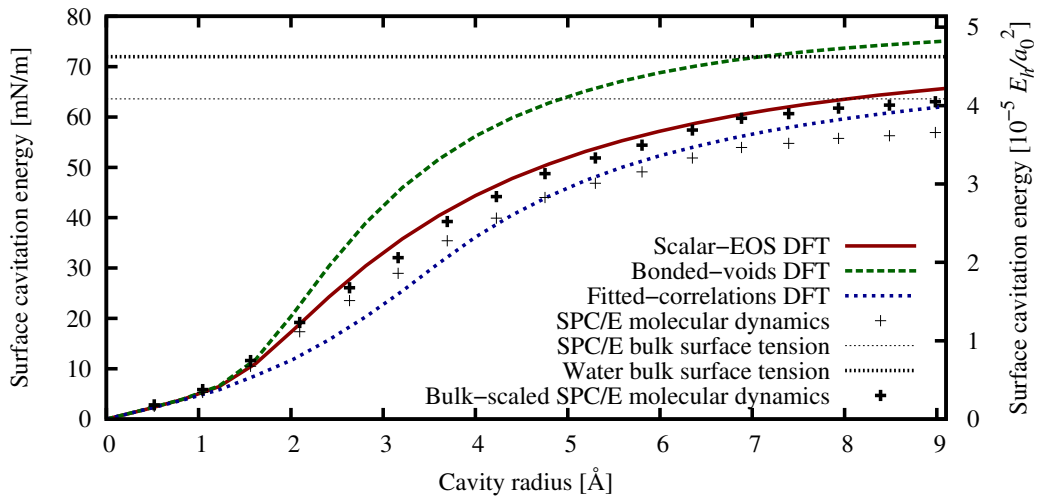

Figure 4.6: Variation of the spherical cavity formation free energy (solvation energy of hard spheres that expel the oxygen sites of water from their interior), with the radius of such spheres, compared to the SPC/E molecular dynamics results of [70]. The SPC/E model underestimates the bulk surface tension of water by 10% [167], and we have included a scaled version of the SPC/E data as a reasonable estimate for real water. The scalar-EOS functional agrees with the bulk-scaled SPC/E data accurately, while the fitted-correlations functional systematically underestimates and the bonded-trimer functional overestimates the free-energy of cavity formation.

required to form cavities of molecular dimensions. A standard test case is the solvation free energy for microscopic hard spheres in the fluid. We compute the cavity formation energies for hard spheres of radii R ranging from 0 to 9 Å, with external potentials $V_O(r) = (1\ E_h)\theta(R - r)$ and $V_H(r) = 0$ that exclude the oxygen site of water from the interior of the spheres. The calculations are performed on a one-dimensional radial grid of extent $r_{\max} = 64$ bohrs (≈ 34 Å) with 512 sample points and basis functions.

Figure 4.6 compares the variation of the hard sphere solvation energy per surface area with sphere radius for all three functionals with SPC/E molecular dynamics estimates for the same from [70]. For large spheres, the surface curvature effects become negligible and the surface energy approaches the planar

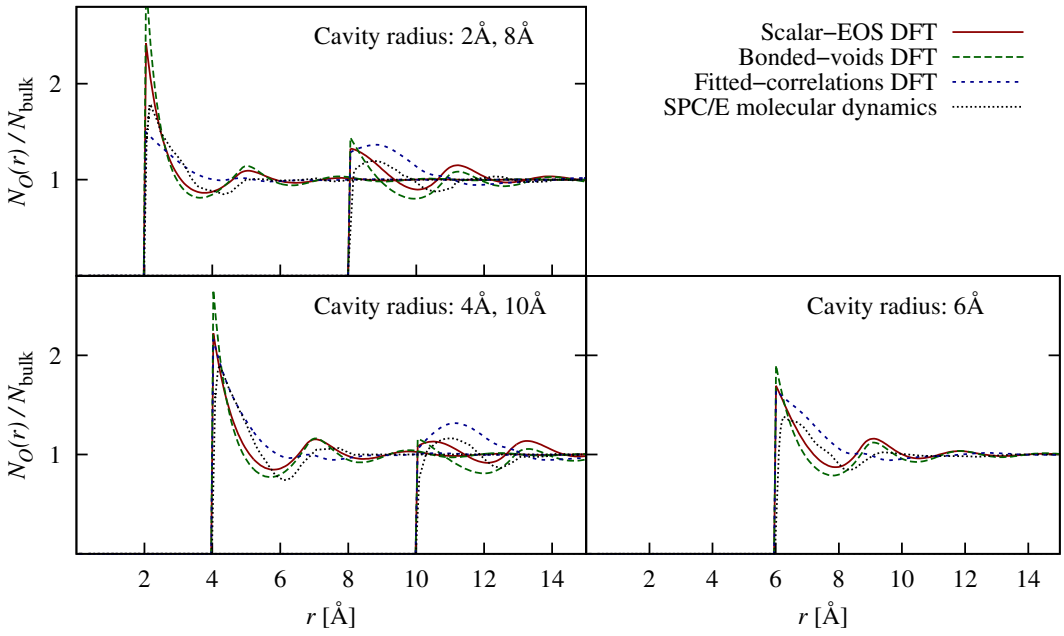

Figure 4.7: Radial density profiles around hard spheres that exclude the oxygen sites of water from their interior, for spheres of radius 2, 4, 6, 8 and 10 Å, compared to the SPC/E molecular dynamics results of [70]. The fitted-correlations functional misses the secondary peaks in the profiles, while the scalar-EOS and bonded-trimer functional overestimate the contact density and the secondary structure, with best agreement provided by the scalar-EOS model.

surface tension; whereas for small enough spheres the cavity formation energy is proportional to the volume ($\Delta\Phi = N_{\text{bulk}}T \times (4\pi R^3/3)$, so that $\Delta\Phi/(4\pi R^2) \propto R$). Note that all three functionals agree perfectly with the molecular dynamics results in the small radius limit, and they all approach the bulk experimental surface tension in the large radius limit (after overshooting the bulk value in the bonded-trimer case). However the SPC/E model underestimates the bulk surface tension to be 65 mN/m [167] compared to the experimental value of 72 mN/m, and therefore the molecular dynamics results for the sphere solvation energies are also underestimated by a similar amount for the larger spheres. Consequently, we include the molecular dynamics results scaled up by the ratio of experimental to SPC/E surface tensions as a reasonable estimate for the hard

sphere cavity formation energy of *real* water in Figure 4.6 (in addition to the unscaled values).[14] The scalar-EOS functional significantly outperforms bonded-trimer and fitted-correlations in its agreement with the bulk-scaled molecular dynamics results, and is the best candidate for an accurate density functional description of cavity formation energies in liquid water.

We next examine the distribution of water around these spherical cavities of selected sizes in Figure 4.7. As expected from the results for the free energies, the density profiles of the scalar-EOS functional are in closest agreement with the SPC/E molecular dynamics results of [70]. The bonded-trimer functional overestimates the structure in the liquid, which is expected since it also overestimated the structure in the pair correlations (Figure 4.4). The fitted-correlations functional severely underestimates the secondary structure in the density profiles despite better qualitative agreement with the experimental pair correlation functions. This is primarily because it incorporates the direct correlations at the bulk liquid density as a quadratic perturbation and does not account for changes in these correlations at the vacuum-liquid interface.

Finally, we turn to the last key ingredient for a successful theory of solvation: nonlinear dielectric response. For liquid water, the response arising from rotations of the strongly polar molecules dominates over the response arising from the polarization of the molecules; Chapter 5 treats liquids where the latter response is important. The typical electric fields in the vicinity of polar molecules are $\sim$ V/Å i.e. 10^{10} V/m, which corresponds to strong non-linearities and significant dielectric saturation. Here, we examine the nonlinear dielectric constant

[14] The TIP4P/2005 pair potential for water captures the bulk surface tension much more accurately than SPC/E [167], and it would be interesting to compare our density functional results to simulations of microscopic hard sphere solvation with that model. However, such results for TIP4P/2005 (analogous to [70] for SPC/E) have not yet been published to our knowledge.

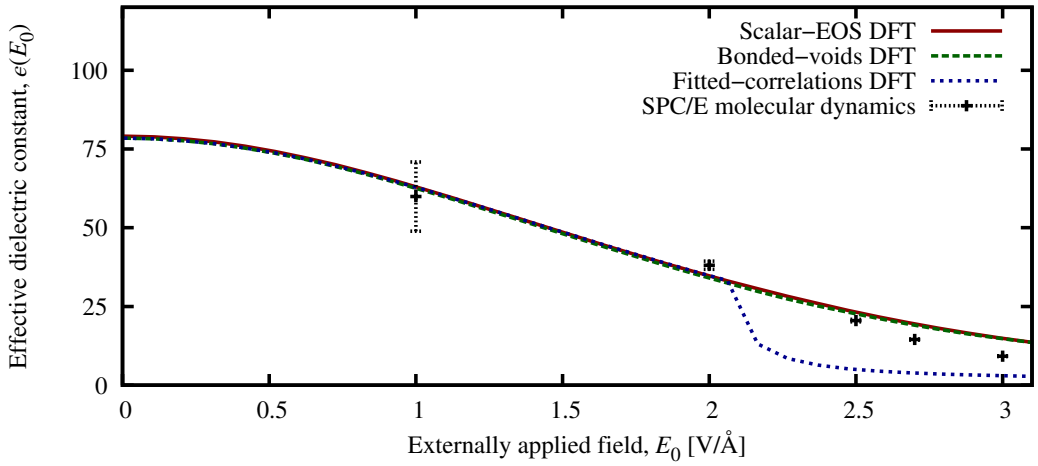

Figure 4.8: Nonlinear dielectric response of the water functionals compared to SPC/E molecular dynamics results from [178]. All three functionals provide essentially the same dielectric response, as this is determined by a competition between the molecular ideal gas entropy and the scaled mean field electrostatics. The minor differences arise from differences in the equations of state due to electrostriction (change of bulk-density in strong fields). The fitted-correlations functional has an unphysical instability accompanied by a rapid increase in density and drop in dielectric constant at an external field ≈ 2 V/Å, due to an underestimation of the compressibility at high pressures by its polynomial excess free energy density model.

defined by $\epsilon(E_0) = E_0/(E_0 - 4\pi P)$, where E_0 is a macroscopic externally applied field and P is the corresponding bulk polarization density in the liquid.

At equilibrium, a liquid in a macroscopic parallel-plate capacitor adopts uniform density and polarization except for microscopic regions around the plates. The free energy of that capacitor is dominated by the bulk; the regions next to the plates only contribute via long-range interactions of the bound sheet-charge densities $\pm P$ in the liquid. Accounting for the interaction of these sheet charges with the external field, and with each other via the scaled mean-field Coulomb interaction, we can show that the effective free energy density minimized by the

macroscopic capacitor at equilibrium is

$$\phi(p_\omega) = T \int \frac{\mathrm{d}\omega}{8\pi^2} p_\omega \left(\ln \frac{p_\omega}{N_{\mathrm{ref}}} - 1 \right) - \sum_\alpha \mu_\alpha N_\alpha + f_{\mathrm{ex}}(\{N_\alpha\}) \\ - \vec{E}_0 \cdot \vec{P} + A_\epsilon(T) \frac{4\pi P^2}{2}. \quad (4.38)$$

Here, f_{ex} is the excess-free energy density of the uniform fluid (which is determined entirely by the equation of state) and $\vec{P} = \int \frac{\mathrm{d}\omega}{8\pi^2} p_\omega \omega \circ \vec{P}_{\mathrm{mol}}$ is the polarization density, with $\vec{P}_{\mathrm{mol}}$ being the dipole moment of the fluid molecule in its reference orientation. We therefore minimize this free energy density on a planar grid with a single grid point to obtain the equilibrium P for each applied E_0, thereby avoiding the need for setting up a capacitor in a large simulation cell.

All three functionals considered here employ the same scaled mean-field electrostatic interaction constrained to produce the bulk dielectric response as proposed by Lischner et al. [97]. The physics of dielectric saturation is captured by an interplay of this term with the entropy of the ideal gas of rigid molecules, which again is common to all three functionals. Consequently, their nonlinear dielectric response is very similar and compares quite well with the SPC/E molecular dynamics results [178] as shown in Figure 4.8. The minor differences between the functionals are due to the different uniform fluid excess free energy densities (f_{ex}) which correspond to different approximations to the equation of state of the fluid. The fitted-correlations functional employs a polynomial model for f_{ex} obtained from the bulk modulus and its pressure derivative at standard room temperature and atmospheric pressure [97], which underestimates the bulk modulus at high compression. This causes the instability at high fields associated with a rapid increase in density, seen as a drop in the dielectric response at ≈ 2 V/Å in Figure 4.8.

4.4 Summary

This chapter constructs a general framework for the classical density-functional theory of rigid-molecular fluids that avoids the inversion problem associated with site-density constraints by switching to the orientation density as the key variable. The independent variables in previous solutions, such as ideal-gas effective site potentials, are compressed maximum-entropy representations of the orientation density. With this perspective, we can motivate other representations with superior convergence properties, that result in variational approximations to the free energy.

The self-representation, directly minimizing over the orientation density $\{p_\omega\}$, exhibits the fastest convergence for conjugate gradients minimization, but requires memory in proportion to the size of the quadrature for orientation integrals. The site-potential representation $\{\psi_\alpha\}$, although exact in principle, is impractical because of its poor convergence, particularly in the presence of strong electric fields. The multipole representation $\{\mu\vec{e}\}$ exhibits comparable convergence to the self-representation without the memory overhead, is effectively more accurate than $\{\psi_\alpha\}$ at practical iteration counts despite being a (variational) approximation, and enables efficient large-scale *ab initio* solvation in polar molecular fluids within the framework of joint density-functional theory.

In addition to the general framework for polar fluids, this chapter constructs a practical free energy functional for liquid water which improves on the accuracy of earlier functionals, while minimizing complexity and avoiding overparametrization. The central idea of this 'scalar-EOS' functional, a hard sphere fluid plus a weighted-density perturbation with a Lennard-Jones form, is easily

extensible to other fluids. The next chapter establishes this recipe for constructing free energy functionals for molecular solvents and incorporates molecular polarizability effects, which are important for nonpolar fluids, in the dielectric response.

CHAPTER 5

LIQUID FREE ENERGY FUNCTIONALS THAT INCLUDE MOLECULAR POLARIZABILITY [1]

Chapter 4 establishes a general framework for practical classical density functional calculations of fluids of rigid molecules, and presents a simplified excess functional for liquid water that adequately captures the cavity formation free energy and nonlinear dielectric response, critical for *ab initio* solvation methods. This 'Scalar-EOS' functional augments a hard sphere fluid with a Lennard-Jones weighted density term, constrained to the bulk equation of state and surface tension of the fluid. These short-ranged terms determine the cavity-formation free energies, while the nonlinear dielectric response follows from a competition between the ideal gas entropy and long-range Coulomb interactions between charged sites on the solvent molecules.

The short-ranged terms generalize to other fluids of small molecules, as Section 5.1 demonstrates for the weakly polar solvent, chloroform, and the nonpolar solvent, carbon tetrachloride. The dielectric response of water is dominated by molecular rotation, and the approach of Chapter 4 ignores contributions from the electronic and vibrational polarizability of the molecules, which are much more important for the less polar solvents. In fact, polarizability and rotations contribute almost equally to the dielectric constant of chloroform, while the dielectric response of carbon tetrachloride is entirely due to polarizability. In addition, the scaled mean-field Coulomb ansatz to account for rotational correlations is strictly valid only for fluids of diatomic molecules [96] and certain

[1] Co-author credits: K. Letchworth-Weaver helped develop the procedure for determining the microscopic parameters of the solvent molecule and performed the electron-density model fits of Section 5.3

triatomic molecules [97]. Section 5.2 presents a modified perturbation scheme that incorporates molecular polarizability contributions, and replaces the scaled mean-field ansatz with a local dipole-density approximation applicable to the rotational and polarization correlations of arbitrary fluids. Finally, Section 5.3 details how the microscopic properties of the solvent molecule required to approximate the fluid free energy functional may be completely determined by electronic density-functional calculations.

5.1 'Scalar-EOS' recipe for free energy functionals

The task of constructing free energy functional approximations for real molecular fluids that capture the detailed microscopic structure in inhomogeneous configurations is extremely challenging. Most approaches obtain the partial radial distributions of the fluids by construction, using structure factors from constituent dependent diffraction experiments, such as anomalous X-ray scattering and neutron diffraction with isotope substitution, or molecular dynamics simulations as input [33, 31, 97, 96, 180]. Such methods therefore rely on experimental data available for few liquids at few state points, or the construction and testing of a pair potential model followed by extensive molecular dynamics calculations. Consequently, they are not easily applicable to a new solvent or even previously studied solvents under different conditions.

Functionals that reproduce pair correlations and triplet functions would accurately describe properties of weakly inhomogeneous fluids, close to the reference bulk condition, but they may fail for interfaces, confined geometries and in strong external potentials. On the other hand, the usefulness of a free energy functional in *ab initio* solvation is determined by its accuracy for the free en-

ergies of forming cavities or interfaces of arbitrary microscopic geometries, and for the interaction with the charge distribution of the electronic system, which is dominated by its dielectric response. Analogous to the local density functional approximation providing remarkable accuracy for electronic density-functional predictions for the structure of matter *despite* missing details in the structure of the exchange-correlation hole, free energy functionals with imperfect pair correlations can successfully describe solvent effects in electronic structure calculations.

The scalar-EOS water functional of Chapter 4 predicts incorrect secondary structure in the partial pair correlation functions (Figure 4.4), but it is substantially more accurate for the free energies of microscopic cavity formation than the 'fitted-correlations' functional [97] which is constrained to experimental pair-correlation functions. Here, we examine the accuracy of the scalar-EOS construction for other molecular fluids, particularly the weakly polar chloroform ($CHCl_3$), which has a permanent dipole moment, and the non-polar carbon tetrachloride (CCl_4) with no permanent dipole.

The scalar-EOS approximation for the grand free energy of an inhomogeneous molecular fluid with probability density $p_\omega(\vec{r})$ of finding a molecule with orientation $\omega \in \mathrm{SO}(3)$ at position $\vec{r}$ is

$$\Phi[p_\omega] = \Phi_{\mathrm{id}}[p_\omega] + \Phi_{\mathrm{HS}}[N_0] + \int d\vec{r} N_0 A_{\mathrm{att}}(w_A * N_0) + \Phi_\epsilon[p_\omega]. \tag{5.1}$$

Here, $\Phi_{\mathrm{id}}[p_\omega]$ is the exact free energy of the ideal gas of rigid molecules with orientation density p_ω (see Section 4.1). $\Phi_{\mathrm{HS}}[N_0]$ is the excess free energy of a hard sphere fluid with density $N_0(\vec{r}) = \int \frac{d\omega}{8\pi^2} p_\omega(\vec{r})$ and with an as yet undetermined hard sphere radius R_{HS}; this term is approximated using fundamental measure theory [134, 159, 135]. The third term of (5.1) is a weighted density ansatz for

the contributions from intermolecular attractions, with the per-molecule excess Helmholtz energy function $A_{\text{att}}(N)$, constrained to the bulk equation of state, and attributed to a convolution of the scalar moment, N_0, of the orientation density. The weight function w_A is taken to be of the normalized Lennard-Jones form given by (4.20) with range $\sigma = 2R_{\text{HS}}$. The last term of (5.1), Φ_ϵ, accounts for long-range orientation-dependent Coulomb interactions and vanishes in the uniform fluid limit.

The fundamental assumption above is the separation of the contributions from interactions into short-ranged (r^{-6} and faster) orientation-averaged and long-range orientation-dependent parts. The hard sphere and weighted density terms capture the short-ranged part, while Φ_ϵ captures the long-ranged part. We next focus on the short-ranged part, which primarily determines the accuracy for cavity-formation energies, and explore the long-ranged part responsible for dielectric response in detail in Section 5.2.

The short-ranged part of the free energy functional (first three terms of (5.1)) is completely specified at this stage, except for the per-molecule excess free energy function $A_{\text{att}}(N)$ for a uniform fluid of density N, and the hard sphere radius R_{HS}. The equation of state of the fluid, $p(N,T)$, determines the grand free energy density of the uniform fluid and results in the differential equation $A'_{\text{att}}(N) = (p(N,T) - p_{\text{HS}}(N,T))/N^2$, where $p_{\text{HS}}(N,T)$ is the Carnahan-Starling equation of state of the hard sphere fluid [23]. This determines the free energy function $A_{\text{att}}(N)$ up to a constant which can be absorbed into the reference chemical potential for the fluid. For water, the Jefferey-Austin equation of state [77] results in the free energy function (4.24), and for the less polar fluids, the generic

Table 5.1: Hard sphere radii, R_{HS}, for which scalar-EOS functionals reproduce the bulk surface tension at $T = 298$ K (experimental values from [62]), compared to van der Waals radii, R_{vdW}, from [131, 14].

Fluid	R_{HS} [Å]	R_{vdW} [Å]
H_2O	1.36	1.385
$CHCl_3$	2.06	2.53
CCl_4	2.17	2.69

Tao-Mason equation of state [158] results in the free energy function

$$A^{\mathrm{TM}}_{\mathrm{att}}(N) = \frac{\alpha T}{\lambda b}\ln\frac{1}{1-\lambda b N} - T(\alpha - B)\left[N - A_1\left(e^{\kappa T_c/T} - A_2\right)\frac{\tan^{-1}(\sqrt{1.8}b^2N^2)}{2\sqrt{1.8}b}\right] - T\frac{V_{\mathrm{HS}}N(4-3V_{\mathrm{HS}}N)}{(1-V_{\mathrm{HS}}N)^2}. \quad (5.2)$$

Tao et al. relate the temperature-dependent functions $\alpha(T)$, $b(T)$ and $B(T)$, as well as the constants λ, κ, A_1 and A_2, to the critical point (T_c, P_c) and acentricity factor, ω, generically for several fluids; see [158] for details. The final term of (4.24) subtracts the free energy corresponding to the Carnahan-Starling hard-sphere equation of state, with the hard sphere volume $V_{\mathrm{HS}} = 4\pi R^3_{\mathrm{HS}}/3$.

The final step of the scalar-EOS recipe constrains the hard sphere radius, R_{HS} to reproduce the bulk liquid-vapor surface tension. Table 5.1 shows the thus obtained hard sphere radii for the three fluids considered here, and compares them to the van der Waals (vdW) radii, R_{vdW}, defined in terms of the effective exclusion volume in the equation of state [131, 14]. The hard sphere radius for water is approximately equal to its vdW radius, whereas those for chloroform and carbon tetrachloride are smaller than their vdW radii. This discrepancy is likely because of a softer interaction in these fluids compared to water, which spreads out the first peak in the pair-correlations over a larger range of radii. Contrast the *O-O* distribution in water (Figure 4.4) with the *C-C* distribution

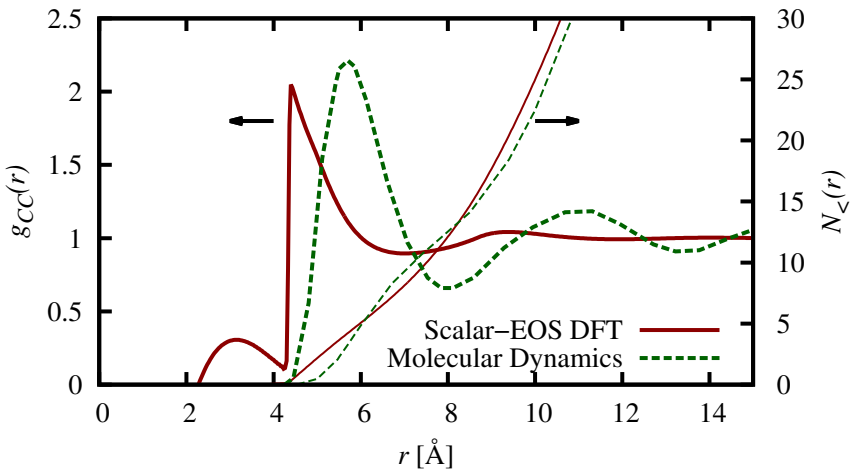

Figure 5.1: Partial *C*-*C* radial distributions for carbon tetrachloride as predicted by the Scalar-EOS density-functional theory, compared to molecular-dynamics results from [143]. Despite differences in the detailed structure, the onset of the first peak and its particle content (evident from the cumulative distribution $N_<(r)$) agree. The hump in $g_{CC}(r)$ between 2 and 4 Å, prior to the onset of the first peak, is a typical artifact introduced when adding a weighted-density perturbation to the hard sphere functional (see also [125, 153, 179], for example). This feature is unphysical and even becomes negative at small radii, but its integral $\int_0^{2R_{\mathrm{HS}}} dr 4\pi r^2 g_{CC}(r) \approx 0$, and it contributes negligibly to the free energies of typical inhomogeneous fluid configurations encountered in molecular solvation.

in carbon tetrachloride (Figure 5.1). The first *O*-*O* experimental peak in water is much narrower and overlaps with the onset of the much broader classical density-functional peak, whereas the *C*-*C* peak in CCl_4 is broader than the classical density-functional one. In both cases, the classical density-functional distributions resemble that of the reference hard sphere fluid, but the onset of the first peak and its particle content agree with experimental measurements and molecular dynamics results. This simple ansatz poorly describes further details of the pair correlations, but evidently captures just enough features of the fluid correlations to accurately predict the free energy of forming microscopic cavities.

Extensive SPC/E [15] molecular dynamics simulations by Huang et al. [167]

provide a reasonable reference estimate for the cavity formation energies in water, but to our knowledge, similar simulation results have not yet been published for carbon tetrachloride and chloroform. However, the accuracy of continuum solvation models [30] that employ scaled-particle theory [131] to estimate the cavity formation energy enables an indirect reference for comparison. Figure 5.2 shows that the spherical cavity formation energies predicted by the scalar-EOS functional and scaled-particle theory agree for small cavities of size comparable to the solvent molecule, which fall in the regime tested by continuum solvation models. The predictions of the two theories diverge for larger spheres, however, with the scalar-EOS functional correctly asymptoting to the bulk surface tension by construction, while scaled-particle theory asymptotes to that of the hard sphere fluid. Molecular dynamics results for these systems would be highly valuable in order to further test the free energy functional.

5.2 Dielectric response including molecular polarizability

The first three terms of the scalar-EOS free energy functional (5.1) describe a hard sphere fluid perturbed by short-ranged orientation-averaged attraction. The final term, $\Phi_\epsilon[p_\omega]$, accounts for long-ranged interactions between charged sites on the solvent molecules, which in competition with the rotational entropy from the first term, describes the dielectric response. Following [96, 97], Chapter 4 approximates the long-ranged correction by the mean-field Coulomb interaction with two modifications. First, it attenuates the Coulomb kernel in reciprocal space at high wave numbers corresponding to the molecular length scale, in order to minimize intramolecular contributions. Second, it introduces an overall scale factor constrained by the bulk linear dielectric constant to ac-

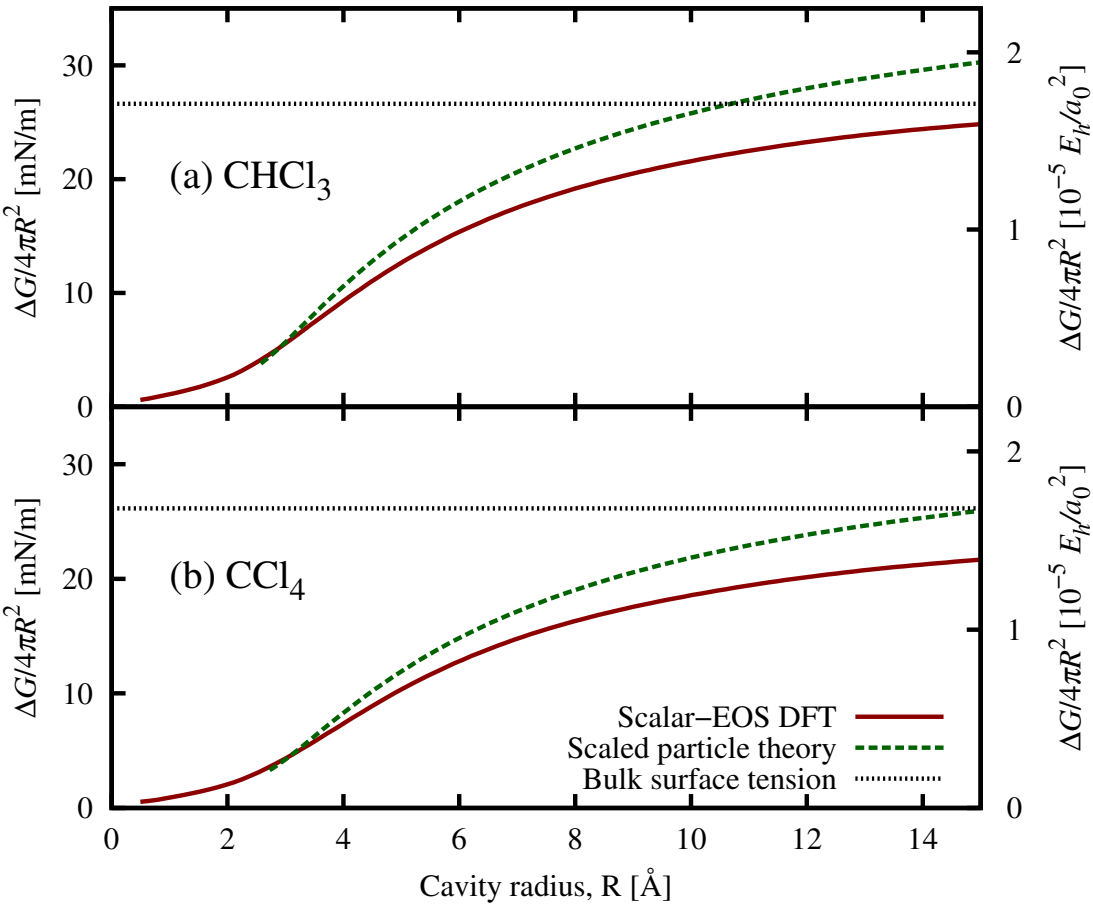

Figure 5.2: Free energy per surface area for creating microscopic spherical cavities in (a) chloroform and (b) carbon tetrachloride, predicted by the scalar-EOS free energy functional compared to scaled-particle theory [131, 14].

count for beyond-mean-field effects. Here, we examine these modifications and propose a new functional form for $\Phi_\epsilon[p_\omega]$ that generalizes to other solvents and includes contributions due to molecular polarizability.

In Chapter 4, the orientation density $p_\omega(\vec{r})$ determines densities $N_\alpha(\vec{r})$ of sites on the solvent molecule with charge Z_α, which then participate in the scaled-mean field Coulomb interaction

$$\Phi_\epsilon[p_\omega] = \frac{A_\epsilon}{2} \sum_{\alpha,\beta} Z_\alpha Z_\beta \int N_\alpha \hat{K} N_\beta \tag{5.3}$$

with a modified Coulomb kernel $\hat{K}$, specified in reciprocal space as $\tilde{K}(G) = 4\pi/G^2 \left(1 + (G/G_c)^4\right)^{-1}$. This high frequency cutoff serves to minimize the effects of the Coulomb interaction at the molecular length scale; this intramolecular contribution primarily results in a self-interaction error in the mean-field picture. Lischner et al. set the cutoff frequency $G_c = 0.33$ bohr^{-1} by examining the crossover of the direct correlation functions for water, extracted from neutron diffraction data, from the long-ranged $\sim 1/G^2$ behavior to a more structured short-ranged behavior [97]. We retain this intuitive picture, but motivate the high frequency attenuation from an alternate perspective that does not require the direct correlation functions.

The Coulomb kernel at length scales larger than the solvent molecule does not contribute to the self-interaction error in the mean-field term, and should remain unmodified; say $K(r > 2R_{\text{vdW}}) = 1/r$, since the vdW diameter $2R_{\text{vdW}}$ is a reasonable estimate for the typical nearest-neighbor distance in the liquid. This constraint is implicitly satisfied by the ansatz $K(r) = w_{\text{MF}}(r) * 1/r * w_{\text{MF}}(r)$ with a unit-norm short-ranged weight function $w_{\text{MF}}(r)$ which satisfies $w_{\text{MF}}(r > R_{\text{vdW}}) = 0$. Note that we choose a separable convolution in real-space, or equivalently a separable product in reciprocal space, so that the resulting interaction may be expressed as the bare Coulomb interaction acting on sites with spherical charge distributions, $Z_\alpha w_{\text{MF}}(r)$, replacing point charges, Z_α. This interpretation of evaluating the mean-field term on an effective charge density, $\rho_{\text{MF}}(\vec{r}) = \sum_\alpha Z_\alpha w_{\text{MF}} * N_\alpha(\vec{r})$, then easily generalizes to multiple response channels (such as polarizations) and for mixtures of fluids.

Now consider a δ-function perturbation of one of the fluid site densities staring from the uniform fluid. The self-interaction error in the above ansatz for

this configuration is simply the self-energy of the spherical charge distribution $w_{\mathrm{MF}}(r)$, up to constants including the magnitudes of the site charge and test perturbation. Minimizing this self-energy under the constraint $w_{\mathrm{MF}}(r > R_{\mathrm{vdW}}) = 0$ results in placing all the charge on the surface of the constraining sphere,

$$w_{\mathrm{MF}}(r) = \frac{\delta(r - R_{\mathrm{vdW}})}{4\pi R_{\mathrm{vdW}}^2}, \tag{5.4}$$

or equivalently, $\tilde{w}_{\mathrm{MF}}(G) = j_0(GR_{\mathrm{vdW}})$ in reciprocal space. Intuitively, the intramolecular interaction is minimized while preserving the intermolecular interaction, by distributing the charge on each site to a sphere that roughly circumscribes a solvent molecule.

Next, we account for molecular polarizability effects so as to extend the approach to fluids for which rotations do not dominate the dielectric response to the same extent as in water. In general, the susceptibility, $\chi(\vec{r}, \vec{r}')$, of a molecule to electric potentials arising from electronic polarization and vibrations can be expanded in an eigenbasis $\chi(\vec{r}, \vec{r}') = \sum_i X_i \rho_i(\vec{r}) \rho_i(\vec{r}')$. However, directly employing such a response in the classical density-functional description would require evaluating that nonlocal operator for each discrete orientation sampled by $p_\omega(\vec{r})$, making it prohibitively expensive. Molecular dynamics simulations demonstrate that it is reasonable to approximate the full nonlocal response by coupled dipole and monopole polarizabilities on each solvent site [143], or even independent dipole polarizabilities on each site [28]. Here, we employ a nonlocal generalization of the latter approach which approximates the response by extended-dipole polarizabilities on each site, resulting in the model susceptibility,

$$\chi_{\mathrm{model}}(\vec{r}, \vec{r}') = -\sum_\alpha \chi_\alpha \nabla' w_\alpha(|\vec{r}' - \vec{R}_\alpha|) \cdot \nabla w_\alpha(|\vec{r} - \vec{R}_\alpha|) \tag{5.5}$$

for one molecule with sites at positions $\vec{R}_\alpha$, with dipole polarizabilities χ_α and

with normalized range functions $w_\alpha(r)$. In terms of the amplitudes, $\vec{\mathcal{P}}_\alpha$, of the polarization along Cartesian directions at each site, the potential energy for a polarized state of that molecule is $\Phi_{\rm pol} = \sum_\alpha \mathcal{P}_\alpha^2/2\chi_\alpha$ with a corresponding induced charge $\rho(\vec{r}) = \sum_\alpha \vec{\mathcal{P}}_\alpha \cdot \nabla w_\alpha(|\vec{r} - \vec{R}_\alpha|)$. In fact, the above susceptibility to electric potential $\phi(\vec{r})$ results from the Euler-Lagrange equation that minimizes the energy $\Phi_{\rm pol} + \int d\vec{r}\phi(\vec{r})\rho(\vec{r})$. Section 5.3 determines the χ_α and $w_\alpha(r)$ that best reproduce the response of a single solvent molecule calculated using electronic density-functional theory.

The nonlocal susceptibility for a molecule assumed above is the most general form that efficiently generalizes to a fluid specified by site-densities $N_\alpha(\vec{r})$ alone, rather than depending on the full orientation density $p_\omega(\vec{r})$ in a nontrivial manner. The potential energy function generalizes to the functional $\Phi_{\rm pol}[\{\vec{\mathcal{P}}_\alpha(\vec{r})\}] = \sum_\alpha \int N_\alpha \mathcal{P}_\alpha^2(\vec{r})/2\chi_\alpha$ in terms of internal variables $\vec{\mathcal{P}}_\alpha(\vec{r})$, with the corresponding charge density simplifying to $\rho(\vec{r}) = -\nabla \cdot \sum_\alpha w_\alpha * N_\alpha \vec{\mathcal{P}}_\alpha$ after integrating by parts. This charge density correctly describes the interaction of the polarization of the fluid with an external electric potential, but suffers from self-interaction errors when included in the mean-field term. Analogous to the solution for the rotational response, we replace $w_\alpha(r)$ by a molecule-sized spherical shell $w_{\rm MF}(r)$ in the contribution to the mean field effective charge $\rho_{\rm MF}$, in order to preserve the intermolecular interactions while suppressing the intramolecular ones.

Finally, we address beyond-mean-field effects that critically affect the dielectric response. In the bulk dielectric response limit (response to small uniform electric fields), the free energy functional corresponding to a fluid of molecules with dipole polarizability χ and number density N, interacting with mean-field

interactions alone reduces to a free energy density function $P^2/N\chi + \frac{1}{2}4\pi P^2 - \vec{P}\cdot\vec{D}$ in terms of the polarization density $\vec{P}$ as the independent variable. The first term is the potential energy of the molecules in the polarized state, the second term is the mean-field interaction of the bound charge in the fluid, which in this case reduces to a long-ranged interaction between sheet charges at the surface of the dielectric (assuming a parallel-plate capacitor geometry), and the final term is the interaction with the externally applied field, $\vec{D}$. Spatially averaging the microscopic quantities in the original molecular picture shows that $\vec{D} = \vec{E} + 4\pi\vec{P}$, where $\vec{D}$ and $\vec{E}$ are precisely the standard external and total electric fields entering the Maxwell equations of macroscopic media [137]. Therefore, the equilibrium polarization, $\vec{P} = N\chi\vec{D}/(1 + 4\pi N\chi)$ results in a net electric field $\vec{E} = \vec{D} - 4\pi\vec{P} = \vec{D}/(1 + 4\pi N\chi)$, and hence predicts a dielectric constant of $\epsilon_b = 1 + 4\pi N\chi$. In the dilute or low polarizability limit, this expression is correct to $O(N\chi)$, but it is impractically inaccurate for any real fluid.

The Clausius-Mossotti relation accounts for local enhancements in the electric field interacting with each molecule of the fluid, relative to the mean electric field in the medium. In particular, it places each molecule in a dielectric cavity within which the field is a factor $C = 1 + (\epsilon_b - 1)/3$ larger than the mean field. Solving for $\epsilon_b = \vec{D}/\vec{E}$ from $\vec{P} = N\chi C\vec{E}$ (response to enhanced field) and $\vec{E} = \vec{D} - 4\pi\vec{P}$ results in the familiar relation, $\epsilon_b = (1 + 2 \times 4\pi N\chi/3)/(1 - 4\pi N\chi/3)$.[2] Adding a correlation term $(C^{-1} - 1)P^2/N\chi$ to the free energy function above, implements the response to an enhanced field by effectively scaling the susceptibility by a factor C. Further note that theories of the bulk dielectric constant

[2]When $4\pi N\chi/3$ approaches and exceeds unity, the Clausius-Mossotti picture predicts a divergence in the dielectric response of the material. This corresponds to the Goldhammer-Herzfeld criterion for the polarization catastrophe [65], where the instability towards infinite polarization is interpreted as a transition to a metallic phase. The final column of Table 5.2 shows that this criterion is not met for the fluids considered in this chapter.

Table 5.2: Field enhancement factors for the rotational and polarization response of water, chloroform and carbon tetrachloride, as constrained by (5.6) using the experimental dielectric constants from [62], compared to that of the Clausius-Mossotti dielectric cavity (labeled by superscript CM). The final two columns report the isotropic dipole polarizability, $\chi_{\rm pol} = \sum_\alpha \chi_\alpha$ obtained from electronic DFT in Section 5.3 (with corresponding experimental values from [62] in parentheses), and its combination with the density, $4\pi N_{\rm bulk}\chi_{\rm pol}/3$, that enters the Goldhammer-Herzfeld criterion for the polarization catastrophe [65]; these liquids remain insulating dielectrics since that combination is less than unity.

Fluid	$C_{\rm rot}$	$C_{\rm rot}^{\rm CM}$	$C_{\rm pol}$	$C_{\rm pol}^{\rm CM}$	$\chi_{\rm pol}[a_0^3]$	$4\pi N_{\rm bulk}\chi_{\rm pol}/3$
H_2O	4.07	26.5	1.20	1.26	10.3 (9.8)	0.21 (0.20)
$CHCl_3$	2.28	1.91	1.25	1.36	62.6 (64.1)	0.29 (0.30)
CCl_4	-	-	1.26	1.38	77.6 (75.6)	0.30 (0.29)

beyond Clausius-Mossotti, such as the Onsager reaction-field method [116] or the Kirkwood bond-restriction approach [80], can all be recast into the above form, but with a different specification of the enhancement factor, C. Within the density-functional perspective, we constrain $C = (\epsilon_b - 1)/(4\pi N\chi)$ to reproduce the experimental bulk dielectric constant and generalize the P^2 term to the inhomogeneous fluid. Notice that in the bulk limit, the P^2 correlation term can be combined with the mean-field term to obtain a scaled mean-field term, which presents an alternate derivation of the approach of Chapter 4 and [96, 97]. However, in going to the inhomogeneous fluid, scaling the mean-field term introduces spurious contributions at other multipole moments; the monopole contributions are particularly unphysical and problematic when dealing with solutions containing ionic species.

In the general case of a fluid with a permanent molecular dipole moment $p_{\rm mol}$, the total dipole susceptibility includes a rotational contribution $\chi_{\rm rot} = p_{\rm mol}^2/(3T)$, in addition to site polarizabilities of strength χ_α; the field-enhancement factors for each contribution would be different in principle.

Within the constraints of available experimental data, we assume separate enhancement factors for rotations, C_{rot}, and polarizations, C_{pol}. At high frequencies, the rotational response freezes out and the polarizations alone produce the high frequency dielectric constant, ϵ_∞, while both contribute to the static dielectric constant, ϵ_b. These constrain the enhancement factors

$$C_{\text{pol}} = \frac{\epsilon_\infty - 1}{4\pi N_{\text{bulk}} \sum_\alpha \chi_\alpha} \quad \text{and} \quad C_{\text{rot}} = \frac{\epsilon_b - \epsilon_\infty}{4\pi N_{\text{bulk}} p_{\text{mol}}^2 / 3T}. \tag{5.6}$$

Table 5.2 compares the enhancement factors for the rotational and polarization contributions with those predicted by the Clausius-Mossotti cavity. As expected, the values agree for the electronic polarizability response for all three fluids, and reasonably so even for the low dielectric-constant rotational response of chloroform, but are completely different for the rotational response of water.

The bulk field enhancement factors do not specify a unique functional for the inhomogeneous fluid. The long-ranged parts of experimental correlation functions are also not sufficiently accurate to distinguish between different inhomogeneous generalizations, and so we propose the simplest form to avoid over-parametrization. The potential energy functional for polarization is explicitly quadratic, exactly as in the bulk linear response limit, and we assume an identical inhomogeneous form for the correlation functional so that C_{pol} simply enhances the site susceptibilities. For the rotational response, whose 'potential energy' is the far more complicated nonlinear ideal gas entropy, we generalize $(C_{\text{rot}}^{-1} - 1)P_{\text{rot}}^2 / N\chi_{\text{rot}}$ to a weighted polarization-density functional employing the mean-field weight function w_{MF} to reflect the cavity assumed in the Clausius-Mossotti derivation.

Collecting the polarizability potential energy, the mean-field interactions and the correlation functional, the final ansatz for the dielectric perturbation

functional is

$$\Phi_\epsilon = \sum_\alpha \int d\vec{r} \frac{N_\alpha \mathcal{P}_\alpha^2}{2C_{\text{pol}}\chi_\alpha} + \int d\vec{r} \int d\vec{r}' \frac{\rho_{\text{MF}}(\vec{r})\rho_{\text{MF}}(\vec{r}')}{2|\vec{r}-\vec{r}'|} + \frac{C_{\text{rot}}^{-1}-1}{N_{\text{bulk}}p_{\text{mol}}^2/3T} \int d\vec{r} \bar{P}_{\text{rot}}^2, \quad (5.7)$$

with the total mean-field effective charge density,

$$\rho_{\text{MF}} = \sum_\alpha Z_\alpha w_{\text{MF}} * N_\alpha(\vec{r}) - \nabla \cdot \sum_\alpha w_{\text{MF}} * N_\alpha \vec{\mathcal{P}}_\alpha, \quad (5.8)$$

and the weighted rotational polarization-density,

$$\vec{\bar{P}}_{\text{rot}} = w_{\text{MF}} * \int \frac{d\omega}{8\pi^2} p_\omega(\vec{r}) \omega \circ \vec{p}_{\text{mol}}, \quad (5.9)$$

where $\omega \circ \vec{p}_{\text{mol}}$ is the dipole moment of the molecule at orientation ω. Interaction of the fluid with an external electric potential, $\phi(\vec{r})$ takes the form $\int d\vec{r}\phi(\vec{r})\rho(\vec{r})$ with the real charge density,

$$\rho(\vec{r}) = \sum_\alpha \rho_\alpha(r) * N_\alpha(\vec{r}) - \nabla \cdot \sum_\alpha w_\alpha(r) * N_\alpha \vec{\mathcal{P}}_\alpha, \quad (5.10)$$

where $\rho_\alpha(r)$ and $w_\alpha(r)$ are spherical charge-density profiles and polarizability range functions respectively, for each site, obtained from electronic density-functional theory calculations in Section 5.3.

At this stage, the free energy functional has the orientation density, p_ω, and the polarization amplitudes, $\vec{\mathcal{P}}_\alpha$, as independent variables. The Euler-Lagrange equations for minimizing this functional (including an interaction with an external electric potential) with respect to $\vec{\mathcal{P}}_\alpha$ show that at the minimum, all those amplitudes can be expressed as

$$\vec{\mathcal{P}}_\alpha(\vec{r}) = C_{\text{pol}}\chi_\alpha \left[w_{\text{MF}}(r) * \vec{\mathcal{E}}(\vec{r}) - w_\alpha(r) * \nabla\phi(\vec{r}) \right] \quad (5.11)$$

in terms of an auxiliary vector field $\vec{\mathcal{E}}(\vec{r})$ (which equals the electric field from ρ_{MF} at the solution). In practice, we use the above relation to minimize the

free energy functional with p_ω expressed using one of the ideal gas representations of Chapter 4, and this auxiliary field $\vec{\varepsilon}(\vec{r})$ as independent variables. We have revised the rigid-molecular fluid framework in the open-source electronic density-functional software, JDFTx [154], to include polarizability contributions as detailed above.

Figure 5.3 compares the nonlinear dielectric response predicted by the scalar-EOS free energy functional with and without molecular polarizability. The differences are minor and occur only at very high fields for water; adding polarizability slightly increases the response relative to rotation-only DFT as well as molecular dynamics [178] results with the SPC/E pair potential model [15] that only captures the rotational response of rigid molecules. In chloroform, the predicted dielectric constants differ significantly at any finite field and agree only in the zero-field limit by construction. Carbon tetrachloride has no permanent dipole moment and presents no rotational contribution to the bulk dielectric response. The electronic polarizability contribution increases with field in the present model due to electrostriction: the density of the fluid increases in response to the applied electric field. Molecular dynamics predictions for the nonlinear response in $CHCl_3$ and CCl_4 using pair potential models with site polarizabilities, such as those of [28, 143], would be invaluable for testing the density functional predictions, but are unfortunately unavailable in the literature.

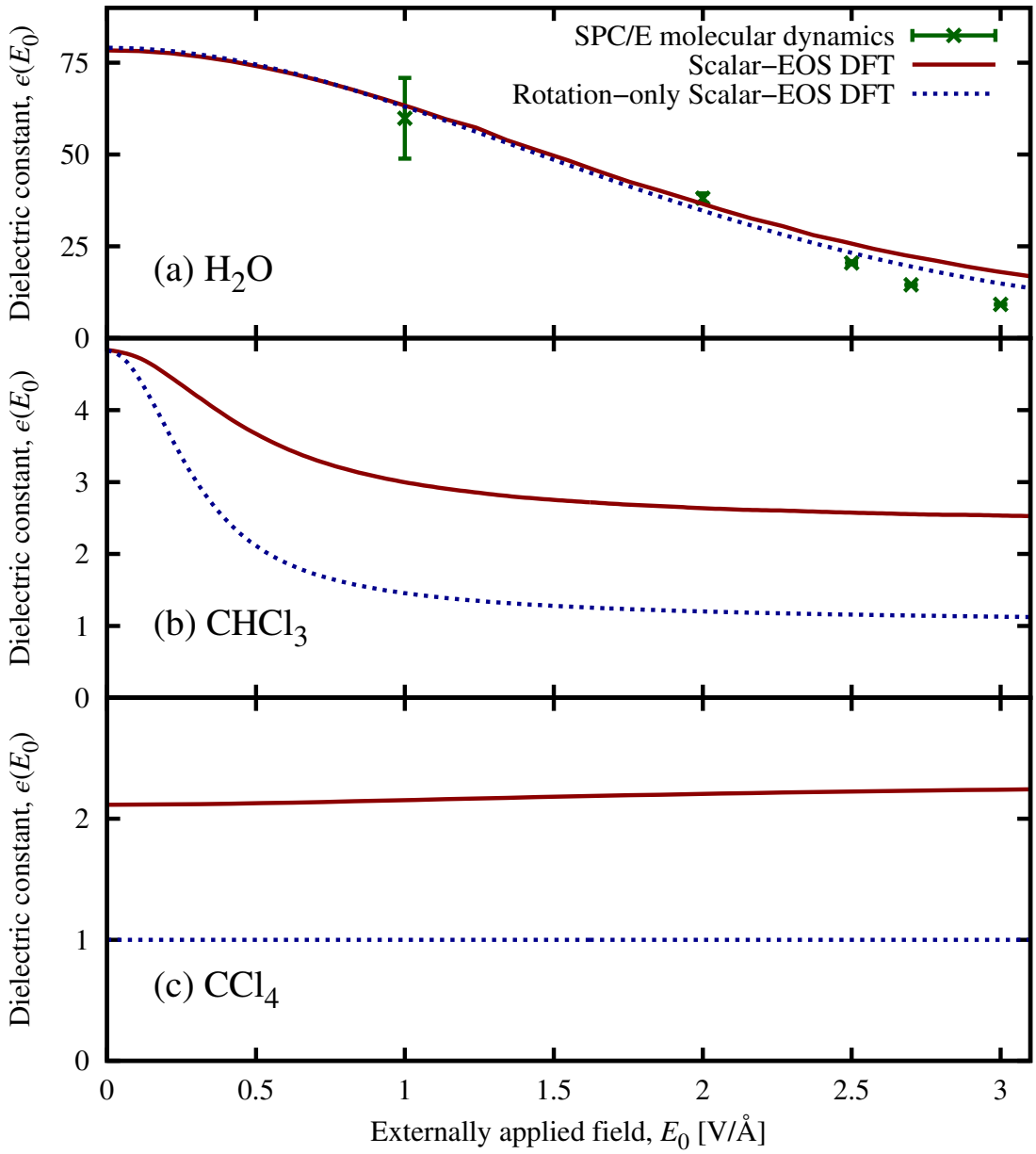

Figure 5.3: Nonlinear dielectric response of (a) water, (b) chloroform and (c) carbon tetrachloride, predicted by scalar-EOS free energy functionals with and without polarizability contributions.

5.3 *Ab initio* determination of solvent molecule parameters

The bulk equation of state and the surface tension of the fluid completely constrain the short-ranged part of the scalar-EOS functional. However, the electric response, which dominates the interaction of the fluid with electronic systems in solvated electronic-structure calculations, is sensitive to microscopic details. The geometry, electron and net charge distribution, and susceptibility of each constituent solvent molecule affect both the short-range and long-range electric response of the fluid. Here, we establish the procedure for determining all these microscopic parameters from electronic density-functional calculations of a single solvent molecule.

A solvent molecule in a liquid environment differs significantly from an isolated or gas phase molecule. Pair potential models created for molecular dynamics simulations of liquids are calibrated to reproduce only the thermodynamic properties of the liquid state, but they may capture these differences indirectly. For example, the dipole moment of the SPC/E model water molecule [15] is 2.35 Debye, in agreement with estimates of 2.3-2.5 Debye [47] based on cubic susceptibility measurements, and in contrast to the gas phase moment of 1.85 Debye. We account for the effect of the surrounding liquid by performing the electronic structure calculation of one quantum-mechanical solvent molecule in contact with a bath of implicit solvent molecules. To determine the microscopic parameters for a given solvent, we typically employ the nonlinear polarizable continuum model of Chapter 6, which approximates solvent effects in an electronic density-functional calculation of a molecule by surrounding it with a continuum nonlinear dielectric. This solvation model can capture the increased liquid-phase dipole moment and other relevant properties of

the quantum-mechanical solvent molecule, even for polar solvents where the saturation of the dielectric response at high electric fields becomes important. In principle, we could obtain the solvent parameters self-consistently within a solvation model which includes full microscopic detail. In practice, however, we find that the parameters determined from a properly constrained and sufficiently detailed polarizable continuum model is adequate for joint density-functional calculations.

First, we obtain the geometry of the solvent molecule directly from the relaxed nuclear positions, $\{\vec{R}_\alpha\}$, within the solvated electronic density-functional calculation. Table 5.3 shows that the bond lengths and angles, thus obtained, agree reasonably with popular molecular dynamics models for water, chloroform and carbon tetrachloride.

Next, the valence electron density from the solvated electronic density-functional calculation is expanded as a sum of spherical contributions around each atom of the solvent molecule. The exponential tails of the electron density play an important role in determining the separation between the solute and solvent via the coupling functional [91] in joint density functional theory as well as in the nonlocal polarizable continuum model (Chapter 8). However, the details of the electron density near the core are unimportant for solute-solvent coupling and the contribution to the electric interaction from spherical charge distributions that do not overlap depends only on their norms. We can therefore rearrange both the electron and nuclear densities within the core region to optimize representability on a Fourier grid without changing the interaction energies. For each electron density center, we employ a cuspless exponential function $\propto (r + a)e^{-r/a}$ which is smooth at the origin and has the correct asymp-

Table 5.3: Microscopic solvent parameters for water, chloroform and carbon tetrachloride from electronic density-functional theory, compared to molecular dynamics models ([78] for H_2O, [28] for $CHCl_3$ and [143] for CCl_4) wherever applicable.

Solvent	Property	Density-functional	Molecular Dynamics
H_2O	r_{OH}	0.967 Å	0.9572 Å
	θ_{HOH}	104.2°	104.52°
	q_O	-0.826	-0.8476
	q_H	+0.413	+0.4238
	$Z_O^{\mathrm{el}}, a_O^{\mathrm{el}}$	6.826, 0.32 a_0	-
	$Z_H^{\mathrm{el}}, a_H^{\mathrm{el}}$	0.587, 0.31 a_0	-
	$\chi_O, a_O^{\mathrm{pol}}$	3.73 a_0^3, 0.32 a_0	-
	$\chi_H, a_H^{\mathrm{pol}}$	3.30 a_0^3, 0.39 a_0	-
$CHCl_3$	r_{CCl}	1.804 Å	1.76 Å
	r_{CH}	1.091 Å	1.07 Å
	θ_{HCCl}	107.8°	107.6°
	q_C	-0.256	+0.5609
	q_H	+0.244	-0.0551
	q_{Cl}	+0.004	-0.1686
	$Z_C^{\mathrm{el}}, a_C^{\mathrm{el}}$	4.256, 0.43 a_0	-
	$Z_H^{\mathrm{el}}, a_H^{\mathrm{el}}$	0.756, 0.26 a_0	-
	$Z_{Cl}^{\mathrm{el}}, a_{Cl}^{\mathrm{el}}$	6.996, 0.44 a_0	-
	$\chi_C, a_C^{\mathrm{pol}}$	6.05 a_0^3, 0.36 a_0	5.92 a_0^3, -
	$\chi_H, a_H^{\mathrm{pol}}$	9.13 a_0^3, 0.41 a_0	0.911 a_0^3, -
	$\chi_{Cl}, a_{Cl}^{\mathrm{pol}}$	15.8 a_0^3, 0.46 a_0	12.89 a_0^3, -
CCl_4	r_{CCl}	1.801 Å	1.783 Å
	q_C	-0.980	-0.6052
	q_{Cl}	+0.245	+0.1513
	$Z_C^{\mathrm{el}}, a_C^{\mathrm{el}}$	4.980, 0.44 a_0	-
	$Z_{Cl}^{\mathrm{el}}, a_{Cl}^{\mathrm{el}}$	6.755, 0.44 a_0	-
	$\chi_C, a_C^{\mathrm{pol}}$	5.24 a_0^3, 0.35 a_0	-
	$\chi_{Cl}, a_{Cl}^{\mathrm{pol}}$	18.1 a_0^3, 0.47 a_0	-

totic exponential behavior. We then fit the valence electron density $n(r)$ to the model form

$$n_{\text{model}}(\vec{r}) = \sum_{\alpha} Z_{\alpha}^{\text{el}} \frac{r_{\alpha} + a_{\alpha}^{\text{el}}}{32\pi(a_{\alpha}^{\text{el}})^4} \exp\left(-r_{\alpha}/a_{\alpha}^{\text{el}}\right), \tag{5.12}$$

where $r_{\alpha} = |\vec{r} - \vec{R}_{\alpha}|$ is the distance from nucleus α, Z_{α}^{el} is the norm and a_{α}^{el} is the exponential length scale associated with the electron density component at site α. We constrain the norms of all sites Z_{α}^{el} to match the lowest multipole moments, employing as many moments as necessary to constrain them (up to dipole for water, quadrupole for chloroform, and octupole for carbon tetrachloride). We then perform a nonlinear least-squares fit for the widths a_{α}^{el}, minimizing the difference between $n(\vec{r})$ and $n_{\text{model}}(\vec{r})$ weighted by the squared distance to the closest nucleus $\min(r_{\alpha}^2)$. The core regions are included in the fit, but have little effect because the points in the exponential tails are more heavily weighted by the residual.

Figure 5.4 compares the valence electron density and the site-spherical model for water. Note that the electron density tails are reproduced well, and the residual in the core regions has zero multipole moments to high order by construction and therefore does not contribute to the electric interaction with another non-overlapping molecule.

The remaining contribution to the charge density, from the core electrons and the nuclei, has norm Z_{α}^{nuc} (determined by the pseudopotential choice for valence/core separation). This charge is confined to the interior regions of the molecule (does not overlap with the cores of other molecules), so for optimum Fourier resolvability, we smooth it with a gaussian distribution of standard deviation $\sigma_{\alpha}^{\text{nuc}} = R_{0\alpha}/6$. These distributions then become effectively zero to numerical precision at the atomic vdW radius $R_{0\alpha}$, which is a reasonable estimate for

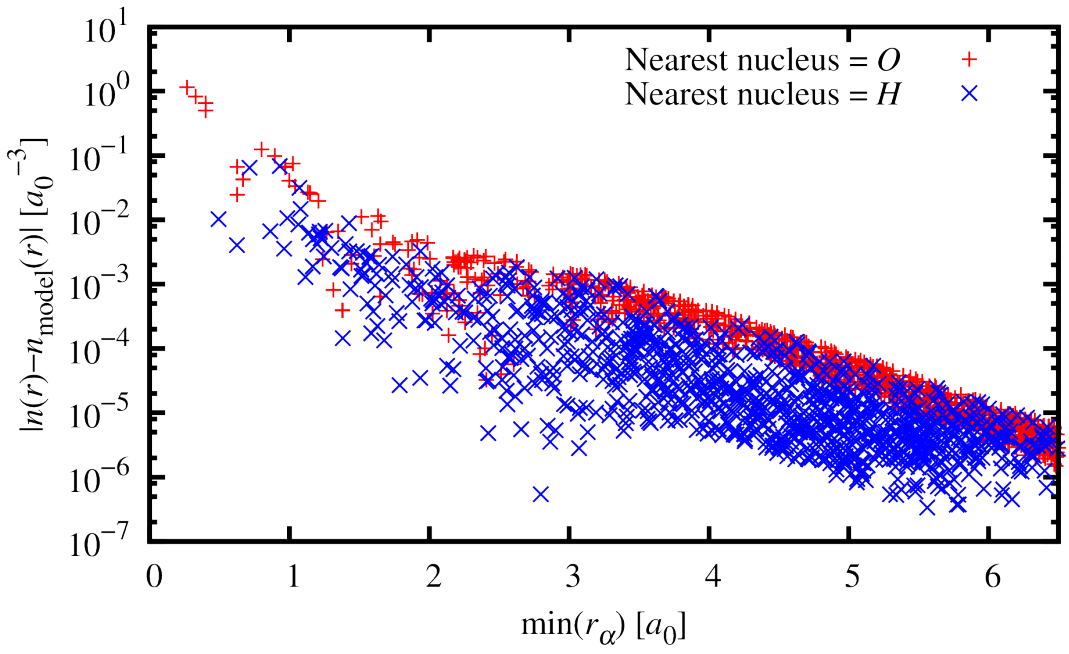

Figure 5.4: Error in the spherical decomposition of the electron density of a water molecule at each point in space, plotted against distance to nearest nucleus.

the typical approach distance of that site to any other atom. Table 5.3 shows the electron density fit parameters and the implied site charges $q_\alpha = Z_\alpha^{\mathrm{nuc}} - Z_\alpha^{\mathrm{el}}$.

Our site charges agree reasonably with those of common pair potentials for the highly polar liquid water, whose thermodynamic properties are sensitive to these parameters in molecular dynamics simulations. However, in weakly polar or nonpolar fluids, the bulk thermodynamic properties do not constrain the multipole moments, since the magnitude of the Coulomb interaction is insignificant compared to the magnitude of the dispersion interaction. Thus, unsurprisingly, the empirically determined molecular dynamics site charges for chloroform [28] differ significantly from our *ab initio* values. The carbon tetrachloride site charges of [143], determined from coupled-cluster calculations in vacuum, do not include polarization effects due to surrounding solvent molecules and

result in an octupole moment of 7.92 Debye-Å^2. (See Table E.1 for conversions to atomic units.) Our *ab initio* model includes solvent effects and produces a octupole moment of 13.2 Debye-Å^2 in much better agreement with the experimental value of (15 ± 3) Debye-Å^2 [39].

From these fits, the total charge density kernel for interactions of the classical fluid with external electric potentials is then given by

$$\rho_\alpha(r) = \frac{Z_\alpha^{\text{nuc}}}{(\sigma_\alpha^{\text{nuc}}\sqrt{2\pi})^3}\exp\left(\frac{-r^2}{2(\sigma_\alpha^{\text{nuc}})^2}\right) - \frac{Z_\alpha^{\text{el}}}{32\pi(a_\alpha^{\text{el}})^4}\left(r + a_\alpha^{\text{el}}\right)\exp\left(\frac{-r}{a_\alpha^{\text{el}}}\right). \tag{5.13}$$

Finally, the electronic polarizability $\chi(\vec{r},\vec{r}')$ in Kohn-Sham electronic density functional theory is formally related to the susceptibility of the corresponding non-interacting system,

$$\chi_{\text{NI}}(\vec{r},\vec{r}') = -4\sum_{c,v}\frac{\psi_c(\vec{r})\psi_v^*(\vec{r})\psi_c^*(\vec{r}')\psi_v(\vec{r}')}{\epsilon_c - \epsilon_v}, \tag{5.14}$$

by $\hat{\chi}^{-1} = \hat{\chi}_{\text{NI}}^{-1} - \delta^2 E_{HXC}[n]/\delta n^2$. Here, (ψ_v, ϵ_v) and (ψ_c, ϵ_c) are occupied and unoccupied Kohn-Sham orbital-eigenvalue pairs respectively, and $E_{HXC}[n]$ is the sum of the Hartree term and the exchange-correlation functional. In practice, we compute a large number of unoccupied Kohn-Sham eigenpairs of the solvated solvent molecule, compute $\hat{\chi}$ from $\hat{\chi}_{\text{NI}}$ as a dense matrix in the occupied-unoccupied basis ($\{\psi_c^*(\vec{r})\psi_v(\vec{r})\}$), and then diagonalize $\hat{\chi}$ to obtain an eigen-expansion $\chi(\vec{r},\vec{r}') = \sum_i X_i\rho_i(\vec{r})\rho_i(\vec{r}')$. We find that 1000 unoccupied orbitals and 500 eigenvectors in the final expansion results in better than 1 % convergence in the total dipole polarizability of the molecule. The penultimate column of Table 5.2 shows that the calculated isotropic linear dipole polarizabilities are within 5 % of the experimental values [62] for all three liquids.

The classical density functional requires the polarizability in the model form, $\hat{\chi}_{\text{model}}$ given by (5.5). In order to properly represent the exponential tail regions

with a smooth core region, we once again pick the cuspless exponential form

$$w_\alpha(r) = \frac{r + a_\alpha^{\mathrm{pol}}}{32\pi(a_\alpha^{\mathrm{pol}})^4} \exp\left(\frac{-r}{a_\alpha^{\mathrm{pol}}}\right) \tag{5.15}$$

for the normalized range functions. We then fit the site dipole polarizabilities, χ_α, and their nonlocality widths, a_α^{pol}, to minimize $\mathrm{Tr}\left((\hat{K}(\hat{\chi} - \hat{\chi}_{\mathrm{model}}))^2\right)$, which effectively measures the error in the screening operator $\hat{\epsilon}^{-1} = 1 - \hat{K}\hat{\chi}$, where $\hat{K}$ is the Coulomb operator. Table 5.3 lists the so obtained polarizability parameters for all three solvents. Note that the width parameters for a particular species are relatively similar in different solvents, while the strengths differ. Also, the empirically-fit solvent-independent polarizability parameters [9] used for each atom in the chloroform pair-potential model [28] compare reasonably to our *ab initio* parameters for *C* and *Cl*, but significantly underestimate the response at the *H* site.

The procedures outlined above for extracting basic microscopic information from *ab initio* calculations of a single solvated solvent molecule are highly detailed and do employ least-squares fitting and some simplifications (such as assuming each site is isotropic). However, if the appropriate approximations are carefully chosen, the result is a powerful tool which is completely generalizable to any type of fluid molecule. Even if experimental or molecular dynamics data is not available to benchmark a particular solvent, these techniques extract the key information required to construct a free energy functional.

5.4 Summary

This chapter builds on the rigid molecule framework of Chapter 4 and extends the scalar-EOS excess functional ansatz to other solvents. Adding molecular

polarizability modes to the dielectric perturbation terms in the functional, and replacing the scaled mean-field correlation ansatz with a weighted polarization-density correlation functional constrained to the static and high frequency dielectric constants, enables the extension of this approach to less polar and non-polar solvents such as chloroform and carbon tetrachloride. Electronic density-functional calculations on a single solvent molecule constrain the molecular geometry, site charge profiles and site polarizability functions. This eliminates the dependence on molecular dynamics pair potential models of the solvent and enables a classical density functional description that relies only on experimental bulk properties and *ab initio* computed microscopic properties.

The free energy functionals developed here form the basis for the fluid terms in joint density-functional solvated electronic-structure calculations [91]. The remainder of this dissertation utilizes the insights gained in constructing this joint density-functional approximation to construct minimally-empirical simplified solvation models.

CHAPTER 6

POLARIZABLE CONTINUUM MODELS WITH NONLINEAR DIELECTRIC AND IONIC RESPONSE [1]

The previous chapters develop accurate free energy functional approximations for liquids, which when coupled to electronic structure methods within the framework of joint density-functional theory, enable a quantum mechanical description of solvated systems without the need for thermodynamic phase-space sampling. The resulting methods [91] are much less computationally demanding than standard molecular dynamics methods, but are still an order of magnitude more expensive than Kohn-Sham electronic density-functional calculations that ignore the solvent.

Polarizable continuum models (PCM's) [163] are a class of highly efficient simplified theories which capture the effect of the fluid by placing the electronic system in an appropriately chosen dielectric cavity, optionally with corrections for physical effects such as cavity formation energies and dispersion interactions. The overhead for computing solvation corrections is negligible in these approaches and they are ideally suited to study complex solvated systems where computational cost is the limiting factor. However, the efficiency of these models typically comes at the cost of empiricism and a loss of key physical features of the fluid.

The empiricism of PCM approaches has been partially mitigated by con-

[1] Preprint online as 'D. Gunceler, K. Letchworth-Weaver, R. Sundararaman, K.A. Schwarz and T.A. Arias, *arXiv*:**1301.6189**', and under review at *Mod. Sim. Mat. Sci. Eng.*. RS developed the theory for nonlinear dielectric response and co-developed the theory for nonlinear ionic fluids with KLW. DG performed the solvation fits and the ionic surface calculations. KLW suggested the study of the ionic surfaces and performed the metal surface calculations. KAS provided the chemistry insights, and co-wrote much of the paper with RS.

structing variants of the model [130, 90] that are highly simplified approximations within the framework of JDFT. So far, PCM approximations [130, 90, 40, 8] have replaced the fluid with a linear dielectric response which turns out to be adequate for the solvation of most molecules and some surfaces, such as those of metals. However, the highly polar surfaces typical of electrochemical systems impose strong electric fields on solvents that invoke a highly nonlinear response; linear response approximations lead to qualitatively incorrect results as we demonstrate in Section 6.2.4.

This chapter presents a systematic framework (Section 6.1.1) for developing PCM-like approximations within joint density-functional theory, and uses it to construct a nonlinear polarizable continuum model (Sections 6.1.3 and 6.1.4) that is both inexpensive and sufficiently accurate to account for complex reactions, including those occurring on ionic surfaces. We show that the nonlinear dielectric model reproduces molecule solvation energies (Section 6.2.2), and with the inclusion of nonlinear ions, potentials of zero charge for metallic surfaces (Section 6.2.3) with accuracy similar to that of the linear model. Finally, we demonstrate that the inclusion of nonlinear dielectric saturation effects facilitates accurate predictions for the free energies of ionic surfaces in solution (Section 6.2.4).

6.1 Theory

6.1.1 Joint density-functional theory framework for PCM's

Joint density-functional theory establishes an exact variational principle for the free energy of a solvated system in terms of the equilibrium electron density

of the solute and the nuclear densities of the solvent. So far, we split this free energy as (1.17) and approximated the electronic density-functional, classical density-functional and coupling terms independently.

The use of a classical density-functional theory for the liquid within JDFT is a powerful tool for studying solvated electronic systems. However, the complexity of the theory can occasionally obscure an intuitive physical interpretation of the results. This intuition may be better obtained from simpler and possibly less accurate versions of the theory that capture the bare minimum of physical effects required to describe the systems and properties of interest.

Polarizable continuum models (PCM) are highly simplified theories that account for liquid effects by embedding the electronic system in a dielectric cavity. The linear response approximation in PCM, however, is inadequate for the study of electrochemical systems that involve liquids in strong electric fields. Here, we develop a general framework for constructing PCM-like approximations within joint density-functional theory, which we use in the following sections to construct a nonlinear PCM with the same optimizable parameters as those of the linear model.

We start by dividing the liquid contributions to the free energy functional into physical effects assumed to be separable in polarizable continuum models, and rewrite the last two terms of (1.17) in the following form

$$\begin{aligned} A_{\text{diel}} &\equiv \Phi_{\text{lq}} + \Delta A \\ &= A_\epsilon[s, \vec{\mathcal{E}}] + A_\kappa[s, \{\eta_i\}] + \int d\vec{r} \int d\vec{r}' \frac{\rho_{\text{lq}}(\vec{r}')}{|\vec{r} - \vec{r}'|} \left(\rho_{\text{el}}(\vec{r}) + \frac{\rho_{\text{lq}}(\vec{r})}{2} \right) + A_{\text{cav}}[s]. \end{aligned} \tag{6.1}$$

Dielectric response dominates the electrostatic interaction of a fluid consisting of neutral molecules alone, and the first term A_ϵ captures the corresponding in-

ternal energy. In addition to neutral solvent molecules, electrolytes typically include charged ions that contribute an additional monopole response. The optional term, A_κ, accounts for the internal energy of the ions if present in the solution. The densities of the molecules and ions of the solvent are modulated by the cavity shape function $s(\vec{r})$, which in turn is determined by the electron density $n(\vec{r})$.

The third term of (6.1) is the mean field electrostatic interaction of the liquid bound charge density ρ_{lq} with itself and the electronic system of total charge density ρ_{el}. Here, $\rho_{\text{lq}} \equiv \rho_\epsilon + \rho_\kappa$ includes dielectric and ionic contributions, while $\rho_{\text{el}} \equiv n + \rho_{\text{nuc}}$ includes contributions from the electrons and the nuclei (or pseudopotential cores) of the subsystem treated using electronic density-functional theory. The contributions from all remaining effects of the fluid, such as cavity formation and dispersion, are gathered into the final term of (6.1), A_{cav}, and are assumed to depend only on the shape of the cavity $s(\vec{r})$. We detail specific approximations for each of these terms in the following subsections.

So far, the dielectric and ionic responses are still fully general, except for the mean-field assumption in their interaction with each other and the electronic system. In reality, these responses are nonlinear as well as nonlocal, while conventional polarizable continuum models [130, 163, 90, 40, 8] assume both linearity and locality. In this chapter, we retain the local response approximation, but develop a nonlinear theory for the microscopic dielectric and ionic response in Sections 6.1.3 and 6.1.4 respectively. We obtain a linear PCM comparable to [90] and [8] in Section 6.1.5 as the low-field limit of our general nonlinear theory. Chapter 8 presents a PCM that incorporates the nonlocal response of the solvent.

6.1.2 Cavity shape function $s(\vec{r})$, and dependent energy $A_{\mathbf{cav}}$

Polarizable continuum models replace the liquid by a dielectric cavity surrounding the electronic system. In variants of the model suitable for treating solid surfaces (which typically require a plane-wave basis), the dielectric constant is smoothly switched from the vacuum value of 1 to the bulk static dielectric constant of the liquid, ϵ_b [130, 90, 40, 8]. The spatial modulation of the dielectric constant may be written as $\epsilon(\vec{r}) = 1 + (\epsilon_b - 1)s(\vec{r})$, so that $s(\vec{r}) \in [0, 1]$ describes the shape of the cavity.

Further, these variants of PCM assume that the cavity shape $s(\vec{r}) = s(n(\vec{r}))$ is determined entirely by the local electron density. The exact functional form of $s(n)$ is not important so long as it switches smoothly between 0 at high electron densities and 1 at low electron densities, and rapidly approaches the extreme values away from the transition region. Following [130], we here use

$$s(n) = \frac{1}{2}\mathrm{erfc}\frac{\ln(n/n_c)}{\sigma\sqrt{2}} \tag{6.2}$$

where the parameter n_c sets the critical electron density around which the cavity smoothly 'switches on', and σ controls the width of that transition.[2]

In the following subsections, we develop an *ab initio* theory for the nonlinear dielectric and ionic response of solvents, which we find to be the dominant effects at the charged or highly polar surfaces in electrochemical systems because of the strong electric fields. The cavity shape function, however, includes unknown parameters that are typically fit [163, 8] to reproduce the solvation energies of small organic molecules. These solvation energies are sensitive to

[2]This functional form is not derived from underlying physical principles and is chosen purely for its numerical properties: smoothness and rapid approach to 0 and 1 away from the transition region; others [40, 8] have successfully employed other functional forms satisfying these properties.

other free energy contributions such as cavity formation and dispersion, which although negligible in the electrochemical systems of interest, cannot be ignored during the determination of fit parameters.

These additional free energy contributions have complicated dependences on the shape of the cavity, for which several empirical approximations have been developed (see [163] for a review). Andreussi and coworkers [8] demonstrated that a simple empirical model expressing the sum of all these effects as an effective surface tension for the cavity works reasonably well for the solvation energies of small organic molecules. Since we need the additional effects only as auxiliary contributions during the fit to the molecular solvation data, we adopt their simplified model here by writing

$$A_{\text{cav}}[s] = \tau \underbrace{\int d\vec{r} \left|\vec{\nabla} s\right|}_{S}, \tag{6.3}$$

where S is a surface area estimate for the cavity described by $s(\vec{r})$, and τ is the effective surface tension that is determined by fitting to solvation energies.

6.1.3 Nonlinear dielectric internal energy, A_ϵ

The dielectric response of liquids includes contributions from molecular polarizability as well as rotations of molecules with permanent dipole moments. The response of highly polar solvents such as water is dominated by rotations. With increasing field strength, the molecular dipoles increasingly align with the electric field, eventually saturating the rotational response. The polarizability response, which includes electronic polarizability and vibrations of the molecules, typically becomes stronger at higher fields. It is therefore important to consider

all these contributions even for solvents whose linear response is dominated by rotations.

The typical electric fields encountered in solvation can significantly saturate the rotational response of solvents, but are usually insufficient to access the nonlinear regime of the remaining contributions. We therefore split the internal energy of the dielectric A_ϵ into rotational $A_{\rm rot}$ and polarization $A_{\rm pol}$ parts, and construct a nonlinear theory for the rotational part alone.

Within the polarizable continuum ansatz, the liquid consists of molecules distributed with the bulk density $N_{\rm mol}$ modulated by the cavity shape function $s(\vec{r})$. The internal energy corresponding to linear polarization response with an effective isotropic molecular dipole polarizability,[3] $\chi_{\rm mol}$, is

$$A_{\rm pol}[\vec{P}_{\rm pol}] = \int d\vec{r} N_{\rm mol} s(\vec{r}) \frac{\vec{P}^2_{\rm pol}(\vec{r})}{2\chi_{\rm mol}}, \tag{6.4}$$

where $\vec{P}_{\rm pol}(\vec{r})$ is the induced dipole moment per molecule. This dipole moment contributes a bound charge, $\rho_{\rm pol}(\vec{r}) = -\vec{\nabla}\cdot(N_{\rm mol} s(\vec{r})\vec{P}_{\rm pol}(\vec{r}))$.

Physically, the nonlinearity of the rotational response arises from a competition between the rotational entropy of the molecules and their interaction with the self-consistent electric field. We therefore begin with the exact rotational entropy for an ideal gas of dipoles with the cavity-prescribed density $N_{\rm mol} s(\vec{r})$ at temperature T, then approximate rotational correlations, and write

$$A_{\rm rot}[p_{\hat{e}}, l] = \int d\vec{r} T N_{\rm mol} s(\vec{r}) \left[\int \frac{d\hat{e}}{4\pi} p_{\hat{e}} \ln p_{\hat{e}} - l(\vec{r}) \left(\int \frac{d\hat{e}}{4\pi} p_{\hat{e}} - 1 \right) - \frac{\alpha \vec{P}^2_{\rm rot}(\vec{r})}{2} \right]. \tag{6.5}$$

[3] Each molecule in the fluid responds to a local electric field which is enhanced relative to the mean electric field, for example, the field enhanced by a dielectric cavity in the Clausius-Mossotti picture (see Section 5.2 for details). Here, $\chi_{\rm mol}$, the response to mean electric fields, is constrained to the bulk optical dielectric constant in (6.8), includes the field enhancement factors (Table 5.2) relative to the actual dipole polarizability, and is therefore an effective polarizability.

Here, $p_{\hat{e}}(\vec{r})$ is the probability that a molecule at location $\vec{r}$ has its dipole oriented along unit vector $\hat{e}$, the second term of (6.5) constrains the normalization of $p_{\hat{e}}(\vec{r})$ with Lagrange multiplier field $l(\vec{r})$, and the final term describes correlations with an as yet undetermined prefactor α.

The final term of (6.5) captures the correlations in dipole rotations within a 'local polarization density approximation (LPDA)'. We choose the simplest possible form for this correction, quadratic in the local dimensionless polarization $\vec{P}_{\text{rot}}(\vec{r}) = \int \frac{d\hat{e}}{4\pi} p_{\hat{e}}(\vec{r})\hat{e}$, and constrain the prefactor α to reproduce the bulk linear dielectric constant ϵ_b. Finally, the rotational response contributes a bound charge $\rho_{\text{rot}}(\vec{r}) = -\vec{\nabla}\cdot(p_{\text{mol}}N_{\text{mol}}s(\vec{r})\vec{P}_{\text{rot}}(\vec{r}))$ within the local response approximation, where p_{mol} is the permanent molecular dipole moment.

The Euler-Lagrange equation for minimizing the total free energy with respect to $p_{\hat{e}}$ implies that, at equilibrium, the orientation distribution must be of the form $p_{\hat{e}} \propto \exp(\vec{\varepsilon}\cdot\hat{e})$ for some vector field $\vec{\varepsilon}(\vec{r})$. Using the remaining Euler-Lagrange equations to eliminate $\vec{P}_{\text{pol}}(\vec{r})$ and $l(\vec{r})$ in favor of $\vec{\varepsilon}(\vec{r})$, the sum of (6.4) and (6.5) simplifies to

$$A_\epsilon[\vec{\varepsilon}(\vec{r})] = \int d\vec{r} T N_{\text{mol}} s(\vec{r}) \left[\varepsilon^2 \left(f(\varepsilon) - \frac{\alpha}{2} f^2(\varepsilon) + \frac{X}{2}(1-\alpha f(\varepsilon))^2 \right) - \ln \frac{\sinh\varepsilon}{\varepsilon} \right], \quad (6.6)$$

with corresponding dielectric bound charge

$$\rho_\epsilon(\vec{r}) = -\vec{\nabla}\cdot\left[p_{\text{mol}}N_{\text{mol}}s(\vec{r})\vec{\varepsilon}\,(f(\varepsilon) + X(1-\alpha f(\varepsilon)))\right]. \quad (6.7)$$

Here, $f(\varepsilon) = (\varepsilon\coth\varepsilon - 1)/\varepsilon^2$ is the effective dimensionless rotational susceptibility defined by $\vec{P}_{\text{rot}} = f(\varepsilon)\vec{\varepsilon}$, and $X \equiv \chi_{\text{mol}}T/p_{\text{mol}}^2$ is its counterpart for the linear polarization response.

The resulting theory for the dielectric has four solvent-dependent parameters (N_{mol}, p_{mol}, X and α), of which the bulk molecular density, N_{mol}, is di-

rectly measurable. The effective molecule dipole moment in the liquid, p_{mol}, differs from the gas-phase value, and in principle, can be determined from measurements of the lowest order nonlinear response coefficient [47]. However, such measurements are difficult and not readily available for most solvents. Instead, we compute p_{mol} as the self-consistent dipole moment of a single solvent molecule in a solvated *ab initio* calculation employing a nonlinear polarizable continuum description of the same solvent. The resulting dipole moment for the solvents used in this work are listed in Table 6.3. Note that p_{mol} is larger than the gas phase dipole moment for all these solvents because charged centers in the molecule are surrounded by bound charges of the opposite sign which favor an increase in the polarization, as shown for water in Figure 6.2. We also find that for water, $p_{\mathrm{mol}} = 0.94ea_0$ gratifyingly agrees with the SPC/E molecular dynamics model value of $0.92ea_0$ [15], in contrast to the gas phase value of $0.73ea_0$.

The remaining solvent-dependent parameters, the correlation factor for rotations α and the combination $X \equiv \chi_{\mathrm{mol}} T/p_{\mathrm{mol}}^2$, are constrained to reproduce the bulk static and high frequency dielectric constants, ϵ_b and ϵ_∞ respectively. Using the bulk linear response of the above functional, we can analytically show that

$$X = \frac{T(\epsilon_\infty - 1)}{4\pi N_{\mathrm{mol}} p_{\mathrm{mol}}^2} \quad \text{and} \quad \alpha = 3 - \frac{4\pi N_{\mathrm{mol}} p_{\mathrm{mol}}^2}{T(\epsilon_b - \epsilon_\infty)}, \tag{6.8}$$

since the rotational response freezes out and does not contribute to ϵ_∞. In principle, ϵ_∞ should be the dielectric constant at infrared frequencies between the rotational and vibrational resonances, but in the absence of experimental data in that frequency regime, we use the readily measurable optical dielectric constant, which is the square of the refractive index.

We have therefore produced a density-functional theory for the nonlinear

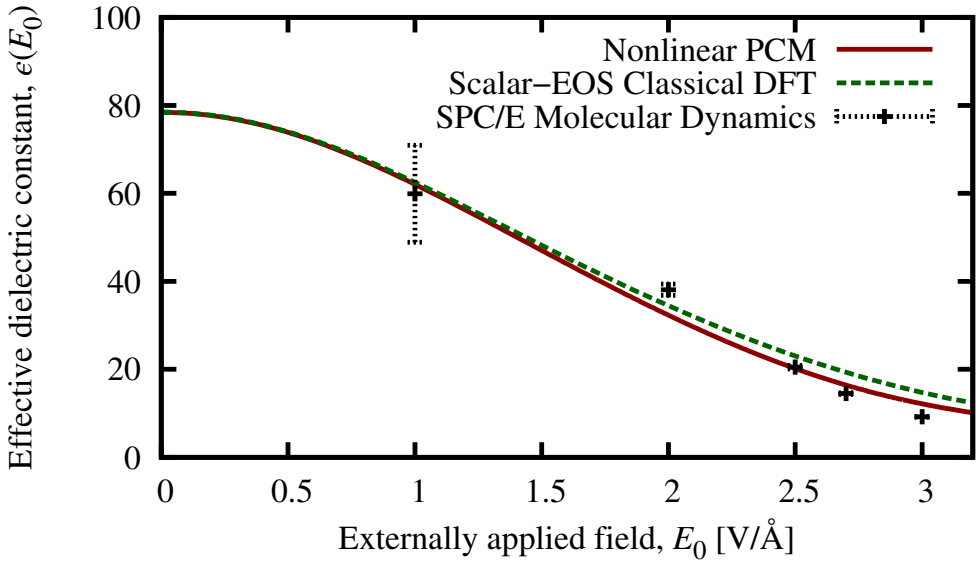

Figure 6.1: Comparison of the effective dielectric constant of water as a function of uniform externally applied field E_0 for the nonlinear PCM model (6.6) compared to SPC/E molecular dynamics results [178] and classical density functional predictions (Chapter 4). The effective dielectric constant is defined by $\epsilon = E_0/E$, where $E = E_0 - 4\pi P$ is the net electric field including the screening due to the dielectric polarization density P. Within this theory, this response is determined entirely by bulk liquid properties ϵ_b, ϵ_∞ and $N_{\rm mol}$, along with the molecule dipole moment $p_{\rm mol}$ obtained from a self-consistent ab initio calculation solvated with the present model.

dielectric response of an arbitrary solvent constrained entirely by measurable macroscopic properties. The response at field strengths relevant for solvation is not accessible experimentally,[4] but it has been estimated using molecular dynamics. Figure 6.1 demonstrates that the bulk nonlinear dielectric response of the present theory is in excellent agreement with molecular dynamics results for water[178] using the SPC/E pair potential model [15]. The present theory, which uses LPDA for rotational correlations, produces essentially the same non-

[4]The present approach does not account for dielectric breakdown, which is typically caused by the acceleration of small concentrations of charge carriers by strong fields to energies large enough to free more carriers, resulting in an avalanche. Moreover, the high electric fields surrounding molecules and surfaces in solution are microscopic (few Å), and their net potential difference is small (few Volts) and therefore insufficient to cause dielectric breakdown.

linear response to uniform electric fields as classical density functional theories with the scaled mean-field electrostatics approximation [97]. The minor differences between the present theory and the classical density functional results (Chapter 4) shown in Figure 6.1 are due to electrostriction; the latter theory accounts for changes in the equilibrium fluid density in the presence of a strong uniform electric field.

6.1.4 Nonlinear ionic system internal energy, A_κ

The previous section derived the dielectric response of liquids from the dipolar rotational and polarization response of liquid molecules to the local electric field. Ionic species in the liquid introduce Debye screening by contributing an additional monopolar response, which changes the local ionic density in response to the local electric potential. A simple description of this response at the linearized Poisson-Boltzmann level suffices for many electrochemical systems [90]. For the electrode-electrolyte interface, this level of theory corresponds roughly to the Gouy-Chapman-Stern model, but misses the nonlinear capacitance effects due to ion adsorption. Here, we explore whether a full Poisson-Boltzmann treatment within the polarizable continuum model ansatz captures these additional details.

To represent the internal free energy of an ionic system comprising several species of charge Z_i and bulk concentrations N_i each, we employ the exact expression for the ideal gas of point particle ions, approximating finite-size effects

with a local density approximation, and write

$$A_\kappa[\{\eta_i(\vec{r})\}] = T\sum_i \int d\vec{r} N_i s(\vec{r}) \Big[\underbrace{(\eta_i(\ln\eta_i - 1) + 1)}_{\text{Ideal gas}} + \underbrace{\frac{(x(\vec{r}) - x_0)^2}{x_0(1-x_0)^2(1-x(\vec{r}))^2}}_{\text{Hard sphere}} \Big]. \quad (6.9)$$

The density of each ionic species is $N_i s(\vec{r})\eta_i(\vec{r})$, represented in terms of the enhancement $\eta_i(\vec{r})$ relative to the cavity prescription of $N_i s(\vec{r})$. The charge-weighted sum of these densities contribute a net ionic bound charge $\rho_\kappa = \sum_i Z_i N_i s(\vec{r})\eta_i(\vec{r})$.

The first ideal gas term in (6.9) along with the mean-field electrostatic interaction in the third term of (6.1) correspond to the Poisson-Boltzmann theory. That theory, however, does not limit the density of the ions in solution and presents an unphysical instability associated with an infinite build-up of ions at regions of strong external potential. We resolve this instability by enforcing a packing limit on the ions via the second term of (6.9). This term captures local hard sphere correlations in terms of the packing fraction $x(\vec{r}) = \sum_i V_i N_i \eta_i(\vec{r})$, where $V_i = 4\pi R_i^3/3$ is the volume per ion for each species (with ionic radius R_i). The functional form of this term is constrained to reproduce $x(\vec{r}) \to x_0 \equiv \sum_i V_i N_i$ in the bulk and to match the divergence in the equation of state of the hard sphere fluid [23] as $x(\vec{r}) \to 1$.

6.1.5 Linear limit

The free energy functional (6.1) with dielectric free energy A_ϵ given by (6.6) and optional ionic free energy A_κ given by (6.9) constitutes our nonlinear polarizable continuum model. Here, we show that the conventional linear polarizable continuum model is a limit of this more general theory.

The rotational response from the dielectric is approximately linear when the energy scale of the molecular dipoles interacting with the field is much lower than the temperature ($p_{\text{mol}}|\vec{\nabla}\phi| \ll T$), where $\phi(\vec{r})$ is the total electrostatic potential. Similarly, the ionic response is approximately linear when $Z|\phi| \ll T$. Using the Euler-Lagrange equations to eliminate $\vec{\varepsilon}(\vec{r})$ and $\eta_i(\vec{r})$ in favor of $\vec{\nabla}\phi(\vec{r})$ and $\phi(\vec{r})$ respectively, expanding the free energy to quadratic order, and simplifying using (6.8) and the definition $\kappa^2 \equiv 8\pi N_{\text{ion}} Z^2/T$, we find

$$A_\epsilon + A_\kappa = \frac{1}{4\pi}\int d\vec{r}\, s(\vec{r})\left[(\epsilon_b - 1)\frac{|\vec{\nabla}\phi|^2}{2} + \kappa^2\frac{\phi^2}{2}\right], \tag{6.10}$$

with the corresponding total bound charge at linear order

$$\rho_{\text{lq}}(\vec{r}) = \frac{1}{4\pi}\left[(\epsilon_b - 1)\vec{\nabla}\cdot(s(\vec{r})\vec{\nabla}\phi) - \kappa^2 s(\vec{r})\phi\right]. \tag{6.11}$$

The Euler-Lagrange equation for this simplified linear-response functional in terms of the single independent variable, ϕ, can be rearranged into the familiar modified Poisson equation (or Helmholtz equation for non-zero κ)

$$\vec{\nabla}^2\phi(\vec{r}) + (\epsilon_b - 1)\vec{\nabla}\cdot(s(n(\vec{r}))\vec{\nabla}\phi(\vec{r})) - \kappa^2 s(n(\vec{r}))\phi(\vec{r}) = -4\pi\rho_{\text{el}}(\vec{r}). \tag{6.12}$$

Finally, substituting the solution of (6.12) in the fluid free energy functional (6.1) with the dielectric and ionic energies given by (6.10), yields an equilibrium value for A_{diel} in the linear limit

$$A_{\text{diel}}^{(\text{linear})} = A_{\text{cav}} + \frac{1}{2}\int d\vec{r}\,\rho_{\text{el}}(\vec{r})\left(\phi(\vec{r}) - \int d\vec{r}'\,\frac{\rho_{\text{el}}(\vec{r}')}{|\vec{r} - \vec{r}'|}\right). \tag{6.13}$$

Thus, the free energy functional approach to polarizable continuum models reduces, in the linear limit, to the standard approach [90, 8] of replacing the vacuum Poisson equation with one modified by the fluid.

6.1.6 Periodic systems and net charge

An important class of applications of the nonlinear polarizable continuum model, and joint density-functional theory in general, is the study of electrochemical systems. These systems pose an interesting challenge as they often involve charged metal or doped semiconducting surfaces. The periodic boundary conditions necessary to accurately describe the delocalized electronic states of such systems complicate the addition of charge, since the energy per unit cell of a periodic system with net charge per unit cell is divergent.

Including a counter electrode [118] to keep the simulation cell neutral avoids this problem, but leads to wasted computational effort on irrelevant portions of the system and complicates the separation of physics at the two electrodes. Introducing Debye screening due to ions in the electrolyte neutralizes the unit cell with fluid bound charge and naturally captures the physics of the electrochemical double layer [90]. More importantly, unlike the Poisson equation obtained without ionic screening, the Helmholtz equation for the electrostatic potential with screening (6.12) has a well-defined constant offset ('zero' of potential) in periodic boundary conditions. The resulting Kohn-Sham eigenvalues, and hence the electron chemical potential, correspond to a zero reference point deep within the fluid, and this enables calibration of the electron chemical potential in DFT against electrochemical reference electrodes. (See [90] for details.)

The electrostatic potential in the nonlinear polarizable continuum model is not obtained from a Helmholtz equation, and the bound charge in the ionic system does not neutralize a net charge in the electronic system at an arbitrary value of the independent variables $\eta_i(\vec{r})$. Here, we present the modifications required to correctly handle periodic systems within the nonlinear ionic screening

model.

The mean-field Coulomb energy per unit cell of volume Ω for the entire system with total charge density $\rho_{\text{tot}} = \rho_{\text{el}} + \rho_{\text{lq}}$ can be written in the plane-wave basis as $U = \frac{1}{2\Omega}\sum_{\vec{G}} \tilde{K}_{\vec{G}} |\tilde{\rho}_{\text{tot}}(\vec{G})|^2$. Here, $\tilde{\rho}_{\text{tot}}(\vec{G}) = \int_\Omega d\vec{r}\rho_{\text{tot}}(\vec{r}) \exp(-i\vec{G}\cdot\vec{r})$ for reciprocal lattice vectors $\vec{G}$, and $\tilde{K}_{\vec{G}} = 4\pi/G^2$ is the plane-wave basis Coulomb kernel. The divergent contribution at $G = 0$ vanishes for neutral unit cells with $Q_{\text{tot}} \equiv \tilde{\rho}_{\text{tot}}(0) = 0$.

The G^{-2} divergence results from the long-range $1/r$ tail of the Coulomb kernel. We can analyze the effect of the divergence by making the Coulomb kernel short-ranged on a length scale L much larger than the unit cell, and set $L \to \infty$ at the end. The exact form of the regularization is not important; picking the Gaussian-screened potential $\text{erfc}(r/L)/r$ (which is also used in the Ewald approach for computing Coulomb energies of periodic arrays of point charges [38]) results in the regularized Coulomb energy

$$U_L = \sum_{\vec{G}\neq 0} \frac{2\pi}{G^2\Omega} |\tilde{\rho}_{\text{tot}}(\vec{G})|^2 + \frac{\pi L^2}{2\Omega} Q_{\text{tot}}^2. \tag{6.14}$$

Note that the first term employs the standard Coulomb kernel in the plane-wave basis which drops the $G = 0$ term by invoking a neutralizing background, and the second term contains the divergent part depending only on the total charge per unit cell.

At finite but large L, the second term of U_L penalizes $Q_{\text{tot}} \neq 0$ and favors equilibrium configurations with small Q_{tot}. The Euler-Lagrange equation for the net charge Q_{tot} is $\lambda \equiv \partial A/\partial Q_{\text{tot}} = -\pi L^2 Q_{\text{tot}}/\Omega$, where A is the total free energy excluding the divergent second term of (6.14). Note that $\partial A/\partial Q_{\text{tot}}$ is finite for systems capable of adjusting their total charge, such as fluids with ionic screening, so

that as $L \to \infty$, $Q_{\text{tot}} \to 0$ in such a manner that $\lambda \propto Q_{\text{tot}} L^2$ remains finite. The absolute potential is also well defined in this situation with a $G = 0$ contribution of $\partial U_L / \partial Q_{\text{tot}} = \pi L^2 Q_{\text{tot}} / \Omega = -\lambda$. Finally, note that

$$U_\infty = \sum_{\vec{G} \neq 0} \frac{2\pi}{G^2 \Omega} |\tilde{\rho}_{\text{tot}}(\vec{G})|^2 - \lambda Q_{\text{tot}} \tag{6.15}$$

results in the same Euler-Lagrange equation and equilibrium free energy as (6.14) in the $L \to \infty$ limit, and therefore the divergent term in the Coulomb energy reduces to a charge-neutrality constraint imposed by Lagrange multiplier λ.[5]

We incorporate this Lagrange multiplier constraint into the ionic free energy in plane-wave calculations, and retain the standard plane-wave Coulomb kernel with $G = 0$ projected out for all electrostatic interactions. The constraint can be solved analytically for local nonlinear ions (Section 6.1.4) in the commonly encountered case of a 'Z:Z' electrolyte consisting of two species of charge $+Z$ and $-Z$ (labeled with indices $i = +, -$) with bulk concentrations N_{ion} each. In this situation, we can show that substituting $\eta_\pm(\vec{r}) = \exp(\pm(\mu_0 + \mu_\pm(\vec{r})))$, where $\mu_0 \equiv -Z\lambda/T$ is obtained by solving the neutrality constraint, reduces the constrained minimization over $\eta_\pm(\vec{r})$ to an unconstrained minimization over $\mu_\pm(\vec{r})$. In particular, the neutrality constraint $Q_+ e^{\mu_0} + Q_- e^{-\mu_0} + Q_{\text{el}} = 0$ yields

$$\mu_0 = \ln \frac{\sqrt{Q_{\text{el}}^2 - 4Q_+Q_-} - Q_{\text{el}}}{2Q_+}, \tag{6.16}$$

where $Q_\pm \equiv \pm N_{\text{ion}} Z \int d\vec{r} s(\vec{r}) e^{\pm\mu(\vec{r})}$ and $Q_{\text{el}} \equiv \int d\vec{r} \rho_{\text{el}}(\vec{r})$ is the total charge of the electronic system. In this case, and for other joint density-functional theories

[5] As noted in Section 1.4, the grand canonical ensemble with charged particles is constrained to include only overall neutral configurations, but with different individual particle numbers. Within this ensemble, the chemical potential of one charged species is dependent on the rest so as to maintain neutrality, which here is enforced by the Euler-Lagrange equation with respect to the Lagrange multiplier λ.

which include ionic screening, the constraint contribution to $\delta A_{\text{diel}}/\delta\rho_{\text{el}}(\vec{r})$ in the electron potential establishes the absolute reference for the Kohn-Sham eigenvalues and the electron chemical potential required for *ab initio* electrochemistry [90].

6.1.7 Implementation

The nonlinear polarizable continuum model presented here and its linear counterpart have been implemented in the open source plane-wave electronic structure software JDFTx [154], designed for joint density-functional theory. The electronic density-functional theory segment of this software is based on conjugate gradients minimization [132] of an analytically continued total energy functional [11], expressed in the DFT++ algebraic formulation [75]. The fluid segment of JDFTx also employs the plane-wave basis and is discretized in the algebraic formulation for classical density-functional theories (Chapter 4).

The valence electron density $n(r)$ needs to be augmented with a core electron density in order to prevent overlap of the fluid with the pseudopotential cores [90]. Hence, we compute the shape function using (6.2) with $n_{\text{cav}}(\vec{r}) = n(\vec{r}) + n_{\text{core}}(\vec{r})$, where n_{core} is the partial core density used for nonlinear core corrections [98].

The electrostatic interactions between the fluid and the material described in the electronic structure portion of the calculation, involve the total charge density (both electronic and nuclear) of the latter, $\rho_{\text{el}}(\vec{r}) = n(\vec{r}) + \rho_{\text{nuc}}(\vec{r})$. Here,[6] the nuclear charge density, $\rho_{\text{nuc}}(\vec{r}) = -\sum_i Z_i e^{-(\vec{r}-\vec{r}_i)^2/(2w^2)}/(2\pi w)^{3/2}$ is widened by a

[6]Note that we employ an electron-is-positive charge convention, so that $\rho_{\text{nuc}} < 0$ and the charge of the electron is +1 in atomic units.

Gaussian resolvable on the charge density grid. The widened nuclear density is used only in the interaction with the fluid; the internal energies of the electronic system employ point nuclei in all terms. This width does not affect the interaction energy since the fluid and nuclear charge densities do not overlap, and the nuclear charge is spherically symmetric. However, it shifts the potential relative to the zero-width case, which we compensate for exactly by adding the correction $-2\pi w^2 \sum_i Z_i/\Omega$ to the electron potential, where Ω is the unit cell volume.

Finally, regarding algorithms, the linear polarizable continuum models are minimized by solving the Helmholtz (or Poisson) equation (6.12) at every electronic iteration. Appropriate preconditioners for the involved linear conjugate gradients solver have been developed previously [90]. The free energy of the nonlinear polarizable continuum model is minimized using the Gummel iteration [54], where the electronic system and the fluid are alternately minimized while holding the state of the other one frozen. This method is guaranteed to be globally convergent because of the variational principle, and typically converges adequately in 5-10 alternations for most systems studied. The fluid free energy A_{diel} is minimized with the scalar fields $\eta_i(\vec{r})$ and vector field $\vec{\varepsilon}(\vec{r})$ as independent variables; the diagonal preconditioner in reciprocal space [7]

$$K_\eta(\vec{G}) = \left[\frac{Z(1-\alpha/3)}{p_{\text{mol}}}\right]^2 \frac{G^2}{(G^2+\kappa^2/\epsilon_b)^2} \tag{6.17}$$

for the η channels with the identity preconditioner on the $\vec{\varepsilon}$ channel yields satisfactory convergence for the nonlinear conjugate gradients algorithm [132].

[7] This preconditioner is derived from an approximation to the Hessian of A_{diel} with respect to $\eta_i(\vec{r})$ and $\vec{\varepsilon}(\vec{r})$ in the bulk linear limit.

6.2 Results

Strong microscopic electric fields at liquid interfaces typical of electrochemical systems necessitate a theory for the nonlinear response of the liquid environment, such as the nonlinear polarizable continuum model of Section 6.1. Section 6.2.2 calibrates the undetermined parameters of this theory against experimental solvation energies of molecules. For these molecules, and for metallic surfaces in Section 6.2.3, we find results comparable to linear PCM's. However, for surfaces of ionic solids in Section 6.2.4, we find that inclusion of nonlinear effects are necessary in order to obtain qualitatively correct results.

6.2.1 Computational Details

We perform all calculations in this chapter using the open source plane-wave density functional software JDFTx [154] at a plane wave cutoff of 30 E_h (1 $E_h \equiv 1$ hartree ≈ 27.21 eV). These calculations employ norm-conserving pseudopotentials generated by the Opium pseudopotential generator [117] with the PBE exchange and correlation functional [128]. The pseudopotentials for metal atoms include partial core corrections [98], which are necessary to prevent the overlap of the fluid density with the pseudopotential cores, as described in Section 6.1.7.

The choice of exchange-correlation functional for molecular and surface systems is not straightforward [101], and some argue that semi-local approximations can be inadequate for these systems [16]. Hybrid functionals which include exact exchange, or quantum Monte Carlo methods, are likely to be more accurate but are significantly more expensive than semi-local methods

and hence unsuitable for rapid screening calculations. Here, we use the semi-local revTPSS exchange-correlation functional [129] which shows considerable promise for accurate calculations of surface phenomena including surface formation energies and molecular adsorption energies [151].

Molecular geometries for the calculations of Section 6.2.2 are from the Computational Chemistry Comparison and Benchmark Database [115]. The surface geometries employed in Sections 6.2.4 and 6.2.3 are constrained to the optimized bulk geometry for the central layer, while the remaining layers are fully relaxed for both the vacuum and fluid calculations. The fluid models assume room temperature, $T = 298$ K, for all calculations.

6.2.2 Calibration to molecular solvation energies

The nonlinear dielectric response of Section 6.1.3 is completely constrained by *ab initio* and experimentally determined parameters, listed in Table 6.3 for the solvents studied in this chapter. However, the cavity shape function and the cavity formation and dispersion terms, which are integral features of any polarizable continuum model, are unknown microscopic quantities that are typically constrained by a fit to solvation energies. Here, we fit the two unknown cavity parameters for the nonlinear model and its linear limit to the same molecular solvation dataset using the same procedure, in order to facilitate a fair comparison between linear polarizable continuum models and our nonlinear theory.

The molecular solvation dataset must contain experimental data that is both reliable and readily available. Organic molecules solvated in water satisfy this criterion and are commonly used in fitting parameters for polarizable contin-

Table 6.1: Fitted parameters of the nonlinear and linear polarizable continuum models (PCM) and the corresponding RMS errors for solvation energies of the molecules listed in Figure 6.3.

	n_c (a_0^{-3})	τ (E_h/a_0^2)	RMS Error [kcal/mol (mE_h)]
Nonlinear PCM	1.0×10^{-3}	9.5×10^{-6}	0.95 (1.5)
Linear PCM	3.7×10^{-4}	5.4×10^{-6}	1.05 (1.7)

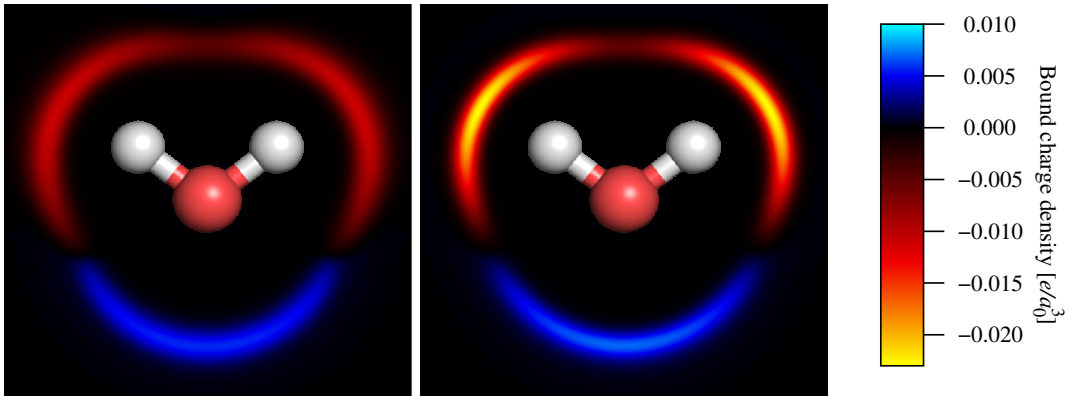

Figure 6.2: Bound charge density in solvent water around a water molecule in the nonlinear and linear models. The smaller hydrogen atoms produce stronger fields on the solvent compared to the oxygen, resulting in much stronger saturation effects in the negative bound charge density surrounding the hydrogens. In spite of the increased bound charge density, the linear model yields approximately the same solvation energy as the nonlinear one because of compensation by the increased cavity size.

uum models [8, 163]. The molecules used in our fit are listed in Figure 6.3, and the known solvent parameters for water are listed in Table 6.3. Of the remaining parameters, we set the shape function width parameter $\sigma = 0.6$ as in [130, 90] since the solvation energies are somewhat insensitive to it. We then determine the cavity transition electron density n_c and the effective cavity surface tension τ by a nonlinear least squares fit to the molecular solvation energy dataset.

The resulting fit parameters and optimized RMS error in solvation energy for the nonlinear and linear versions of the model are summarized in Table 6.1. The

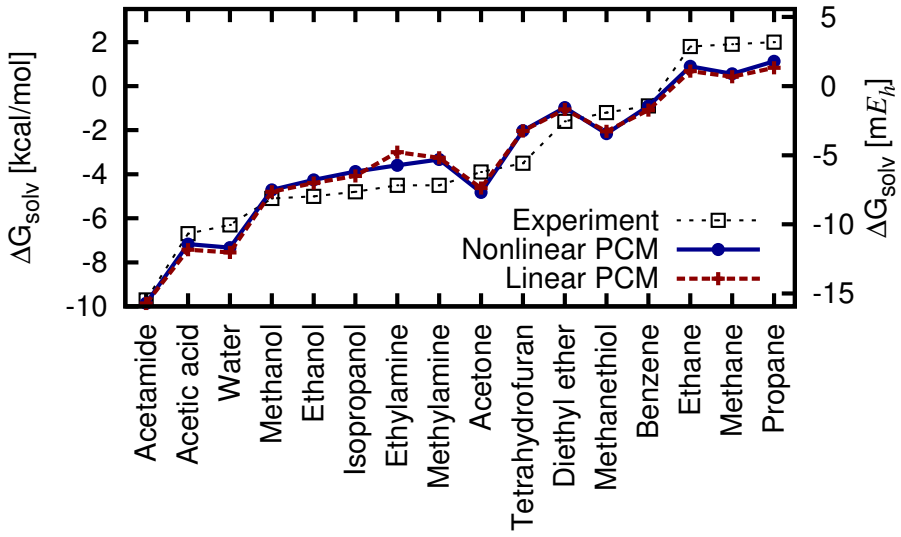

Figure 6.3: Solvation energies of molecules in water predicted by the nonlinear and linear polarizable continuum models compared against the experimental values from [157, 105].

smaller n_c, and hence larger cavities, for the linear model as compared to the nonlinear one offset the overestimation of electrostatic interactions because of the lack of saturation effects. The lowered cavity surface tension τ in the linear model then compensates for the increase in cavity area. Figure 6.2 demonstrates the consequences of these differences in the solvent bound charge density surrounding a water molecule. The solvation energies predicted by the two models are in agreement as seen in Figure 6.3, in spite of significantly larger bound charge densities in the linear case. Because of this cancellation, the linear model yields comparable accuracy to the nonlinear one for the solvation of organic molecules in water, but this is no longer the case when stronger electric fields come into play, as in some of the electrochemical systems we study next.

Table 6.2: Offset between theoretical and experimental PZC's, V_{SHE}, determined by a fit using the systems of Figure 6.4(a), with corresponding RMS errors. V_{SHE} represents the potential difference between an electron solvated deep in the fluid and the Standard Hydrogen Electrode. V_{dip} represents the potential arising from the dipole moment at the fluid-metal interface, and is obtained as the difference between the theoretical PZC and the work function, averaged over the systems considered for each fluid model.

	V_{SHE} (V)	V_{dip} (V)	RMS Error (V)
Nonlinear PCM	4.62	0.46	0.09
Linear PCM	4.68	0.40	0.09

6.2.3 Solvation of metallic surfaces

Unlike the typical electrochemical interface, noble metal electrodes in electrolyte are less prone to complex chemical interactions at the surface, making them suitable candidates for an initial evaluation of our theory. Reactions are highly sensitive to the electron chemical potential, which in experiments is typically reported relative to the standard hydrogen electrode (SHE). The potential of the SHE relative to vacuum is difficult to establish experimentally; the estimates from different experimental methods range from 4.4 V to 4.9 V [165]. To make direct contact with experimental electrochemical observables, this experimentally uncertain quantity can be calibrated [90] in density-functional theory by comparing the theoretical chemical potentials for solvated neutral metal surfaces against the experimental potentials of zero charge (PZC's), which are the measured electrode potentials of neutral surfaces. The calibrations of the reference electrode potential within the linear and nonlinear models are remarkably similar, as shown in Figure 6.4(a) and Table 6.2.

The potential of zero charge includes contributions from the work function, which is essentially independent of the fluid theory, and from the dipole mo-

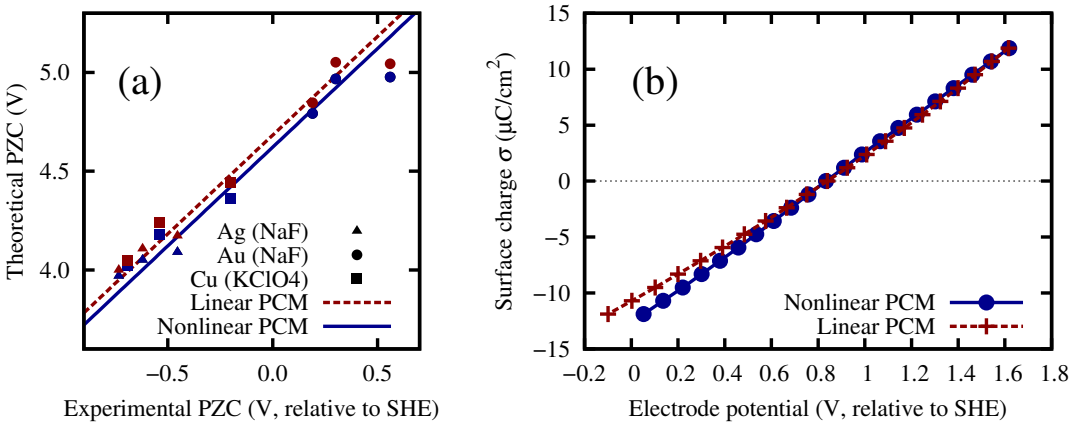

Figure 6.4: (a) Potentials of zero charge (PZC's) for the (111), (100) and (110) surfaces (left to right) each for silver (circles), gold (triangles), and copper (squares), predicted by the nonlinear and linear theories, compared to experiment [165]. The diagonal line for each theory compares theoretical and experimental values up to an overall fitted offset. (See Table 6.2.) The silver and gold surfaces are solvated in aqueous 1 M NaF electrolyte (ionic radii Na: 1.16 Å F: 1.19 Å), while the copper surface is in aqueous 1 M $KClO_4$ electrolyte (ionic radii K: 1.52 Å and ClO_4: 2.26 Å). (b) Charge on a Pt(111) surface in 1 M aqueous $KClO_4$ as a function of potential relative to the standard hydrogen electrode (SHE) for the two theories.

ment in the interfacial layers of the liquid. The minor differences in the calibrations of the two theories stem from this dipole moment contribution, as shown for aqueous electrolytes in Table 6.2. The variation of surface charge with electrode potential is also similar for the two models, as shown for the solvated Pt(111) surface of Figure 6.4(b). In particular, the derivative of that variation, the so-called 'double-layer' capacitance, at the potential of zero charge is 14 and 15 $\mu F/cm^2$ for linear and nonlinear PCM respectively, which agrees well with an experimental estimate of 20 $\mu F/cm^2$ [122] for the above system.

The agreement in the results of the linear and nonlinear theories demonstrated in Figures 6.4(a,b) and Table 6.2 is because of the same cancellation of errors at play for solvation of molecules. The linear theory misses saturation in the rotational dielectric response, thereby overestimating it, yet compensates

with an increase in cavity size. This cancellation of errors is possible since the typical magnitudes of electric fields under typical operating potentials are similar to those of the molecular case, as shown in Figure 6.7.

Both models predict an approximately linear variation of surface charge with electrode potential (Figure 6.4(b)), which corresponds to a constant capacitance. This prediction contrasts with the experimental observation of a capacitance minimum at the potential of zero charge [122] because of ion adsorption on the electrode surface. The formation of this so-called inner Helmholtz layer between the solid surface and the solvent is precluded by the cavity ansatz of polarizable continuum models. These details require either a higher level of theory capable of describing layering effects of ions such as a classical density-functional approach, or the inclusion of explicit ions into the quantum mechanical calculation. Nonetheless, both the linear and nonlinear PCM adequately describe the basic features of the ideal electrochemical interface, and are suitable for describing chemical reactions at metal electrode surfaces so long as all chemical bonds are treated quantum-mechanically.

6.2.4 Solvation of ionic surfaces

The surfaces of electrodes typically contain ionic compounds whose structure and composition vary with the chosen electrolyte and operating conditions. Reactions at the surface of a lithium metal anode, for example, can form Li_2O, LiOH and LiF at the solid electrolyte interface [79, 141]. Here, we study these surfaces in contact with different organic solvents typical of battery systems as a testbed for fluid models applicable to these systems.

Table 6.3: Parameters describing water and commonly used lithium battery solvents, Dimethyl Carbonate (DMC), Tetrahydrofuran (THF), Dimethylformamide (DMF), Propylene Carbonate (PC) and Ethylene Carbonate (EC). The vacuum dipoles (p_{vac}) and self-consistent solvated dipoles p_{mol} are computed using density-functional theory as described in Section 6.1.3. All remaining parameters are constrained by measured bulk properties [148].

Solvent	ϵ_b	ϵ_∞	p_{vac} (ea_0)	p_{mol} (ea_0)	N_{mol} (a_0^{-3})	τ (E_h/a_0^2)
Water	78.4	1.78	0.73	0.94	4.938×10^{-3}	9.5×10^{-6}
DMC	3.1	1.87	0.16	0.16	1.059×10^{-3}	2.05×10^{-5}
THF	7.6	1.98	0.69	0.90	1.100×10^{-3}	1.78×10^{-5}
DMF	38.0	2.05	1.50	2.19	1.153×10^{-3}	2.26×10^{-5}
PC	64.0	2.02	1.97	2.95	1.039×10^{-3}	2.88×10^{-5}
EC	90.5	2.00	1.93	2.88	1.339×10^{-3}	3.51×10^{-5}

The solvents selected for this study are listed in Table 6.3. Because of the dearth of experimental data for corresponding solvation energies, we here use the cavity shape parameters determined by the fit in Section 6.2.2. We replace the effective surface tension τ by the experimental surface tension, ignoring dispersion effects which are insignificant on the scale of the electrostatic energies in these highly polar systems. All remaining physical parameters that determine the dielectric response are constrained by experiment and *ab initio* calculations, as discussed in Section 6.1.3.

The linear and nonlinear models predict similar solvation energies for the aforementioned ionic compounds of lithium in solvents with low dielectric constants, as shown in Figure 6.5. However, with increasing dielectric constant, the magnitude of the solvation energy increases more rapidly for the linear model, leading to disagreement by up to a factor of two for the most polar solvents. The linear model overestimates the electrostatic interaction because of a lack of saturation effects, but unlike the molecular case, the increase in cavity size is insufficient to compensate for this error. In fact, for lithium fluoride in ethy-

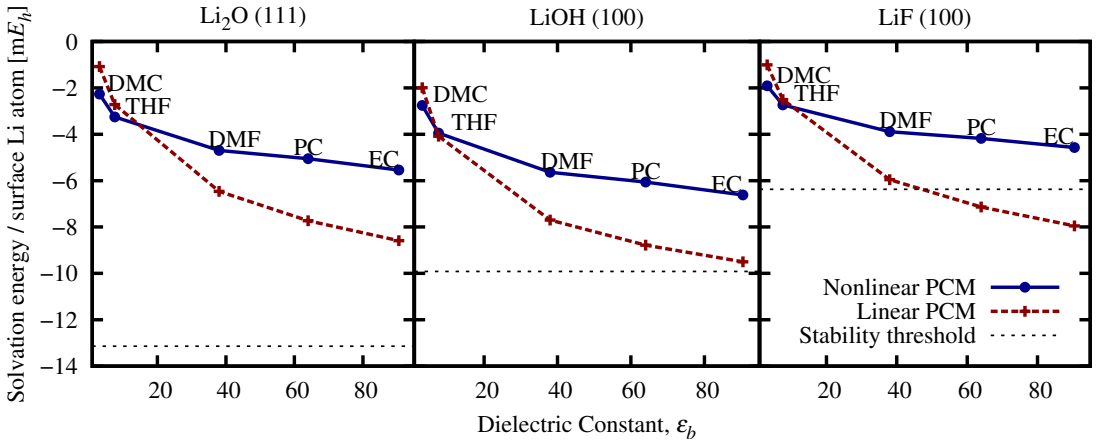

Figure 6.5: Solvation energies predicted by the nonlinear and linear models for surfaces of Li_2O, LiOH and LiF in the organic solvents from Table 6.3. With increasing dielectric constant, the predictions of the linear model diverge from those of the nonlinear model, since the former misses saturation effects. This leads to qualitative differences here, unlike the case of the solvated molecules of Figure 6.3. For some surfaces, the linear model suggests, perhaps incorrectly, that the flat surface is unstable by lowering the solvated surface energy relative to the bulk solid.

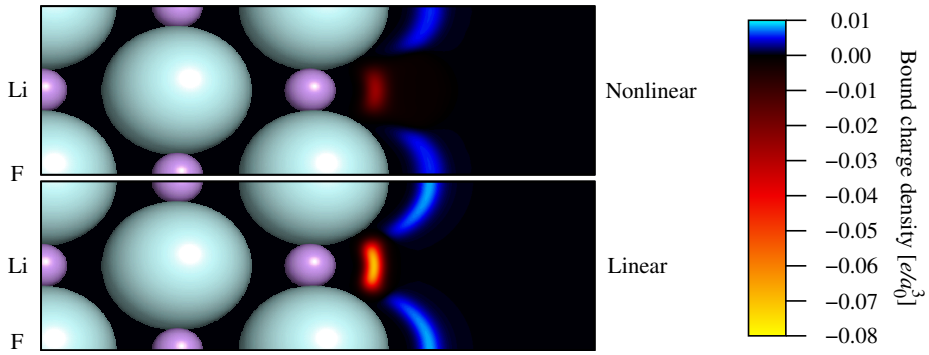

Figure 6.6: Bound charge density in solvent ethylene carbonate (EC) around a LiF (100) surface in the nonlinear and linear models, shown in a (011) slice. Saturation effects are stronger next to the smaller Li^+ cations which produce significantly stronger fields on the solvent compared to the larger F^- anions. In contrast to a water molecule in liquid water (Figure 6.2), these effects are strong enough to qualitatively alter solvation energies, as shown in Figure 6.5.

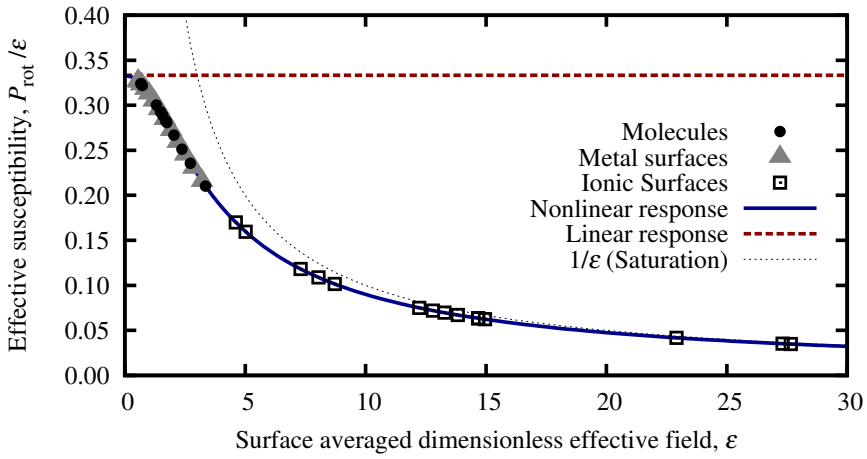

Figure 6.7: Effective rotational susceptibility at the average value of the dimensionless effective field ε (defined in section 6.1.3) at the cavity surface (solvent-solute interface) for solvated molecules (circles), charged metal surfaces (triangles) and ionic surfaces (squares). The reduction in susceptibility because of saturation effects captured by the nonlinear model is missed by the linear one. Unlike the case of molecules and metal surfaces, the order of magnitude overestimation of the susceptibility by the linear model for ionic surfaces is not compensated by the increase in cavity size.

lene carbonate, as seen in Figure 6.6, the linear model overestimates the bound charge density by an order of magnitude. Indeed, in this case, the result is a qualitative difference in the predicted stability of the solvated surface relative to the solid, with the linear model even predicting the solid to be thermodynamically unstable with respect to the formation of surfaces in this system.

The qualitative inadequacy of the linear model for ionic surfaces derives from the significantly stronger electric fields in these systems compared to solvated molecules and metallic surfaces. Figure 6.7 compares the average dimensionless electric field ε (defined in section 6.1.3) and the corresponding rotational susceptibility at the solute-solvent interface for all the systems discussed above. The least polar neutral ionic surface still imposes a higher electric field than the most polar molecule or charged metallic surface at chemically relevant

electrode potentials. The order of magnitude reduction in rotational susceptibility because of saturation effects in the ionic surfaces, compared to the modest reduction in other cases, necessitates a nonlinear theory for the study of these systems.

6.3 Summary

Ab initio studies provide key insights into chemical processes in a wide range of systems, but have not yet approached electrochemistry with a realistic description of the electrolyte environment. Continuum solvation models provide an intuitive and computationally-efficient description of the environment and enable a focused study of the complex subsystems that require treatment at the electronic structure level. Our results indicate that standard polarizable continuum models fit to molecular solvation data perform poorly when applied to polar surfaces. Consequently, one must exercise caution when attempting to apply standard solvation models available in both quantum chemical [163, 45, 113] and condensed matter [8, 48] *ab initio* software packages. As an alternative, the nonlinear theory presented here and implemented in [154] leverages the computational simplicity of the standard polarizable continuum models and extends their applicability to systems with the strong electric fields associated with ionic surfaces in electrochemical systems.

The importance of nonlinear solvent response depends on the strength of local electric fields at the interface, which in turn varies dramatically with system type, as highlighted in Figure 6.7. For systems with moderate field strengths, such as the molecules and metal surfaces studied here, the linear models can

compensate for the overestimated electrostatic response through an increase in cavity size. However, for systems with higher field strengths, such as ionic surfaces, this compensation is insufficient. The nonlinear polarizable continuum model developed here consistently describes all of these systems, and along with the technique developed in Section 6.1.6 to determine the electron chemical potential, enables electronic structure predictions for real electrochemical systems as a function of electrode potential.

This chapter presents a general framework for developing polarizable continuum models, and focuses on the dominant electric response while employing a simple empirical form for the remaining energy contributions such as cavity formation and dispersion. The parameters determining the cavity size and these auxiliary energy contributions are fit to solvation energies and are expected to depend on the solvent. The next chapter develops a more detailed description for these auxiliary terms and attempts to construct a PCM whose parametrization is somewhat less solvent dependent.

CHAPTER 7

WEIGHTED-DENSITY FUNCTIONALS FOR CAVITY FORMATION AND DISPERSION ENERGIES [1]

The polarizable continuum model of Chapter 6 develops a nonlinear theory of the dielectric and ionic response and adopts a simple effective surface tension model [8] for cavity formation and dispersion energies. This approach then fits two parameters, the electron density determining the cavity size (n_c) and the effective surface tension (τ), to solvation energies of molecules in the solvent of interest. However, the actual cavity formation and dispersion energies are not proportional to the cavity area (see Figure 4.6 for the size dependence of the cavity formation energy), and the accuracy for solvation energies relies on cancellation of errors arranged for by the fit. Consequently, the fit parameters lack physical meaning and are highly solvent-dependent.

Traditional polarizable continuum models [163] adopt a much more complicated parametrization. They typically invoke two cavities, a smaller one bounded by the 'solvent excluded surface' (SES) and a larger one bounded by the 'solvent accessible surface' (SAS). The SAS bounds the region of space accessible to centers of the solvent molecules such that spheres centered on the solvent molecules do not overlap with spheres centered on solute atoms. The SES bounds the region of space which overlaps with any solvent sphere with center placed on or outside the SAS. The radii used in determining the solute and solvent spheres are taken to be atomic van der Waals (vdW) radii, or are fit to solvation datasets per atom, and sometimes per functional group. The electric response is computed on the SES cavity and the cavity formation and

[1] Co-author credits: D. Gunceler performed the solvation energy fits.

dispersion energies are computed on the SAS cavity. (See [163] for details.) The SAS cavity corresponds to the region of space from which fluid molecule centers are excluded, as in the hard sphere solvation calculations of chapters 3, 4 and 5, and therefore enables a more rigorous analysis of the cavity formation energy than the empirical cavity of Chapter 6. However, methods of this class typically require a much larger set of adjustable parameters, such as solvent-dependent scale factors on the vdW radii to determine the cavity used for computing the electrostatic contributions.

This chapter develops the methods necessary to combine the best of both approaches above. Section 7.1 analyzes the nonlocality in the solvent response in order to define an 'electrostatic radius' that sets the spacing between the solvent-center cavity and that used for electric response, without any fit parameters. Section 7.2 then develops a technique to generate cavities spaced by such a distance, but still determined by a single critical electron density n_c. Sections 7.3 and 7.4 present intuitive models for the cavity formation and dispersion energies respectively, that capture the correct cavity shape and size dependence of those terms. Finally, Section 7.5 presents solvation energy results for the resulting polarizable continuum model for water, chloroform and carbon tetrachloride and demonstrates the possibility of almost solvent-independent parametrization of simplified solvation models.

7.1 Electrostatic radii of solvents

The fundamental need for empirical parameters in polarizable continuum models arises from the locality assumption: the nonlocal response of the solvent is replaced by that of a continuum dielectric. This assumption is compensated for

by choosing the boundary of the dielectric appropriately: the optimum boundary lies between the SAS (solvent centers) and SES (solvent edges) and is selected by fitting some cavity size parameter, critical electron density n_c or radius scale factor depending on the approach, to solvation energies. Here, we analyze the nonlocal response of the solvent, obtained from electronic density-functional calculations of one solvent molecule, to determine the distance of this optimum dielectric boundary from the solvent-center surface (SAS).

We start by computing the charge density of a single solvent molecule $\rho_{\text{mol}}(\vec{r})$ using electronic density-functional theory, and expanding its electronic and vibrational susceptibility obtained from density-functional perturbation theory in an eigen-basis

$$\chi_{\text{mol}}(\vec{r},\vec{r}') = -\sum_i X_i \rho_i(\vec{r})\rho_i(\vec{r}') \tag{7.1}$$

with normal modes of strength X_i with characteristic charge density $\rho_i(\vec{r})$.

Next, consider a single solvent molecule with its center pinned at the origin that is free to rotate and in thermal equilibrium at temperature T. In the absence of any external fields, this molecule adopts all orientations $\omega \in \text{SO}(3)$ with equal probability $p_\omega = 1$ (normalized so that $\int \frac{d\omega}{8\pi^2} p_\omega = 1$). With a perturbing field, the orientation density is altered to first order in the field and in each orientation, the molecule is polarized by the field, again to first order. By collecting the total induced charge at first order, we can show that the net susceptibility of the free rotor at T is

$$\begin{aligned}\chi_T(\vec{r},\vec{r}') &= \int \frac{d\omega}{8\pi^2}\left[\frac{-1}{T}\rho_{\text{mol}}(\omega\circ\vec{r})\rho_{\text{mol}}(\omega\circ\vec{r}) - \sum_i X_i\rho_i(\omega\circ\vec{r})\rho_i(\omega\circ\vec{r}')\right] \\ &= -\int \frac{d\omega}{8\pi^2}\sum_{i=0} X_i\rho_i(\omega\circ\vec{r})\rho_i(\omega\circ\vec{r}').\end{aligned} \tag{7.2}$$

The second line simplifies the notation by extending the sum over polarizability

modes to include rotation as mode 0 with strength $X_0 = 1/T$ and characteristic charge density $\rho_0(\vec{r}) = \rho_{\text{mol}}(\vec{r})$.

Finally, in order to estimate the extent of the nonlocality of the response, we adopt a simple model of the solvent consisting of a fixed distribution of free-rotor solvent molecules at temperature T. The net susceptibility of a semi-infinite slab of such a solvent with bulk molecular density N_{bulk} is therefore

$$\chi(\vec{r},\vec{r}') = -\int d\vec{R} N_{\text{bulk}} \theta(\vec{R}\cdot\hat{z}) \int \frac{d\omega}{8\pi^2} \sum_{i=0} X_i \rho_i(\omega\circ\vec{r}-\vec{R})\rho_i(\omega\circ\vec{r}'-\vec{R}). \tag{7.3}$$

Approximating the interaction between molecules at the mean-field level, the bound charge density in the solvent is then $\rho_{\text{bound}} = \hat{\chi}\phi_{\text{tot}} \equiv \int d\vec{r}'\chi(\vec{r},\vec{r}')\phi_{\text{tot}}(\vec{r}')$, where ϕ_{tot} is the total electrostatic potential. For an applied external potential ϕ_{ext}, the total potential then satisfies the self consistency relation

$$\begin{aligned} \phi_{\text{tot}} &= \phi_{\text{ext}} + \hat{K}\rho_{\text{bound}} = \phi_{\text{ext}} + \hat{K}\hat{\chi}\phi_{\text{tot}} \\ \Rightarrow \quad (1-\hat{K}\hat{\chi})\phi_{\text{tot}} &= \phi_{\text{ext}}, \end{aligned} \tag{7.4}$$

where $\hat{K}$ is the Coulomb operator.

To this model solvent slab, we apply a uniform external field normal to the slab with $\phi_{\text{ext}}(\vec{r}) = -Dz$, and numerically solve the one-dimensional integral equation (7.4) with the non-local $\hat{\chi}$ given by (7.3) to obtain the total potential and bound charge density in the solvent. Figure 7.1 shows the resultant bound charge density at the interface for liquid water. In contrast, the bound charge density in a continuum dielectric would be a δ-function centered at $z = 0$.

The interaction energy of this bound charge with a sheet charge $\sigma\delta(z+L)$ for some large enough L so that the two charge densities do not overlap is $U_{\text{NL}} = \sigma\int dz\rho_{\text{bound}}(z)(z+L)$. Similarly, the interaction energy of this sheet charge with a continuum dielectric bounded at $z = -R_{\text{el}}$ is $U_\epsilon = \sigma(L-R_{\text{el}})\int dz\rho_{\text{bound}}(z)$.

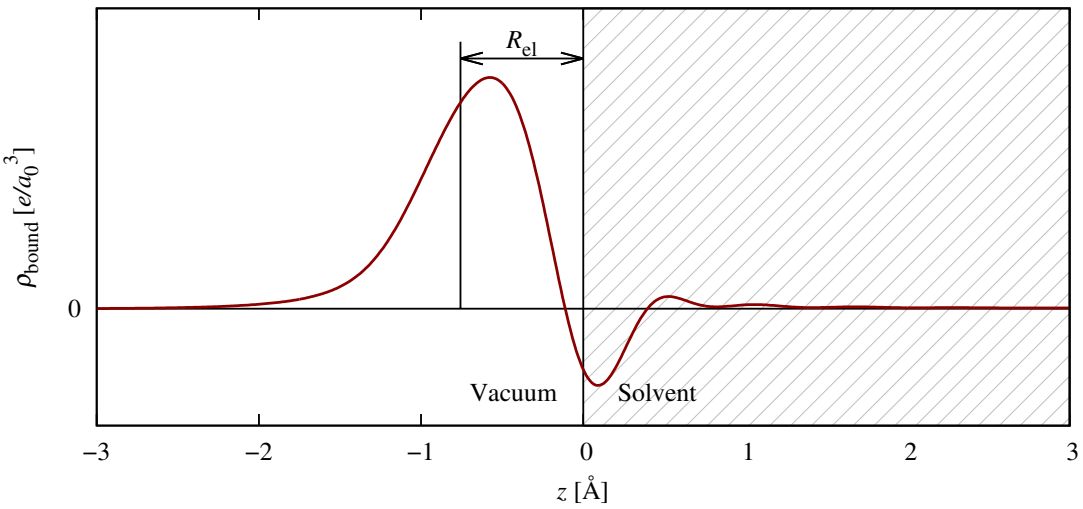

Figure 7.1: Determination of electrostatic radius, shown here for water, as the first moment of the bound charge density at the interface of the solvent slab with model nonlocal response given by (7.3), under a uniform externally applied field.

The magnitude of the bound charge for the nonlocal response and a continuum dielectric with the same bulk dielectric constant are identical, and therefore the interaction energies $U_\epsilon = U_{\mathrm{NL}}$ for all L if

$$R_{\mathrm{el}} \equiv -\frac{\int dz \rho_{\mathrm{bound}}(z) z}{\int dz \rho_{\mathrm{bound}}(z)}. \tag{7.5}$$

This defines the electrostatic radius of a solvent, R_{el}, as the distance by which a continuum dielectric boundary should be placed closer to the source charge compared to the solvent-center surface in order to match the energetics of the nonlocal response in a planar geometry. At lowest order, this optimum distance is unaffected upon moving from a planar interface to the cavity geometry around an electronic system, and we set the separation between the electric response cavity and the SAS to R_{el}, computed *ab initio* as detailed above.

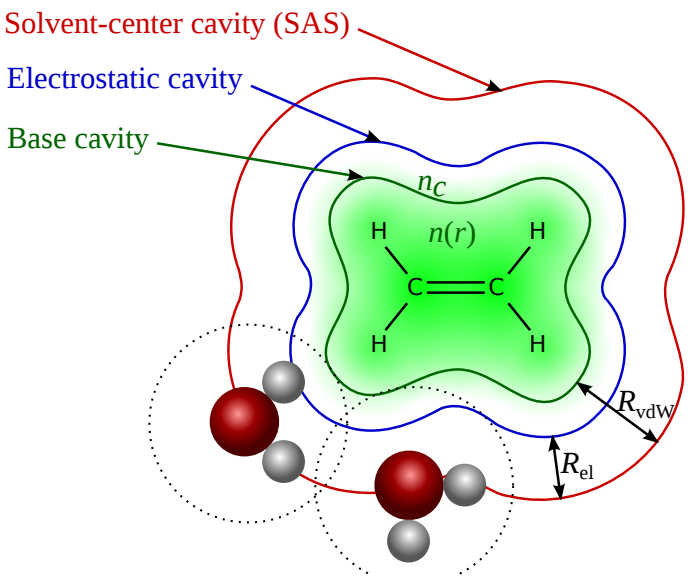

Figure 7.2: Relation between various cavity surfaces in a PCM description of an ethylene molecule in water. The solvent accessible surface (SAS) is obtained by expanding the base cavity, which roughly corresponds to the SES, by the solvent van der Waals radius (R_{vdW}). The electric response is smaller than the SAS by the electrostatic radius, R_{el}, and is hence obtained by expanding the base cavity by $R_{vdW} - R_{el}$. The base cavity is then expected to be a property of the solute alone, and hence solvent independent.

7.2 Cavity expansion

The electrostatic radius (R_{el}) defined above links the cavity for electrostatic response to the surface of solvent centers (SAS). In traditional PCM's, the SAS is determined from the union of atom-centered spheres of radii equal to the sum of solute atom and solvent vdW radii. Combining that definition of the SAS with the *ab initio* computed R_{el} would eliminate solvent-dependent scale parameters in the cavity determination. However, our goal is to take a step forward and avoid atom-dependent parameters, if possible.

Here, we transfer the physical intuition behind the atomic vdW radius approach to the isodensity approach, where the cavities are determined from the

electron density. vdW radii are defined in terms of the distance of nearest approach of two closed-shell electronic systems [102], and hence are expected to be a reasonable descriptor for the typical spacing between solute and solvent molecules in the domain of validity of solvation models; in any case, covalent bonds with the solvent would require inclusion of the bonded solvent molecules in the quantum-mechanical calculation.

Consequently, we propose the following program (see Figure 7.2). The electron density of the solute is thresholded at a critical density n_c to determine a base cavity, which corresponds roughly to the SES of traditional models. This cavity is a property of the solute alone, and the resulting n_c can therefore expected to be independent of the solvent.

The solvent-center cavity used for computing the cavity formation and dispersion energies is obtained by expanding this base-cavity by the solvent vdW radius, R_{vdW}, which can be defined in terms of the equation of state and other thermodynamic properties of the fluid [131], and has been tabulated for many fluids [14]. The cavity for electric response is expected to be R_{el} smaller than the solvent-center cavity as discussed previously. We therefore obtain this cavity by expanding the base cavity by $R_{\mathrm{vdW}} - R_{\mathrm{el}}$.

At this stage, all cavities required for the model can be determined from a single critical electron density n_c, along with thermodynamic and *ab initio* computed properties of the solvent. In the rest of this section, we develop a practical method to construct the expanded cavities in a plane-wave basis calculation.

Only the exponential tail regions of the electron density participate in the determination of the cavity, since the nearest approach of closed shell systems

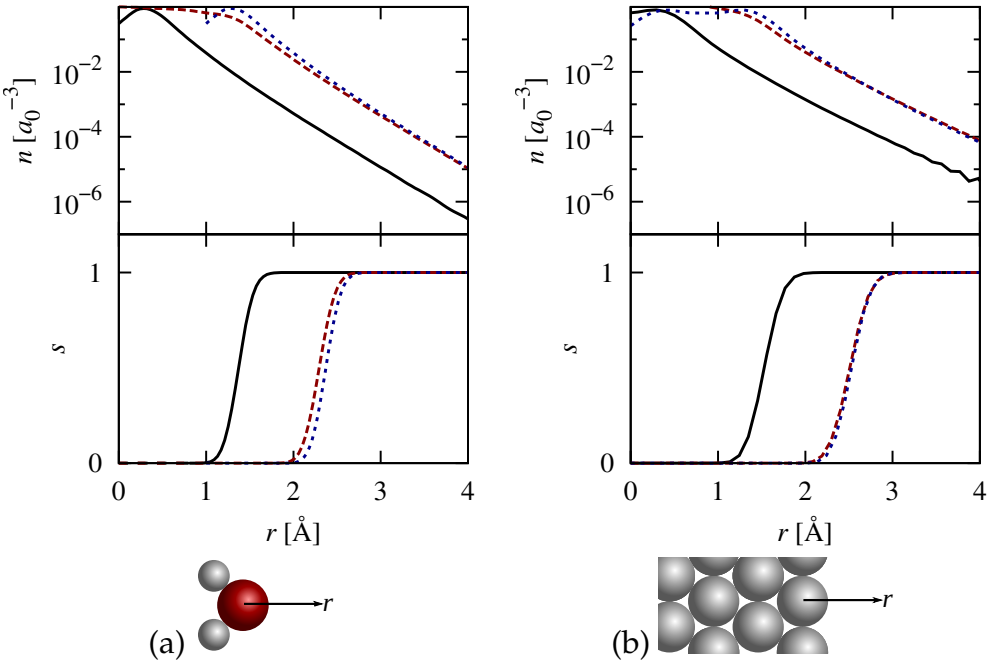

Figure 7.3: Accuracy of electron density expansion functional for (a) water with an approximately spherical electron density tail and (b) Pt(111) surface with an approximately planar electron density tail. In the upper (lower) panels, the solid black lines show the original electron density (cavity), the dashed red lines plot the corresponding quantities for the electron density expanded by 1 Å, and the dotted blue lines plot the original quantity shifted outwards by 1 Å.

only involves overlap of these low electron density regions. It turns out that we can exploit this exponential structure to much more reliably expand the electron density rather than the cavities obtained by thresholding them.

Isodensity PCM's describe the cavities by functions $s(\vec{r})$ that smoothly switch from 0 in the cavity to 1 in the bulk fluid. Following [130] and Chapter 6, we employ the error-function form

$$s_R[n](\vec{r}) = \frac{1}{2}\mathrm{erfc}\frac{\ln(\eta_R[n]/n_c)}{\sigma\sqrt{2}}, \tag{7.6}$$

except we use $\eta_R[n]$, the electron density expanded by R, instead of the original electron density n to obtain an expanded cavity. In particular, the electrostatic cavity is $s_{\mathrm{el}} \equiv s_{R_{\mathrm{vdW}}-R_{\mathrm{el}}}$ and the solvent-center cavity is $s_{\mathrm{SAS}} \equiv s_{R_{\mathrm{vdW}}}$.

Finally, we specify the functional $\eta_R[n]$ that expands the exponential tails of the electron density. Convolving the electron density by a weight function with range R almost achieves the required task, since the result at any location is dominated by the highest electron density within the range, which would be from R 'inwards' from that location. In particular, with a spherical kernel $w(r) = \theta(R - r)/2\pi R^3$ (with a convenient dimensionless normalization), a planar electron density $n = \exp(-z/a)$ yields a convolved density $\bar{n} = \exp(-(z - R)/a) \times a^2(R - a)/R^3 + O(\exp(-(z + R)/a))$, which exhibits the desired shifting of the exponential tail but includes an undesirable prefactor that depends on the electron density length scale, a. A gradient of the convolution picks up a factor of $1/a$, and can be combined with the above to eliminate this dependence. In fact, $|R\nabla\bar{n}|^2/\bar{n} = \exp(-(z - R)/a)) + O(a/R)$ and $R \gg a$ for typical electron densities. This form, however, rapidly approaches zero in the core region of pseudized electron densities. A sum of the convolved density, $\bar{n} = n * \theta(R - r)/2\pi R^3$, and the combination with its gradient,

$$\eta_R[n] = \bar{n} + \frac{|R\nabla\bar{n}|^2}{\bar{n}} \tag{7.7}$$

retains the leading order electron density length-scale independence and remains non-zero in the pseudopotential cores. Figure 7.3 demonstrates the accuracy of this functional in expanding realistic electron densities and the resulting cavities. The errors in cavity separation for planar electron densities, the regime of the above construction, are only ~ 0.01 Å, whereas they approach ~ 0.03 Å for worst-case spherical densities with curvature radii comparable to the expansion radius R. Typical separations between solute and solvent atoms, which do not form covalent bonds with each other, are ~ 3 Å, so that the worst-case error above results in a 1 % error in the capacitance of the dielectric cavity, and hence a 1 % error in the electrostatic contribution to the solvation energy. This com-

ponent of the energy typically varies from $\sim$ 10 mE_h for organic molecules to $\sim$ 100 mE_h for ions, so that the worst-case error would be $\sim$ 1 mE_h (room temperature) for ions, which is within the target accuracy of $\sim$ 1 kcal/mol (1.6 mE_h) for simplified solvation models.

7.3 Weighted-density cavity formation model

The analyses of Sections 7.1 and 7.2 establish a solvent-center cavity and a dielectric cavity within an iso-density approach with a single critical electron density parameter n_c. The remaining ingredients necessary to form a complete polarizable continuum description of the solvent are models for the sub-dominant contributions beyond the mean-field electrostatic interactions, such as the cavity formation and dispersion energies, given the solvent-center cavity described in term of the shape function, $s_{\mathrm{SAS}}(\vec{r})$.

The simplest approximation to the cavity formation free energy is an effective surface tension model, with an empirical tension parameter fit to solvation free energies. This accounts for the reduced free energy per unit surface relative to the bulk surface tension for microscopic molecular cavities, but therefore underestimates the cavity contribution for a planar interface, which should in fact be the bulk surface tension. A model accounting for the cavity geometry is necessary to describe both limits accurately.

The cavities in traditional polarizable continuum models are typically composed of spheres. Scaled-particle theory (SPT) [131], based on the statistical mechanics of hard sphere fluids, provides an accurate estimate of the free energy of inserting a hard sphere of arbitrary size into a hard sphere fluid. PCM's

employ various combination rules [163] to estimate the free energy for forming a cavity composed as a union of spheres, such as applying SPT to a sphere of surface area or volume equal to that of the cavity, or linearly combining the cavity formation energy of spheres weighted by exposed surface area. (See [30] for a detailed comparison of these methods.)

These combination rules do not result from physical principles and have primarily evolved from empirical evidence. Furthermore, isodensity PCM's produce arbitrary-shaped cavities that do not decompose into spheres for which SPT may be applied. In principle, classical density functional theory with free energy functional approximations, such as those of chapters 3-5, can provide an estimate of this term. This involves minimizing a free energy functional in an external potential that excludes the fluid from the interior of the cavity, which incurs a significant computational cost compared to the solution of the modified dielectric equation for the electrostatic term. Here, we motivate a low computational cost, closed-form physical model for the cavity-formation energy for arbitrary cavities that compares favorably with classical-density functional results.

We start from the intuitive picture of surface tension resulting from the energy cost of missing neighbors for the molecules at the surface of the fluid. A convolution of the cavity shape function, $\bar{s} = w * s$, with a normalized short-ranged weight function $w(r)$, measures the neighborhood of a molecule, ranging from 0 for an isolated molecule, through 1/2 for a surface molecule, to 1 for a molecule in the bulk. In particular, we select the spherical shell weight function $w(r) = \delta(r - \sigma_{\text{vdW}})/4\pi\sigma_{\text{vdW}}^2$ with the solvent vdW diameter $\sigma_{\text{vdW}} = 2R_{\text{vdW}}$, so as to estimate the fraction of nearest neighbor molecules present at each location.

We then make a weighted-density ansatz for the cavity formation free energy, $G_{\text{cav}} = pV + \int d\vec{r} f(\bar{s})$ with an as yet undetermined local function f, after separating out the ideal gas contribution pV for a cavity of volume $V = \int(1 - s)$ in a fluid at pressure p and temperature T.

Next, we constrain the undetermined function to known physical limits. The free energy to form a cavity of volume V that is much smaller than molecular dimensions in a fluid of bulk density N_{bulk} at temperature T, is dominated by ideal gas contributions and reduces to $(p + N_{\text{bulk}}T)V$ to lowest order in V. On the other hand, the weighted density ansatz above yields $G_{\text{cav}} = f(1) + (f'(1) + p)V + O(V^2)$ in the limit of small cavities, which implies $f(1) = 0$ and $f'(1) = N_{\text{bulk}}T$.

The opposite regime of droplets corresponds to fluid at bulk density in the interior of some volume V, with zero density outside. When we take the limit $V \to 0$, this configuration contains $N_{\text{bulk}}V \ll 1$ molecules on average (no longer a droplet in the conventional sense), and its free energy corresponds to that of extracting and isolating $N_{\text{bulk}}V$ molecules from the bulk fluid. The free energy required to isolate one molecule from the bulk fluid is related to its vapor pressure, p_{vap}, as $T(\ln \frac{N_{\text{bulk}}T}{p_{\text{vap}}} - 1)$. In this limit, the ansatz predicts $G_{\text{cav}} = f(0) + f'(0)V + O(V^2)$, yielding the constraints $f(0) = 0$ and $f'(0) = N_{\text{bulk}}T(\ln \frac{N_{\text{bulk}}T}{p_{\text{vap}}} - 1)$.

In addition to these four constraints from the droplet and cavity limits, we require the model to reproduce the bulk surface tension σ_{bulk} for planar interfaces. The simplest function $f(\bar{s})$ that can satisfy these five constraints is a fourth order polynomial, and solving for the constraints for that functional form yields

the model free energy

$$G_{\text{cav}}[s] = p \int (1 - \bar{s}) + N_{\text{bulk}} T \int \bar{s}(1 - \bar{s}) \left[\bar{s} + (1 - \bar{s})\gamma + 15 \left(\frac{\sigma_{\text{bulk}}}{N_{\text{bulk}} T R_{\text{vdW}}} - \frac{1 + \gamma}{6} \right) \bar{s}(1 - \bar{s}) \right], \quad (7.8)$$

where $\gamma \equiv \ln \frac{N_{\text{bulk}} T}{p_{\text{vap}}} - 1$.

This specifies a model for the free energy associated with forming a cavity of arbitrary shape described by a shape function $s(\vec{r})$, constrained entirely by bulk measurable properties of the solvent, with no adjustable parameters. Figure 7.4 compares the predictions of this model against classical density functional theory calculations using the free energy functional approximations of Chapter 5 for all constant curvature surfaces: spherical and cylindrical cavities as well as droplets. The model reproduces the high positive and negative as well as zero curvature results by construction (small cavity, small droplets and planar interface limits respectively). The weighted density ansatz with the spherical shell weight function of radius R_{vdW} perfectly 'interpolates' between these limits for all solvents considered, ranging from the highly polar (water) to the non-polar (carbon tetrachloride). The results are also in agreement with scaled-particle theory in its domain of validity: small spherical cavities, but the present model is valid for arbitrary geometries and does not require combination rules for application to PCM free energies for solvated molecules.

Figure 7.5 further explores the accuracy for non-spherical geometries by considering the cavity formation energy for dumbbell-shaped objects composed as the union of two spherical cavities, as a function of the separation between the sphere centers. The weighted-density model best reproduces the classical density-functional results, including the non-monotonicity around separations for which the two cavities just touch; this corresponds to a highly non-analytical

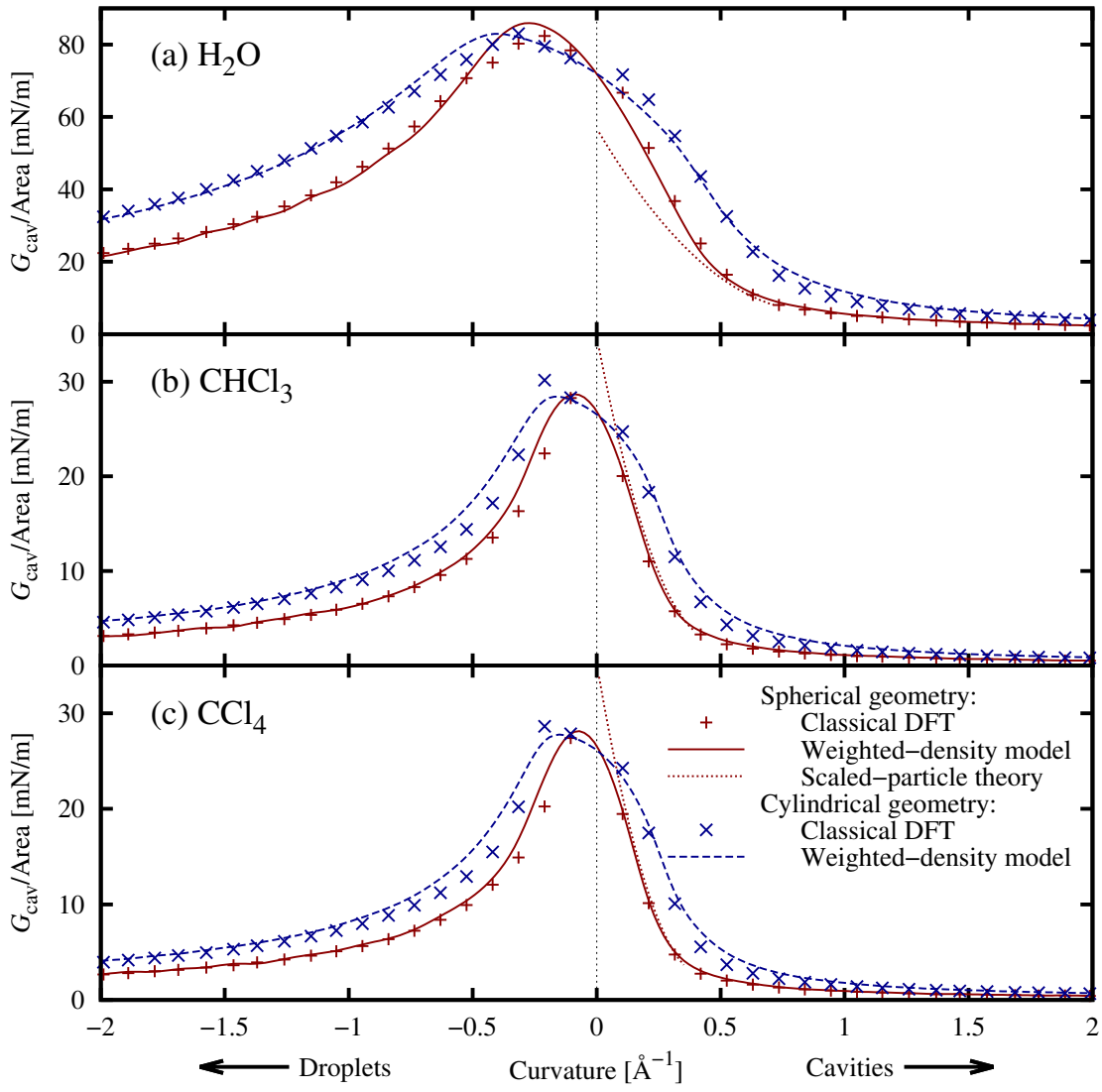

Figure 7.4: Dependence on the curvature of the fluid-vacuum interface, of the cavity formation energy per surface area for (a) water, (b) chloroform and (c) carbon tetrachloride as predicted by the weighted density model (7.8) and scaled-particle theory [131] (valid for spherical cavities only) compared to classical density functional results for spherical and cylindrical cavities (fluid outside surface) as well as droplets (fluid inside surface).

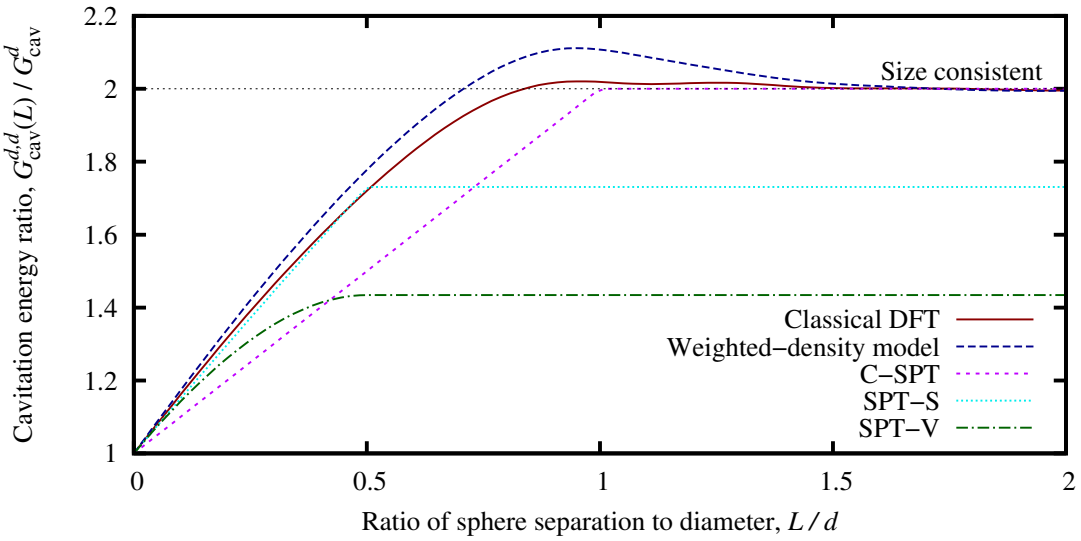

Figure 7.5: Ratio of cavity formation energies for a union of two spherical solvent-center cavities of diameter d ($G^{d,d}_{\rm cav}(L)$) to that of a single isolated cavity ($G^{d}_{\rm cav}$) as a function of sphere center separation L, as predicted by the weighted density model and several traditional PCM combination rules compared to classical density functional results. Zero separation corresponds to a single spherical cavity, while infinite separation corresponds to two isolated spherical cavities. A size-consistent model must yield 2 in the limit of infinite separation. The figure presents results for water, with solute spheres of radius equal to the solvent $R_{\rm vdW}$, which results in solvent-center cavities of diameter $d = 4R_{\rm vdW} = 5.54$ Å, and for which the isolated cavity formation energy is $G^{d}_{\rm cav} = 4.3$ kcal/mol (6.9 mE_h).

geometry involving cusps and infinite surface curvatures. Further, the minor deviations from the density-functional results are only for this problematic non-analytical geometry. On the other hand, amongst the traditional PCM combination rules, only the Claviere-Peirotti method (C-SPT) [86] that combines the sphere results weighted by the exposed surface areas exhibits size-consistency, that is it evaluates to twice the cavity formation energy for two infinitely separated spherical cavities, compared to that for a single cavity. The other methods that apply scaled-particle theory to a sphere with either surface area or volume equal to the non-spherical cavity (SPT-S and SPT-V respectively [30]) sacrifice the size consistency, but are more accurate for small separations where the re-

sulting cavity approaches a sphere. Clearly, as expected, the weighted density model consistently exhibits the best results for highly non-spherical geometries.

7.4 Dispersion model

The final energetic contributions relevant to solvation free energies are the dispersion interactions between the solute and the solvent, and to a lesser extent, the Pauli repulsion between the electrons of the solute and the solvent at their interface. Quantum chemistry solvation methods sometimes couple solvent polarizabilities to virtual excitations in the solute system to obtain a physical model for the dispersion interactions [7]; such methods are much more expensive than standard electronic density-functional calculations, require unoccupied levels and can be prohibitively expensive in plane-wave basis calculations. On the other hand, empirical pair-potential estimates for these additional terms [163] are moderately accurate and efficient for use in density-functional calculations.

Here, we neglect the repulsion energies and adopt a simplified empirical formulation for the dispersion energies (which absorbs the error introduced by neglecting repulsion) based on the pair-potential dispersion corrections employed in electronic density-functional theory [53, 162]. For simplicity, we adapt the form introduced by Grimme [53], which expresses the dispersion corrections for a system with a collection of atoms at positions $\vec{R}_i$ as

$$E_{\text{disp}} = -s_6 \sum_{i<j} \frac{\sqrt{C_{6i} C_{6j}}}{r_{ij}^6} f_{\text{dmp}} \left(\frac{r_{ij}}{R_{0i} + R_{0j}} \right), \tag{7.9}$$

where $r_{ij} \equiv |\vec{R}_i - \vec{R}_j|$, $C_6 i$ are effective interaction strengths for each atom type derived from *ab initio* atomic polarizabilities, and R_{0i} are atomic vdW radii (tab-

ulated for all main group elements in [53]). The damping function $f_{\text{dmp}}(x) = 1/(1 + e^{-d(x-1)})$ with $d = 23$ serves to attenuate the short-ranged contributions to the correction, since they are partially captured by the approximate exchange-correlation functional, and the empirical scale parameter s_6 compensates for differences between various exchange-correlation functionals.

In adapting this pair-potential model to describe solvent-solute interactions in PCM, we make two modifications. First, the damped r^{-6} potential is still singular at zero separation and not integrable ($\int dx 4\pi x^2 f_{\text{dmp}}(x)/x^6 = \infty$). This makes no difference since atoms never get close enough for this unphysical behavior to contribute, but the lack of integrability precludes evaluating the interaction with continuous distributions of atoms using a convolution. Therefore, we eliminate the $x = 0$ singularity and instead employ the value and derivative matched piecewise function

$$f_{\text{dmp}}(x) = \begin{cases} 1/(1 + e^{-d(x-1)}), & x > 0.03 \\ 0.00114x^6, & x \leq 0.03 \end{cases} \tag{7.10}$$

which is identical to the original function at all relevant distances.

Second, the simplified PCM description of the solvent does not specify spatial distributions for each atom of the solvent molecule, but only the distribution of the solvent molecule centers, $N_{\text{bulk}} s(\vec{r})$. Consequently, we additionally assume a uniform orientation distribution of the molecules comprising the cavity resulting in a spatial distribution $N_j(\vec{r}) = N_{\text{bulk}} s(\vec{r}) * \delta(r - R_j^{\text{solv}})/4\pi(R_j^{\text{solv}})^2$ for atom j of the solvent molecule that is at a distance R_j^{solv} from the center of the solvent molecule. This results in a model solvent-solute dispersion interaction

$$E_{\text{disp}}[s] = -s_6 \sum_{i,j} \int d\vec{r} N_j(\vec{r}) \frac{\sqrt{C_{6i} C_{6j}}}{|\vec{R}_i - \vec{r}|^6} f_{\text{dmp}}\left(\frac{|\vec{R}_i - \vec{r}|}{R_{0i} + R_{0j}}\right), \tag{7.11}$$

where the index i runs over the atoms of the explicit electronic system and j over the atoms of one solvent molecule. The empirical scale factor s_6 absorbs the errors arising from the neglect of repulsion as well as the uniform orientation distribution assumption, in addition to those inherent to the pair-potential approximation, such as the neglect of three-body (Axilrod-Teller) terms and beyond.

The disadvantage of this simplified description is the introduction of one solvent-dependent empirical parameter, which we mitigate in the following fits to solvation energies. In particular, we show that this single parameter can be calibrated to the solvation energy of a single non-polar molecule which is dominated by the dispersion interaction. Along with the solvent-independent n_c, this allows the application of the method to an arbitrary solvent without requiring extensive fits to solvation energy data sets.

7.5 Solvation energies

The previous sections establish the relations between the cavity for electric response and that of the solvent centers, and formulate weighted-density models for the cavity formation and dispersion energies that capture the true shape and size dependence of these contributions. Combining these with the nonlinear electric and ionic response of Chapter 6, we arrive at the modified nonlinear polarizable continuum model,

$$A_{\text{diel}} = A_\epsilon[s_{\text{el}}, \vec{\mathcal{E}}] + A_\kappa[s_{\text{el}}, \mu] + \int d\vec{r} \int d\vec{r}' \frac{\rho_{\text{lq}}(\vec{r}')}{|\vec{r} - \vec{r}'|} \left(\rho_{\text{el}}(\vec{r}) + \frac{\rho_{\text{lq}}(\vec{r})}{2} \right) + G_{\text{cav}}[s_{\text{SAS}}] + E_{\text{disp}}[s_{\text{SAS}}]. \quad (7.12)$$

Table 7.1: Fit parameters and residuals for nonlinear PCM with weighted-density cavity formation and dispersion terms

Solvent	n_c [a_0^{-3}]	s_6		RMS error [kcal/mol (mE_h)]	
		Fit	Fixed	Fit	Fixed
H_2O		0.54	0.50	1.1 (1.8)	1.2 (1.9)
$CHCl_3$	1.0×10^{-2}	1.31	1.08	0.6 (1.0)	1.0 (1.6)
CCl_4		1.24	1.20	0.5 (0.8)	0.6 (1.0)

Here, the first two terms, the dielectric and ionic response, employ the electrostatic cavity, $s_{\mathrm{el}}(\vec{r})$, whereas the final two terms, for cavity formation and dispersion, employ the solvent-center cavity, $s_{\mathrm{SAS}}(\vec{r})$. The solute electron density determines both cavities with a single critical density, n_c, according to (7.6). Bulk solvent properties and *ab initio* calculations on a single solvent molecule determine all terms in this model, except n_c and the dispersion scale factor, s_6.

The critical density n_c corresponds to the base cavity in Figure 7.2, which we expect to be a property of the solute alone and hence solvent-independent. (The solvent-dependence of the electrostatic cavity size is due to the nonlocality of the true response of the solvent; this effect enters the calculation of the electrostatic radius in Section 7.1 and we no longer expect it to affect the base cavity size and n_c.) The dispersion scale factor, s_6, absorbs errors due to the neglect of repulsion terms and the assumption of isotropic solvent distribution in (7.11), and may depend on the solvent. We therefore fit a single n_c and an s_6 per solvent to the solvation energies of several small molecules in water, chloroform and carbon tetrachloride. Table 7.1 shows the resulting fit parameters and residuals, and Figure 7.6 shows the solvation energies of each molecule compared to experimental data from [157, 105].

A single n_c indeed fits the solvation energies of vastly different solvents,

Table 7.2: Fit parameters and residuals for nonlinear PCM with empirical cavity surface tension

Solvent	n_c $[a_0^{-3}]$	τ $[E_h/a_0^2]$	RMS error [kcal/mol (mE_h)]
H_2O	1.0×10^{-3}	9.5×10^{-6}	1.0 (1.6)
$CHCl_3$	2.4×10^{-5}	-9.2×10^{-6}	0.8 (1.3)
CCl_4	1.2×10^{-4}	-9.0×10^{-6}	1.1 (1.8)

ranging from the small polar water, to the much larger non-polar carbon tetrachloride. The dispersion factor s_6 varies between the solvents, but remains within 35% of the range 0.75-1.2 covered by different electronic functionals in [53].

In contrast, the original nonlinear PCM of Chapter 6, which employs an empirical surface tension τ on the surface of the electric response cavity to account for both cavity formation and dispersion, requires wildly different n_c's for the three solvents, covering three orders of magnitude, as Table 7.2 shows. Further, the effective surface tensions for the less polar solvents, chloroform and carbon tetrachloride, are negative since the attractive dispersion effects dominate over the repulsive cavity formation energies. This negative tension contributes a strong attractive well to the electron potential, which occasionally renders the electronic density functional unstable with respect to leaking electrons into the cavity. It is therefore advisable to avoid the effective surface tension approach of [8] and Chapter 6 for nonpolar dispersion-dominated solvents.

More importantly, the current model with physical cavity formation and dispersion terms obtains the same accuracy as the previous models, and does so with fewer parameters. Indeed, Table 7.1 shows that the fit results in $\sim$ 1 kcal/mol (1.6 mE_h) accuracy for all three solvents, which is sufficient for the

(a) H_2O

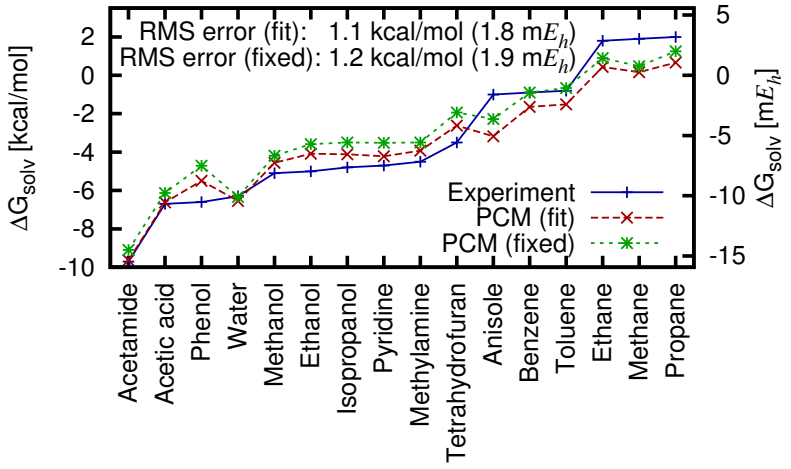

(b) $CHCl_3$

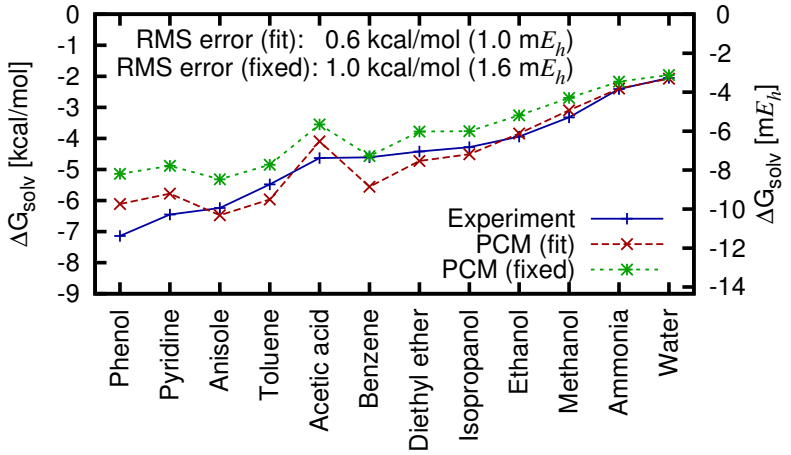

(c) CCl_4

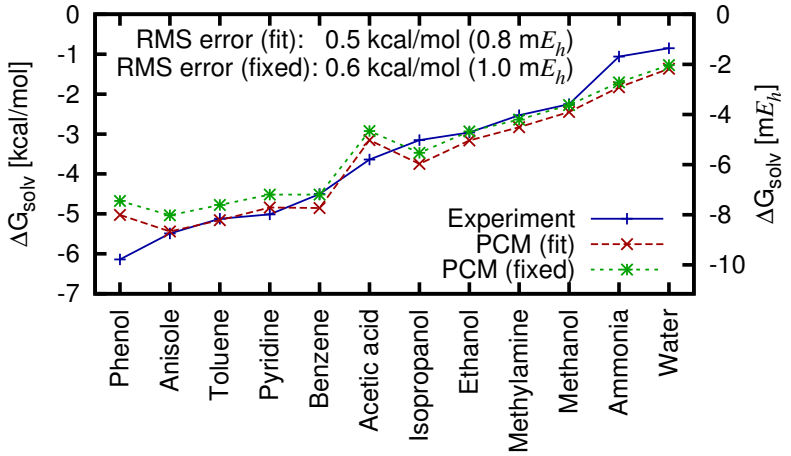

Figure 7.6: Solvation energies predicted by nonlinear PCM with weighted-density cavity formation and dispersion terms for molecules in (a) water, (b) chloroform and (c) carbon tetrachloride, compared to experiment. Phenol and acetic acid seem to be outliers in (b) and (c), probably due to a weak chemical bond between the solute and solvent in the experiment that is missed by the solvation model.

study of chemical reactions in solution.

Finally, the use of a common n_c for all solvents makes it easier to extend the method to other solvents, requiring the determination of a single fit parameter s_6 for each new solvent. In the absence of extensive data for a new solvent, it should be possible to use the solvation energy of just *one* solute to calibrate this single parameter. The ideal molecule for this purpose should be large, polarizable and non-polar, so that dispersion interactions dominate its solvation energy and constrain s_6 reliably. Figure 7.6 shows that fixing s_6 to reproduce the solvation energy of benzene in each solvent only marginally worsens the errors relative to the full fits. The resulting 'fixed' s_6 parameters are similar to the fit ones, and the residual remains in the ~ 1 kcal/mol (1.6 mE_h) regime, as Table 7.1 shows.

7.6 Summary

The polarizable continuum model presented in this chapter replaces the empirical cavity determination and effective cavity surface tension approximations of Chapter 6, with a single solvent-independent isodensity parameter and physical models for the cavity formation and dispersion free energy contributions that capture the correct cavity-shape dependences of those terms.

One key ingredient that allows a solvent-independent parametrization of the cavity sizes is the electrostatic radius of Section 7.1 which is based on the nonlocal response of the solvent molecule, and hence accounts for finite-size effects of the molecule. The next chapter takes this approach to its logical conclusion, and presents a non-empirical polarizable continuum model with a single cavity

that directly evaluates the nonlocal response of the solvent.

CHAPTER 8

NONLOCAL POLARIZABLE CONTINUUM MODELS

Traditional polarizable continuum models treat the effect of solvents on the electronic structure of solutes, as the response of a continuum dielectric surrounding the solute. This drastic simplification of the solvent effect necessitates several empirical parameters governing the cavity shape and size as well as for the cavity formation and dispersion corrections, typically fit to a database of solvation energies.

Chapter 6 incorporates nonlinear dielectric response in the minimal isodensity PCM of [8], which requires only two fit parameters for each solvent: a critical electron density, n_c, that determines the cavity size, and an effective surface tension, τ, to empirically account for cavity formation and dispersion contributions. Chapter 7 develops non-empirical models for these additional terms and prescribes a first-principles method to account for solvent molecule finite-size effects by appropriately sizing the continuum dielectric. The resulting polarizable continuum model fits the solvation energies of vastly different solvents with a single critical density, n_c. For each solvent, it requires the adjustment of a single semi-empirical parameter, the dispersion scale factor, s_6, which Section 7.5 determines from the dispersion-dominated solvation energy of a *single* nonpolar molecule.

The solvent independence of the cavity size parameter in Chapter 7 stems from the introduction of an electrostatic radius - the extra length of continuum dielectric necessary to reproduce the electric interaction of the solvent in a parallel plate capacitor. The electrostatic radius, in turn, results from a simple ansatz that approximates the nonlocal response of a solvent by the linear response of

freely orientable and polarizable solvent molecules in thermal equilibrium. The calculation of this property requires the solution of a one-dimensional integral equation, only once per solvent. However, the final model requires construction of two cavities, one corresponding to solvent molecule centers for the non-empirical cavity formation and dispersion terms, and another smaller by the electrostatic radius for the dielectric response.

In this chapter, we replace the effect of the solvent directly by a nonlocal dielectric response which eliminates the need for multiple cavities. Section 8.1 presents an intuitive solvent-independent model for this single solvent-center cavity based on the overlap between the solute and solvent electron densities. Section 8.2 derives the nonlocal response of the solvent as a linear-response approximation to the classical density-functional theory of Chapter 5, and presents an angular momentum expansion which enables practical calculations with this model at computational cost comparable to traditional polarizable continuum models. Finally, Section 8.3 demonstrates the accuracy of this model for the solvation energies of organic molecules in a variety of solvents including water, chloroform and carbon tetrachloride, with a single semi-empirical dispersion scale factor for each solvent, constrained to reproduce the solvation energy of a single nonpolar molecule.

8.1 Density-product cavity determination

The fundamental assumption in all polarizable continuum models is the formation of a cavity, that is the exclusion of the solvent from a region of space occupied by the solute. Variants of the model differ in the details of determining this cavity; most models require two cavities, a relatively physical one correspond-

ing to the centers of the solvent molecules which enters calculations of the cavity formation and dispersion energies, and a somewhat empirical one for the electric response. The previous chapter established a scheme for constraining the second empirical cavity to the physical solvent-center cavity via the electrostatic radius derived from the nonlocal response, and this chapter subsequently eliminates the need for the second cavity altogether. Here, we develop a universal prescription for the cavity of solvent centers from an intuitive picture of solute-solvent electron density overlap.

Traditional polarizable continuum models [163] construct the solvent-center cavity from the exclusion of a sphere with the vdW radius of the solvent, by spheres with atomic vdW radii centered on the solute atoms. This follows from the basic intuition of vdW radii determining the distance of nearest approach of two closed-shell non-bonded atoms or molecules [102]. Chapter 7 generalizes this approach to isodensity PCM's by determining a base cavity that roughly corresponds to the atomic vdW radii from the solute electron density, and then expanding that cavity by the solvent vdW radius. A critical electron density parameter, n_c, fit to solvation energies in multiple solvents, determines this base cavity.

The interaction potential of two neutral closed-shell atoms comprises primarily the Pauli repulsion between the electrons and the attractive dispersion interactions. With reducing separation between the atoms, the former rises sharply when the electron densities begin to overlap, while the latter varies more gradually. The repulsive interaction, and hence the electron density overlap, should therefore dominate the determination of the approach distance. Indeed, Figure 8.1 shows that the atom separation, R_{12}, at which the electron den-

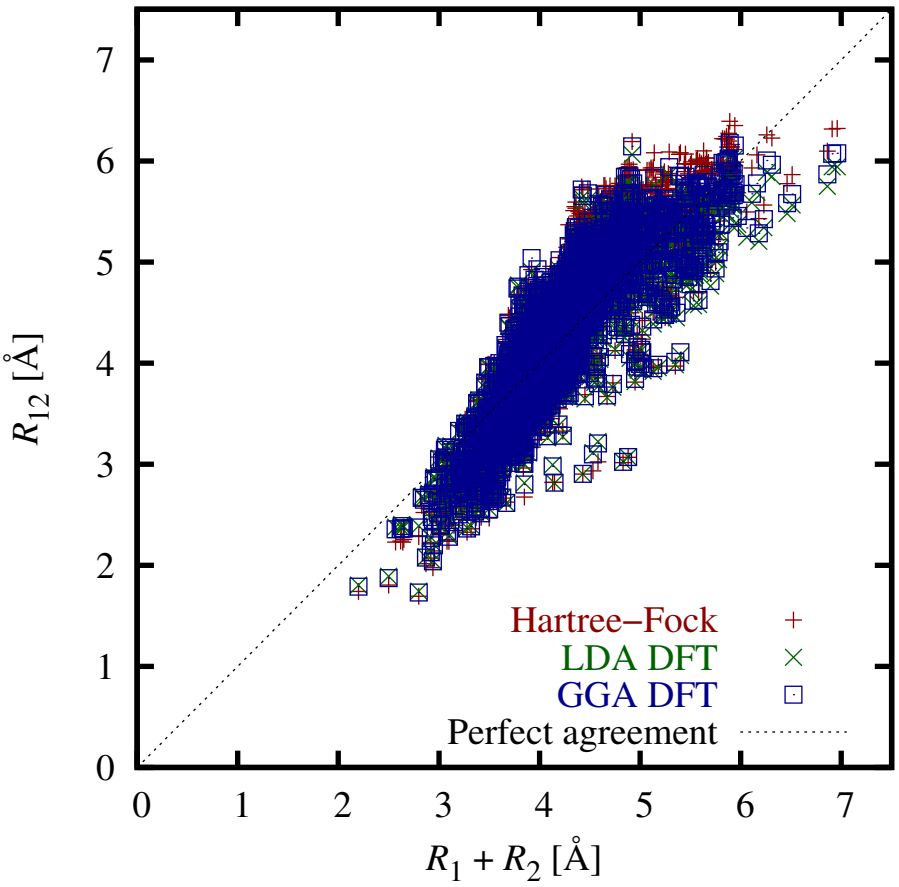

Figure 8.1: Atom separation, R_{12}, at which electron density overlap equals $\bar{n}_c = 1.2 \times 10^{-3}\ a_0^{-3}$, compared to sum of van der Waals radii, $R_1 + R_2$, for all pairs of atoms with vdW radii tabulated in [62, 102]. Differences between LDA, GGA and Hartree-Fock densities affect the correlation negligibly. This later enables a definition of the cavity shape as a function of the electron density overlap (8.2) which transitions from 0 to 1 at distance $R_{12} \approx R_1 + R_2$ from the solute nuclei (where 1 is solute and 2 is solvent).

sity overlap $\bar{n}(R_{12}) = \int d\vec{r} n_1(\vec{r}) n_2(\vec{r})$ crosses a threshold value of

$$\bar{n}_c = 1.2 \times 10^{-3}\ a_0^{-3} \tag{8.1}$$

correlates well with the sum of vdW radii [62] of the two atoms. Here, $n_1(\vec{r})$ and $n_2(\vec{r})$ are spherical electron densities of the two atoms (all-electron densities computed using OPIUM [117]), centered R_{12} apart, and we obtain $\bar{n}_c$ by

minimizing $\sum_{ij}(R_i + R_j - R_{ij})^2$. The minor differences between ground state densities from Hartree-Fock theory and electronic density functional theory with PZ-LDA [127] or PBE-GGA [128] exchange-correlation approximations do not affect these results.

The above correlation provides a universal threshold on the density product that can estimate the approach distance of non-bonded systems. We utilize this capability to determine the cavity for simplified solvation models without requiring any fits to solvation energies. In particular, the cavity shape functional

$$s(\vec{r}) = \frac{1}{2}\,\mathrm{erfc}\,\ln\frac{n_{\mathrm{lq}}^0(r) * n(\vec{r})}{\bar{n}_c} \tag{8.2}$$

smoothly transitions from vacuum ($s = 0$) to bulk fluid ($s = 1$) as the overlap of the electron density of a solvent molecule centered at $\vec{r}$ with the solute electron density, $n(r)$, crosses the universal overlap threshold $\bar{n}_c$. In principle, the overlap depends on the orientation of the solvent molecule, whereas the cavity only prescribes the spatial distribution. For simplicity, we assume a uniform orientation distribution of solvent molecules, which results in an orientation-averaged overlap measured by the convolution $n_{\mathrm{lq}}^0(r) * n(\vec{r})$. Here,

$$n_{\mathrm{lq}}^0(r) = \int \frac{d\hat{n}}{4\pi} n_{\mathrm{lq}}(r\hat{n}) \tag{8.3}$$

is a spherical average of the solvent molecule electron density $n_{\mathrm{lq}}(\vec{r})$, obtained from a solvated electronic density-functional calculation as Section 5.3 describes. Therefore, *ab initio* data completely constrains this cavity prescription for any solvent.

8.2 Spherically-averaged liquid susceptibility ansatz (SaLSA)

Having determined the orientation-averaged distribution of solvent molecules from the solute and solvent electron densities, we next need to describe the interactions between the two subsystems in this configuration. Sections 7.3 and 7.4 already prescribe non-empirical approximations for the the cavity formation and dispersion energies for a solvent configuration specified by a spatial distribution of centers, $N_{\text{bulk}}s(\vec{r})$, while assuming a uniform orientation distribution. We now treat the nonlocal electric response of the solvent in this configuration, completely constrained by *ab initio* and bulk properties of the solvent, to complete our non-empirical simplified solvation model.

We begin with a free energy functional for the solvent (following Chapter 5),

$$\begin{aligned}\Phi[p_\omega] = \Phi_0[N_0] + T\int d\vec{r}\int \frac{d\omega}{8\pi^2}p_\omega(\vec{r})\left[\ln\frac{p_\omega(\vec{r})}{N_{\text{bulk}}s(\vec{r})} - 1\right] \\ + \sum_\alpha \int d\vec{r}\frac{N_\alpha(\vec{r})\mathcal{P}_\alpha(\vec{r})^2}{2C_{\text{pol}}\chi_\alpha} + \frac{C_{\text{rot}}^{-1}-1}{N_{\text{bulk}}p_{\text{mol}}^2/3T}\int d\vec{r}\left(\int\frac{d\omega}{8\pi^2}p_\omega(\vec{r})\omega\circ\vec{p}_{\text{mol}}\right)^2 \\ + \int d\vec{r}\int d\vec{r}'\left(\rho_{\text{el}}(\vec{r}) + \frac{\rho_{\text{lq}}(\vec{r})-\rho_{\text{lq}}^0(\vec{r})}{2}\right)\frac{1}{|\vec{r}-\vec{r}'|}(\rho_{\text{lq}}(\vec{r}')-\rho_{\text{lq}}^0(\vec{r}')), \quad (8.4)\end{aligned}$$

in terms of $p_\omega(\vec{r})$, the probability of finding a solvent molecule centered at $\vec{r}$ with orientation $\omega \in$SO(3), and $\vec{\mathcal{P}}_\alpha$, the amplitude of polarization at each solvent molecule site, as independent variables. Briefly, the second term is the rotational entropy at temperature T, the third term is the potential energy for molecular polarization with site susceptibilities χ_α, the fourth term is a polarization density functional for rotational correlations for a solvent molecule with permanent dipole moment p_{mol}, and the final term is the mean-field interaction of the liquid charge density

$$\rho_{\text{lq}}(\vec{r}) = \sum_\alpha \rho_\alpha(r) * N_\alpha(\vec{r}) - \nabla\cdot\sum_\alpha w_\alpha(r) * N_\alpha\vec{\mathcal{P}}_\alpha, \quad (8.5)$$

with itself as well as with the solute charge density $\rho_{\text{el}}(\vec{r})$. We calculate the liquid site densities $N_\alpha(\vec{r})$ from the orientation density (Chapter 4), and derive all involved parameters from bulk properties and *ab initio* calculations of a single solvent molecule. For example, the bulk static and high frequency dielectric constants, ϵ_b and ϵ_∞ constrain the local field enhancement factors,

$$C_{\text{pol}} = \frac{\epsilon_\infty - 1}{4\pi N_{\text{bulk}} \sum_\alpha \chi_\alpha} \quad \text{and} \quad C_{\text{rot}} = \frac{\epsilon_b - \epsilon_\infty}{4\pi N_{\text{bulk}} p_{\text{mol}}^2/3T}. \tag{8.6}$$

(See Chapter 5 for details.)

The primary difference, here, is that we have collected all the contributions that depend only on the spherically-averaged density $N_0 = \int \frac{d\omega}{8\pi^2} p_\omega(\vec{r})$, such as the chemical potential, hard-sphere free energy and weighted-density excess functional into the first term, $\Phi_0[N_0]$. We also move the mean-field Coulomb interactions involving the liquid charge density in the initial uniform-orientation and unpolarized configuration, ρ^0_{lq}, given by (8.5) with $p_\omega = N_{\text{bulk}} s(\vec{r})$ and $\vec{\mathcal{P}}_\alpha = 0$, into the first term of (8.4). All subsequent terms of (8.4) are then exactly zero in that initial configuration.

We now assume that the orientation-independent interactions determine the cavity, for which the $s(\vec{r})$ given by (8.2) provides a reasonable guess, and that the cavity formation and dispersion terms absorb the resulting energy contributions (the scale factor in the dispersion term can absorb the so-called repulsion energy as demonstrated by the polarizable continuum model of Chapter 7). After assuming this PCM-like energy separation, we calculate the nonlocal electric contribution from the free energy functional (8.4), perturbatively about the cavity-prescribed initial configuration.

The perturbative treatment of (8.4) begins with an angular momentum expansion of the orientation density, $p_\omega(\vec{r}) = N_{\text{bulk}} s(\vec{r})(1 + \sum_{lmm'} x^l_{mm'}(\vec{r}) D^l_{mm'}(\omega))$,

where $D^l_{mm'}(\omega)$ are Wigner D-matrices (irreducible representations of SO(3) [174]). We then expand the free energy to quadratic order in the independent variables $x^l_{mm'}(\vec{r})$ (rotation) and $\vec{\mathcal{P}}_\alpha(\vec{r})$ (polarization), formally solve the corresponding linear Euler-Lagrange equations and substitute those solutions back into the quadratic form. After some tedious but straightforward algebra involving orthogonality of D-matrices, addition of spherical harmonics and their transformation under the D-matrices, as well as Fourier transforms to simplify convolutions (see Appendix D for details), we can show that the resulting free energy to second order is exactly

$$\Phi_{\text{SaLSA}} = \frac{1}{2}\int d\vec{r}\rho_{\text{el}}(\vec{r})\left[(\hat{K}^{-1}-\hat{\chi})^{-1}-\hat{K}\right]\rho_{\text{el}}(\vec{r}). \tag{8.7}$$

Here, $\hat{K}$ is the Coulomb operator and $\hat{\chi}$ is the nonlocal 'spherically-averaged liquid susceptibility' (SaLSA), expressed conveniently in reciprocal space as

$$\begin{aligned}\hat{\chi}(\vec{G},\vec{G}') \equiv -N_{\text{bulk}}\tilde{s}(\vec{G}-\vec{G}')\sum_{lm}\frac{C^l_{\text{rot}}}{T}\frac{P_l(\hat{G}\cdot\hat{G}')}{4\pi}\tilde{\rho}^{lm}_{\text{mol}}(G)\tilde{\rho}^{lm*}_{\text{mol}}(G') \\ -\sum_\alpha \tilde{N}^0_\alpha(\vec{G}-\vec{G}')C_{\text{pol}}\chi_\alpha\vec{G}\cdot\vec{G}'\tilde{w}_\alpha(G)\tilde{w}^*_\alpha(G'),\end{aligned} \tag{8.8}$$

where $\tilde{f}(\vec{G})$ denotes the Fourier transform of $f(\vec{r})$ for any f.

The first term of (8.8) is the rotational response from a cavity-prescribed distribution, $N_{\text{bulk}}s$, of molecules with charge density ρ_{mol}, decomposed into angular momentum channels as $\tilde{\rho}_{\text{mol}}(\vec{G}) = \sum_{lm}\tilde{\rho}^{lm}_{\text{mol}}(G)Y_{lm}(\hat{G})$. The prefactor $C^l_{\text{rot}} = C_{\text{rot}}$, the field enhancement factor for $l = 1$, and it equals unity for all other l.

The second term of (8.8) is the polarization response from molecule sites with non-local polarizabilities χ_α with range function $w_\alpha(r)$ (Chapter 5). The site densities, N^0_α, correspond to the initial configuration of $p_\omega = N_{\text{bulk}}s(\vec{r})$ (i.e. with $x^l_{mm'} = 0$); the polarization contributions from finite $x^l_{mm'}$ configurations appear

only at higher order in perturbation theory. In fact, $N_\alpha^0(\vec{r}) = N_{\text{bulk}} s(\vec{r}) * \delta(r - R_\alpha)/4\pi R_\alpha^2$ for a site at a distance R_α from the solvent center, which is exactly the site density set involved in the dispersion interaction term (Chapter 7).

For practical calculations, we rearrange (8.7) to $\Phi_{\text{SaLSA}} = \int(\phi - \phi_0)\rho_{\text{el}}/2$, where $\phi_0 = \hat{K}\rho_{\text{el}}$ is the electrostatic potential in vacuum and ϕ is the total (mean-field) electrostatic potential which solves the modified Poisson-like equation $(\nabla^2 + 4\pi\hat{\chi})\phi = -4\pi\rho_{\text{el}}$.

The $l = 1$ rotational and polarization terms in $\hat{\chi}\phi$ have the structure $\nabla \cdot w * N(\vec{r})w * \nabla\phi$ which resembles the Poisson equation for an inhomogeneous dielectric, except for additional convolutions with weight functions $\tilde{w}(G)$. Therefore, retaining only the $l = 1$ terms and reducing the molecules to points so that $\tilde{w}(G)$ becomes a constant, recovers the usual local dielectric limit employed by PCM's.

For neutral solvent molecules, the $l = 0$ term captures the interaction of the solute with a spherical charge distribution of zero net charge, and is zero except for small contributions from non-zero but negligible overlap of the solute and solvent charges. However, note that the response easily generalizes to mixtures, and for ionic species in the solution, the $l = 0$ terms convert the Poisson-like equation to a Helmholtz-like equation (with additional convolutions that introduce the nonlocality). This naturally captures the Debye-screening effects of electrolytes, resulting in well-defined absolute potentials necessary for the study of electrochemical systems [90].

Practical calculations with our nonlocal SaLSA approach employ a plane-wave basis, where the convolutions are essentially of zero cost, and truncate the angular momentum expansion at finite l. The iterative conjugate gradients

Table 8.1: Convergence of the nonlocal dielectric energy Φ_{SaLSA} with the maximum included angular momentum, $l_{\max}$ for several solutes in water.

Solute	Φ_{SaLSA} [kcal/mol (mE_h)]			
	$l_{\max} = 0$	$l_{\max} = 1$	$l_{\max} = 2$	$l_{\max} = 3$
Water	-1.4 (-2.3)	-6.2 (-9.8)	-6.3 (-10.0)	-6.5 (-10.3)
Methanol	-1.4 (-2.3)	-5.0 (-8.0)	-5.1 (-8.2)	-5.3 (-8.4)
Ethanol	-1.6 (-2.5)	-5.0 (-7.9)	-5.1 (-8.1)	-5.3 (-8.4)
Isopropanol	-1.7 (-2.8)	-5.1 (-8.2)	-5.3 (-8.4)	-5.4 (-8.7)
Benzene	-1.7 (-2.7)	-3.9 (-6.2)	-4.0 (-6.4)	-4.1 (-6.6)
Methylamine	-1.4 (-2.2)	-4.3 (-6.8)	-4.4 (-7.0)	-4.5 (-7.2)
Toluene	-1.9 (-3.1)	-4.2 (-6.7)	-4.4 (-6.9)	-4.5 (-7.2)
Phenol	-2.2 (-3.5)	-6.8 (-10.9)	-7.0 (-11.1)	-7.2 (-11.4)
Anisole	-2.2 (-3.5)	-5.5 (-8.7)	-5.6 (-8.9)	-5.8 (-9.2)
Pyridine	-2.0 (-3.2)	-5.4 (-8.7)	-5.6 (-8.9)	-5.7 (-9.1)

method, with a diagonal preconditioner derived from the bulk response, rapidly converges the solution of this modified Poisson-like equation. Truncated up to $l = 1$, the cost of this nonlocal Poisson solve is only a factor of 2-3 higher than that of the standard local case. The computational cost scales quadratically with the highest included angular momentum, $l_{\max}$. The higher angular momenta $l > 1$ have successively smaller contributions because of the usual properties of multipole expansions for the interactions between two mostly non-overlapping charge distributions. Consequently, the $l = 1$ term dominates for pure solvents, whereas the $l = 0$ term dominates for electrolytes (solutions with ions). Table 8.1 shows the convergence of Φ_{SaLSA} with $l_{\max}$ for several solutes in water. The dominant contribution is from $l = 1$, as expected. In the following, we truncate calculations at $l = 2$ as a reasonable trade-off between computational effort and accuracy, noting that the typical contributions from $l = 3$ are less than 0.2 kcal/mol (0.3 mE_h), well within the typical accuracy $\sim$ 1 kcal/mol (1.6 mE_h) achievable in solvation models.

Table 8.2: Fit parameters and residuals for the SaLSA nonlocal solvation model

Solvent	s_6		RMS error [kcal/mol (mE_h)]	
	Fit	Fixed	Fit	Fixed
H_2O	0.68	0.61	1.5 (2.4)	1.8 (2.9)
$CHCl_3$	1.34	1.18	0.7 (1.1)	1.3 (2.1)
CCl_4	1.62	1.53	0.7 (1.1)	0.8 (1.3)

8.3 Solvation energies

The spherically-averaged liquid susceptibility ansatz (SaLSA) results in the free energy, Φ_{SaLSA} given by (8.7), with the nonlocal response χ given by (8.8), and with all microscopic parameters from *ab initio* calculations of a solvated solvent molecule (Chapter 5). The correlation of atomic vdW radii with the convolution of solute and solvent electron densities thresholded on a universal critical density product (8.1), prescribes a cavity shape function $s(\vec{r})$ given by (8.2) with no adjustable parameters. Finally, the cavity for nonlocal response is precisely the cavity bounding solvent centers and is therefore directly applicable in the physical weighted-density models for cavity formation and dispersion energies of Chapter 7. Combining these terms results in the SaLSA nonlocal solvation model,

$$A_{\text{diel}} = \Phi_{\text{SaLSA}} + G_{\text{cav}}[s] + E_{\text{disp}}[s], \tag{8.9}$$

which bulk solvent properties and *ab initio* calculations completely constrain, except for the dispersion scale factor, s_6, in E_{disp}[s].

Following the approach of Chapter 7, we fit the s_6 for each solvent to molecule solvation energies. Table 8.2 shows that the SaLSA model fits the solvation energies with an accuracy of ~ 1 kcal/mol (1.6 mE_h) for all solvents, without adjusting the cavity size parameter, $\bar{n}_c$. In fact, the residuals in the solvation

energies are only 50% worse compared to the polarizable continuum model of Chapter 7; the latter also fits its cavity size parameter to solvation. The optimum s_6 parameters differ for the three fluids, but remain within 35% of the range 0.75-1.2 covered by different electronic functionals in [53], just as for the PCM of Chapter 7.

Finally, calibration of s_6 to a single non-polar molecule can replace the solvation fit, thereby simplifying the extension of the approach to other solvents. In fact, fixing s_6 to the solvation energy of benzene works for water, chloroform as well as carbon tetrachloride, as Figure 8.2 shows, similar to the case of Chapter 7. Table 8.2 shows that this 'fixed' s_6 is similar to the fit values, and the residual is less than 2 kcal/mol (3 mE_h) in all cases. This allows the construction of a simplified solvation model that captures microscopic details of the solvent response, which is adequate for first principles calculations of processes in solution and requires the solvation energy of only a single molecule in that solvent as input.

8.4 Summary

This chapter combines the nonlocal electric response of the solvent, derived from the linear response of classical density functional theory, with the non-empirical cavity formation and dispersion functionals of Chapter 7. With the angular momentum expansion of Section 8.2, this enables a non-empirical solvation model that captures details of the solvent effect at a level comparable to full joint density functional theory, but at computational cost comparable to traditional empirical polarizable continuum models. This combination of accuracy,

(a) H_2O

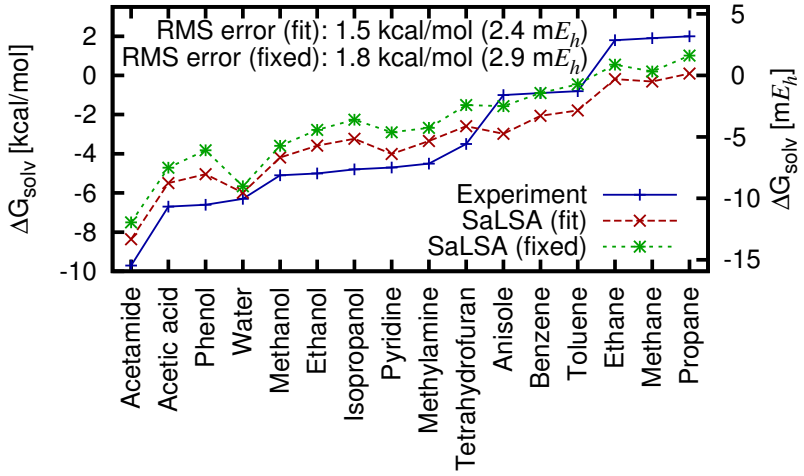

(b) $CHCl_3$

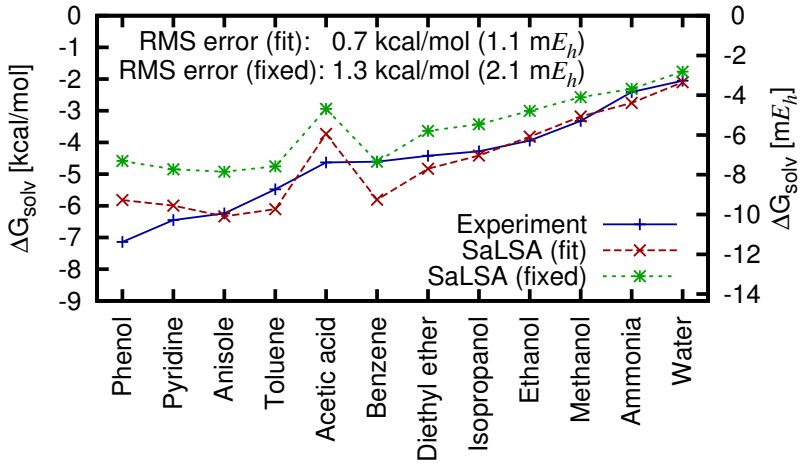

(c) CCl_4

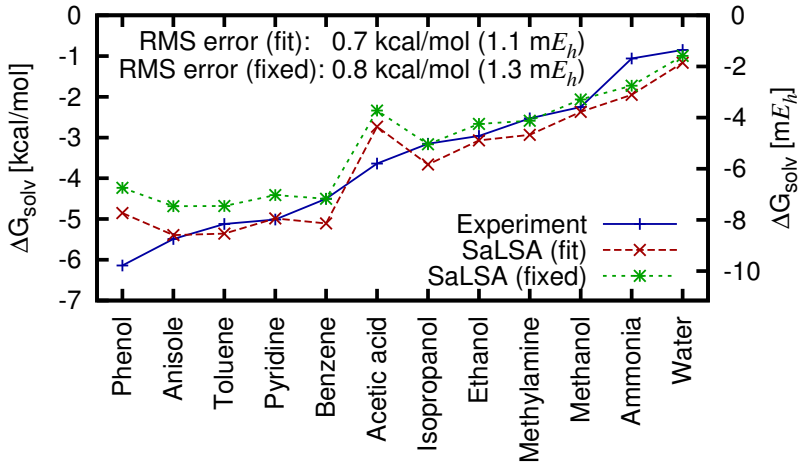

Figure 8.2: Solvation energies predicted by the SaLSA nonlocal solvation model for molecules in (a) water, (b) chloroform and (c) carbon tetrachloride, compared to experiment. Phenol and acetic acid seem to be outliers in (b) and (c), probably due to a weak chemical bond between the solute and solvent in the experiment that is missed by the solvation model.

rigor and efficiency make it the ideal candidate for studies of complex solvated systems, which we demonstrate next for a well-studied model electrochemical system: the underpotential deposition of copper on platinum.

CHAPTER 9

UNDERPOTENTIAL DEPOSITION

Electrochemical interfaces are a key component of many technologically important systems involving catalysis, energy conversion and storage, such as fuel cells and batteries. The large number of solvent and adsorbent configurations highly sensitive to the electrode potential, significantly complicates first principles studies of such systems.

Ab initio solvation theories can mitigate some of this complexity by abstracting the effect of the solvent, thereby enabling a focused study of the configurations and reactions of adsorbents on the surface. Here, we apply our nonlocal solvation theory to understand in full microscopic detail, an experimentally well-studied and prototypical electrochemical process: the underpotential deposition of copper on the (111) surface of single-crystalline platinum.

9.1 Experimental studies and phenomenology

The application of sufficiently negative (reductive) potentials on an electrode immersed in a solution containing metal ions, reduces those ions and results in bulk electro-deposition of metal on the surface. Additionally, for many pairs of metals, a single monolayer of one metal deposits on a surface of the other at an under potential, that is, at a potential less favorable than for bulk deposition. This phenomenon of under-potential deposition (UPD) has several technological applications since it enables precise synthesis of heterogeneous metal interfaces, and it also serves as an archetype for fundamental studies of electrochemical processes; see [64] for an extensive review.

The basic reason for underpotential deposition is that the heterogeneous binding between the two metals is stronger than the homogeneous binding of the depositing metal to itself. Indeed, metal pairs that exhibit underpotential deposition also display analogous phenomena in vapor adsorption [119]. However, the process in solution is far more complicated and highly sensitive to the composition of the solution because of competing adsorbates [173], as well as to the structure of the electrode surface [114].

Voltammetry, the measurement of electrode current while scanning the electrode potential, finds a peak in the current at the potential where the monolayer deposition occurs. For the electro-deposition of copper on the (111) surface of platinum (denoted by Cu/Pt(111)) from an acidic sulphate solution containing Cu^{2+} cations, this peak occurs at an under-potential shift of 0.44 V relative to that for bulk deposition [83]. Scanning the potential in the opposite direction yields an almost symmetric reverse current peak, indicating that the process is reversible and in quasi-equilibrium. The exact location of the peak, however, is sensitive to the concentrations of the solutions and the identity of the anions [104, 51, 100]. In fact, the UPD potential correlates linearly with the oxidation potential of the anionic species [172], indicating co-adsorption of and partial charge transfer to the anions.

The UPD of Cu/Pt(111) in the presence of chloride anions is particularly interesting and the subject of considerable debate in the literature. Voltammetry for this system exhibits two well-separated under-potential peaks (Figure 9.1(d)). Certain LEED and in situ X-ray scattering studies of this system [103] find evidence of a 2×2 bilayer of copper and chloride ions co-adsorbed on the surface (Figure 9.1(b)) at potentials between the two peaks, suggesting that

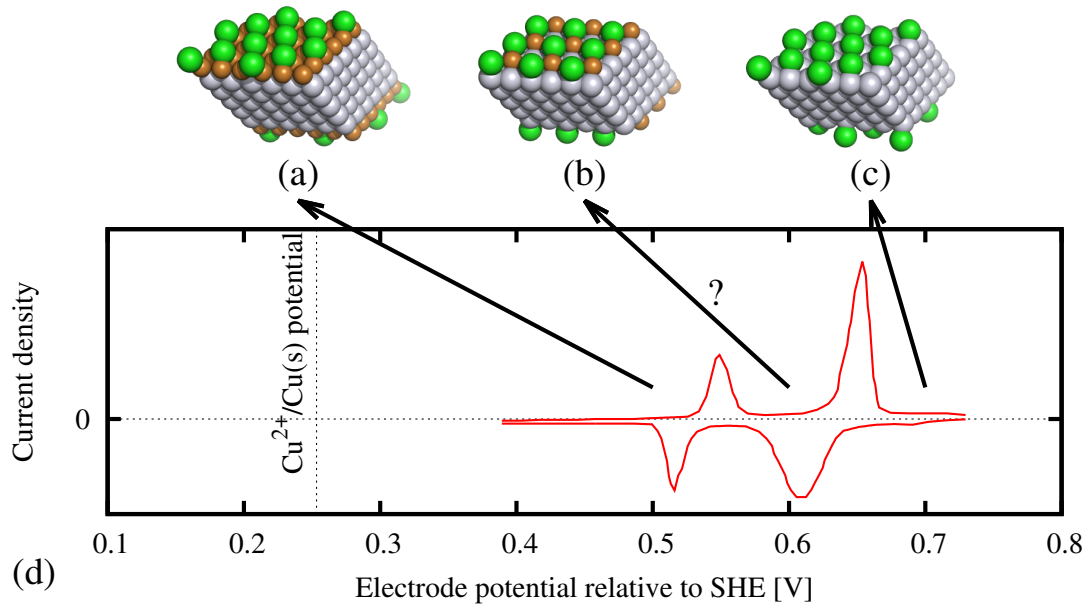

Figure 9.1: Experimental surface structures for UPD of Cu/Pt(111) with Cl^- for (a) full copper monolayer, (b) partial copper monolayer (proposed by [103]) and (c) no copper coverage, as well as (d) voltammogram from [17] measured at concentrations of 10^{-3} mol/liter of Cu^{2+} and 10^{-4} mol/liter of Cl^-.

one peak corresponds to a formation of a partial layer, and the second peak, to the formation of the full monolayer. In contrast, other studies [144, 17, 5] do not find this signature and propose that the additional peak arises from adsorption and desorption of chloride ions alone.

Phenomenological models of under-potential deposition correlate work function differences of the metals to the UPD shifts [84], predict these shifts with reasonable accuracy after including experimentally input surface coverages and adsorption energies [150, 149], and even predict the shape of the voltammetric peaks using statistical models for the phase transitions on the surface [18, 71]. However, such models do not incorporate the microscopic detail necessary to resolve debates such as the identity of the two peaks in the UPD of Cu/Pt(111) in the presence of chloride anions.

9.2 First-principles calculations

First principles calculations can provide detailed microscopic information about the structure of the electrode surface and processes occurring on it, but complexity and computational cost force several simplifying assumptions and limit the realism of studies for these systems. Traditional density-functional studies of underpotential deposition include only the substrate metal and the adsorbed monolayer [88], which results in a significant underestimation of the UPD shift, or even an incorrect prediction of over-potential monolayer deposition in some systems [139]. Here, we study the UPD of Cu/Pt(111) with chloride anions in full microscopic detail, including the effect of chloride adsorption on the surface.

9.2.1 Computational details

We focus our detailed electronic structure description on the platinum surface, copper layers and adsorbed chloride ions, while describing the aqueous solution with dissolved ions using the nonlocal solvation model of Chapter 8. For the electronic system, we employ Kohn-Sham electronic density-functional theory with the revTPSS meta-GGA exchange-correlation functional [129], since it is systematically more accurate than generalized-gradient approximations for surfaces [151]. We perform all calculations in JDFTx [154] with norm-conserving pseudopotentials[1] and a plane-wave cutoff of 30 E_h.

[1]The platinum and copper pseudopotentials predict lattice constants for the face-centered cubic metals within 0.5 % of all-electron FP-LAPW (full potential linear augmented plane-wave) calculations from [142]. The chlorine and hydrogen pseudopotentials predict bond lengths of H_2, Cl_2 and HCl molecules within 1 %, and formation energy of HCl within 1 mE_h, compared to all-electron calculations in the aug-cc-pVTZ basis set from [115].

We treat the electrolyte as an aqueous solution with 1 mol/liter each of cations and anions; these ions in solution merely provide a convenient means to provide an absolute reference for the electrode potential [90] and their details do not affect the processes on the surface.[2] The high concentration of these ions results in a Debye screening length of 3 Å at room temperature (298 K), which rapidly screens interactions between periodic images of the surface in the normal direction. Specifically, our unit cells are 47 Å long in the surface normal direction, and the smallest image distance of 25 Å in any of the configurations below benefits from a 1 in 10^4 isolation due to the electrolyte.

We use a Fermi smearing of 4 mE_h for Brillouin zone integration, which leads to better than 0.4 mE_h or 0.01 eV convergence with a $6 \times 6 \times 6$ Monkhorst-Pack $\vec{k}$-point mesh for bulk face-centered cubic platinum. A five layer slab configuration with a 6×6 Monkhorst-Pack $\vec{k}$-point mesh in the plane results in similar convergence for the (111) surface energies. The calculations use the equilibrium DFT lattice constant of 3.94 Å, which is within 0.5% of the experimental value of 3.92 Å. The difference in electron entropies amongst all the configurations we consider below is less than 1 mE_h, indicating that the elevated electron temperature for Fermi smearing leads to negligible errors.

9.2.2 Free energy and reference potentials

Having described the computational setup for the pristine Pt(111) electrode in solution, we now proceed to study the formation of copper monolayers and adsorption of ions on its surface. The platinum surface is in electrical contact with

[2] Ions at the polarizable continuum level of description do not specifically adsorb on the surface (Chapter 6), and we account for chemically active ions at the electronic density-functional level.

a voltage source connected to a reference electrode in the experimental system, which translates to an electron reservoir in the calculation. The electrolyte at the interface is in contact with the bulk electrolyte, which is a reservoir for cupric and chloride ions. The appropriate ensemble that describes the unit cell of the calculation is, therefore, grand canonical in electrons as well as the ionic species in solution,

$$\Phi = A - \sum_{\alpha} \mu_{\alpha} N_{\alpha} - \mu \left(n - \sum_{\alpha} N_{\alpha} n_{\alpha} \right). \tag{9.1}$$

Here, A is the Helmholtz energy of the solvated electronic density-functional calculation with n valence electrons per cell, μ is the chemical potential for electrons, N_{α} is the number of ions of species α per cell, and μ_{α} are the corresponding chemical potentials. A fraction of the valence electrons enter the system along with the ions, specifically n_{α} for each ion of species α, and the electron chemical potential tracks the remainder that enter from the electrode.

All calculations employ inversion-symmetric unit cells, with identical adsorbent configurations on both surfaces of the five layer platinum slab. The configurations vary in their transverse periodicity, including 1×1, $\sqrt{3} \times \sqrt{3}$ and 2×2 super-structures relative to the bare platinum (111) surface. The free energy (9.1) is extensive in the two lateral directions, and we normalize it per platinum surface atom in order to compare energies from calculations with these different unit cells.

In our calculations below, α includes Cu^{2+}, Cl^{-} and H^{+} ions referenced to the bulk electrolyte at the experimental concentrations, as well as Pt referenced to the bulk solid. The Pt chemical potential μ_{Pt}, which we set to the energy per atom of bulk platinum, does not affect the results in any way, since all calculations have the same five layer platinum electrode. However, including Pt in the

set of α's, subtracts a large constant energy contribution ($\mu_{\mathrm{Pt}} N_{\mathrm{Pt}}$) and a constant slope with electrode potential ($n_{\mathrm{Pt}} N_{\mathrm{Pt}}$), which leads to significantly clearer plots of free energy versus electrode potential.

The reference condition for each ionic species is the bulk electrolyte, but directly calculating the free energy of ions in solution to the necessary accuracy is beyond the capability of current solvation theories. Instead, we connect the ions in solution to a manageable reference state via standard experimental electrode potentials. The electrode potential, $V_{\mathrm{Cu(s)/Cu^{2+}}}$, for copper reduction, $\mathrm{Cu^{2+}} + 2e^- \rightleftharpoons \mathrm{Cu(s)}$, determines the cupric ion chemical potential to be

$$\mu_{\mathrm{Cu^{2+}}} = A_{\mathrm{Cu(s)}} - 2\mu_{e^-}(V_{\mathrm{Cu(s)/Cu^{2+}}}) + T \ln [\mathrm{Cu^{2+}}]. \tag{9.2}$$

Here, $A_{\mathrm{Cu(s)}}$ is the Helmholtz energy per atom from an electronic density-functional calculation of face-centered cubic metallic copper, and the function $\mu_{e^-}(V_{\mathrm{el}})$ converts experimental electrode potentials measured relative to a reference electrode, to electron chemical potentials within our theory, as we describe at the end of this section. The final term accounts for the difference in entropy of cupric ions between the standard concentration of 1 mol/liter and the actual concentration in the bulk electrolyte; $[Cu^{2+}]$ is therefore the concentration of cupric ions in mol/liter.

Analogously, the electrode potential, $V_{\mathrm{Cl_2(g)/Cl^-}}$, for chlorine reduction, $\mathrm{Cl_2(g)} + 2e^- \rightleftharpoons 2\mathrm{Cl^-}$, determines the chloride ion chemical potential

$$\mu_{\mathrm{Cl^-}} = \frac{1}{2}\left(E_{\mathrm{Cl_2}} + \mathrm{ZPE}_{\mathrm{Cl_2}} - TS_{\mathrm{Cl_2}}\right) + \mu_{e^-}(V_{\mathrm{Cl_2(g)/Cl^-}}) + T \ln [\mathrm{Cl^-}]. \tag{9.3}$$

The relation is similar to that for copper, but the evaluation of the gas phase free energy includes the ground-state electronic density-functional energy for a single chlorine molecule, $E_{\mathrm{Cl_2}}$, as well as zero-point vibrational energy and

Table 9.1: Experimental electrode potentials relative to the standard hydrogen electrode, and thermodynamic data that determine chemical potentials for ionic species.

Ion	Electrode	$V_{\text{electrode}}$ [V] (from [62])	Ref. state	ZPE [mE_h] (from [115])	S (from [62])
Cu^{2+}	$Cu(s)/Cu^{2+}$	+0.342	Cu(s)	-	-
Cl^-	$Cl_2(g)/Cl^-$	+1.358	$Cl_2(g)$	1.23	26.83
H^+	$H^+/H_2(g)$	+0.000	$H_2(g)$	9.84	15.72

entropy contributions that are not negligible (unlike analogous contributions from phonons in solid copper). Similarly, the electrode potential, $V_{H^+/H_2(g)}$, for the reaction, $2H^+ + 2e^- \rightleftharpoons H_2(g)$, determines the H^+ chemical potential

$$\mu_{H^+} = \frac{1}{2}\left(E_{H_2} + \text{ZPE}_{H_2} - TS_{H_2}\right) - \mu_{e^-}(V_{H^+/H_2(g)}) + T\ln[H^+]. \tag{9.4}$$

Table 9.1 summarizes the experimental data involved in the determination of the ionic chemical potentials.

Finally, we calibrate the experimental electrode potentials to theoretical electron chemical potentials using the potentials of zero charge of single crystalline metal electrodes, following [90]. Figure 9.2 correlates the measured electrode potentials of neutral surfaces [165] to the electron chemical potentials, μ, governing the Fermi occupation of Kohn-Sham orbitals in electronic density-functional calculations of those surfaces. The optimum correlation for revTPSS calculations with the nonlocal SaLSA solvation theory is $\mu_{e^-}(V_{\text{el}}) = -(V_{\text{el}} + 4.50\ \text{V})$, with a root-mean squared deviation of 0.09 V. The intercept, which accounts for the unknown absolute potential of the standard hydrogen electrode and absorbs systematic offsets in theoretical predictions, is reasonably close in comparison to the previous value of 4.44 V for PBE exchange-correlation and PCM solvation [90].

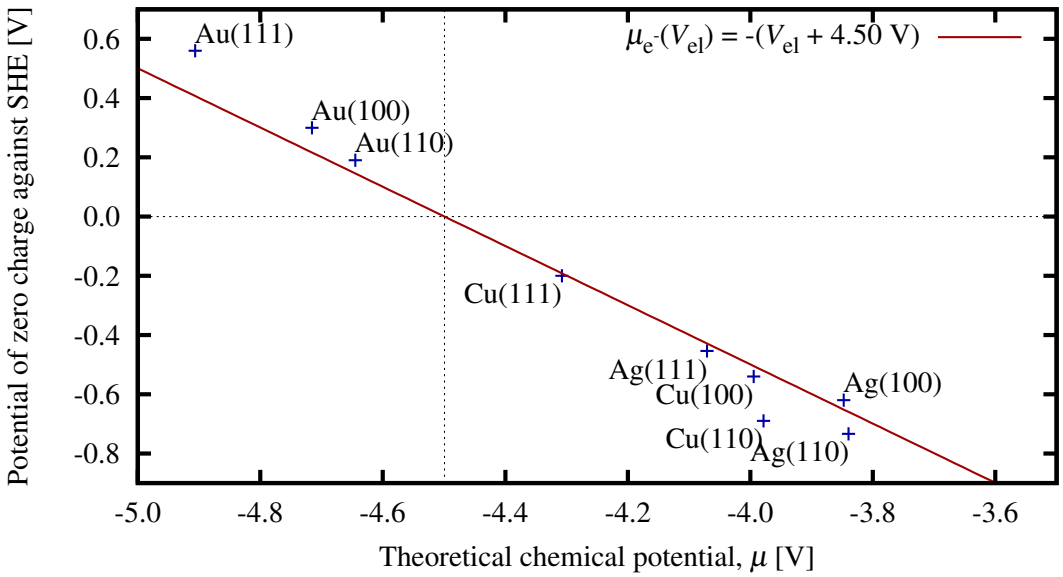

Figure 9.2: Calibration of experimental electrode potentials, measured relative to the standard hydrogen electrode (SHE), against theoretical electron chemical potentials, μ, by correlating measured potentials of zero charge [165] with μ in density-functional calculations of neutral single-crystalline metal surfaces.

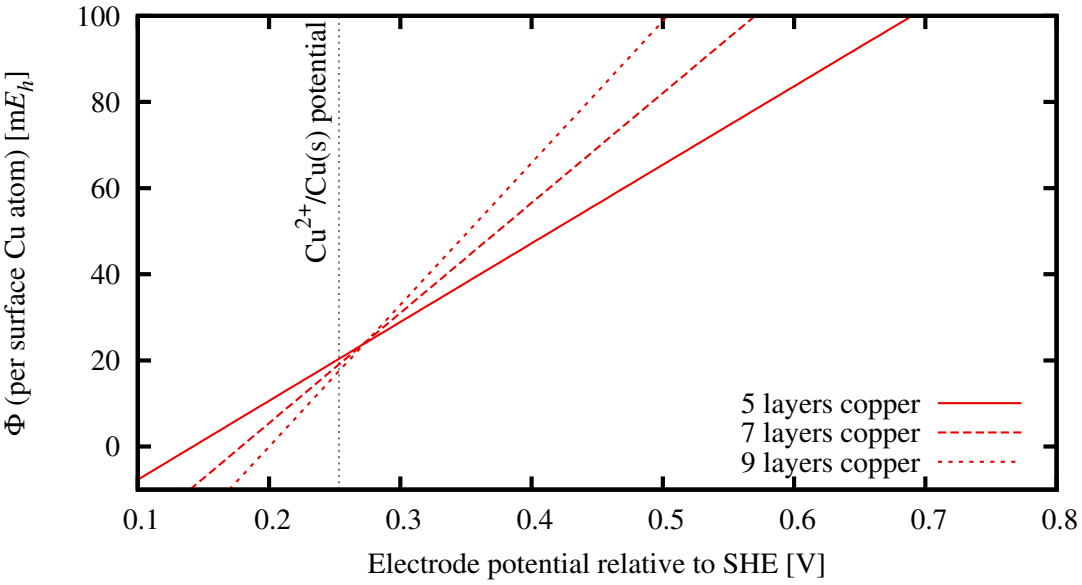

Figure 9.3: Free energy curves (per Cu surface atom) for copper electrodes in a solution containing 10^{-3} mol/liter Cu^{2+} ions, with the stable configuration switching from fewest layers to most layers close to the bulk reduction potential.

Now, we can calculate the grand free energy, Φ given by (9.1), for any electrode surface comprising platinum, copper, chlorine and hydrogen, as a function of experimental electrode potential referenced to the standard hydrogen electrode. The configuration with the lowest free energy at a given electrode potential is the most stable, and points where the two lowest free energy curves cross mark transitions, which would correspond to a peak in the voltammogram. For example, Figure 9.3 plots the free energy of copper electrodes in a solution containing 10^{-3} mol/liter Cu^{2+} ions, with varying number of copper layers. Fewer layers are stable at higher potentials, and more layers at lower potentials, with the cross-over occurring close to the bulk reduction potential; the small discrepancy ~ 0.02 V in the cross-over potential is a measure of the error in the surface energy per atom of finite slabs from the macroscopic limit.

9.2.3 Results

We begin by considering only the deposition of copper on platinum, while ignoring the co-adsorption of other species such as the anions and H^+. Figure 9.4 shows the free energies of the platinum surface with no, partial (2×2), one and two monolayers of copper, in a solution with 10^{-3} mol/liter of Cu^{2+} and 10^{-4} mol/liter of Cl^-, overlaid on the experimental voltammogram [17] at those concentrations. At high potentials, the platinum surface is the most stable. With reducing potential, it transitions directly to the full monolayer of copper at a potential much lower than either voltammogram peak. Finally, the second monolayer becomes stable close to the bulk reduction potential of copper. Without including co-adsorbed anions, the underpotential shift is significantly smaller than the experimental value, exactly as in previous first-principles calculations

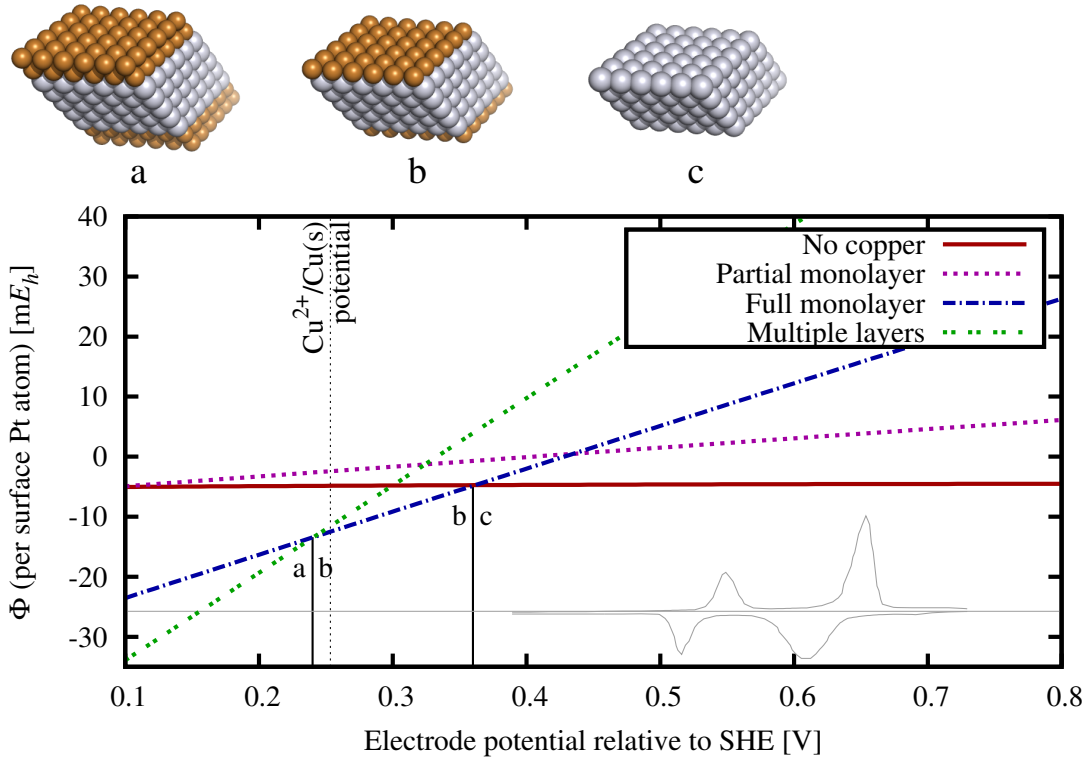

Figure 9.4: Free energies (per Pt surface atom) versus electrode potentials for Pt(111) surface configurations comprising Cu alone, overlaid with the experimental voltammogram from [17]. The vertical lines mark transitions in the stable configuration, and the top panels show the stable configurations in each regime. The partial monolayer (2×2 Cu) is not stable at any potential, and the full monolayer deposition occurs at much lower potentials than any of the voltammogram peaks.

[139]. The partial monolayer is never the stable configuration, which we could attribute at this stage to the the underestimation of monolayer stability in the absence of co-adsorbents.

Next, we include chloride and hydrogen in addition to copper on the surface. In particular, we calculate the free energy (9.1) for various $\sqrt{3} \times \sqrt{3}$ and 2×2 configurations of chloride alone, as well as chloride with hydrogen, on each of the previously considered Cu configurations. The chloride prefers the fcc hollow sites on any of the full metal layers, and the threefold hollow sites on the

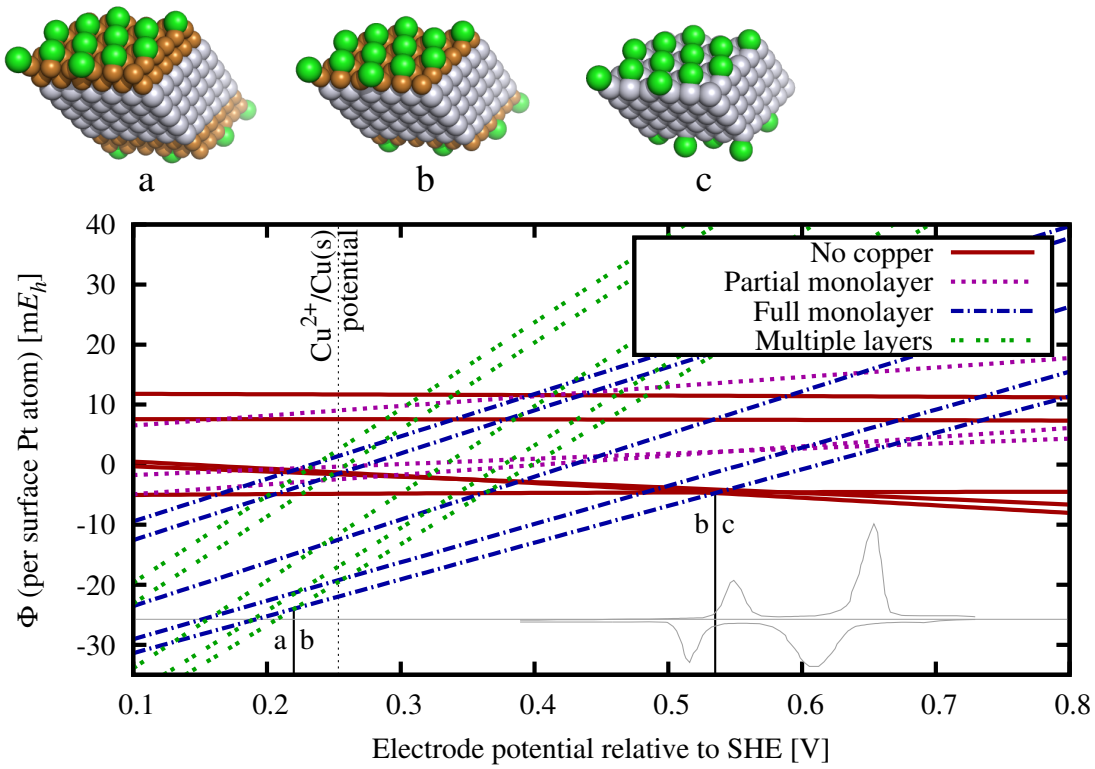

Figure 9.5: Free energies (per Pt surface atom) versus electrode potentials for Pt(111) surface configurations comprising Cu, Cl and H. Lines of each group have the same Cu coverage, and in order of least stable to most stable correspond to 2×2 (H,Cl), $\sqrt{3} \times \sqrt{3}$ (H,Cl), clean surface, 2×2 Cl, and $\sqrt{3} \times \sqrt{3}$ Cl, with the following exceptions. The partial Cu monolayer group contains only the 2×2 and no Cl configurations from the above list. The most stable configuration of the no Cu group transitions from clean surface to $\sqrt{3} \times \sqrt{3}$ Cl, just left of the b↔c transition. Partial monolayers with 2×2 Cu are not stable at any potential, but the potential for full monolayer deposition is in excellent agreement with the left voltammogram peak.

2×2 copper layers (as in Figure 9.1(b)). In each case, the hydrogen prefers the atop site above the chloride. Figure 9.5 shows the optimum free energies from each group of equal copper, chloride and hydrogen coverage as a function of electrode potential.

The free energy curves within each group of equal copper coverage are mostly parallel with a few exceptions. The systems with hydrogen are always

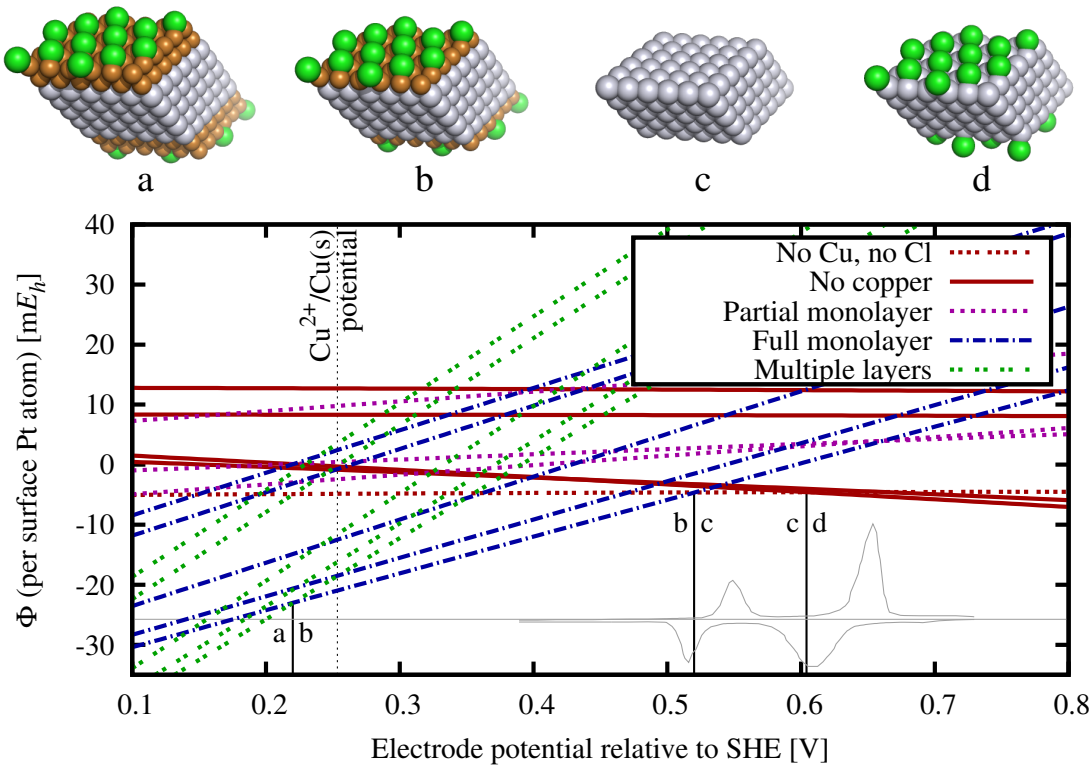

Figure 9.6: Same as Figure 9.5, but with μ_{Cl^-} reduced by 3 mE_h. The transition from clean Pt surface to $\sqrt{3} \times \sqrt{3}$ adsorbed Cl moves to slightly higher potentials and agrees with the right voltammogram peak. Full monolayer deposition remains in excellent agreement with the left voltammogram peak.

the least stable, indicating that co-adsorption of hydrogen is not important in the UPD process. The chloride coverage in increasing order of stability is none, 2×2 and then $\sqrt{3} \times \sqrt{3}$. Therefore the clean surfaces of Figure 9.4 are completely masked by the more stable chloride covered surfaces. The picture does not change qualitatively: the partial monolayers are still never the most stable configuration, and are unstable by about the same energy $\sim$ 10 mE_h per Pt surface atom. However, the transition to the full monolayer now occurs in quantitative agreement with the left voltammogram peak.

The platinum surfaces without copper transition from no chloride coverage to $\sqrt{3} \times \sqrt{3}$ at a potential and free energy very close to the b↔c transition in

Figure 9.5. This transition would result in a second peak in the voltammogram, if it occurred at a slightly higher potential. Figure 9.6 shows that indeed a shift in the chemical potential of the chloride ions of just 3 mE_h moves this transition to quantitative agreement with the second experimental peak. It is reasonable to expect errors of this magnitude to arise from density functional approximations for the reference molecule, or from the neglect of vibrational energies in the solid.

The free energy per surface atom of the partial monolayer, on the other hand, is at least 10 mE_h higher than the most stable configuration at all electrode potentials, and this difference is not sensitive to errors in the reference chemical potentials. Further, the copper-chlorine plane distance of (1.2 ± 0.3) Å in the experimentally proposed 2×2 partial monolayer structure of [103], disagrees with the theoretical prediction of 0.6 Å. Our calculations, therefore, strongly suggest the adsorption of chloride, rather than the formation of a partial monolayer, as the reason for the second voltammetric peak in the presence of chloride ions.

Some differences remain between the scenario in Figure 9.6 and experimental proposals [5]. The latter identify the left voltammetric peak with full copper monolayer formation and the right peak with chloride desorption off the copper, but do not propose structures for adsorbed anions. Our present calculations predict desorption of chloride from the copper monolayer only at potentials ≈ -0.6 V, far below the bulk copper reduction potential ≈ 0.25 V. A likely alternative explanation, more consistent with the experimental proposal, would be a switch from adsorbed chloride to sulfate or bisulfate; exploring this scenario would require more calculations with larger supercells.

9.3 Summary

This chapter presents a first principles study of the underpotential deposition of copper on the (111) surface of platinum in the presence of chloride ions, with full microscopic detail. The nonlocal solvation theory of Chapter 8 captures the effect of the solvent, and with ionic screening, fixes absolute potentials that enables calibration of the experimental electrode potentials. A grand canonical model of the surface allows direct comparison of surface configurations with varying coverages of copper, chlorine and hydrogen.

Our computational results favor chloride adsorption [144, 17, 5] as the likely explanation for the additional voltammetric peak, rather than the formation of a partial monolayer [103]. Further calculations that include sulfate and bisulfate adsorption are necessary to confirm the exact chloride adsorption scenario proposed based on experimental measurements.

CHAPTER 10

OUTLOOK

Joint density-functional theory provides a rigorous framework to study the electronic structure of a system in solution. It formally combines electronic density-functional theory for the solute with classical density-functional theory for the solvent. The former is an exact theory for the electronic ground state energy in terms of the electron density at fixed nuclear positions (Born-Oppenheimer surface), whereas the latter is an exact theory for the equilibrium free energy of a liquid in terms of its nuclear densities.

The exact free energy functional for the solvated system, $\Phi_{\text{JDFT}}[n, \{N_\alpha\}]$, in terms of the solute electron density, $n(\vec{r})$, and the solvent nuclear densities, $\{N_\alpha(\vec{r})\}$, is unknown and needs to be approximated. The exact partitioning (1.17) of this functional into electronic, liquid and coupling functionals enables the development of approximations for each piece independently, and the selection of different levels of approximation for each piece depending on the system of interest and the computational resources available.

Approximations to the electronic density functional, $F_{\text{HK}}[n]$, abound in the literature, particularly within the Kohn-Sham formalism with an approximate exchange and correlation functional. Of these, hybrid density functionals, which include a fraction of the exact non-local exchange energy, are particularly accurate and widely employed for first principles predictions of chemical reactions of molecules. In periodic systems, with state-of-the-art methods for computing the exchange energy, they require a greater number of $\vec{k}$-points than semi-local functionals to resolve the singularity in the Coulomb kernel at zero wave-vector. The convergence with $\vec{k}$-points for these methods is particularly

slow for the highly anisotropic and asymmetric unit cells (supercells) encountered in the study of chemical reactions at solid-liquid interfaces.

Chapter 2 analytically proves truncation of the Coulomb kernel on the Wigner-Seitz cell of the $\vec{k}$-point sampled superlattice as the ideal regularization method for computing the exchange energy. For a wide variety of systems with varying electronic structure, symmetry and dimensionality, this method exhibits $\vec{k}$-point convergence comparable to that of traditional semi-local functionals, and far superior to that of previous methods for computing the exact exchange energy. Although hybrid functional calculations employing this method no longer require extra $\vec{k}$-points beyond semi-local calculations, the computational cost of the exact exchange energy in the plane-wave basis is still far greater (often $100 - 1000\times$) in comparison to semi-local approximations. The widespread application of hybrid density functionals to the study of processes at solid surfaces, such as heterogeneous catalysis, is still limited by computational resources. The development of more efficient algorithms for computing the exchange energy, in addition to the regularization methods developed here, would therefore be beneficial. Linear-scaling algorithms using maximally-localized Wannier functions [176] enable such calculations for large insulating systems, but analogous general methods that can handle metallic systems remain to be developed. The Wannier-like functions of Section 2.1 which include Fourier transforms of the occupations, in combination with the localization optimization methods of [107], might provide a route to such a general method.

Approximations to the the free energy functionals of liquids, within the framework of classical density-functional theory, also abound in the literature [57], but most of these approximations target model liquids with simplified

Hamiltonians, primarily composed of pairwise-additive potentials, and primarily for mono-atomic or simple fluids of spherical particles without orientation or internal degrees of freedom. First principles studies of solvated systems using joint density-functional theory, however, require free energy functional approximations for real liquids that target the full Hamiltonian and account for all these degrees of freedom.

Chapter 4 presents a practical framework for classical density-functional calculations of molecular liquids including orientational degrees of freedom, by extending the approach of [96] for exactly computing the free energy of a non-interacting system of rigid (but orientable) molecules with the same density as the interacting system. Chapter 5 extends this approach further by perturbatively accounting for vibrations and electronic polarizability of the molecules in the liquid, and establishes a procedure for determining the geometry of the solvent molecule, its charge distribution, and its susceptibility from electronic density functional calculations. The task that remains, then, is to evaluate the contributions to the free energy arising from interactions between the molecules, for any given set of nuclear densities.

Chapter 3 presents one such excess free energy functional for water by constructing a model Hamiltonian from an intuitive picture of empty spaces in the tetrahedral network of hydrogen bonds and calibrating the parameters of that Hamiltonian to the experimental equation of state of water. Chapter 4 then shows that a much simpler ansatz consisting of repulsive contributions treated using fundamental measure theory (an excess functional for the hard sphere fluid), short-ranged attractive contributions treated using a weighted-density functional constrained to the experimental equation of state, and the long-

ranged Coulomb interactions between the charge densities of the molecules treated with a mean-field term (scaled to account for dipole correlations [97]), works remarkably well for the inhomogeneous water configurations typically encountered in the solvation of molecules within joint density-functional theory. Chapter 5 refines this approach further by accounting for rotational correlations and compensating for self-interaction errors using a polarization-density correlation functional, and demonstrates its generality by constructing free energy functionals for chloroform and carbon tetrachloride.

Within this theory, the Coulomb interactions between all the electrons and the nuclei in the fluid are treated at the mean field level. The kinetic energy of the electrons contributes to the internal energy of the molecules and is responsible for the short-ranged repulsion between molecules. The nuclear kinetic energy is captured in part by the free energy of the non-interacting system of rigid but orientable molecules with vibrations treated perturbatively, and the remainder contributes to the effective intermolecular potential. The task of the excess functional is to treat all the effects arising from intermolecular interactions. Within our ansatz, fundamental measure theory captures the effect of the short-ranged repulsion and the weighted-density functional captures the remaining interactions beyond the mean-field Coulomb term. The range of this weighted-density term is dominated by the dispersion interaction, which is the longest-ranged component of electron correlations, as well as the thermally-averaged beyond-mean-field interaction between orientable molecules with permanent dipole moments, both of which decay as r^{-6}. We find that selecting a weight function with an r^{-6} tail, such as the Lennard-Jones potential, leads to accurate predictions for the free energy for forming microscopic vacuum-liquid interfaces typically encountered in solvation of molecules, and these results are

insensitive to the precise form of the weight function at short distances.

The free energy functionals developed here are accurate for typical applications of joint density-functional theory, despite not capturing details (such as the secondary structure) of the measured partial pair-correlation functions. Other functionals which do capture these details by construction must therefore be more accurate at least for some inhomogeneous liquid configurations that are weak perturbations about the bulk fluid. A recent free energy functional for water employs direct correlation functions from integral equation theory to constrain perturbations about a hard sphere reference fluid [180], and another uses three-body terms from simplified molecular dynamics models for water to capture orientational correlations [76]. The pair correlations of these functionals are in much better agreement with experiment, but they still treat the entire molecule as a single site and hence lack the microscopic detail necessary for coupling to electronic density-functional calculations of solutes, within the framework of joint density-functional theory. Combining the description of intermolecular correlations from these functionals with the framework presented here could potentially lead to even more accurate functionals suitable for joint density-functional theory. The application of joint density-functional theory to electrode-electrolyte interfaces in technologically important systems such as batteries and fuel cells also requires the development of accurate functionals for mixtures of fluids, ionic liquids and electrolytes that include the necessary microscopic detail.

The final term in the formal partitioning (1.17) of the total free energy is the interaction between the electronic system and the liquid. We show [91] that the mean-field Coulomb interaction between the two systems, along with

a local-density approximation for the kinetic energy, exchange and correlations, augmented by dispersion corrections to account for long-range electron correlations, is sufficient to predict the solvation energies of molecules in water with an accuracy approaching k_BT at room temperature. This theory includes a single fit parameter in the semi-empirical model for the dispersion interactions, which is currently the weak link in all our solvation theories; a better model for dispersion should improve the reliability of these theories and could perhaps eliminate this sole fit parameter.

A second track followed in this dissertation is the construction of simplified solvation models within the framework of joint density-functional theory. The starting point is the empirical polarizable continuum model (PCM), which approximates the effect of the liquid simply by placing the electronic system in a cavity of molecular dimensions within a continuum dielectric, and then empirically correcting for other energy contributions such as the free energy of forming the cavity and dispersion interactions between the fluid and the electronic system. Chapter 6 minimally extends this model by replacing a continuum linear dielectric with one that accounts for the nonlinearity because of saturation of the rotational response (when all molecular dipole moments align with the external field). The empirical corrections for the remaining free energy take the form of an effective surface tension that is fit to solvation energies. Introducing this nonlinearity in the response, eliminates the linear model's overestimation of the electrostatic contribution to the solvation energy of highly polar ionic surfaces, and results in a PCM-like model suitable for the study of electrochemical systems.

Chapter 7 examines the PCM cavity assumption and concludes that account-

ing for the nonlocality of the fluid response is critical for reducing the empiricism of the model, since the cavity size parameters in these models compensate for the lack of finite molecule-size effects. We show how an *ab initio* calculation of the nonlocal response can be used to predict the ideal cavity size for a continuum dielectric, and this leads to a single universal solvent-independent cavity size parameter (critical electron density, n_c, in the isodensity polarizable continuum models). We also replace the empirical effective surface tension with a physical model for the cavity formation energy along with pair-potential dispersion corrections, which then capture the correct dependence of these energy contributions with the geometry of the system, ranging from small molecules to the surfaces of solids.

Chapter 8 directly incorporates the nonlocal response of the solvent into a simplified solvation model which retains the computational efficiency of PCM's, but matches the microscopic detail of joint density-functional theory. In fact, we show that this model can be derived as the linear response limit of joint density-functional theory, once we assume that the configuration of the fluid in the absence of electrostatic interactions between the fluid and the electronic system resembles a PCM cavity (uniform orientation density except within a cavity of molecular dimensions). The terms in this theory parallel those of joint density-functional theory, with mean-field Coulomb interactions between the electronic system and the fluid in both theories, the cavity formation free energy in place of the liquid free energy functional, and identical dispersion corrections for long-ranged electron correlations in both theories. The accuracy of this theory for molecular solvation energies also approaches k_BT at room temperature, and the increased computational efficiency and the ease of generalization to mixtures such as electrolytes, makes it the ideal candidate for large-scale first-principles

calculations of electrochemical systems. The weak link, as before, is the model for dispersion interactions which introduces the only fit parameter in the theory. Additionally, the angular momentum expansion employed in the derivation of this theory so far works only for the linear response limit; generalizing this derivation to obtain a nonlocal and nonlinear simplified solvation model would be of considerable interest.

Finally, Chapter 9 studies a complex electrochemical system using the nonlocal solvation model of Chapter 8. For many pairs of metals, a single monolayer of one metal deposits on the surface of the other (from an electrolyte containing metal ions) at an electrode potential less favorable than for bulk deposition, a phenomenon called underpotential deposition. A particularly well-studied example is the deposition of copper on the (111) surface of platinum from a solution also containing chloride ions, which exhibits transitions at two distinct potentials less favorable than bulk deposition instead of just one. Experimental investigations of this system using X-ray and electron diffraction led to two conflicting proposals for the additional transition: the formation of a partial monolayer of copper, or the desorption of chloride ions from the surface. Our solvation model enabled first-principles calculations of a platinum (111) surface in solution with several configurations of copper and adsorbed chloride ions, without explicitly dealing with the solvent molecules. Our calculations indicate that the partial monolayer is unlikely to be the most stable configuration at any electrode potential, and that chloride desorption is probably the correct identification of the second transition in this system. A more complete picture of this phenomenon requires the study of co-adsorption of other anions in the solution, as well as examining trends in results for different crystal orientations of the surface and different pairs of metals. However, even these pre-

liminary first-principles calculations using a joint density-functional solvation model provides microscopic information about the structure at the interface, complementary to experimental data, and resolves a long-standing experimental debate about the nature of the transitions with changing electrode potential in this system.

APPENDIX A

EFFICIENT QUADRATURES FOR ORIENTATION INTEGRALS

Efficient discretization of the orientation integrals is critical to the performance of any of the representations of Section 4.1.2 and determines the very practicality of the p_ω (self) representation. Here, we list efficient quadratures for discretizing integrals over ω, $\int \frac{d\omega}{8\pi^2} f(\omega) \to \sum_i W_i f(\omega_i)$.

The simplest approach is to label orientations by ZYZ-Euler angles $\omega = (\alpha, \beta, \gamma)$ and use the outer product of a Gauss-Legendre quadrature for $\beta \in [0, \pi]$ and Gauss-Fourier quadratures for the periodic $\alpha, \gamma \in [0, 2\pi)$. More efficient quadratures may be constructed as an outer product using the $\mathbb{S}_2 \times \mathbb{S}_1$ structure of SO(3), or by working directly on SO(3) without an outer product structure [52].

In [52], quadratures on SO(3) are optimized to minimize the RMS error in the integrals of all $D^j_{m_1 m_2}(\omega)$ up to some $j_{\max}$. We focus on quadratures that are *exact* up to some $j_{\max}$,

$$\sum_i W_i D^j_{m_1 m_2}(\omega_i) = \sum_i W_i d^j_{m_1 m_2}(\beta_i) e^{i(m_1 \alpha_i + m_2 \gamma_i)} = \delta_{j0} \tag{A.1}$$

for all $|m_1|, |m_2| \leq j \leq j_{\max}$, and can be optimized further using the symmetry of the molecule at hand. For simplicity, we only consider $\mathbb{Z}_n$ symmetry about a single axis, chosen to be the z-axis of the molecule frame without loss of generality. The quadratures considered then fall into 3 classes:

1. Symmetry groups of Platonic solids [52]
2. Outer products of a spherical j-design [60] on $\mathbb{S}_2(\alpha, \beta)$ with a uniform quadrature on $\mathbb{S}_1(\gamma)$

3. Outer product quadrature on all 3 Euler angles α, β and γ.

Each of these these classes consists of uniformly spaced nodes of equal weights in γ for each (α, β). Grouping the nodes as $(\alpha_k, \beta_k, \gamma_k + 2n\pi/n_\gamma)$ for $n \in 0, \ldots, n_\gamma - 1$ with total weight W_k for each group, (A.1) can be reduced to

$$\sum_k W_k d^j_{m_1 m_2}(\beta_k) \mathrm{e}^{i(m_1\alpha_k + m_2\gamma_k)} = \delta_{j0} \tag{A.2}$$

for all $|m_1|, |m_2| \leq j \leq j_{\max}$ such that m_2 is a multiple of n_γ. Therefore if $n_\gamma > j_{\max}$ (which is the case for all but the Icosahedron rotation group), (A.2) further simplifies to

$$\sqrt{4\pi} \sum_k W_k Y^j_m(\beta_k, \alpha_k) = \delta_{j0} \tag{A.3}$$

for all $|m| \leq j \leq j_{\max}$ using the relations of D^j_{m0} to the spherical harmonics.

A spherical $j_{\max}$-design is a set of points on the unit sphere that satisfies (A.3) with uniform weights W_k, and hence it yields an SO(3) quadrature exact to $j_{\max}$ when combined with a uniform quadrature with $j_{\max} + 1$ nodes on $\mathbb{S}_1(\gamma)$. We use the spherical designs with the smallest number of nodes for each $7 \leq j_{\max} \leq 21$ tabulated in [60] to form the quadratures of class (b). The quadratures of lower order reduce to class (a), specifically the rotation groups of the Tetrahedron at $j_{\max} = 2$, Octahedron at $j_{\max} = 3$ and Icosahedron at $j_{\max} = 5$.

The Gauss-Legendre quadrature with n_β nodes on $\cos\beta \in [-1, 1]$ is exact for the integration of all polynomials up to order $2n_\beta - 1$. The outer product of this with a uniform quadrature with $2n_\beta$ nodes on $\alpha \in [0, 2\pi)$ satisfies (A.3) for $j_{\max} = 2n_\beta - 1$, and hence also (A.1) to that order when combined with $2n_\beta$ uniform samples on γ.

Finally the reduction by $\mathbb{Z}_n$ symmetry about the z-axis in the molecule frame amounts to replacing $\mathbb{S}_1(\gamma)$ with $\mathbb{S}_1/\mathbb{Z}_n$. This is achieved by a uniform sampling

of $\lceil n_\gamma/n \rceil$ points on $\gamma \in [0, 2\pi/n)$, which retains the exactness to $j_{\max}$ for functions with this symmetry with a reduction of up to n in the number of nodes required.

The accuracy of these quadratures for classical density functional theory of rigid molecules is explored in Section 4.3.2. The quadratures considered there are listed in Table A.1 along with their $j_{\max}$, the number of nodes for sampling $\mathrm{SO}(3)/\mathbb{Z}_n$ in general and $\mathrm{SO}(3)/\mathbb{Z}_2$ in particular, which is the case relevant for water. Note that the Euler quadrature with $n_\beta = 3$ needs almost twice as many nodes as the Icosahedron group for the same $j_{\max} = 5$, but the relative inefficiency of the Euler quadratures decreases with $j_{\max}$ and becomes less than 1% between the $n_\beta = 11$ Euler quadrature and the 21-design at $j_{\max} = 21$.

Table A.1: List of explored quadratures, their degree of exactness $j_{\max}$, and the number of nodes in sampling $\mathrm{SO}(3)/\mathbb{Z}_n$. The Euler angles corresponding to the platonic solid rotation groups are listed in [52]. The j-designs are constructed as an outer product of the spherical j-designs with fewest points for each j from [60] used for (α, β) with $\lceil (j+1)/n \rceil$ uniform samples on $\gamma \in [0, 2\pi/n)$. Each Euler(n_β) quadrature is an outer product of a n_β-point Gauss-Legendre quadrature on $\cos\beta \in [-1, 1]$, a uniform $2n_\beta$-point quadrature on $\alpha \in [0, 2\pi)$, and a uniform $\lceil 2n_\beta/n \rceil$-point quadrature on $\gamma \in [0, 2\pi/n)$.

	$j_{\max}$	Number of quadrature nodes for	
		$\mathrm{SO}(3)/\mathbb{Z}_n$	$\mathrm{SO}(3)/\mathbb{Z}_2$
Tetrahedron	2	$4 \times \lceil 3/n \rceil$	8
Octahedron	3	$6 \times \lceil 4/n \rceil$	12
Icosahedron	5	$12 \times \lceil 5/n \rceil$	36
7-design	7	$24 \times \lceil 8/n \rceil$	96
8-design	8	$36 \times \lceil 9/n \rceil$	180
9-design	9	$48 \times \lceil 10/n \rceil$	240
10-design	10	$60 \times \lceil 11/n \rceil$	360
11-design	11	$70 \times \lceil 12/n \rceil$	420
12-design	12	$84 \times \lceil 13/n \rceil$	588
13-design	13	$94 \times \lceil 14/n \rceil$	658
14-design	14	$108 \times \lceil 15/n \rceil$	864
15-design	15	$120 \times \lceil 16/n \rceil$	960
16-design	16	$144 \times \lceil 17/n \rceil$	1296
17-design	17	$156 \times \lceil 18/n \rceil$	1404
18-design	18	$180 \times \lceil 19/n \rceil$	1800
19-design	19	$204 \times \lceil 20/n \rceil$	2040
20-design	20	$216 \times \lceil 21/n \rceil$	2376
21-design	21	$240 \times \lceil 22/n \rceil$	2640
Euler(n_β)	$2n_\beta - 1$	$2n_\beta^2 \times \lceil 2n_\beta/n \rceil$	$2n_\beta^3$

APPENDIX B

ONE-DIMENSIONAL DISCRETIZATION FOR SPECIAL GEOMETRIES

The discretization of three-dimensional space according to Section 4.3.1, along with the orientation quadratures of Appendix A provide a practical route to computations with the rigid-molecular classical density functional framework of Section 4.1 in arbitrary geometries and basis sets. However, the development and testing of new excess functionals for liquids primarily require calculations in high-symmetry external potentials. Here, we detail the formulation of highly-efficient discretizations of planar, cylindrical and spherical geometries on a one-dimensional grid, which allow for the rapid prototyping of excess functionals employed in Section 4.3.3 and [153].

The discretization of space is performed in the framework of Section 4.3.1, but with special basis sets exploiting the symmetry. The three geometries we consider here are

1. Planar, where all spatial dependence is along z,
2. Cylindrical, with dependence only on the distance from the z-axis ρ, and
3. Spherical, with dependence only on distance from origin r.

Each of these geometries require only a one-dimensional discretization. For the planar geometry, we impose mirror-symmetry boundary conditions at the ends of the grid, and pick a basis of cosines and a corresponding quadrature grid suited for the Discrete Cosine Transform [3]. For the spherical and cylindrical geometries, we impose Neumann boundary conditions at some maximum radius, and choose a finite basis of spherical and cylindrical Bessel functions

Table B.1: Definition of the basis functions for the high-symmetry geometries - planar, cylindrical and spherical - with one-dimensional discretizations of sample count S, and matrix elements of the operators of Section 4.3.1 for each of these basis sets. The basis functions are labeled by $i = 0, 1, \cdots, S-1$ for each basis set, and X_i, x_i, Y_i and y_i, are the i^{th} roots of $J_0(x)$, $j_0(x)$, $J_0'(x)$ and $j_0'(x)$ respectively, with $Y_0 = y_0 \equiv 0$. The quadrature grid has the same number of points S as the basis size, and are labeled by $j = 0, 1, \cdots, S-1$.

	Planar	Cylindrical	Spherical
Coordinate system	(x, y, z)	(ρ, ϕ, z)	(r, θ, ϕ)
Symmetry	$f(\vec{r}) \to f(z)$	$f(\vec{r}) \to f(\rho)$	$f(\vec{r}) \to f(r)$
Boundary conditions	$f'(0) = f'(L) = 0$	$f'(\rho_{\max}) = 0$	$f'(r_{\max}) = 0$
Basis $b_i(\vec{r})$	$\tilde{w}_i \cos(G_i z)$, $G_i = i\pi/L$, $\tilde{w}_i = \frac{2}{(1+\delta_{i0})L}$	$\tilde{w}_i J_0(G_i \rho)$, $G_i = Y_i/\rho_{\max}$, $\tilde{w}_i = \frac{J_0^{-2}(Y_i)}{\pi \rho_{\max}^2}$	$\tilde{w}_i j_0(G_i r)$, $G_i = y_i/r_{\max}$, $\tilde{w}_i = \frac{j_0^{-2}(y_i)}{(2-\frac{2}{3}\delta_{i0})\pi r_{\max}^3}$
Quadrature grid $\{\vec{r}_j\}$	$z_j = (j+\frac{1}{2})\frac{L}{S}$	$\rho_j = X_{j+1}\frac{\rho_{\max}}{Y_S}$	$r_j = x_{j+1}\frac{r_{\max}}{y_S}$
$\mathcal{I}_{ji}$	$\tilde{w}_i \cos\left((j+\frac{1}{2})\pi\frac{i}{S}\right)$	$\tilde{w}_i J_0\left(X_{j+1}\frac{Y_i}{Y_S}\right)$	$\tilde{w}_i j_0\left(x_{j+1}\frac{y_i}{y_S}\right)$
$\mathcal{J}_{ij}$	$w_j \cos\left((j+\frac{1}{2})\pi\frac{i}{S}\right)$, $w_j = \frac{L}{S}$	$w_j J_0\left(X_{j+1}\frac{Y_i}{Y_S}\right)$, $w_j = \frac{4\pi\rho_{\max}^2}{Y_S^2 J_1^2(X_{j+1})}$	$w_j j_0\left(x_{j+1}\frac{y_i}{y_S}\right)$, $w_j = \frac{4\pi^2 r_{\max}^3}{y_S^3 j_1^2(x_{j+1})}$
$O_{i'i}$	$\tilde{w}_i \delta_{i'i}$		
$\mathcal{L}_{i'i}$	$-G_i^2 \tilde{w}_i \delta_{i'i}$		
$(\mathcal{J}^\dagger O \mathcal{J})_{j'j}$	$w_j \delta_{j'j}$		
$(g(r)*)_{i'i}$	$\delta_{i'i} \int 4\pi r^2 \mathrm{d}r g(r) j_0(G_i r)$		

respectively, along with a quadrature grid suited for the Discrete Bessel Transform [89] .[1] The definition of the basis functions, quadrature grid and the matrix elements for the operators of Section 4.3.1 are summarized in Table B.1.

All three basis sets are based on the eigenfunctions of the three-dimensional Laplace equation in various geometries, and are therefore intricately linked to the three-dimensional plane-wave basis: the basis functions are indexed by G_i,

[1]The Discrete Bessel Transform of [89] is based on Dirichlet boundary conditions; the extension of that approach to Neumann boundary conditions is straightforward, and the results are summarized in Table B.1.

the magnitude of the corresponding plane-wave momentum. Consequently, the Laplacian and convolutions by spherical functions are diagonal in these basis sets as well, as indicated in Table B.1. The transform operators $\mathcal{I}$ and $\mathcal{J}$ reduce to the 'DCT type III' and 'DCT Type II' fast Fourier transforms [44] respectively in the planar geometry (or 'IDCT' and 'DCT' in the notation of [3]); the cylindrical and spherical transforms lack an analogous $O(S \ln S)$ method and are implemented as matrix-vector multiplies with a precomputed Bessel function matrix.

The basis-independent discretization of the scalar-EOS excess functional (4.35), and site-density excess functionals in general, carries over to the planar, cylindrical and spherical geometries without modification. The discretization of the rigid-molecular ideal gas free energy and the generation of site-densities from independent variables carries over unmodified for the planar geometry, but is slightly complicated for the cylindrical and spherical geometries by the fact that the translation operator breaks the symmetry of the basis set and does not have a one-dimensional representation.

We can however compute the site-densities using (4.34) and the orientation-density in the site-potential representation using (4.31) for these basis sets as well, with minor modifications to the translation operators in those equations. First, we pick a covariant reference orientation for the molecule, (relative to the local coordinate frame $(\hat{\rho}, \hat{\phi}, \hat{z})$ or $(\hat{r}, \hat{\theta}, \hat{\phi})$), so that $p_\omega(\vec{r})$ is invariant under the cylindrical or spherical symmetry for each ω and permits a one-dimensional representation.[2] Consequently, the translations involved in (4.34) and (4.31) would be relative to the local coordinate frame as well, and hence position-

[2]If we used an invariant reference orientation as in the three-dimensional case, $p_\omega(\vec{r})$ would be covariant under the symmetry, so that the spatial dependence of $p_\omega(\vec{r})$ for each ω would not be cylindrically or spherically symmetric, and would therefore lack a one-dimensional representation.

dependent; we therefore need to generalize the translation operators $\mathcal{T}_{\vec{a}}$ to 'warp' operators $\mathcal{T}_{\vec{a}(\vec{r})}$ defined by $\mathcal{T}_{\vec{a}(\vec{r})} f(\vec{r}) = f(\vec{r} + \vec{a}(\vec{r}))$. It can be shown that the expressions of Section 4.3.1 remain valid without modification upon this generalization.

The translation operator for the planar basis is a simple one-dimensional restriction of its three-dimensional counterpart, and it generalizes to

$$\mathcal{T}_{\vec{a}(\rho)} f(\rho) = f\left(\sqrt{(\rho + \vec{a} \cdot \hat{\rho})^2 + (\vec{a} \cdot \hat{\phi})^2}\right) \tag{B.1}$$

for the cylindrical basis with $f(\rho) \equiv f(2\rho_{\max} - \rho)$ for $\rho > \rho_{\max}$, and

$$\mathcal{T}_{\vec{a}(r)} f(r) = f\left(\sqrt{r^2 + a^2 + 2r\vec{a} \cdot \hat{r}}\right) \tag{B.2}$$

for the spherical basis with $f(r) \equiv f(2r_{\max} - r)$ for $r > r_{\max}$.[3] We could compute the matrix elements of these operators in the Bessel basis and apply the translation as a dense-matrix multiply in basis space, but those suffer from Nyquist frequency ringing problems similar to their three-dimensional counterparts. Instead, we compute these operators in real space using approximate sampling operators $\mathcal{S}_{\vec{a}(\vec{r})}$ based on constant or linear-spline interpolation which preserve non-negativity of scalar fields.

The results for the scalar-EOS water functional in Section 4.3.3 and the bonded-voids water functional in [153] were computed using the discretization scheme of Section 4.3.1, in the planar and spherical bases, with the warp operator $\mathcal{S}$ computed using linear-spline interpolation as discussed above. The planar and spherical bases have an additional rotational symmetry about the local $\hat{z}$ and $\hat{r}$ axes respectively at any point in space which renders the integral over Euler angle α trivial, so that a quadrature on $\mathbb{S}_2(\gamma, \beta)$ with no α sampling

[3] The covariant reference frame ensures that $\vec{a} \cdot \hat{\rho}$ and $\vec{a} \cdot \hat{\phi}$ depend only on ρ (and not ϕ and z), and that $\vec{a} \cdot \hat{r}$ depends only on r.

suffices; the one-dimensional calculations employ this additional optimization by using the Euler(n_β) quadratures of Appendix A, but with $n_\alpha = 1$ irrespective of n_β.

APPENDIX C

TRUNCATED COULOMB POTENTIALS

Computations for periodic systems frequently employ the plane-wave basis [124], which presents the advantage of systematic and exponential basis-set convergence controlled by a single parameter, namely the kinetic energy cutoff, or equivalently, the Nyquist frequency. This advantage can be extended to non-periodic systems and systems with lower-dimensional periodicity such as slabs and wires by using truncated Coulomb potentials [136, 73]. Additionally, in Chapter 2, truncated Coulomb potentials proved particularly useful in the computation of the exchange energy even for periodic systems.

As shown above, truncation of the potential on the Wigner-Seitz cell leads to the most accurate method for the exchange energy, and it is also the most efficient method for lower-dimensional geometries since, as discussed by Ismail-Beigi [73], it localizes the $G = 0$ singularity of the Coulomb kernel to a single point. However, the singular Fourier integrals required to construct plane-wave Wigner-Seitz truncated Coulomb kernels cannot be solved analytically in general, and are prohibitively expensive to compute numerically. Here, we develop a general and efficient $O(N \ln N)$ construction for these kernels based on the minimum-image convention (MIC) method [106]. Finally, as a practical matter, we note that determining the Coulomb kernel is a one-time computation because the corresponding storage requirements are modest.

To establish our normalization conventions for the plane-wave basis, we expand periodic charge densities as $\rho(\vec{r}) = \sum_{\vec{G}} e^{i\vec{G}\cdot\vec{r}}\tilde{\rho}_{\vec{G}}$ where $\vec{G}$ are reciprocal lattice vectors of the crystal which has a unit cell of volume Ω. The interaction energy

under a translationally invariant potential

$$\begin{aligned} U_{12} &= \int_{\Omega} d\vec{r}_1 \int d\vec{r}_2 \rho_1^*(\vec{r}_1) K(\vec{r}_1 - \vec{r}_2) \rho_2(\vec{r}_2) \\ &= \Omega \sum_{\vec{G}} \tilde{\rho}^*_{1\vec{G}} \tilde{\rho}_{2\vec{G}} \tilde{K}_{\vec{G}} \end{aligned} \tag{C.1}$$

is then diagonal in reciprocal space, with $\tilde{K}_{\vec{G}} = \int d\vec{r} e^{-i\vec{G}\cdot\vec{r}} K(r)$. Here, we denote integrals over unit cells by $\int_{\Omega} d\vec{r}$ and integrals over all space by $\int d\vec{r}$. For the long-ranged Coulomb interaction $K(r) = 1/r$, the plane-wave kernel $\tilde{K}_{\vec{G}} = 4\pi/G^2$ is singular at $\vec{G} = 0$, and the interaction energy is finite only for neutral unit cells. In practice, the interaction energies of charged subsystems are computed by excluding the $\vec{G} = 0$ term, which amounts to adding a uniform neutralizing background charge to each subsystem.

Treating non-periodic systems in the plane-wave basis requires the elimination of interactions between different unit cells in a translationally-invariant manner in order to preserve the efficiency and accuracy of the Fourier spectral method. If the Coulomb potential is truncated so that it is zero outside the first Wigner-Seitz cell and the charge densities are confined to half the domain of truncation, then the interaction within each unit cell remains unmodified and the interaction between unit cells is exactly zero. The simplest choice for accomplishing this truncates the Coulomb potential outside a sphere of radius R smaller than the in-radius of the Wigner-Seitz cell, leading to the analytical plane-wave kernel,

$$\tilde{K}^{\text{sph}}_{\vec{G}} = \int_{|\vec{r}|<R} d\vec{r} e^{-i\vec{G}\cdot\vec{r}} \frac{1}{r} = \begin{cases} 2\pi R^2, & \vec{G} = 0 \\ \frac{4\pi}{G^2}(1 - \cos GR), & \vec{G} \neq 0. \end{cases} \tag{C.2}$$

C.1 Minimum-image convention (MIC) method

From the above arguments, the natural choice for the truncated potential is clearly

$$\tilde{K}^{\mathrm{WS}}_{\vec{G}} = \int_{\mathrm{WS}} d\vec{r} e^{-i\vec{G}\cdot\vec{r}} \frac{1}{r}, \tag{C.3}$$

where $\int_{\mathrm{WS}}$ represents integration over the first Wigner-Seitz cell. However, the singularity at the origin and the polyhedral domain of integration preclude general analytical solutions and straightforward numerical quadratures. Martyna and Tuckerman introduced an approximate construction for Coulomb potentials truncated on parallelepiped domains based on range-separation techniques. Here, we generalize this so-called minimum-image convention (MIC) method [106] to Wigner-Seitz cells of arbitrary lattice systems.

Employing a range-separation parameter α, analogously to the Ewald approach [38] for the Coulomb energy of a periodic assembly of charges, we approximate this kernel by

$$\begin{aligned} \tilde{K}^{\mathrm{WS}}_{\vec{G}} &= \int_{\mathrm{WS}} d\vec{r} e^{-i\vec{G}\cdot\vec{r}} \left(\frac{\operatorname{erfc} \alpha r}{r} + \frac{\operatorname{erf} \alpha r}{r} \right) \\ &\approx \frac{4\pi}{G^2} \left(1 - \exp \frac{-G^2}{4\alpha^2} \right) + \frac{\Omega}{N_{\vec{r}}} \sum_{\vec{r} \in \mathrm{WS}} e^{-i\vec{G}\cdot\vec{r}} \frac{\operatorname{erf} \alpha r}{r}, \end{aligned} \tag{C.4}$$

where the discrete sum over $\vec{r}$ is a quadrature on the Wigner-Seitz cell with $N_{\vec{r}}$ nodes as described below. The short-ranged first term is localized to the Wigner-Seitz cell by choice of α, so that it is unaffected by the truncation and can be evaluated analytically. The error in this term can be reduced to machine precision ϵ by choosing $\alpha = \sqrt{-\ln \epsilon}/R_{\mathrm{in}}$, where R_{in} is the in-radius of the Wigner-Seitz cell. The $\vec{G} = 0$ component is well-defined because of the finite real-space range, and is understood to be equal to its $G \to 0$ limit given by π/α^2.

The second term of (C.4) has a long-ranged smooth integrand and is approximated by a Gauss-Fourier quadrature, evaluated as a fast Fourier transform (FFT) in practice. This quadrature consists of nodes on a uniform parallelepiped mesh with uniform weights, which we remap using the periodicity of the lattice to the first Wigner-Seitz cell. In the interior of the integration domain, the integrand is bandwidth-limited as $\exp(-G^2/4\alpha^2)$, and the error in the Fourier quadrature can be reduced to ϵ by choosing an FFT resolution such that the Nyquist frequency exceeds $2\alpha\sqrt{-\ln\epsilon} = -2\ln\epsilon/R_{\text{in}}$. The cusps in the periodic repetition of the integrand at the boundaries of the Wigner-Seitz cell cause an additional error in the kernel, but this error does not contribute in the Coulomb energy of charge distributions that are confined to the half-sized Wigner-Seitz cell and are resolvable on the chosen Fourier grid [106].

C.2 Partially-truncated Coulomb kernels

Next, we generalize the above construction to systems with lower-dimensional periodicity, where the Coulomb kernel is truncated along some lattice directions and remains long-ranged along the others. In these geometries, the kernel is still singular around $\vec{G} = 0$, albeit with a slower divergence: $\ln G$ for one periodic direction or $1/G$ for two periodic directions in contrast to $1/G^2$ for the fully periodic case. A general shape for the truncation domain in the non-periodic directions leads to a kernel which is singular for an entire line or plane of reciprocal lattice vectors passing through $\vec{G} = 0$. Ismail-Beigi [73] pointed out that Wigner-Seitz truncation localizes the singularity to the single point $\vec{G} = 0$ in all these cases.

We can understand the special property of the Wigner-Seitz truncation by writing the Coulomb kernel truncated on an arbitrary domain D as

$$\tilde{K}^{\mathrm{D}}_{\vec{G}} = \int d\vec{r} e^{-i\vec{G}\cdot\vec{r}} \frac{1}{r} \theta_D(\vec{r}) = \int d\vec{k} \frac{4\pi}{k^2} \tilde{\theta}_D(\vec{G} - \vec{k}), \tag{C.5}$$

where $\theta_D(\vec{r})$ is a function that is 1 for $\vec{r} \in D$ and 0 otherwise, and $\tilde{\theta}_D$ is its Fourier transform. Since $\theta_D(\vec{r})$ is constant along periodic directions, $\tilde{\theta}$ is zero for wave-vectors with any component along those directions. In general, the singularity from $4\pi/k^2$ 'infects' all wave-vectors with no component along the periodic directions. Hence, the singularity is spread to a plane of points for one-dimensional or wire-like systems, and a line of points for two-dimensional or slab-like systems. However, the Fourier transform of a θ-function with a shape that tiles with the periodicity of the lattice, such as the Wigner-Seitz cell, is zero at all non-zero reciprocal lattice vectors. This confines the singularity to $G = 0$ for these special cases.

Now consider, without loss of generality, the slab geometry with its one truncated direction along z, and let L be the unit cell length along that direction. The Fourier transform of $1/r$ over the two periodic directions evaluates to $2\pi e^{-G_\rho|z|}/G_\rho$ where G_ρ is the component of the wave-vector along the untruncated directions. At $G_\rho = 0$, removing the singular part $2\pi/G_\rho$ results in a residue $-2\pi|z|$, the potential arising from an infinite plane of charge with the arbitrary offset in potential fixed to be zero at the plane. Note that, although this choice of zero of potential does not change the total energy for a neutral charge distribution, care must be exercised to ensure that it be consistent for all interactions between charged subsystems of an overall neutral system. Finally, the remaining integral over the Wigner-Seitz cell in the truncated direction, i.e. $z \in [-L/2, L/2)$, can also be performed analytically [73, 136], so that the Coulomb kernel for truncation in

slab geometries becomes

$$\tilde{K}_{\vec{G}}^{\text{slab}} = \begin{cases} \frac{4\pi}{G^2}\left(1 - \cos\frac{G_z L}{2}\exp\frac{-G_\rho L}{2}\right), & G \neq 0 \\ -\pi L^2/2, & G = 0. \end{cases} \tag{C.6}$$

Similarly, for the wire geometry with the single periodic direction along z, the partial Fourier transform of $1/r$ over the periodic direction is $2K_0(G_z\rho)$, where $\rho = \sqrt{r^2 - z^2}$ is the usual cylindrical coordinate, and K_0 is the modified Bessel function of the second kind. At $G_z = 0$, removing the logarithmically divergent part results in a residue $-2\ln\rho$ so that the regularized partial Fourier transform of the Coulomb potential at $G_z = k$ is

$$C_k(\rho) \equiv \begin{cases} 2K_0(k\rho), & k \neq 0 \\ -2\ln\rho, & k = 0. \end{cases} \tag{C.7}$$

The remaining Fourier transform over the two truncated directions is analytically computable for a cylindrical truncation domain [136], but that choice spreads the divergence beyond $G = 0$ as mentioned previously. On the other hand, the Fourier transform of (C.7) with a Wigner-Seitz truncation domain is not known in closed form for any two-dimensional lattice system [73]. Accordingly, we generalize the MIC approach [106] and approximate the partially-truncated wire-geometry Coulomb kernel by

$$\tilde{K}_{\vec{G}}^{\text{wire}} \approx \frac{4\pi}{G^2}\left(1 - \exp\frac{-G^2}{4\alpha^2}\right) + \frac{\Omega_\perp}{N_{\vec{r}_\perp}} \sum_{\vec{r}_\perp \in \text{WS}_\perp} e^{-i\vec{G}\cdot\vec{r}_\perp} \bar{C}^\alpha_{|G_z|}(r_\perp) \tag{C.8}$$

where $r_\perp$ are nodes for the two dimensional Gauss-Fourier quadrature mapped down to the Wigner Seitz cell, $\text{WS}_\perp$, of the truncated directions with area $\Omega_\perp$.

Here, we introduce a smooth, long-ranged special function $\bar{C}^\alpha_k(\rho)$, which plays the same role for $C_k(\rho)$ that $\text{erf}(\alpha r)/r$ plays for $1/r$ in the fully-truncated

case of (C.4). Operationally, this function is defined by the two-dimensional convolution

$$\begin{aligned}\bar{C}_k^\alpha(\rho) &\equiv e^{\frac{-k^2}{4\alpha^2}}\left(\frac{\alpha}{\pi}e^{-\alpha^2\rho^2} * C_k(\rho)\right) \\ &= e^{\frac{-k^2}{4\alpha^2}}\int_0^\infty 2\alpha^2\rho' d\rho' e^{-\alpha^2(\rho^2+\rho'^2)} I_0(2\alpha^2\rho\rho') C_k(\rho'). \end{aligned} \tag{C.9}$$

For $k = 0$, (C.9) reduces to the analytical expression $\bar{C}_0^\alpha(\rho) = -2\ln\rho - \Gamma_0(\alpha^2\rho^2)$, but for $k \neq 0$, $\bar{C}_k^\alpha(\rho)$ needs to be parametrized numerically.[1] The choice of α and FFT resolution in (C.9) follow the discussion for the fully-truncated MIC construction, except that R_{in} is the radius of the two dimensional Wigner-Seitz cell $\text{WS}_\perp$, and independent two-dimensional fast Fourier transforms produce the results for each plane of constant G_z.

C.3 Ewald sums for reduced-dimensional systems

The plane-wave Coulomb kernels above, truncated over the Wigner-Seitz cell in one, two or three lattice directions, enable the calculation of Coulomb interaction energies in slab, wire and isolated geometries respectively. However, a purely reciprocal-space method is only practical if at least one of the two charge densities, $\rho_1(\vec{r})$ or $\rho_2(\vec{r})$ in (C.1), is bandwidth limited. The interaction energy of point nuclei with each other does not satisfy this criterion and requires the use of an Ewald sum [38]. Generalizing the standard Ewald method to an arbitrary combination of truncated and periodic lattice directions, gives the interaction

[1] Efficient subroutines for evaluating $\bar{C}_k^\alpha(\rho)$ and constructing truncated kernels are available as a part of the open source density-functional software, JDFTx [154].

energy for a set of point charges Z_i at locations $\vec{r}_i$ in the first unit cell, as

$$E_{\text{ewald}} = \sum_{\substack{\vec{R},i,j \\ i\neq j \text{ if } \vec{R}=0}} \frac{Z_i Z_j}{2} \frac{\operatorname{erfc} \eta|\vec{r}_i + \vec{R} - \vec{r}_j|}{|\vec{r}_i + \vec{R} - \vec{r}_j|} + \sum_{\vec{G},i,j} \frac{Z_i Z_j}{2\Omega_{\text{per}}} e^{-i\vec{G}\cdot(\vec{r}_i - \vec{r}_j)} g^{\eta}_{\vec{G}}(\vec{r}_i - \vec{r}_j) - \frac{\eta}{\sqrt{\pi}} \sum_i Z_i^2. \tag{C.10}$$

Here, the first term evaluates the contribution from the short-ranged part $\operatorname{erfc}(\eta r)/r$ of the Coulomb potential, the second term captures the contribution from the remaining long-ranged part $\operatorname{erf}(\eta r)/r$, and the third term exactly cancels the self interactions introduced by the second term. The standard range-separation parameter η is adjusted to simultaneously optimize the convergence of the sum over lattice vectors $\vec{R}$ as well as that over reciprocal lattice vectors $\vec{G}$, but the total energy is of course formally independent of the value of this parameter. (When some lattice directions are truncated, $\vec{R}$ and $\vec{G}$ correspond to the lattice vectors and reciprocal lattice vectors of the lower dimensional Bravais lattice of periodic directions alone.) Finally, in the second term, Ω_{per} is the volume, area or length of the unit cell along the periodic directions alone and $g^{\eta}_{\vec{G}}(\vec{r})$ is related to the (partial) Fourier transform over those directions of the long-ranged part of the Coulomb potential.

When all three directions are periodic, $g^{\eta}_{\vec{G}}(\vec{r}) = \exp \frac{-G^2}{4\eta^2}$, the double sum over point charges factorizes into the square of the structure factor, and (C.10) reduces to the standard Ewald sum [38]. Next, for the slab geometry truncated, without loss of generality, along the z direction, we find

$$g^{\eta}_{\vec{G}}(\vec{r}) = \begin{cases} \frac{\pi}{G}\left(f^{\eta}_G(z) + f^{\eta}_G(-z)\right), & G \neq 0 \\ -2\pi\left(z \operatorname{erf}(\eta z) + \frac{e^{-\eta^2 z^2}}{\eta\sqrt{\pi}}\right), & G = 0, \end{cases} \tag{C.11}$$

where $f^{\eta}_G(z) \equiv e^{Gz}\operatorname{erfc}(G/2\eta + \eta z)$, and this reduces (C.10) to the 'Ewald 2D' formula [67, 147].

The Ewald sum for the wire geometry with one periodic and two truncated directions does not seem to have been addressed previously, perhaps because $g^{\eta}_{\vec{G}}$ is not analytically expressible in that case. In fact, we can show that $g^{\eta}_{\vec{G}}(\vec{r}) = \bar{C}^{\eta}_{G}(\sqrt{r^2 - z^2})$, precisely the function defined in (C.9), which was introduced for our generalization of the MIC method to this geometry. Finally, when all three lattice directions are truncated, the Coulomb kernel has no $G = 0$ singularity, and an Ewald sum is not required. In this case, the Coulomb energy of a set of point charges is computed directly in real space as a sum over all pairs in one unit cell.

APPENDIX D

DERIVATION OF THE SPHERICALLY-AVERAGED LIQUID SUSCEPTIBILITY

In Section 8.2, evaluating free energy functional (8.4) to quadratic order, that is within a linear response approximation, results in the quadratic form (8.7) with a spherically-averaged susceptibility given by (8.8). Here, we present the derivation of that result.

The free energy functional (8.4) excluding the zeroth order terms (Φ_0) is

$$\begin{aligned}\Delta\Phi = T\int d\vec{r}\int\frac{d\omega}{8\pi^2}p_\omega(\vec{r})\left[\ln\frac{p_\omega(\vec{r})}{N_{\text{bulk}}s(\vec{r})}-1\right]\\ +\sum_\alpha\int d\vec{r}\frac{N_\alpha(\vec{r})\mathcal{P}_\alpha(\vec{r})^2}{2C_{\text{pol}}\chi_\alpha}+\frac{C_{\text{rot}}^{-1}-1}{N_{\text{bulk}}p_{\text{mol}}^2/3T}\int d\vec{r}\left(\int\frac{d\omega}{8\pi^2}p_\omega(\vec{r})\omega\circ\vec{p}_{\text{mol}}\right)^2\\ +\int d\vec{r}\int d\vec{r}'\left(\rho_{\text{el}}(\vec{r})+\frac{\rho_{\text{lq}}(\vec{r})-\rho_{\text{lq}}^0(\vec{r})}{2}\right)\frac{1}{|\vec{r}-\vec{r}'|}(\rho_{\text{lq}}(\vec{r}')-\rho_{\text{lq}}^0(\vec{r}')).\end{aligned}\quad\text{(D.1)}$$

See the paragraphs following (8.4) for a detailed description of each term above. The zeroth order configuration corresponds to orientation density, $p_\omega(\vec{r}) = N_{\text{bulk}}s(\vec{r})$ and polarization amplitudes, $\vec{\mathcal{P}}_\alpha(\vec{r}) = 0$. The free energy is already explicitly quadratic in $\mathcal{P}_\alpha(\vec{r})$; we substitute

$$p_\omega(\vec{r}) = N_{\text{bulk}}s(\vec{r})\left[1+\sum_{lmm'}x_{mm'}^l(\vec{r})D_{mm'}^l(\omega)\right]\quad\text{(D.2)}$$

and expand Φ to quadratic order in $x_{mm'}^l(\vec{r})$, the coefficients for the irreducible representations of the rotation group, $D_{mm'}^l(\omega)$ [174], in the orientation density.

In the first term of (D.1), the integrand $p_\omega(\vec{r})\left[\ln\frac{p_\omega(\vec{r})}{N_{\text{bulk}}s(\vec{r})}-1\right]$, with $p_\omega(\vec{r}) = N_{\text{bulk}}s(\vec{r})(1+x)$ where $x = \sum_{lmm'}x_{mm'}^l(\vec{r})D_{mm'}^l(\omega)$, expands to $N_{\text{bulk}}s(\vec{r})x^2/2 + O(x^3)$. Performing the orientation integrals using the orthogonality relations of the

Wigner D-matrices, the first term of (D.1) simplifies to

$$\int d\vec{r} N_{\text{bulk}} s(\vec{r}) \sum_{lmm'} \frac{T}{2(2l+1)} \left(x^l_{mm'}(\vec{r})\right)^2 + O(x^3), \tag{D.3}$$

where $O(x^3)$ denotes cubic and higher order terms in $x^l_{mm'}(\vec{r})$. The inner integral in third term of (D.1), $\int \frac{d\omega}{8\pi^2} p_\omega(\vec{r}) \omega \circ \vec{p}_{\text{mol}}$, is zero for all $l \neq 1$, and simplifying the contribution at $l = 1$ yields the same form as the first term above, but with an additional factor of $(C^{-1}_{\text{rot}} - 1)$. Therefore, the first and third terms of (D.1) combine to

$$\int d\vec{r} N_{\text{bulk}} s(\vec{r}) \sum_{lmm'} \frac{T}{2(2l+1)C^l_{\text{rot}}} \left(x^l_{mm'}(\vec{r})\right)^2 + O(x^3), \tag{D.4}$$

where $C^l_{\text{rot}} = C_{\text{rot}}$ for $l = 1$ and unity for $l \neq 1$.

Substituting the simplified form of the first and third terms, and noting that the site densities $N_\alpha(\vec{r}) = N^0_\alpha(\vec{r}) + O(x)$ (by the definition of $N^0_\alpha(\vec{r})$ as the densities at uniform orientation density),

$$\begin{aligned}\Delta\Phi = &\int d\vec{r} N_{\text{bulk}} s(\vec{r}) \sum_{lmm'} \frac{T}{2(2l+1)C^l_{\text{rot}}} \left(x^l_{mm'}(\vec{r})\right)^2 + \sum_\alpha \int d\vec{r} \frac{N^0_\alpha(\vec{r})}{2C_{\text{pol}}\chi_\alpha} \left(\mathcal{P}_\alpha(\vec{r})\right)^2 \\ &+ \int d\vec{r} \int d\vec{r}' \left(\rho_{\text{el}}(\vec{r}) + \frac{\Delta\rho_{\text{lq}}(\vec{r})}{2}\right) \frac{1}{|\vec{r} - \vec{r}'|} \Delta\rho_{\text{lq}}(\vec{r}') + O(x^3) + O(x\mathcal{P}^2_\alpha). \end{aligned} \tag{D.5}$$

The change in charge density of the liquid, $\Delta\rho_{\text{lq}}(\vec{r}) \equiv \rho_{\text{lq}}(\vec{r}) - \rho^0_{\text{lq}}(\vec{r})$ includes contributions due to changes in the orientation density (with expansion coefficients $x^l_{mm'}(\vec{r})$) as well as due to polarization (with amplitudes $\mathcal{P}_\alpha(\vec{r})$), and is given by

$$\begin{aligned}\Delta\rho_{\text{lq}}(\vec{r}) = &\int d\vec{r}' N_{\text{bulk}} s(\vec{r}') \sum_{lmm'} x^l_{mm'}(\vec{r}') \int \frac{d\omega}{8\pi^2} D^l_{mm'}(\omega) \rho_{\text{mol}}(\omega \circ (\vec{r} - \vec{r}')) \\ &- \nabla \cdot \sum_\alpha w_\alpha(r) * N^0_\alpha(\vec{r}) \vec{\mathcal{P}}_\alpha(\vec{r}). \end{aligned} \tag{D.6}$$

Here, the rotational contribution is in terms of the charge density $\rho_{\text{mol}}(\vec{r})$ of the liquid molecule in the reference orientation at the origin. Consequently, $\rho_{\text{mol}}(\omega \circ (\vec{r} - \vec{r}'))$ is the charge density at position $\vec{r}$ of a molecule with orientation ω centered at $\vec{r}'$.

Now, we assume periodic boundary conditions on a supercell of volume Ω and expand each physical quantity in the plane-wave basis, $f(\vec{r}) = \sum_{\vec{G}} \tilde{f}(\vec{G}) e^{i\vec{G}\cdot\vec{r}}$, where $\vec{G}$ are reciprocal lattice vectors corresponding to that supercell. Using the convolution theorem, we can rewrite (D.5) and (D.6) in terms of the plane-wave coefficients as

$$\begin{aligned}\Delta\Phi = \Omega \sum_{\vec{G},\vec{G}'} N_{\text{bulk}} \tilde{s}(\vec{G}-\vec{G}') \sum_{lmm'} \frac{T}{2(2l+1)C^l_{\text{rot}}} \tilde{x}^{l*}_{mm'}(\vec{G}) \tilde{x}^{l}_{mm'}(\vec{G}') \\ + \Omega \sum_{\vec{G},\vec{G}'} \sum_{\alpha} \frac{\tilde{N}^0_\alpha(\vec{G}-\vec{G}')}{2C_{\text{pol}}\chi_\alpha} \tilde{\vec{\mathcal{P}}}^*_\alpha(\vec{G}) \tilde{\vec{\mathcal{P}}}_\alpha(\vec{G}') \\ + \Omega \sum_{\vec{G}} \left(\tilde{\rho}_{\text{el}}(\vec{G}) + \frac{\Delta\tilde{\rho}_{\text{lq}}(\vec{G})}{2} \right) \tilde{K}(G) \Delta\tilde{\rho}^*_{\text{lq}}(\vec{G}), \quad \text{(D.7)}\end{aligned}$$

where $\tilde{K}(G) = 4\pi/G^2$, and

$$\begin{aligned}\Delta\tilde{\rho}_{\text{lq}}(\vec{G}) = \sum_{lmm'} \sum_{\vec{G}'} N_{\text{bulk}} \tilde{s}(\vec{G}-\vec{G}') \tilde{x}^l_{mm'}(\vec{G}') \int \frac{d\omega}{8\pi^2} D^l_{mm'}(\omega) \tilde{\rho}_{\text{mol}}(\omega \circ \vec{G}) \\ - i\vec{G} \cdot \sum_\alpha \tilde{w}_\alpha(G) \sum_{\vec{G}'} \tilde{N}^0_\alpha(\vec{G}-\vec{G}') \tilde{\vec{\mathcal{P}}}_\alpha(\vec{G}). \quad \text{(D.8)}\end{aligned}$$

Next, we expand the charge density of the molecule in the basis of spherical harmonics multiplied by radial functions

$$\tilde{\rho}_{\text{mol}}(\vec{G}) = \sum_{lm} \tilde{\rho}^{lm}_{\text{mol}}(G) Y_{lm}(\hat{G}). \quad \text{(D.9)}$$

The charge density of the rotated molecule $\tilde{\rho}_{\text{mol}}(\omega \circ \vec{G})$ then expands to

$$\begin{aligned}\tilde{\rho}_{\text{mol}}(\omega \circ \vec{G}) &= \sum_{LM} \tilde{\rho}^{LM}_{\text{mol}}(G) Y_{LM}(\omega \circ \hat{G}) \\ &= \sum_{LMM'} \tilde{\rho}^{LM}_{\text{mol}}(G) D^L_{MM'}(\omega) Y_{LM'}(\hat{G}) \quad \text{(D.10)}\end{aligned}$$

using the transformation of spherical harmonics under rotations [174]. Substi-

tuting into (D.8) and simplifying using the orthogonality of $D^l_{mm'}(\omega)$,

$$\Delta\tilde{\rho}_{\rm lq}(\vec{G}) = \sum_{lmm'}\sum_{\vec{G}'} N_{\rm bulk}\tilde{s}(\vec{G}-\vec{G}')\tilde{x}^l_{mm'}(\vec{G}')\frac{1}{2l+1}\tilde{\rho}^{lm}_{\rm mol}(G)Y_{lm'}(\hat{G}) \\ - i\vec{G}\cdot\sum_\alpha \tilde{w}_\alpha(G)\sum_{\vec{G}'}\tilde{N}^0_\alpha(\vec{G}-\vec{G}')\tilde{\vec{\mathcal{P}}}_\alpha(\vec{G}). \quad \text{(D.11)}$$

Finally, the Euler-Lagrange equations for minimizing (D.7) with respect to $\tilde{x}^l_{mm'}(\vec{G})$ and $\tilde{\vec{\mathcal{P}}}_\alpha(\vec{G})$ yield

$$\tilde{x}^l_{mm'}(\vec{G}) = \frac{-C^l_{\rm rot}}{T}\tilde{\rho}^{lm*}_{\rm mol}(G)Y^*_{lm'}(\hat{G})\underbrace{\tilde{K}(G)\left(\tilde{\rho}_{\rm el}(\vec{G})+\Delta\tilde{\rho}_{\rm lq}(\vec{G})\right)}_{\equiv\tilde{\phi}_{\rm tot}(\vec{G})} \\ \text{and}\quad \tilde{\vec{\mathcal{P}}}_\alpha(\vec{G}') = -i\vec{G}C_{\rm pol}\chi_\alpha\tilde{w}^*_\alpha(G)\underbrace{\tilde{K}(G)\left(\tilde{\rho}_{\rm el}(\vec{G})+\Delta\tilde{\rho}_{\rm lq}(\vec{G})\right)}_{\equiv\tilde{\phi}_{\rm tot}(\vec{G})}, \quad \text{(D.12)}$$

where $\phi_{\rm tot}$ is the net electrostatic potential in the system. Eliminating $\tilde{x}^l_{mm'}(\vec{G})$ as well as $\tilde{\vec{\mathcal{P}}}_\alpha(\vec{G})$ in favor of $\tilde{\phi}_{\rm tot}(\vec{G})$ as the independent variable, (D.7) and (D.11) simplify to

$$\Delta\Phi = -\frac{\Omega}{2}\sum_{\vec{G},\vec{G}'}\hat{\chi}(\vec{G},\vec{G}')\tilde{\phi}^*_{\rm tot}(\vec{G})\tilde{\phi}_{\rm tot}(\vec{G}') \\ + \Omega\sum_{\vec{G}}\left(\tilde{\rho}_{\rm el}(\vec{G})+\frac{\Delta\tilde{\rho}_{\rm lq}(\vec{G})}{2}\right)\tilde{K}(G)\Delta\tilde{\rho}^*_{\rm lq}(\vec{G}) \\ \text{and}\quad \Delta\tilde{\rho}_{\rm lq}(\vec{G}) = \sum_{\vec{G}'}\hat{\chi}(\vec{G},\vec{G}')\tilde{\phi}_{\rm tot}(\vec{G}') \quad \text{(D.13)}$$

with the nonlocal spherically-averaged liquid susceptibility,

$$\hat{\chi}(\vec{G},\vec{G}') \equiv -N_{\rm bulk}\tilde{s}(\vec{G}-\vec{G}')\sum_{lmm'}\frac{C^l_{\rm rot}}{T}\frac{Y_{lm'}(\hat{G})Y^*_{lm'}(\hat{G}')}{2l+1}\tilde{\rho}^{lm}_{\rm mol}(G)\tilde{\rho}^{lm*}_{\rm mol}(G') \\ - \sum_\alpha \tilde{N}^0_\alpha(\vec{G}-\vec{G}')C_{\rm pol}\chi_\alpha\vec{G}\cdot\vec{G}'\tilde{w}_\alpha(G)\tilde{w}^*_\alpha(G'). \quad \text{(D.14)}$$

Using the addition theorem for spherical harmonics in the first term, this sus-

ceptibility reduces to (8.8), given by

$$\hat{\chi}(\vec{G},\vec{G}') \equiv -N_{\text{bulk}}\tilde{s}(\vec{G}-\vec{G}')\sum_{lm}\frac{C^l_{\text{rot}}}{T}\frac{P_l(\hat{G}\cdot\hat{G}')}{4\pi}\tilde{\rho}^{lm}_{\text{mol}}(G)\tilde{\rho}^{lm*}_{\text{mol}}(G') - \sum_{\alpha}\tilde{N}^0_\alpha(\vec{G}-\vec{G}')C_{\text{pol}}\chi_\alpha\vec{G}\cdot\vec{G}'\tilde{w}_\alpha(G)\tilde{w}^*_\alpha(G'). \quad \text{(D.15)}$$

The Euler-Lagrange equation for minimizing the free energy with respect to ϕ_{tot} is $\hat{\chi}\phi_{\text{tot}} = \hat{\chi}\hat{K}(\hat{\chi}\phi_{\text{tot}} + \rho_{\text{el}})$, using an operator notation for simplicity (instead of explicit matrices and vectors with $\vec{G}, \vec{G}'$ indices). We can formally rearrange this to $(\hat{K}^{-1} - \hat{\chi})\phi_{\text{tot}} = \rho_{\text{el}}$, which resembles a Poisson equation (since $\hat{K}^{-1} = -\nabla^2/4\pi$), but includes a nonlocal material response. In this operator notation, the free energy at the equilibrium is

$$\begin{aligned}
\Delta\Phi &= \Omega\left[-\frac{1}{2}\phi^\dagger_{\text{tot}}\hat{\chi}\phi_{\text{tot}} + \Delta\rho^\dagger_{\text{lq}}\hat{K}\left(\rho_{\text{el}} + \frac{1}{2}\Delta\rho_{\text{lq}}\right)\right] \\
&= \Omega\left[-\frac{1}{2}\phi^\dagger_{\text{tot}}\hat{\chi}\phi_{\text{tot}} + \frac{1}{2}\left(\rho_{\text{el}} + \Delta\rho_{\text{lq}}\right)^\dagger\hat{K}\left(\rho_{\text{el}} + \Delta\rho_{\text{lq}}\right) - \frac{1}{2}\rho^\dagger_{\text{el}}\hat{K}\rho_{\text{el}}\right] \\
&= \Omega\left[-\frac{1}{2}\phi^\dagger_{\text{tot}}\hat{\chi}\phi_{\text{tot}} + \frac{1}{2}\phi^\dagger_{\text{tot}}\left(\rho_{\text{el}} + \Delta\rho_{\text{lq}}\right) - \frac{1}{2}\rho^\dagger_{\text{el}}\hat{K}\rho_{\text{el}}\right] \\
&= \Omega\left[\frac{1}{2}\phi^\dagger_{\text{tot}}\left(-\underbrace{\hat{\chi}\phi_{\text{tot}}}_{\Delta\rho_{\text{lq}}} + \rho_{\text{el}} + \Delta\rho_{\text{lq}}\right) - \frac{1}{2}\rho^\dagger_{\text{el}}\hat{K}\rho_{\text{el}}\right] \\
&= \frac{\Omega}{2}\rho^\dagger_{\text{el}}\left[(\hat{K}^{-1} - \hat{\chi})^{-1} - \hat{K}\right]\rho_{\text{el}}
\end{aligned} \quad \text{(D.16)}$$

using $\phi_{\text{tot}} = \hat{K}(\rho_{\text{el}} + \Delta\rho_{\text{lq}})$ and by substituting the Euler-Lagrange equation. The final expression above, upon transformation to real space, yields (8.7).

APPENDIX E

CONVERSIONS BETWEEN CONVENTIONAL AND ATOMIC UNITS

Table E.1: Value in atomic units of conventional units used for experimental measurements. Multiply by the number in the third column to convert quantities to atomic units, and divide by it to convert from atomic units.

Quantity	Measurement unit	Value in atomic units
Energy	eV	$3.6749325 \times 10^{-2}\ E_h$
	kJ/mol	$3.8087989 \times 10^{-4}\ E_h$
	kcal/mol	$1.5936015 \times 10^{-3}\ E_h$
	cm^{-1} (photon wave number)	$4.5563353 \times 10^{-6}\ E_h$
Temperature	K	$3.1668154 \times 10^{-6}\ E_h$
Entropy	J/(mol K)	0.12027221
Length	Å	$1.8897262\ a_0$
Concentration	mol/liter	$8.9238929 \times 10^{-5}\ a_0^{-3}$
Pressure	Pa	$3.3989313 \times 10^{-14}\ E_h/a_0^3$
	bar	$3.3989313 \times 10^{-9}\ E_h/a_0^3$
Surface energy	mN/m = dyn/cm	$6.4230494 \times 10^{-7}\ E_h/a_0^2$
	eV/nm^2	$1.0290850 \times 10^{-4}\ E_h/a_0^2$
Dipole moment	Debye	$0.3934303\ ea_0$
Electric charge	C	$6.2415096 \times 10^{18}\ e$
Electric potential	V	$3.6749325 \times 10^{-2}\ E_h/e$
Capacitance	F	$1.6984011 \times 10^{20}\ e^2/E_h$
Capacitance/area	F/m^2	$0.47560074\ e^2/(E_h a_0^2)$
Molar mass	g/mol	$1822.8885\ m_e$

BIBLIOGRAPHY

[1] C. Adamo and V. Barone. *J. Phys. Chem.*, 110:6158, 1999. p.11, 28, 44, 57

[2] R. F. Adamski and K. M. Merz. *Z. Kristallogr.*, 111:350, 1959. p.46

[3] N. Ahmed, T. Natarajan, and K. R. Rao. *IEEE Trans. Comp.*, C-23:90, 1974. p.237, 239

[4] M. P. Allen and D. J. Tildesley. Computer Simulation of Liquids. 1989. p. 12, 18

[5] M. S. Zei amd K. Wu, M. Eiswirth, and G. Ertl. *Electrochimica Acta*, 45:809, 1999. p.211, 222, 223

[6] M. D. Amos and G. Jackson. *J. Chem. Phys.*, 96:4604, 1992. p.63, 64

[7] C. Amovilli and B. Mennucci. *J. Phys. Chem. B*, 101:1051, 1997. p.187

[8] O. Andreussi, I. Dabo, and N. Marzari. *J. Chem. Phys*, 136:064102, 2012. p. 143, 145, 146, 147, 154, 162, 170, 172, 191, 195

[9] J. Applequist, J. R. Carl, and K.-K. Fung. *J. Am. Chem. Soc.*, 94:2952, 1972. p.140

[10] T. A. Arias. *Rev. Mod. Phys.*, 71:1999, 267. p.95, 100

[11] T. A. Arias, M. C. Payne, and J. D. Joannopoulos. *Phys. Rev. Lett*, 69(7):1077, 1992. p.158

[12] J. A. Barker and D. Henderson. *Rev. Mod. Phys.*, 48:587, 1976. p.12, 18

[13] A. D. Becke. *J. Chem. Phys.*, 98:5648, 1993. p.11, 28

[14] D. Ben-Amotz and K. G. Willis. *J. Phys. Chem.*, 97:7736, 1993. p.121, 124, 178

[15] H. J. C. Berendsen, J. R. Grigera, and T. P. Straatsma. *J. Phys. Chem.*, 91:6269, 1987. p.63, 75, 90, 122, 132, 134, 150, 151

[16] S.J. Binnie. *Ab initio surface energetics: beyond chemical accuracy*. PhD thesis, University College London, 2011. p.160

[17] H. Bludau, K. Wu, M.S. Zei, M. Eiswirth, H. Over, and G. Ertl. *Surf. Sci.*, 402:786, 1998. p.211, 218, 219, 223

[18] L. Blum and D. A. Huckaby. *J. Chem. Phys.*, 94:6887, 1991. p.211

[19] M. Born and R. Oppenheimer. *Annalen der Physik*, 389(20):457, 1927. p.2

[20] D. R. Bowler and T. Miyazaki. *J. Phys.: Cond. Matt.*, 22:074207, 2010. p.11

[21] K. S. Brown and J. P. Sethna. *Phys. Rev. E*, 68:021904, 2003. p.65

[22] R. Car and M. Parrinello. *Phys. Rev. Lett.*, 55:2471, 1985. p.12

[23] N. F. Carnahan and K. E. Starling. *J. Chem. Phys.*, 51:635, 1969. p.86, 120, 153

[24] P. Carrier, S. Rohra, and A. Görling. *Phys. Rev. B*, 75:205126, 2007. p.29, 33, 42, 44

[25] D. M. Ceperley and B. J. Alder. *Phys. Rev. Lett.*, 45:566, 1980. p.10

[26] D. Chandler, J. McCoy, and S. Singer. *J. Chem. Phys.*, 85:5971, 1986. p.19, 70, 77

[27] D. Chandler, J. McCoy, and S. Singer. *J. Chem. Phys.*, 85:5978, 1986. p.19, 70, 78, 79, 82, 103

[28] T.-M. Chang, L. X. Dang, and K. A. Peterson. *J. Phys. Chem. B*, 101:3413, 1997. p.126, 132, 136, 138, 140

[29] G. N. I. Clark, A. J. Haslam, A. Galindo, and G. Jackson. *Molecular Physics*, 104:3561, 2006. p.61, 88

[30] C. Colominas, F. J. Luque, J. Teixido, and M. Orozco. *Chem. Phys.*, 240:253, 1999. p.123, 182, 186

[31] W. A. Curtin and N. W. Ashcroft. *Phys. Rev. A*, 32:2909, 1985. p.19, 20, 61, 88, 118

[32] J. A. Dean. *Lange's Handbook of Chemistry*. McGraw-Hill, 15 edition, 1999. p.73, 109

[33] K. Ding, D. Chandler, S. J. Smithline, and A. D. J. Haymet. *Phys. Rev. Lett.*, 59:1698, 1987. p.20, 61, 78, 79, 88, 118

[34] P. A. M. Dirac. *Proc. Royal Soc. London. A*, 123:714, 1929. p.2

[35] P. A. M. Dirac. *Proc. Cam. Phil. Soc.*, 26:376, 1930. p.6

[36] P. A. M. Dirac. *Proc. Camb. Phil. Soc.*, 26:376, 1930. p.9

[37] I. Duchemin and F. Gygi. *Comp. Phys. Comm*, 181:855, 2010. p.33, 40

[38] P. Ewald. *Ann. Phys.*, 369:253, 1921. p.40, 156, 244, 248, 249

[39] K. M. Ewool and H. M. Strauss. *J. Chem. Phys*, 58:5835, 1973. p.139

[40] J.-L. Fattebert and F. Gygi. *Int. J. Quant. Chem.*, 93:139, 2003. p.143, 145, 146

[41] E. Fermi. *Rend. Accad. Naz. Lincei*, 6:602, 1927. p.9

[42] R. Fletcher and C. M. Reeves. *Comp. J.*, 7:149, 1964. p.72, 101

[43] W. M. C. Foulkes, L. Mitas, R. J. Needs, and G. Rajagopal. *Rev. Mod. Phys.*, 73:33, 2001. p.5

[44] M. Frigo and S. G. Johnson. *Proc. IEEE*, 93:216, 2005. p.239

[45] M. J. Frisch et al. Gaussian 09. Gaussian Inc. Wallingford CT 2009. p.170

[46] P. Frodl and S. Dietrich. *Phys. Rev. A*, 45:7330, 1992. p.77

[47] R. L. Fulton. *J. Chem. Phys.*, 130:204503, 2009. p.134, 150

[48] P. Giannozzi et al. PWSCF. *J. Phys.: Condens. Mat.*, 21:395502, 2009. p.170

[49] G. J. Gloor, F. J. Blas, E. M. del Rio, E. de Miguel, and G. Jackson. *J. Phys. Chem. C*, 111:15513, 2007. p.61

[50] G. J. Gloor, G. Jackson, F. J. Blas, E. M. del Rio, and E. de Miguel. *J. Chem. Phys*, 121:12740, 2004. p.61

[51] R. Gomez, H. S. Yee, G. M. Bommarito, J. M. Feliu, and H. D. Abru na. *Surf. Sci*, 335:101, 1995. p.210

[52] M. Graf and D. Potts. *Num. Func. Anal. and Optim.*, 30:665, 2009. p.72, 233, 236

[53] S. Grimme. *J. Comput. Chem*, 27:1787, 2006. p.24, 187, 188, 191, 206

[54] H. K. Gummel. *IEEE Trans. Elec. Devices*, 11:455, 1964. p.159

[55] F. Gygi and A. Baldereschi. *Phys. Rev. B*, 34:4405, 1986. p.29, 32

[56] L. Haar, J. S. Gallagher, and G. Kell. *NBS/NRC Steam Tables*. Taylor & Francis, 1984. p.63, 65

[57] J.-P. Hansen and I. R. McDonald. *Theory of Simple Liquids, Third Edition*. Academic Press, 3 edition, 2006. p.18, 87, 225

[58] H. Hansen-Goos and R. Roth. *J. Phys.: Cond. Matt.*, 18:8413, 2006. p.62, 70, 86

[59] H. Hansen-Goos and R. Roth. *J. Chem. Phys.*, 124:154506, 2006. p.64

[60] R. H. Hardin and N. J. A. Sloane. Spherical designs, a library of putatively optimal spherical t-designs, 2002. p.233, 234, 236

[61] D. E. Hare and C. M. Sorensen. *J. Chem. Phys.*, 87:4840, 1987. p.63, 65

[62] W. M. Haynes, editor. *CRC Handbook of Physics and Chemistry 93rd ed*. Taylor and Francis, 2012. p.46, 121, 129, 139, 198, 216

[63] L. Hedin. *Phys. Rev.*, 139:A796. p.11

[64] E. Herrero, L. J. Buller, and H. D. Abru na. *Chem. Rev.*, 101:1897, 2001. p. 209

[65] K. F. Herzfeld. *Phys. Rev.*, 29:701, 1927. p.128, 129

[66] J. Heyd, G. E. Scuseria, and M. Ernzerhof. *J. Chem. Phys.*, 118:8207, 2003. p.29

[67] D. M. Heyes, M. Barber, and J. H. R. Clarke. *J. Chem. Soc. Faraday Trans. II*, 73:1485, 1977. p.249

[68] P. Hohenberg and W. Kohn. *Phys. Rev.*, 136:B864, 1964. p.6

[69] N. A. W. Holzwarth and X. Xu. *Phys. Rev. B*, 84:113102, 2011. p.30

[70] D. M. Huang, P. L. Geissler, and D. Chandler. *J. Phys. Chem. B*, 105:6704, 2001. p.73, 74, 110, 111, 112

[71] D. A. Huckaby and L. Blum. *J. Electroanal. Chem.*, 315:255, 1991. p.211

[72] M. S. Hybertsen and S. G. Louie. *Phys. Rev. B*, 34:5390, 1986. p.11, 29

[73] S. Ismail-Beigi. *Phys. Rev. B*, 73:233103, 2006. p.242, 245, 246, 247

[74] S. Ismail-Beigi and T. A. Arias. *Phys. Rev. Lett.*, 82:2127, 1999. p.36, 49

[75] S. Ismail-Beigi and T. A. Arias. *Comp. Phys. Comm.*, 128:1, 2000. p.78, 93, 94, 95, 100, 101, 158

[76] G. Jeanmairet, M. Levesque, R. Vuilleumier, and D. Borgis. *J. Phys. Chem. Lett.*, 4:619, 2013. p.228

[77] C. A. Jefferey and P. H. Austin. *J. Chem. Phys*, 110:484, 1999. p.62, 63, 64, 65, 91, 92, 120

[78] W. L. Jorgensen, J. Chandrasekhar, J. D. Madura, R. W. Impey, and M. L. Klein. *J. Chem. Phys.*, 79:926, 1983. p.136

[79] Kiyoshi Kanamura, Soshi Shiraishi, and Zenichiro Takehara. *J. Electrochem. Soc.*, 143(7):2187–2197, 1996. p. 166

[80] J. G. Kirkwood. *J. Chem. Phys*, 7:911, 1939. p.129

[81] W. Kohn. *Phys. Rev.*, 115:809, 1959. p.35

[82] W. Kohn and L. Sham. *Phys. Rev.*, 140:A1133, 1965. p.9

[83] D. M. Kolb. *Advances in Electrochemistry and Electrochemical Engineering*, volume 11. Wiley, 1978. p.210

[84] D. M. Kolb, M. Przasnyski, and H. Gerischer. *Electroanal. Chem. Interf. Electrochem.*, 54:25, 1974. p.211

[85] A. V. Krukau, O. A. Vydrov, A. F. Izmaylov, and G. E. Scuseria. *J. Chem. Phys*, 125:224106, 2006. p.44, 57

[86] J. Langlet, P. Claverie, J. Caillet, and A. Pullman. *J. Phys. Chem.*, 92:1617, 1988. p.186

[87] E. Leiva. *Electrochimica Acta*, 41:2185, 1996. p.14

[88] E. Leiva. *Electrochimica Acta*, 41:2185, 1996. p.212

[89] D. Lemoine. *J. Chem. Phys*, 101:3936, 1994. p.238

[90] K. Letchworth-Weaver and T. A. Arias. *Phys. Rev. B*, 86:075140, 2012. p. 143, 145, 146, 152, 154, 155, 158, 159, 162, 164, 203, 213, 216

[91] K. Letchworth-Weaver, R. Sundararaman, and T. A. Arias. *(under preparation)*. p.23, 24, 26, 135, 141, 142, 228

[92] M Levy. *PNAS*, 76:6062, 1979. p.6

[93] Y. Levy and J. N. Onuchic. *Ann. Rev. Biophys.*, 35:389, 2006. p.12

[94] P. Liao, J. A. Keith, and E. A. Carter. *J. Am. Chem. Soc.*, 134:13296, 2012. p. 15

[95] E. H. Lieb and J. L. Lebowitz. *Advances in Mathematics*, 9:316, 1972. p.1, 16

[96] J. Lischner and T. A. Arias. *Phys. Rev. Lett.*, 101:216401, 2008. p.19, 61, 70, 77, 78, 80, 82, 103, 117, 118, 123, 129, 226

[97] J. Lischner and T. A. Arias. *J. Phys. Chem. B*, 114:1946, 2010. p.20, 61, 75, 78, 80, 84, 88, 91, 106, 107, 108, 109, 114, 118, 119, 123, 125, 129, 152, 227

[98] S. G. Louie, S. Froyen, and M. L. Cohen. *Phys. Rev. B*, 26(4):1738, 1982. p. 158, 160

[99] H. Löwen. *Journal of Physics: Condensed Matter*, 14:11897, 2002. p. 23

[100] C. A. Lucas, N. Markovic, and P. N. Ross. *Phys. Rev. B*, 56:3651, 1997. p. 210

[101] R. J. Magyar, A. E. Mattsson, and P. A. Schultz. *Metallic Systems: A Quantum Chemist's Perspective*, chapter Some Practical Considerations for Density Functional Theory Studies of Chemistry at Metal Surfaces. CRC Press, 2011. p. 160

[102] M. Mantina, A. C. Chamberlin, R. Valero, C. J. Cramer, and D. G. Truhlar. *J. Phys. Chem. A*, 113:5806, 2009. p. 178, 197, 198

[103] N. Markovic, H. A. Gasteiger, C. A. Lucas, I. M. Tidswell, and P. N. Ross. *Surf. Sci.*, 335:91, 1995. p. 210, 211, 222, 223

[104] N. Markovic and P. N. Ross. *Langmuir*, 9:580, 1993. p. 210

[105] Bryan Marten, Kyungsun Kim, Christian Cortis, Richard A. Friesner, Robert B. Murphy, Murco N. Ringnalda, Doree Sitkoff, and Barry Honig. *J. Phys. Chem.*, 100:11775–11788, 1996. p. 23, 163, 190

[106] G. J. Martyna and M. E. Tuckerman. *J. Chem. Phys*, 110:2810, 1999. p. 37, 242, 244, 245, 247

[107] N. Marzari and D. Vanderbilt. *Phys. Rev. B*, 56:12847, 1997. p. 35, 225

[108] N. D. Mermin. *Phys. Rev.*, 137:A1441, 1965. p. 7

[109] H. J. Monkhorst and J. D. Pack. *Phys. Rev. B*, 13:5188, 1976. p. 32

[110] J. J. Mortensen, K. Kaasbjerg, S. L. Frederiksen, J. K. Nørskov, J. P. Sethna, and K. W. Jacobsen. *Phys. Rev. Lett.*, 95:216401, 2005. p. 65

[111] K. Moulopoulos and N. W. Ashcroft. *Phys. Rev. A*, 43:1685, 1991. p. 16

[112] J. E. Moussa, P. A. Schultz, and J. R. Chelikowsky. *J. Chem. Phys.*, 136:204117, 2012. p. 29

[113] M.W.Schmidt et al. GAMESS. *J. Comput. Chem.*, 14:1347, 1993. p.170

[114] H. D. Abru na, J. M. Feliu, J. D. Brock, L. J. Buller, E. Herrero, J. Li, R. Gomez, and A. Finnefrock. *Electrochimica Acta*, 43:2899, 1998. p.210

[115] NIST. *Computational Chemistry Comparison and Benchmark Database*. `http://cccbdb.nist.gov`. p.161, 212, 216

[116] Onsager. *J. Am. Chem. Soc.*, 58:1486, 1936. p.129

[117] OPIUM. *Pseudopotential generation project*. `http://opium.sf.net`. p. 160, 198

[118] M. Otani and O. Sugino. *Phys. Rev. B*, 73:115407, 2006. p.155

[119] M. T. Paffett, C. T. Campbell, T. N. Taylor, and S. Srinivasan. *Surf. Sci.*, 154:284, 1985. p.210

[120] J. Paier, R. Hirschl, M. Marsman, and G. Kresse. *J. Chem. Phys.*, 122:234102, 2005. p.40, 44

[121] J. Paier, M. Marsman, K. Hummer, G. Kresse, I. C. Gerber, and J. G. Angyan. *J. Chem. Phys.*, 124:154709, 2006. p.44

[122] T. Pajkossy and D. M. Kolb. *Electrochimica Acta*, 46:30633071, 2001. p.165, 166

[123] R G Parr and W Yang. *Density-Functional Theory of Atoms and Molecules*. Oxford University Press, 1989. p.8, 10

[124] M. C. Payne, M. P. Teter, D. C. Allan, T. A. Arias, and J. D. Joannopoulos. *Rev. Mod. Phys.*, 64:1045, 1992. p.242

[125] B. Peng and Y.-X. Yu. *J. Phys. Chem. B*, 112:15407, 2008. p.19, 87, 89, 90, 99, 122

[126] J. K. Percus. *Journal of Statistical Physics*, 15:505, 1976. p.19, 85

[127] Perdew and Zunger. *Phys. Rev. B*, 23:5048, 1981. p.10, 199

[128] J. P. Perdew, K. Burke, and M. Ernzerhof. *Phys. Rev. Lett.*, 77:3865, 1996. p. 10, 23, 24, 44, 46, 57, 160, 199

[129] J. P. Perdew, A. Ruzsinszky, G. I. Csonka, L. A. Constantin, and J. Sun. *Phys. Rev. Lett.*, 103:026403, 2009. p.10, 161, 212

[130] S. A. Petrosyan, J.-F. Briere, D. Roundy, and T .A. Arias. *Phys. Rev. B*, 75:205105, 2007. p.21, 143, 145, 146, 162, 179

[131] R. A. Pierotti. *Chem. Rev.*, 76:717, 1976. p.121, 123, 124, 178, 181, 185

[132] E. Polak and G. Ribiere. *Rev. Fr. Inform. Rech. Oper.*, 16:35, 1969. p.103, 158, 159

[133] Z. Raza, D. Alfe, C. G. Salzmann, J. Klimeš, A. Michaelidesade, and B. Slater. *Phys. Chem. Chem. Phys.*, 13:19788, 2011. p.46, 51

[134] Y. Rosenfeld. *Phys. Rev. Lett.*, 63:980, 1989. p.19, 62, 77, 85, 119

[135] R. Roth. *J. Phys. Cond. Matt.*, 22:063102, 2010. p.19, 62, 71, 77, 86, 99, 119

[136] C. A. Rozzi, D. Varsano, A. Marini, E. K. U. Gross, and A. Rubio. *Phys. Rev. B*, page 205119, 2006. p.242, 246, 247

[137] G. Rusakoff. *Am. J. Phys.*, 38:1188, 1970. p.128

[138] E. E. Salpeter and H. A. Bethe. *Phys. Rev.*, 84:1232, 1951. p.11, 29

[139] C. Sanchez and E. P. M. Leiva. *Electrochimica Acta*, 45:691, 1999. p.212, 219

[140] K. A. Schwarz, R. Sundararaman, K. Letchworth-Weaver, T. A. Arias, and R. G. Hennig. *Phys. Rev. B*, 85:201102(R), 2012. p.22

[141] Soshi Shiraishi, Kiyoshi Kanamura, and Zenichiro Takehara. *J. Appl. Electrochem.*, 29:869–881, 1999. p.
166

[142] J. L.F. Da Silva, C. Stampfl, and M. Scheffler. *Surf. Sci.*, 600:703. p.212

[143] J.-C. Soetens, G. Jansen, and C. Millot. *Mol. Phys.*, 96:1003, 1999. p.122, 126, 132, 136, 138

[144] Y. Soldo, E. Sibert, G. Tourillon, J. L. Hazemann, J. P. Levy, D. Aberdam, R. Faure, and R. Durand. *Electrochimica Acta*, 47:3081, 2002. p.211, 223

[145] A. K. Soper. *Chem. Phys.*, 258:121, 2000. p. 62, 68, 69, 92, 106, 107, 108

[146] J. Spencer and A. Alavi. *Phys. Rev. B*, 77:193110, 2008. p. 30, 34, 40, 43

[147] E. Spohr. *J. Chem. Phys*, 107:6342, 1997. p. 249

[148] SpringerMaterials. *The Landolt-Bornstein Database*. `http://www.springermaterials.com`. p. 167

[149] V. Sudha and M. V. Sangaranarayanan. *J. Phys. Chem. B*, 107:3907, 2003. p. 211

[150] V. Sudha and M. V. Sangaranarayanan. *J. Chem. Sci*, 117:207, 2005. p. 211

[151] J. Sun, M. Marsman, A. Ruzsinszky, G. Kresse, and J. P. Perdew. *Phys. Rev. B*, 83:121410(R), 2011. p. 161, 212

[152] R. Sundararaman and T. A. Arias. Fluid1D: a sub-project of JDFTx. `http://svn.code.sf.net/jdftx/code/trunk/fluid1D`, 2012. p. 94, 106

[153] R. Sundararaman, K. Letchworth-Weaver, and T. A. Arias. *J . Chem. Phys.*, 137:044107, 2012. p. 89, 106, 107, 109, 122, 237, 240

[154] R. Sundararaman, K. Letchworth-Weaver, and T. A. Arias. JDFTx. `http://jdftx.sourceforge.net`, 2012. p. 44, 72, 78, 94, 101, 132, 158, 160, 170, 212, 248

[155] G. Sutmann. *J. Electroanal. Chem.*, 450:289, 1998. p. 75

[156] Attila Szabo and Neil S. Ostlund. *Modern Quantum Chemistry: Introduction to Advanced Electronic Structure Theory*. Dover Publications, 1996. p. 5, 60

[157] David J. Tannor, Bryan Marten, Robert Murphy, Richard A. Friesner, Doree Sitkoff, Anthony Nicholls, Murco Ringnalda, William A. Goddard, and Barry Honig. *J. Am. Chem. Soc.*, 116:11875–11882, 1994. p. 23, 163, 190

[158] F.-M. Tao and E. A. Mason. *J. Chem. Phys*, 100:9075, 1994. p. 121

[159] P. Tarazona. *Phys. Rev. Lett.*, 84:694, 2000. p. 19, 62, 70, 86, 119

[160] A. Taylor and R. M. Jones. *Silicon Carbide - A High Temperature Semiconductor*. Pergamon Press, 1960. p. 46

[161] L. H. Thomas. *Proc. Cambridge Phil. Soc.*, 23:542, 1927. p. 9

[162] A. Tkatchenko and M. Scheffler. *Phys. Rev. Lett.*, 102:073005, 2009. p. 187

[163] J. Tomasi, B. Mennucci, and R. Cammi. *Chem. Rev.*, 105:2999, 2005. p. 25, 142, 145, 146, 147, 162, 170, 172, 173, 182, 187, 197

[164] H. Totsuji. *Phys. Rev. A*, 38:5440, 1988. p. 16

[165] S. Trasatti and E. Lust. *Modern Aspects of Electrochemistry*, 33:1–215, 1999. p. 164, 165, 216, 217

[166] P. Vassilev, R. A. van Santen, and M. T. M. Koper. *J. Chem. Phys.*, 122:054701, 2005. p. 13

[167] C. Vega and E. de Miguel. *J. Chem. Phys.*, 126:154707, 2007. p. 110, 111, 112, 122

[168] J. D. Weeks, D. Chandler, and H. C. Andersen. *J. Chem. Phys.*, 54:5237, 1971. p. 87

[169] B. Wenzien, G. Cappellini, and F. Bechstedt. *Phys. Rev. B*, 51:14701, 1995. p. 29, 33

[170] M. S. Wertheim. *Phys. Rev. Lett.*, 10:321, 1963. p. 86

[171] M. S. Wertheim. *J. Chem. Phys.*, 87:7323, 1987. p. 61, 64, 88

[172] J. H. White and H. D. Abru na. *J. Phys. Chem*, 94:894, 1990. p. 210

[173] J. H. White and H. D. Abru na. *J. Electroanal. Chem*, 300:521, 1991. p. 210

[174] E P Wigner. *Group theory and its application to the quantum mechanics of atomic spectra*. Academic Press, New York, 1959. p. 84, 202, 251, 253

[175] A. J. Williamson, G. Rajagopal, R. J. Needs, L. M. Fraser, W. M. C. Foulkes, Y. Wang, and M. Y. Chou. *Phys. Rev. B*, 55:R4851, 1997. p. 30, 34

[176] X. Wu, A. Selloni, and R. Car. *Phys. Rev. B*, 79:085102, 2009. p.35, 225

[177] X. Xu and W. A. Goddard. *J. Chem. Phys.*, 121:4068, 2004. p.11, 28

[178] I.-C. Yeh and M. Berkowitz. *J. Chem. Phys.*, 110:7935, 1999. p.75, 113, 114, 132, 151

[179] Y.-X. Yu and J. Wu. *J. Chem. Phys.*, 117:2368, 2002. p.71, 122

[180] S. Zhao, Z. Jin, and J. Wu. *J. Phys. Chem. B*, 115:6971, 2011. p.61, 118, 228